Low-Mass Drell-Yan Cross-Section Measurements with the LHCb Experiment

---

Dissertation

zur

Erlangung der naturwissenschaftlichen Doktorwürde
(Dr. sc. nat.)

vorgelegt der
Mathematisch-naturwissenschaftliche Fakultät
der

Universität Zürich

von
Nicola Chiapolini
von
Winterthur ZH

Promotionskomitee
Prof. Dr. Ulrich Straumann (Vorsitz)
Dr. Jonathan Anderson
Dr. Katharina Müller

Zürich, 2015

Abstract

The LHCb experiment is one of the four main experiments at CERN's flagship accelerator LHC. It is designed for the study of particles containing b or c quarks. However, due to its very forward angular coverage of approximately 30 to 250 mrad, the experiment is well suited to contribute to electroweak physics as well. Measurements of electroweak boson production at LHCb provide important insight into the parton distribution functions of the proton. In addition precision measurements can test the Standard Model where predictions are most precise.

This thesis presents the measurements of the low-mass Drell-Yan production cross section with subsequent decay into two muons. For the main analysis, the full 1 fb^{-1} collected by LHCb in 2011 at $\sqrt{s} = 7$ TeV is analysed. The cross section is measured differentially as a function of the di-muon mass and the di-muon rapidity. The results obtained are in agreement with the predictions calculated at next-to-next-to leading order in perturbative quantum chromodynamics. The previous measurement based on the data collected in 2010 is included in the appendix of this thesis.

Zusammenfassung

Das LHCb Experiment ist eines der vier Hauptexperimente an CERNs Vorzeigebeschleuniger LHC. Es wurde konstruiert um Teilchen zu untersuchen, die b und c Quarks enthalten. Aufgrund seiner vorwärts gerichteten Winkelabdeckung von ungefähr 30 bis 250 mrad, ist das Experiment aber auch gut positioniert um die Physik der elektro-schwachen Wechselwirkung zu untersuchen. Messungen der Produktion elektro-schwacher Bosonen durch LHCb leisten einen wichtigen Beitrag zum Wissen über die Parton-Verteilungsfunktionen des Protons. Dort wo exakte Vorhersagen bestehen, erlauben Präzisionsmessungen zudem das Standard Modell zu überprüfen.

Diese Arbeit präsentiert eine Messung des Wirkungsquerschnitts für Drell-Yan Produktion bei tiefen Massen mit anschliessendem Zerfall in zwei Muonen. Für die Hauptanalyse, wird das gesamte Datenset von 1 fb^{-1} analysiert, das im Jahr 2011 bei $\sqrt{s} = 7$ TeV von LHCb gesammelt wurde. Der Wirkungsquerschnitt wird als Funktion der Di-Muon Masse sowie der Di-Muon Rapidität bestimmt. Die Resultate stimmen mit den theoretischen Vorhersagen überein. Die Vorhersagen wurden mit störungstheoretischer Quantenchromodynamik bis zu übernächster Ordnung berechnet. Die vorherige Messung basierend auf den Daten aus dem Jahr 2010 ist dieser Arbeit im Anhang beigefügt.

Contents

Chapter 1

Introduction

Like the LEGO models I built as a boy, the universe is built from a small set of building blocks. Particle physics pushes the boundaries of our knowledge about these building blocks. It stands on the shoulders of many a great physicist. Thanks to them we have a very powerful model to describe the fundamental forces and particles found in nature. Still, as with every science, there remain many open questions and with every answer new questions arise.

While the founding experiments of our field were the work of a handful of physicists, today's experiments are the collaborative effort of groups with several thousand people. While early experiments could be lifted by a single captive balloon, today's experiments contain more iron than the Eiffel Tower. In addition to the scientific problems, many organisational, logistic and sometime political challenges must therefore be overcome to succeed. The results published in these last years prove, what our common effort achieves. Physicists from all parts of the world and with diverse cultural backgrounds, are united and motivated by the search for deeper insight into the laws of nature.

With this thesis I summarise and present my contribution to our common undertaking. The first part (Part I) presents the context of this thesis: CERN, the LHCb experiment and the Standard Model of particle physics. In its last chapter a general introduction into Drell-Yan cross section measurements is presented.

The main work is contained in the second part (Part II). It presents a cross section measurement for Drell-Yan production in the di-muon decay channel. The full integrated luminosity of 1 fb^{-1} collected by LHCb in 2011 at $\sqrt{s} = 7$ TeV was analysed. The cross section was measured differentially as a function of the di-muon mass and the di-muon rapidity. The previous measurement based on the data collected in 2010 is included in the appendix (Appendix C).

Part I

The Context

Chapter 2

CERN and the LHCb Experiment

2.1 CERN

The European Organisation for Nuclear Research (CERN) is an international organisation with seat in Geneva. The organisation is dedicated to advance fundamental physics and operates the worlds largest particle physics laboratory. The organisation and its laboratory look back on 60 years of history. In 1952, based on the proposal of visionary European scientists, 11 countries signed an agreement establishing a provisional European council for nuclear research (Conseil Européen pour la Recherche Nucléaire, CERN). By fall 1954, Geneva had been selected as the location for the CERN Laboratory; construction had started and the 12 founding members had ratified the convention establishing the organisation. The first accelerator, the 600 MeV Synchrocyclotron, started up in 1957. At that time, pure physics research concentrated on understanding the inside of the atom. As the frontier of knowledge was pushed to smaller scales, the focus of CERN shifted towards particle physics and larger and more powerful accelerators were needed. Over the years a large chain of accelerators was built (Fig. 2.1).

The research program enabled by these tools led to many important discoveries and inventions, including the discovery of the electroweak bosons, the invention of the world wide web and the discovery of a Higgs like boson. Today, CERN unites 21 member states and over 10 000 scientists, doing research at one of its many experiments (CERN 2014a; CERN 2014b).

2.2 The LHC

CERN's present flagship accelerator, the Large Hadron Colider (LHC), is located in a ring-shaped tunnel 100 m under the Swiss-French border. The ring-tunnel has a circumference of 27 km and houses more then 9500 superconducting magnets. Figure 2.2 shows a diagram

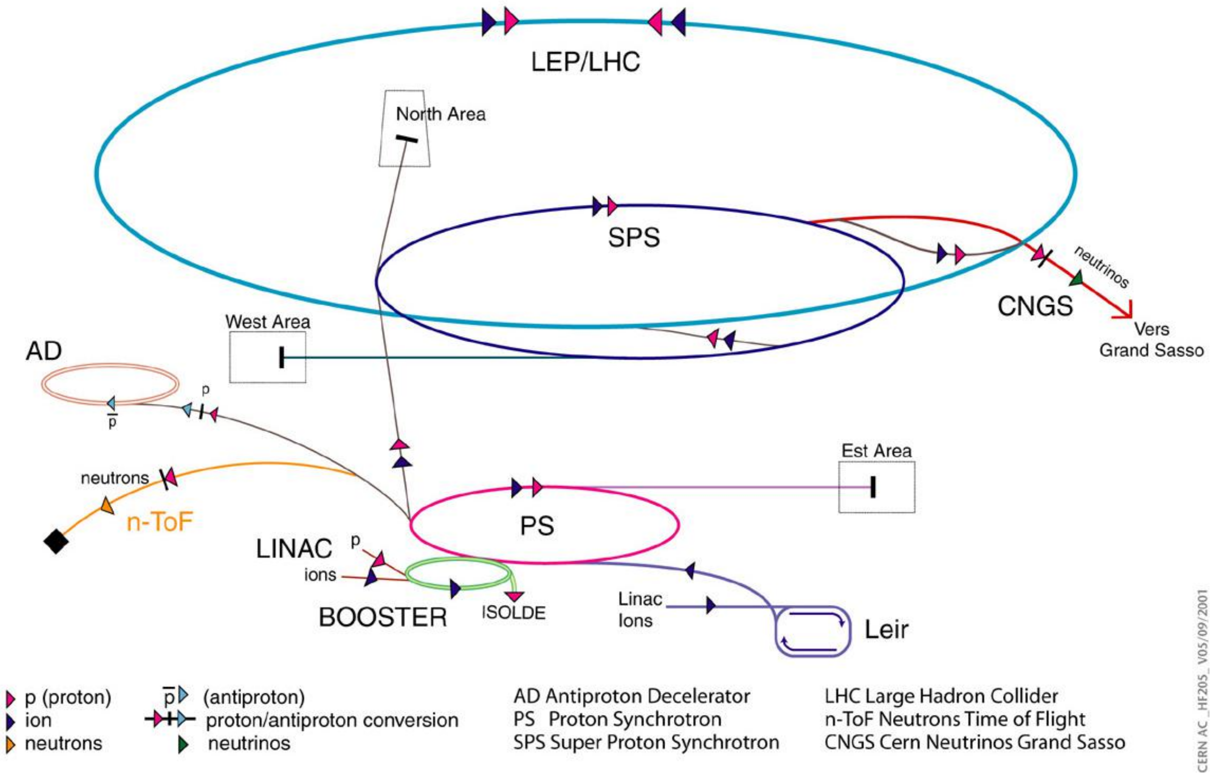

Figure 2.1: The CERN accelerator chain including operating and approved projects (Caron 2001).

of a dipole magnet as used at the LHC. Embedded in the magnets are two beam pipes - tubes kept at ultrahigh vacuum. Inside these tubes the high-energy particle beams circulate in opposite directions. Particle beams consist of sequences of bunches, each containing up to 1.7×10^{11} particles (Evans and Bryant 2008). For the studies presented in this thesis, both beams contained protons. Alternatively the LHC can be operated with lead ions. The two beams are brought to collision at four collision points. Into huge caverns around these collision points the main LHC experiments ALICE, ATLAS, CMS and LHCb were built. LHCb is described in detail in Section 2.3.

The LHC was designed to run with two proton beams with an energy of 7 TeV each. During the three years of Run 1, the accelerator was not operated at its design configuration however. An accident shortly after the first start-up in 2008 had highlighted a problem in many high-current connections between the superconducting magnets. The decision was then taken to run at a safe energy of approximately half the design energy and to delay the repair works until the first long shutdown that started in 2013. After this shutdown, the LHC will be operated at its nominal energy. Table 2.1 gives an overview of the run conditions during the years of Run 1, compared to the designed values.

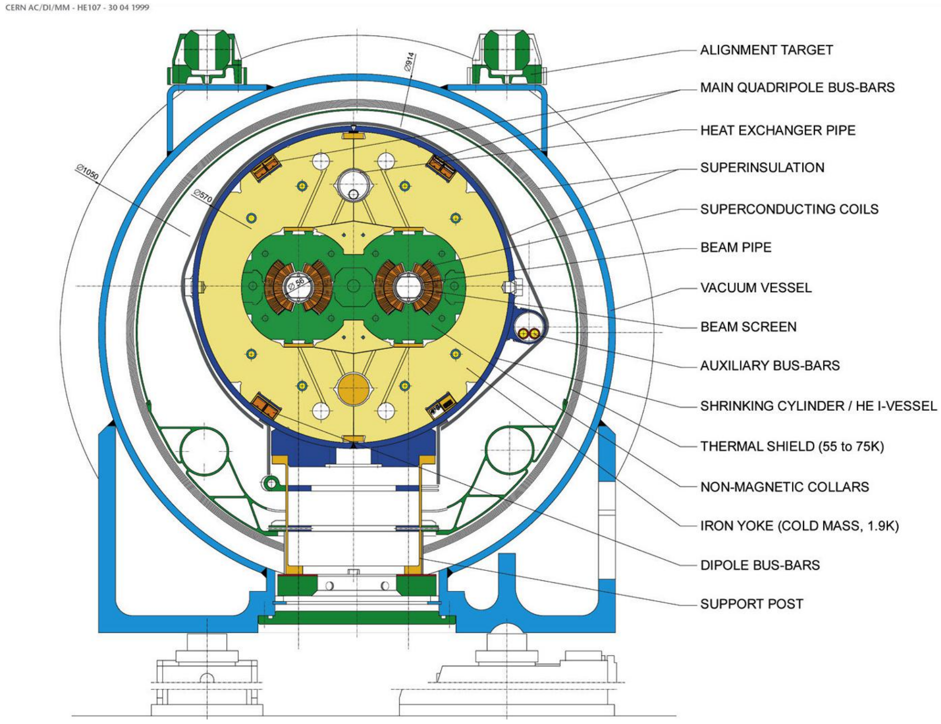

Figure 2.2: Diagram of an LHC dipole magnet (CERN, AC Team 1999).

Table 2.1: Properties of the LHC beam during Run 1.

	design	2010	2011	2012
beam energy of one beam	7 TeV	450 GeV	3.5 TeV	4 TeV
max number of bunches	2808	368	1380	1380

2.3 The LHCb Experiment

The LHCb detector (LHCb Collaboration 2008) is a single-arm forward spectrometer with an angular coverage of approximately 30 to 250 mrad. It is designed for the study of particles containing b or c quarks. The detector includes a high-precision tracking system consisting of four parts (VELO, TT, Magnet and T1-T3) explained in more detail in Section 2.3.1. Different types of charged hadrons are identified using information from two ring-imaging Cherenkov detectors (RICH). Photon, electron and hadron candidates are identified by a calorimeter system consisting of scintillating-pad (SPD) and preshower (PS) detectors, an electromagnetic calorimeter (ECAL) and a hadronic calorimeter (HCAL). Muons are identified by a system composed of alternating layers of iron and multiwire proportional chambers (M1-M5). The trigger consists of a hardware and a software stage. The hardware stage is based on information from the calorimeter and muon systems, while the software stage, applies a more complete event reconstruction.[1]

The trigger system is discussed in Section 2.3.2. Figure 2.3 shows the LHCb detector with its different subsystems. The collision point is located to the left of the picture inside the VELO. The incoming proton beams travel along the beam pipe in the center of the detector. The LHCb coordinate system is defined such that the z-axis points from the collision point into the detector along the beam pipe. The y-axis points upwards while the x-axis points horizontally outwards of the LHC ring, such that the three axes form a right-handed coordinate system. In addition the positive and negative x-direction are often refered to as A-side (Access) and C-side (Cryo) respectively.

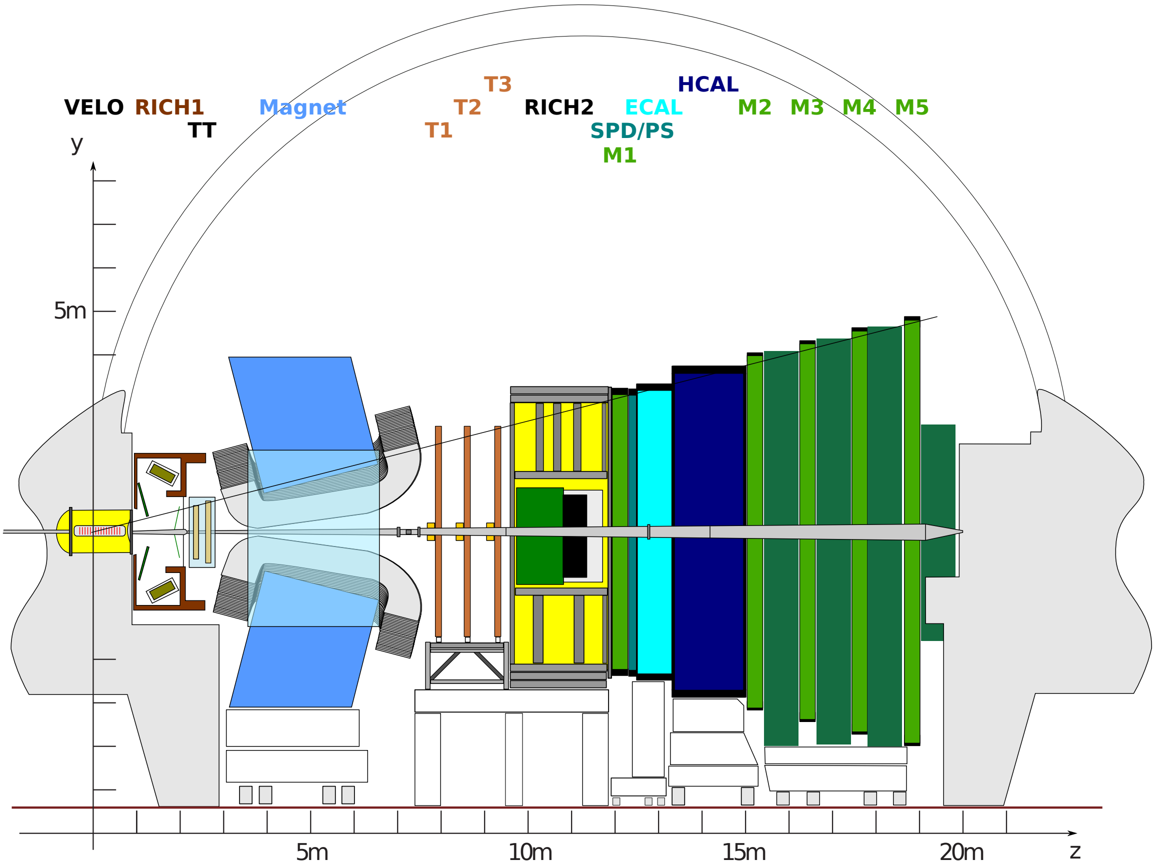

Figure 2.3: Side view of the LHCb detector from the inside of the LHC ring.

The measurements from the different sub-detector are combined in the reconstruction. A first reconstruction happens already in the trigger system, but the full information is only processed offline. Both the trigger system, as well as the offline reconstruction, use the same code base. The reconstruction software creates a tree of data-objects representing

---

[1] This paragraph is a minimally modified version of the the official wording for the LHCb detector description used in most LHCb publications.

the measurements from different sets of sub-detectors. The top-level data-objects are events. An event contains all the information attributed to one bunch crossing.

2.3.1 The Tracking System

The tracking system consists of the following parts:

VELO The vertex locator (LHCb Collaboration 2001) is a silicon-strip vertex detector surrounding the *pp* interaction region. The VELO is designed to precisely measure the position of the collision point and provide a first measurement of the flight path of the decay products. It consists of 21 modules, each containing two silicon microstrip sensors. The two sensors measure the radius (r) and azimuthal angle (ϕ) respectively, thereby allowing a precise measurement in all three dimensions and a fast reconstruction of tracks. The inner edge of the sensors is 8 mm away from the beam. To prevent damage from stray particle beams, the VELO has to be opened during the injection phase of the LHC. The VELO therefore consists of two movable halfs that can be retracted from the beam into a parking position. An illustration of one VELO half is shown in Fig. 2.4a.

TT The Tracker Turicensis is a large-area silicon-strip detector located upstream of the dipole magnet. A detailed description of the TT is given in Section 4.1.

Magnet The dipole magnet consists of two saddle shaped aluminium coils inside an iron yoke and is operated at environment temperature. The field created by the magnet has its main component along the y-axis. In the z-direction the field has a large gradient, resulting in field of less then 2 mT inside the RICH envelopes but an overall bending power of 4 Tm. The magnet deflects charged particles in the positive or negative x-direction allowing the determination of the charge of a passing particle based on the observed curvature. To minimise systematic effects, the polarity of the magnetic field can be reversed. Data taken with the two different polarities are assigned to the magnet Up or the magnet Down dataset, depending on the direction of the field's y-component.

T1, T2, T3 The T-Stations (Arink et al. 2014) are three tracking stations placed downstream of the magnet. Each station consists of silicon-strip detectors (IT) in the inner and straw drift tubes (OT) in the outer region (see Fig. 2.4b). Silicon-strip detectors are used for the IT, as the particle flux is highest close to the beam pipe. An IT station contains four boxes with four sensor layers each. The boxes are places around the beam pipe, at a distance of 9.9 cm at the closest point. Using drift tubes in the OT allows coverage of the full LHCb acceptance at an acceptable price. The drift tubes are arranged into two staggered layers to form modules. In total, the OT comprises about 55 000 single straw tube channels. A standard module measures 4.9 m × 0.34 m, but smaller modules are used in the region above and below IT. Each module is a standalone unit and is served separately with drift gas and high voltage.

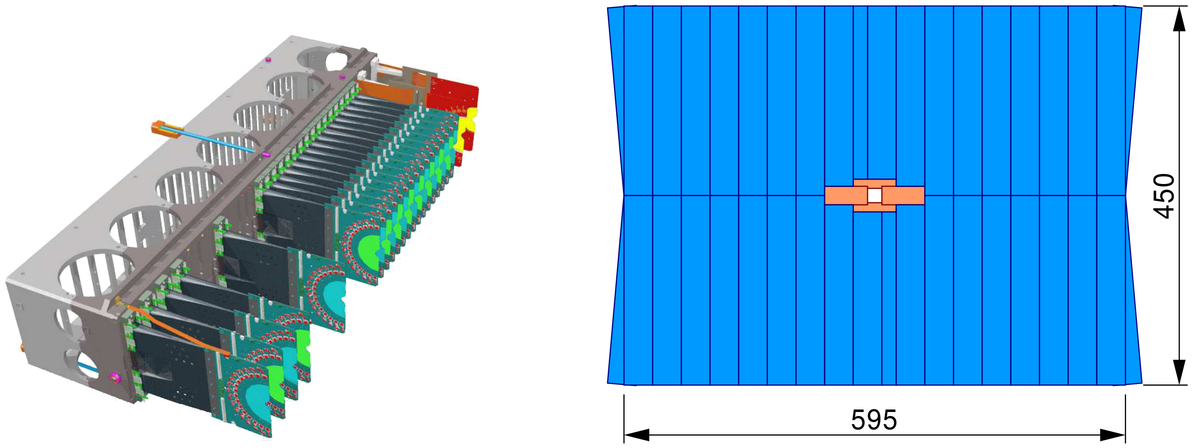

(a) Exploded view of the module support and the modules of one VELO half (taken from LHCb Collaboration 2008).

(b) Front view of a tracking station with the OT modules in blue and the IT modules in orange. Dimensions are given in cm (taken from LHCb Collaboration 2002).

Figure 2.4: Illustrations for two sub-detectors of LHCb.

A particle passing the three tracking sub-detectors leaves so called hits, usually charge deposits, that are then registered in the readout electronics. In addition to the tracking parts listed above, the multiwire proportional chambers of the muon systems (Alves Jr. et al. 2013) allow for a rough position measurement as well. The muon stations can therefore be used as additional tracking detectors when reconstructing particle trajectories. This is exploited in the Muon-TT method (De Cian et al. 2013) used to determine track reconstruction efficiencies (see Section 9.4).

The data-objects reconstructed from the information from the different components of the tracking system are called tracks. Tracks should correspond to the true trajectory of a particle passing the detector. The algorithms used to reconstruct tracks and to identify muons are discussed in Sections 2.3.1.2 and 2.3.1.3.

2.3.1.1 Properties of Tracks

Based on the reconstructed tracks several properties of decays are determined. For the studies presented in this thesis, the following variables are important.

vertex location A vertex is the location of a source of several particles. The primary vertex (PV) is at the interaction point of the colliding protons. It is reconstructed by searching for points with many intersecting particle trajectories. The VELO allows the measurement of vertices with very high accuracy (see Fig. 2.8b). However vertices can only be reconstructed for particles that decay inside the VELO. Several vertices can be associated with a single bunch crossing. If more than one proton collision happens in the bunch crossing, several PVs will be reconstructed. In addition, short-lived particles may decay inside the VELO creating a secondary vertex (SV).

impact parameter The impact parameter is the distance of closest approach of an extrapolated particle trajectory to a given vertex. Especially important is the minimum impact parameter (MinIP) of a trajectory with respect to each of the PVs reconstructed in a collision. A track with a large MinIP has a low probability of belonging to a primary decay product. The impact parameter resolution achieved by LHCb is shown in Fig. 2.8a.

vertex χ^2 The vertex χ^2 is calculated from the impact parameters of all tracks associated with the given vertex. Vertices with a high χ^2 have a large probability that one or more of its tracks have been wrongly associated.

track χ^2 The track χ^2 expresses how well reconstructed trajectory matches the measured hits. It is calculated from the distances between the measured hits and the extrapolated position of the reconstructed trajectory.

momentum The full momentum (p) can be determined from the bending radius of a track in the magnet. In addition the transverse momentum (p_{T}) and the individual momentum components are determined. Here, p_{T} is the component of the momentum perpendicular to the beam pipe.

angles For each trajectory the azimuthal angle (ϕ) in the x-y plane, as well as the zenith angle (θ) to the beam pipe, are determined. For both angles the value at the vertex is stored.

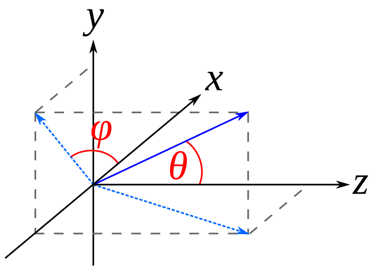

Figure 2.5: Angles ϕ and θ as defined in the LHCb coordinate system.

rapidity An alternative measure for θ is the rapidity (y). This variable is defined as

$$y \equiv \frac{1}{2} ln \left(\frac{E + p_z}{E - p_z} \right) \tag{2.1}$$

where E is the energy and p_z the component of the momentum along the z-axis. The resulting quantity is invariant under Lorentz boosts along the z-axis.

pseudorapidity Instead of y, the pseudorapidity (η) is often used. This coordinate is calculated from θ directly with

$$\eta \equiv -ln \left(tan \left(\frac{\theta}{2} \right) \right) \tag{2.2}$$

and is numerically close to the rapidity.

2.3.1.2 Track Reconstruction

The different tracking detectors of LHCb measure individual points along the flight path of the passing particles. The task of the track reconstruction is then twofold. First all points belonging to the path of a single particle need to be found and second, the properties of this track need to be determined as precisely as possible. The first part is the pattern recognition while the second is the track fitting. There are many different approaches for both tasks. LHCb uses a Kalman Filter for the track fit and has implemented several pattern recognition algorithms. The main challenge for pattern recognition is the magnetic field. Without the magnetic field, particle tracks would, to a good approximation, be straight lines. Inside the VELO where the magnetic field can be neglected, track segments can therefore be reconstructed easily.

The two main pattern recognition algorithms are ,,Track Matching" (Needham and Van Tilburg 2007) and ,,Forward Tracking" (Callot and Hansmann-Menzemer 2007). Forward Tracking starts with a track segment from VELO and adds a single candidate hit in the T stations, to form a track hypothesis. Other hits in a window around this hypothesis are then projected onto a virtual reference plane (see Fig. 2.6). In this projection, hits truly belonging to the hypothesis form a cluster. These hits are then selected and fitted with a third order polynomial. By adding different candidate hits to the VELO segment, several preliminary tracks are constructed. At the end, the best track candidate is selected based on the χ^2 and other quality criteria.

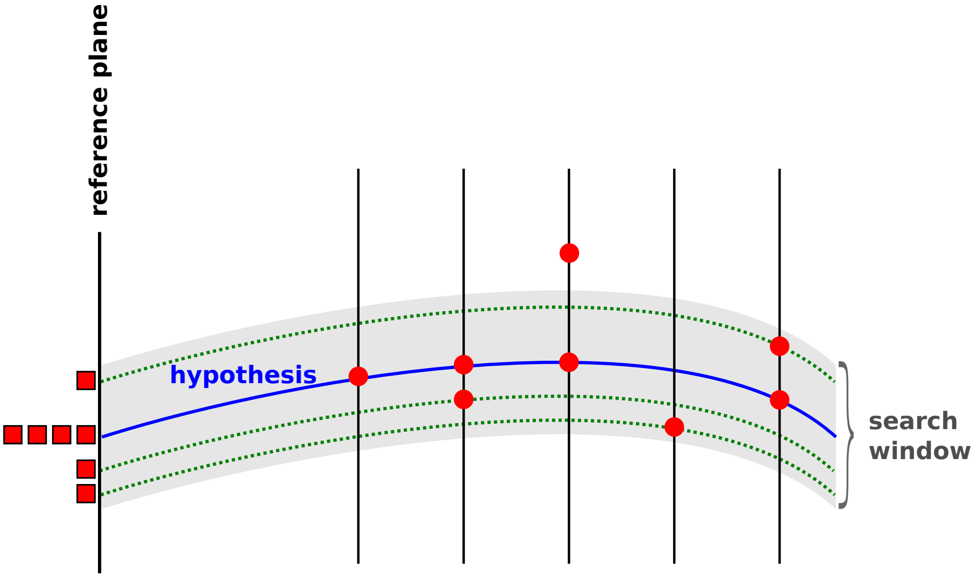

Figure 2.6: Illustration of the projection step in the Forward Tracking.

Track Matching constructs standalone track segments from the hits in the T stations. Each T station segment is then combined with all the available VELO segments. Such a pair of segments is then extrapolated to a plane inside the magnet. Based on the distance of the two extrapolated positions (in terms of χ^2), the compatibility of the two segments is then determined. Once all combinations for a given T segment are processed, the pair with the best χ^2 is selected. It should be noted, that neither of the two pattern recognition algorithms uses hits from TT to identify tracks. Track reconstruction efficiency is therefore independent of the TT and the muon stations, and can be assessed with the Muon-TT method.

After all hits of a track have been identified, the final track fit is performed. For this a Kalman Filter (Van Tilburg and Merk 2005) is run on the hits found by the pattern recognition. A Kalman Filter is a computationally fast procedure and has several other advantages. Important for track fitting is the possibility to account for multiple scattering, the effect of detector material on the flight path, in the fit. The fit is initialised with the track state in the T-stations, as obtained by the track finding algorithms. It is then run towards VELO repeating the following two steps, illustrated in Fig. 2.7:

Prediction Based on the present state of the fit, the parameters for the next state are predicted, using a fifth order Runge-Kutta method (Weisstein 2014). In this step multiple scattering is taken into account by increasing the uncertainty on the direction of the trajectory.

Filtering The prediction for this state is updated with the information from the measurement at this position.

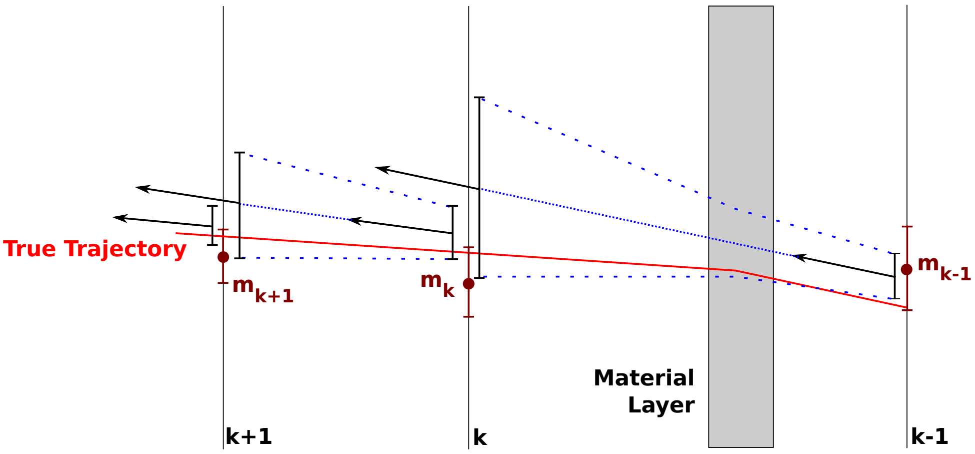

Figure 2.7: Illustration for the Kalman fitting procedure (based on Van Tilburg and Merk 2005).

Once the final state is reached, a smoothing step is performed. In this step, all track states are updated recursively with the full information included in the final state.

Once tracks have been found and fitted, a final track selection is performed and hits in TT are added. Since there are several pattern recognition algorithms, tracks reconstructed by more than one algorithm must be noticed and consolidated. Tracks belonging to the same particle trajectory are called clones. A specific clone killing algorithm compares the hits associated with two tracks. If the tracks share a large number of hits, the track associated with less hits is discarded.

2.3.1.3 Muon Identification

Muons in LHCb are identified by linearly extrapolating reconstructed tracks into the muon stations. A field of interest is built around the extrapolated positions inside of which hits are searched for. The field of interest depends on the momentum of the track, and the region within the muon system and is different in x and y. Based on the momentum of the track, a different number of hits is required to identify a track as a muon. The conditions are listed in Table 2.2.

Table 2.2: Stations required for muon identification.

p [GeV/c]	required stations
3 – 6	M2, M3, M4
6 – 10	M2, M3, M4 or M5
> 10	M2, M3, M4, M5

For additional discrimination a muon likelihood function is created. It is based on the comparison of the slopes between the track segments in the muon system and the main track and on the distances between the extrapolated track and the associated hits.

2.3.1.4 Performance of the Tracking System

The combined tracking system provides a momentum measurement with relative uncertainty that varies from 0.4% at 2 GeV/c to 0.6% at 100 GeV/c, and an impact parameter measurement with a resolution of 20 µm for tracks with large transverse momentum. For events containing a single primary vertex, a primary vertex resolution of 13.1 µm, 12.5 µm and 69.2 µm in (x, y, z) is achieved (Tobin 2013).

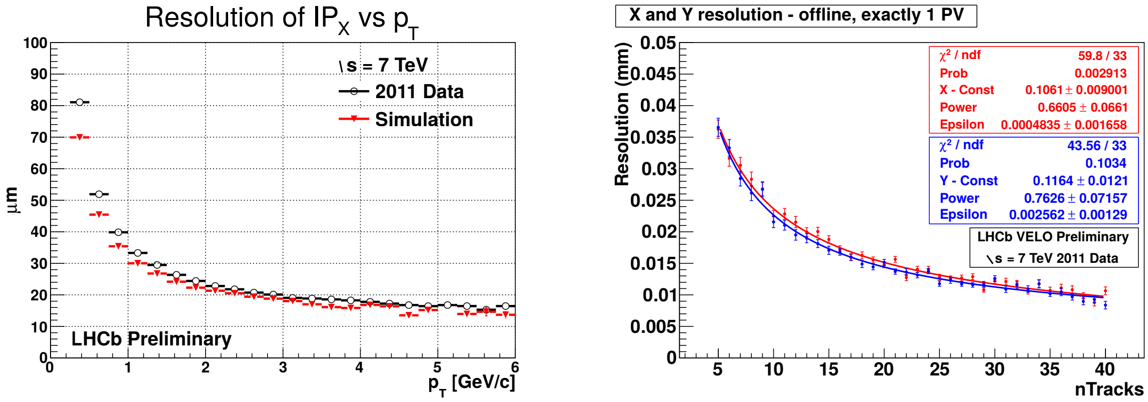

(a) Impact parameter resolution as a function of p_{T}

(b) Primary vertex resolution in x (red) and y (blue) as a function of track multiplicity

Figure 2.8: Illustrations of the tracking performance of LHCb (Tobin 2013).

2.3.2 The Trigger System

The amount of data produced in proton-proton collisions at 40 MHz is much larger than the amount of data that the readout system of the LHCb experiment can process. Therefore a trigger system (LHCb Collaboration 2013) is needed to select the bunch crossings of interest. LHCb uses a multi-stage trigger system illustrated in Fig. 2.9. This system reduces the rate from 11 MHz for bunch crossings with at least one inelastic pp interaction to 3 kHz. The trigger system consists of a hardware and software stage. Each stage fires if one or more of the implemented conditions are fulfilled. These different conditions are called trigger lines and the information which trigger lines accepted an event is stored together with the event.

The hardware stage is called First Level Trigger (`L0`). It is built from custom-designed hardware and runs fully synchronous with the 40 MHz nominal bunch crossing signal of

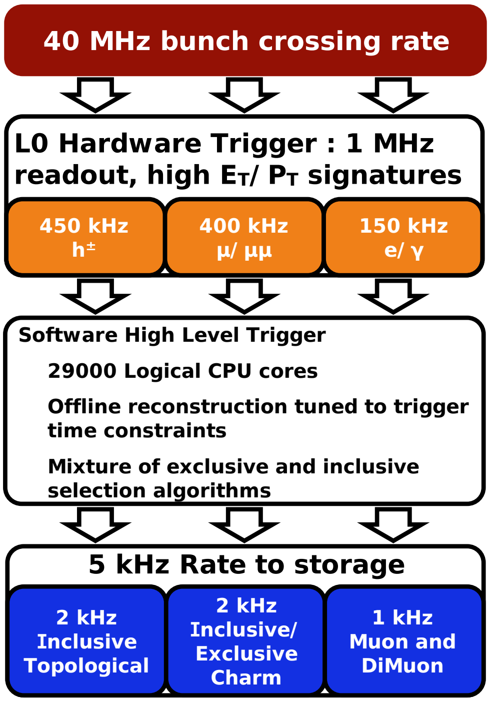

Figure 2.9: Schematic of the LHCb trigger system (LHCb Collaboration 2014b).

the LHC. Only information from the muon systems and the calorimeter is used for the `L0` trigger decision. For the analysis presented in this thesis, the decisions based on the muon information are important. Here, two separate conditions are implemented. The single muon trigger line requires one muon with a high p_{T}, while the di-muon trigger fires if the product of the two highest p_{T} muons reaches a given threshold. Over all its lines, the `L0` system reduces the readout rate to below 1.1 MHz. At this rate the whole detector can be read out and the full information is then used in the software stage.

The software stage is called High Level Trigger and consists of two sub-stages (`HLT1`) and (`HLT2`). The `HLT1` uses a partial event reconstruction to reduce the rate to 43 kHz, `HLT2` then performs a more complete event reconstruction. Events with a very high occupancy could potentially delay a trigger decisions significantly. To reject such events, global vetos, the global event cuts (GEC), are applied to all events entering the `HLT`. The GEC set thresholds on the multiplicities of most sub-detectors. Over both sub-stages combined, the `HLT` contains more than 150 trigger lines. Again mainly the muon lines will be relevant for the analysis presented in this thesis. The detailed conditions applied by these lines will be discussed in the relevant chapters.

2.3.2.1 Stripping

Stripping is the central offline event selection and therefore related to the trigger system. A central event selection is run offline to prepare data files of reduced size, tailored for specific analysis needs. In analogy to the trigger lines, the stripping uses stripping lines to select events. The decision whether or not to include an event is based on several requirements optimised for the targeted analysis. Due to storage constraints some stripping lines are prescaled and retain only a fixed fraction of the events that pass its requirements. Overall almost 1000 stripping lines exist in LHCb. Only 75 of these target studies of the electroweak interaction and less then 10 are used for the analyses presented below. Both the efficiencies of the trigger as well as the stripping lines have to be taken into account in the analyses.

Chapter 3

The Standard Model

The Standard Model (SM) is the canonical framework to describe particle physics and covers electromagnetic, weak, and strong interactions. Within the last decades the SM has proven very powerful, predicting several new particles and describing interactions with impressive precision. Examples of such successes are the prediction of the third generation quarks or the Weak gauge bosons as well as their masses.(D0 Collaboration 1995; CDF Collaboration 1995; UA2 Collaboration 1992; UA1 Collaboration 1987) Surely however, the biggest success of the SM to date is the prediction and subsequent discovery of the Higgs boson (ATLAS Collaboration 2012; CMS Collaboration 2012).

Despite these successes, the SM has several shortcomings and most particle physicists agree that there must be new physics (NP) beyond the Standard Model. These shortcomings include the need for fine-tuning of the Higgs boson mass and the exclusion of gravity. Fine-tuning refers to the fact that the Higgs mass must lay within very stringent limits in order for the SM predictions to agree with observation. A Higgs mass too far from this fine-tuned value would result in vastly different results.

The SM describes the basic building blocks of the universe and the rules governing their interaction. These building blocks are point-like particles carrying various charges and possessing several other properties. It is important to keep in mind that particles in the SM are quantum mechanical objects. These particles interact due to different forces, each coupling to one of the charges and possibly changing properties of the particles. In general, the strength of an interaction depends on the charge of the involved particles as well as their distance.

In the following, this Chapter introduces the different particles in Section 3.1, while Section 3.2 explains the general formalism of the SM. The topics relevant for this thesis are explained in more detail in Sections 3.3 and 3.4. Section 3.3 explains the mechanisms at play in boson production and the topic of parton distribution functions (PDFs) is covered in Section 3.4.

3.1 The Particles

The SM groups particles according to a multitude of properties. First of all particles are divided into matter and anti-matter. For each particle a corresponding anti-particle exists. The anti-particle has the same mass and spin, but opposite charge as its matter partner. The visible universe consists of matter exclusively. Anti-matter is created in several processes in nature, but annihilates again quickly with a corresponding matter particle. For example, anti-matter can be produced, when a cosmic ray hits the the atmosphere (C. D. Anderson 1933). To simplify the presentation, only the matter particles are presented below.

Classifying particles only, the most important property is the spin of the particles. Or more precisely whether the spin has an integer or half-integer value. Particles with integer spin are classified as bosons while fermions have half-integer spin. Both classes exist as combined as well as elementary particles. The elementary fermions are the basic constituents of matter and combine to more complex objects. The elementary bosons mediate the fundamental forces between particles, they are so called gauge bosons.

3.1.1 Elementary Fermions

An overview of the classification of elementary fermions presented in the following is given in Table 3.1. All elementary fermions have a spin of $\frac{1}{2}$. The fermions are again grouped in to two main classes, leptons and quarks, according to their interaction with the strong force. Leptons are not affected by the strong force while quarks are. Both of these classes contain three generations with two particles each. Overall, each generation therefore consists of four particles: A negatively charged and a neutral lepton as well as an up- and a down-type quark. Each of the six different quarks is said to have a different flavour. As can be seen from Table 3.1 the mass of the particles increases for later generations. The second and third generation fermions can therefore decay, leading to the observed dominance of first generation fermions in nature. However the total number of quarks, as well as the number of leptons of each family are conserved in most interactions in the SM.

3.1.2 Elementary Bosons

In the SM there are four groups of bosons, one for each of the three fundamental forces and one for the Higgs mechanism. All bosons are summarised in Table 3.2. The photon (γ) is the gauge boson of electromagnetism. The weak force has three gauge bosons, the neutral Z- as well as the electrically charged W^+- and W^--bosons. The two W bosons build a particle/anti-particle pair, as can be seen by their identical mass but opposite charge. The gauge bosons of the strong force are the gluons (g).

Table 3.1: Summary of the fermions in the SM. The values listed below the particles are the masses according to (Particle Data Group 2012). The charges are electric charges given in units of the elementary charge.

	1. GENERATION	2. GENERATION	3. GENERATION	CHARGE
	Leptons			
CHARGED LEPTONS	electron e 0.511 MeV/c^2	muon μ 106 MeV/c^2	tauon τ 1.78 GeV/c^2	-1
NEUTRINOS	e neutrino ν_e < 2 eV/c^2	μ neutrino ν_μ < 2 eV/c^2	τ neutrino ν_τ < 2 eV/c^2	0
	Quarks			
UP-TYPE QUARKS	up u 2.3 MeV/c^2	charm c 1.28 GeV/c^2	top t 173.5 GeV/c^2	$+\frac{2}{3}$
DOWN-TYPE QUARKS	down d 4.8 MeV/c^2	strange s 95 MeV/c^2	bottom b 4.18 GeV/c^2	$-\frac{1}{3}$

The Higgs boson was the last particle predicted by the SM to be confirmed experimentally. It is responsible for the masses of the other elementary particles. Without the Higgs mechanisms, all particles of the SM would be massless. They acquire their masses due to the interaction with the Higgs boson. As photons and gluons do not couple to the Higgs boson, these particles are expected to have no mass.

Table 3.2: Summary of the bosons in the SM. The values listed below the particles are the masses according to (Particle Data Group 2012).

ELECTROMAGNETIC	WEAK		STRONG	HIGGS MECHANISM
photon γ $< 1 \times 10^{-18}$ eV/c^2	Z boson Z 91.2 GeV/c^2	W boson $W^{\pm}$ 80.4 GeV/c^2	gluon g 0	Higgs boson H^0 126 GeV/c^2

3.1.3 Interactions

As mentioned in the introduction to Section 3.1, the interactions are mediated by the fundamental bosons. Particles interact by exchanging virtual bosons. The lifetime and therefore the range of a virtual boson is limited by Heisenberg's uncertainty principle: $E \cdot t < \frac{\hbar}{2}$. Due to this, the mass of the gauge boson defines the range of the corresponding force. In addition the charges a boson carries, explain several effects described below.

3.1.3.1 Electromagnetism

The electromagnetic force is the only fundamental force of the standard model directly observable in every day life. It is the force between particles carrying a non-zero electric charge. Due to the fact that both positive and negative electric charge exists, the electromagnetic force can be attractive as well as repulsive. As photons are mass-less, the electromagnetic force theoretically has an infinite range. Its strength decreases however with increasing distances. Still the electromagnetic force clearly dominates at large ranges, while it is negligible at the scale of TeV proton-proton collisions.

3.1.3.2 Weak Interaction

The weak force couples to the weak charge. As all elementary fermions carry the same weak charge, the magnitude of the charge is not relevant for the understanding of purely weak interactions. The important aspects of the weak interaction are its short range, its mixing with the electromagnetic interaction and its role in particle decays. The range of the weak interaction is limited by the large masses of its gauge bosons. Only at distances below the order of 1×10^{-18} m the weak interaction is comparable to the electromagnetic interaction in strength. Interactions mediated by the weak force can therefore be considered as point interactions. Due to the mixing of weak and electromagnetic interaction, the Z boson couples with different strengths to the differently charged fermions. In addition the contribution from photons and Z bosons to the Drell-Yan production cross section can only be disentangled partially. A thorough introduction to the unified electroweak theory can be found in (Horejsi 2002). Finally, heavy quarks can decay into lighter ones only by emitting a weak gauge boson. Due to the GIM-mechanism (Glashow, Iliopoulos, and Maiani 1970) quark decays mediated by a Z boson are heavily suppressed, leaving only $W^{\pm}$ for flavour changing processes. As the charged gauge bosons change the charge of affected particles, the possible combinations can be grouped into pairs. For the first generation, these are

$$\begin{pmatrix} e^- \\ \nu_e \end{pmatrix}, \begin{pmatrix} u \\ d' \end{pmatrix}$$

As illustrated in Fig. 3.1, an electron neutrino emitting a W^+ boson will therefore turn into an electron, while a u-quark emitting a W^+ turns into a d'-quark. The d' is the weak eigenstate of the first generation down-type quark.

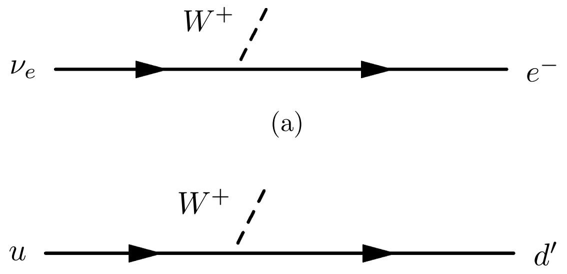

(a)

(b)

Figure 3.1: Examples of flavour changing processes.

Weak eigenstates exist for all down-type quarks and are a linear combination of the mass eigenstates described in Section 3.1.1. As the $W^\pm$ bosons couple to these weak eigenstates, charged weak interactions can mix quark flavours from different generations. This mixing is described by the CKM-Matrix (Cabibbo 1963; Kobayashi and Maskawa 1973) but is not central to the analysis presented in this thesis and is therefore not discussed further. A small aside on leptons will however be included. The “down-type” leptons, the neutrinos, are massless in the SM. Therefore their mass eigenstates should not mix and the weak eigenstate are expected to be pure. However, the observation of neutrino oscillation (Cleveland et al. 1998; Super-Kamiokande Collaboration 1998) has shown that neutrinos do in fact have mass and mixed mass eigenstates exist for neutrinos as well. On the other hand, no charged lepton flavour violation has been observed yet (Bernstein and Cooper 2013).

3.1.3.3 Strong Interaction

The charge of the strong interaction is called colour charge. The theory describing the strong interaction is therefore called Quantum Chromo Dynamics (QCD). Three different charges, red, green and blue, as well as the corresponding anti-colours exist. A quark can carry each of the three colours. Each quark-type therefore exists in a red, a blue and a green version. The anti-quarks correspondingly exist in three anti-coloured versions. Gluons carrie a combination of colour and anti-color charge each. As there are 8 possible independent combinations, 8 different gluon-types exist. The strong force is attractive for all combinations of colour charges. As gluons themselves are coloured, they can interact with each other. Combined with the production of virtual quarks and gluons, this causes the coupling strength of the strong interaction to increase for larger distances.

3.1.4 Combined Particles

As a result of the increasing coupling strength between coloured particles, only colour neutral objects exist in nature. This can be achieved by either combining a colour with its corresponding anti-colour or by combining all three colours in equal amounts. Therefore quarks come in groups of either two or three. Such combined particles containing quarks are named baryons and split into mesons and hadrons. Particles consisting of two quarks are called mesons. A meson always contains a quark/anti-quark pair carrying colour and anti-colour. As the spin of a quark is $\frac{1}{2}$, mesons have integer spin and therefore are bosons. Particles containing three quarks are called hadrons. The constituents of a hadron are either all quarks or all anti-quarks, each carrying a different colour charge. Hadrons have a combined spin of either $\frac{1}{2}$ or $\frac{3}{2}$ and are fermions. The fact that quarks are confined to colour neutral objects at the same time ensures that all particles observed in nature have integer electromagnetic charge. Table 3.3 summarises the elementary and combined particles of the SM.

The charged leptons can build combined particles as well. An electron and a positron for example can form a short lived bound state called positronium. At the collision energies of the LHC however, leptons are observed as free particles only.

Table 3.3: Summary of the particles in the SM. For a detailed list of the elementary particles see Tables 3.1 and 3.2

		FERMIONS	BOSONS
ELEMENTARY		leptons & quarks *e.g.*: e, μ	gauge bosons, Higgs *e.g.*: Z, $W^{\pm}$
COMPOSITE	baryons	hadrons *e.g.*: p, Σ	mesons *e.g.*: π, J/ψ, K
	general	combination of $2n+1$ fermions *e.g.*: Deuterium	combination of $2n$ fermions *e.g.*: Hydrogen, Positronium

3.1.4.1 Baryon Structure

The most well known baryons are the proton and neutron the constituents of the atomic nuclei. A proton consists of $2\,u$ and $1\,d$ quark while the neutron contains $1\,u$ and $2\,d$. The quarks in baryons discussed so far are the so called valence quarks. They define the properties of a baryon. Beside these valence quarks all baryons contain a sea of additional quark/anti-quark pairs and gluons. Sea-quarks exist in the constraints of the uncertainty principle and their quantum numbers cancel. However sea-quarks can take part in processes resulting from the collision of baryons and are therefore relevant for particle physics experiments.

Valence and sea quarks are collectively called partons. Each parton carries a part of the energy and momentum of its baryon. Especially the longitudinal momentum fraction (x) carried by a parton is an important variable to describe particle collisions. The probability to find a parton of given type depends on x and is described by a parton distribution function (PDF). Good knowledge of PDFs is necessary for precise predictions of processes involving hadrons. PDFs will be discussed again in Section 3.4.

3.2 The Formalism

The mathematical tool used to describe the SM are locally gauge invariant field theories. These theories are extensions of the tools and approaches developed for classical and quantum mechanics. In particular, the fact that any dynamic system can be described by its Lagrangian ($\mathcal{L}$) is used. For each fundamental interaction a Lagrangian can be found that matches the observed physics. In these Lagrangians particles are represented by quantum fields defined at all points in space time. The interactions are described by additional fields corresponding to the different gauge bosons. These gauge boson fields enter the Lagrangians in the covariant derivative and the field strength tensors. The Lagrangian of the electromagnetic interaction can serve as an example.

$$\mathcal{L}_{QED} = \overline{\psi}(x)(i\gamma_\mu D^\mu - m)\psi(x) - \frac{1}{4}F_{\mu\nu}(x)F^{\mu\nu} \tag{3.1}$$

Here $\psi(x)$ is the particle field for a fermion with mass m, D^μ is the covariant derivative and $F_{\mu\nu}$ is the field strength tensor. The need for a boson field as well as for the covariant derivative arises from the requirement that the Lagrangian of the fundamental interactions should be locally gauge invariant. This is to say, they should be independent of specific transformations applied to the fermion fields. For the electromagnetism the transformations in question correspond to the group of unitary transformations $U(1)$. The Lagrangian in the example above should therefore not change under phase transformations of the form

$$\psi(x) \to e^{i\theta(x)}\psi(x) \tag{3.2}$$

Equation (3.1) fulfils this requirement if the boson field A_μ transforms as

$$A_\mu \to A_\mu - \frac{1}{e}\partial_\mu\theta(x) \tag{3.3}$$

The covariant derivative and the field strength tensors are then defined as follows

$$D_\mu \equiv \partial_\mu + ieA_\mu(x) \tag{3.4}$$

$$F_{\mu\nu} \equiv \partial_\mu A_\nu - \partial_\nu A_\mu \tag{3.5}$$

The full Lagrangian for the SM contains a part for each of the fundamental interactions. Each part is invariant under the transformations of a given group. In addition to $U(1)$ for the electromagnetic force these are $SU(2)$ for the weak and $SU(3)$ for the strong force. However in the full Lagrangian, the part for the electromagnetic force is combined with the part for the weak interaction. For this thesis, the most important consequence of this combined electroweak force is the fact that both the photon as well as the Z boson are linear combinations of the underlying fields. Based on the Lagrangian, the corresponding Hamilton operator as well as the equation of motion for the field can be determined. A detailed introduction into the formalism of the SM can be found in (B. R. Martin and Shaw 2005) or many other textbooks.

3.2.1 Perturbative Calculations

Many of the calculations for processes of the SM can be simplified significantly when using a perturbative approach. In particular, the scattering amplitudes can be expressed as expansion series in powers of the gauge coupling constant. The individual terms of such a series correspond to a specific process and can be visualised as Feynman diagrams. Figure 3.2 shows an example diagram. In Feynman diagrams incoming and outgoing particles are represented by open ended lines, while the exchanged bosons correspond to internal lines. Vertices of multiple lines correspond to an interaction between particles. As every term in an expansion series can be represented by a diagram, the series can also be determined from the diagrams. Therefore the scattering amplitude for a process of choice can be calculated by summing the terms for the diagrams up to the required complexity. An important caveat is the need for the coupling constant to be small. Only in this case, the higher order terms of the series and thereby the more complex processes have a negligible effect on the overall result. This will be relevant in the next section, when the full scattering process is discussed.

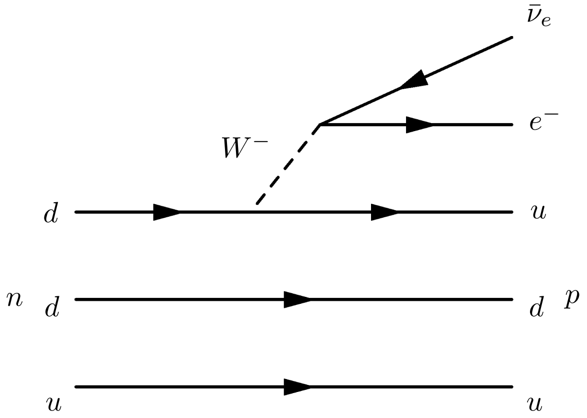

Figure 3.2: Feynman diagram of a β-decay. Only the top most quark line is involved in the process.

3.3 Boson Production

The process studied in this thesis is the production of a neutral gauge boson that then decays into two muons (the Drell-Yan process). This section will review the theoretical background of a generic boson production process. The specifics of the Drell-Yan process will be discussed in Section 5.1. In general boson production processes have four stages:

1. initial parton showering
2. hard scattering
3. final parton showering
4. hadronisation

At the centre of a boson production process at LHC is the scattering of two partons from the incoming protons, producing a boson. The boson then decays into a pair of particles. Figure 3.3 shows the relevant leading order Feynman diagram as well as a possible higher order diagram including final state radiation.

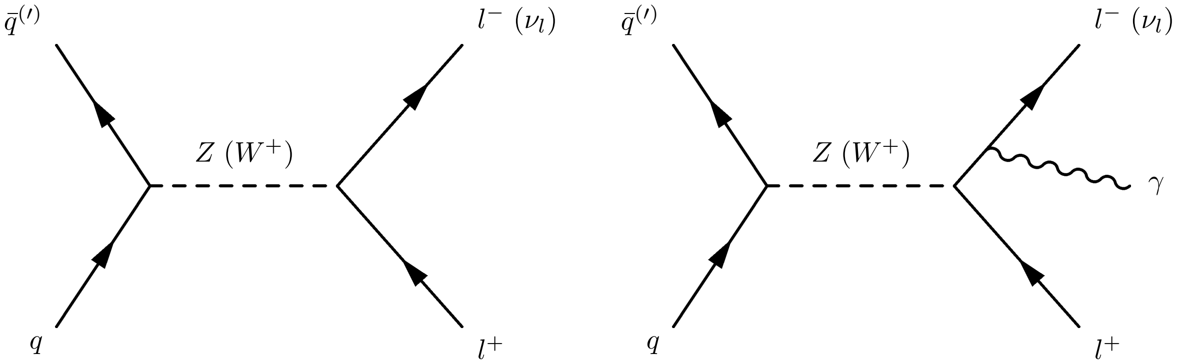

(a) leading order diagram

(b) diagram including final state radiation.

Figure 3.3: Possible Feynman diagrams of electroweak boson production at LHC.

The partonic cross section, $\hat{\sigma}$, for such a process can be calculated by perturbative Quantum Chromo Dynamics (pQCD). As described in (Campbell, J. W. Huston, and W. J. Stirling 2007), the cross section at hadron level can be obtained using the factorisation theorem. The cross section for the production of a final state X in the collision of two protons A and B is then given by

$$\sigma_{AB\to X} = \int dx_a dx_b \cdot f_{a/A} f_{b/B} \cdot \hat{\sigma}_{ab\to X} \tag{3.6}$$

here $f_{q/H}$ is the PDF describing the quark q in the hadron H.

Higher order Feynman diagrams need to be taken into account when calculating $\hat{\sigma}$, if a precise result is to be obtained. This can be very time consuming. Therefore even in the best cases only diagrams up to next-to-next-to-leading order (NNLO) are included in the calculations. Even higher order corrections can then be estimated using the parton shower model. In a parton shower, a highly energetic particle is allowed to radiate off some of its energy by emitting quarks, gluons and photons. The corrections from parton showering are usually calculated with Monte-Carlo methods. The procedure is explained in detail in the manuals of the common Monte-Carlo generators like Pythia or Herwig (Sjöstrand, Mrenna, and Skands 2006; Corcella et al. 2001).

If the boson decays into quarks, a third step is needed. As explained in Section 3.1.3.3, quarks need to form colour neutral combined particles. This process is called hadronisation and it involves processes for which the strong coupling constant is large. Therefore the caveat mentioned in Section 3.2.1 applies and hadronisation can not be calculated perturbatively. Instead hadronisation is usually modelled using phenomenological approaches (Andersson et al. 1983; Gottschalk 1984).

To fully describe a proton-proton collision, the partons not involved in the hard scattering must be considered as well. These remnants of the protons and their interactions from the underlying event. These interactions are usually soft and involve several coloured particles. Models of such interactions are implemented in modern Monte-Carlo generators. The observable effect of the underlying event are a large number of low energetic particles.

3.4 Partron Distribution Functions

Parton distribution functions (PDFs) are understood as functions describing the structure of the proton. More precisely, they give the probability density at a given energy scale (Q^2) to find a parton with a given x within the proton. PDFs describe non-perturbative effects and are process independent. They can not be calculated from any theoretical model, instead they are determined by fitting the results from different measurements.

Several collaborations perform such fits, resulting in a number of different PDF sets. For the analyses covered in this thesis, the Nnpdf (Ball et al. 2010), Cteq6m (Nadolsky et al. 2008) PDF sets were used. As there is no theoretical motivation for the parametrisation of the individual functions, each collaboration uses its own approach. Nnpdf tries to avoid the choice of a functional form completely. Instead the PDF shape is determined by a neural network. The more common approach is to parametrise the PDF with a polynomial function and then perform a χ^2 optimisation.

A typical parametrisation for a PDF is

$$f(x, Q_0^2) = (1-x)^{\eta}(1+\epsilon x^{0.5}+\gamma x)x^{\delta} \tag{3.7}$$

Such a parametrisation is valid for a parton of type f in a process at the reference energy scale chosen for the paramterisation (Q_0^2). The η-term describes the falling distribution for x towards 1 where the PDF must reach 0. For small x values, the PDF is dominated by the polynomial in the δ-term.

A set of PDF functions usually contains seven independent distributions, one describing the gluons and six for quarks:

$\boldsymbol{u_V}$	up-type valence quarks
$\boldsymbol{d_V}$	down-type valence quarks
$\boldsymbol{\overline{u}}$	up-type sea quarks and anti-quarks
$\boldsymbol{\overline{d}}$	down-type sea quarks and anti-quarks
$\boldsymbol{c = \overline{c}}$	charm-type sea quarks and anti-quarks
$\boldsymbol{s = \overline{s}}$	strange-type sea quarks and anti-quarks

Since the mass of bottom-quarks is much larger than the scale Λ_{QCD} of QCD, the heavy parton distributions can be calculated perturbatively.

Independent of the parametrisation and approach choosen, the correlations between the different data points included in the fit must be taken into account. This is especially crucial, as the datasets typically include measurements from widely different experiments such as deep-inelastic scattering from HERA and jet production at Tevatron. A thorough review of PDF fitting and the datasets can be found in (De Lorenzi and Mc Nulty 2011).

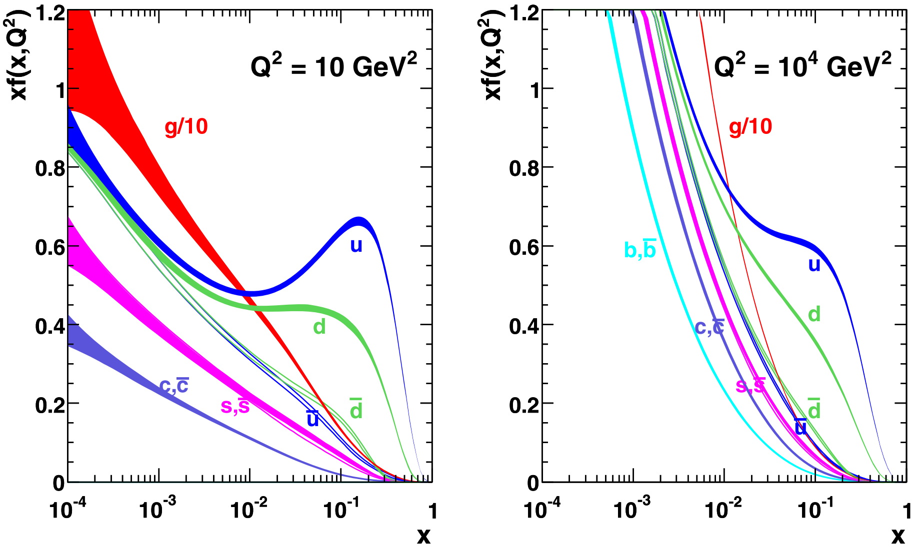

Figure 3.4: MSTW 2008 NLO PDF. The error bands correspond to the 68 % confidence level (A. Martin, W. Stirling, et al. 2009).

As mentioned above, a given PDF is determined for a fixed Q_0^2. Usually a Q_0^2 in the range of 1 to 3 GeV^2 is used. PDFs can then be extrapolated to $Q^2 > Q_0^2$ using the DGLAP (Altarelli and Parisi 1977) equations. This DGLAP evolution is necessary to include data sets from measurements at and to calculate predictions for higher Q^2.

Figure 3.4 shows the PDF from MSTW08 (A. Martin, W. Stirling, et al. 2009) for two different Q^2. The effect of the evolution is prominently visible. At low Q^2 the three valence quark contribution to the u and d PDFs dominate as expected and show a clear maximum at large x. For high Q^2 the relative importance of the valence quarks is reduced while the sea-partons increase in relevance.

Chapter 4

TT Detector Alignment

The LHCb detector consists of many sub-detectors. For a precise reconstruction of particle trajectories, the position with respect to the collision point of all sub-detectors used in tracking is crucial. These subdetectors were therefore carefully installed in their planned locations and their positions measured with state of the art tools. The full geometrical information on the detector is then stored in the detector description. However to achieve the high precision necessary for the scientific program of LHCb, the detector description needs to be update based on the reconstructed tracks. This step is called detector alignment and uses a Kalman filter (Kalman R. E. 1960) to minimise the track χ^2. The resulting adjustments are then stored in the detector description as well. The updated detector description used for the event reconstruction is produced with a global alignment including all sub-detectors (Hulsbergen 2009). However the alignment software can be run for an individual sub-detector as well. This allows to check the global alignment and investigate problems.

This work was performed in close cooperation with Christophe Salzmann and a detailed description of the alignment process as well as the results can be found in his thesis (Salzmann 2011). In the following this chapter will describe the TT detector in more detail and present a summary of the studies performed together with Ch. Salzmann.

4.1 Tracker Turicensis

The TT is built from individual silicon sensors combined into four detector layers and mounted in a steel frame. The frame consists of two halves, fixed to a rail on top and bottom. The sub-detector can be opened by moving the two halves horizontally outwards. Figure 4.1 shows a schematic of the whole sub-detector. The four layers are grouped in pairs (TTa and TTb) with a gap of approximately 30 cm between the pairs. The two inner layers of the detector are tilted by ±5° to allow for a position measurement along the y-axis as well. The layers of TTb cover a larger area, to have the same angular acceptance as the

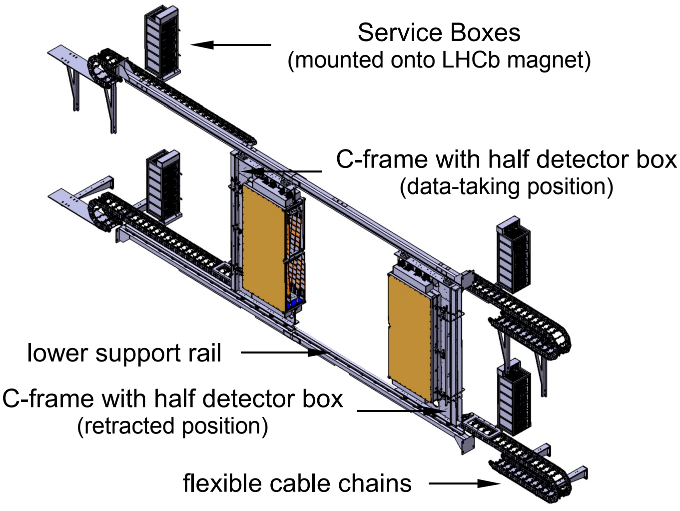

Figure 4.1: Schematic view of the TT and its mounting.

layers closer to the interaction point. Figure 4.2 shows an illustration of the four layers. The individual sensors have an active surface of roughly 100 cm^2 each. For mounting, seven sensors are combined into a half-module. Two half-modules are then fastened together and fixed to the frame at the upper and lower end. To assure a continuous active region, neighbouring half-modules are mounted staggered and overlapping. Two different overlaps are used to account for the change in the expected angle of incidence. A special case are the two half-modules directly above and below the beam pipe. These are mounted with a larger offset in z and are not connected to each other. For readout, each half-module is divided into several readout sectors. Half-modules at the centre of the detector have three sectors containing four, two and one sensors respectively. Outer half-modules have two sectors with four and three sensors. The hit resolution achieved by TT was measured to be 59 µm. (Tobin 2013)

With more than 99 % of its 143 360 readout channels fully operational (Elsasser 2014), the performance of TT throughout the first running period was excellent. At the end of 2012, shortly before the first long shutdown of the LHC, the detector still held the highest reliability figure of any silicon tracking detector at LHC.

4.2 Aligning TT

In the alignment software the TT sub-detector is represented by several objects:

- The sub-detector as a whole with its reference point in the middle of the gap between the TTa and TTb;
- The two stations TTa and TTb;

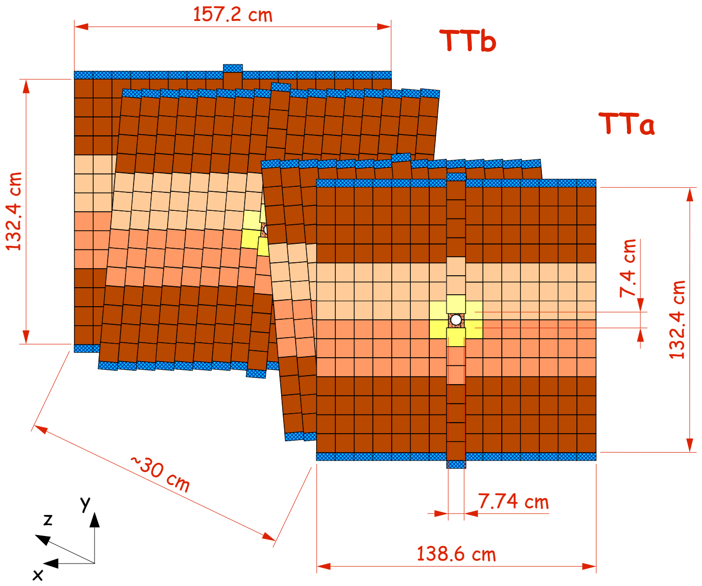

Figure 4.2: The four detector layers of TT. The shading indicates the different readout sectors.

- The individual layers, called TTaX, TTaU, TTbV, and TTbX (in order of increasing z);
- The half-layers, grouping all modules of a layer attached to the same mounting frame into one object;
- The full-modules, consisting of an upper and a lower half-module;
- The half-modules;
- The individual sensors.

Each of these elements can be aligned in six degrees of freedom, three translations and three rotations. Needless to say, many of these degrees of freedom are correlated and aligning for all of them simultaneously can lead to completely unphysical results. For TT several puzzling effects were observed. The alignment seemed to increase the size of the detector layers by moving the modules further apart in x. This effect can be seen in Fig. 4.3 below. In addition the whole station was shifted in z direction for more then physically possible.

To investigate these problems many different configuration settings for the alignment were tested. As the resulting movements of the individual parts had to be assessed, a tool to visualise these movements was needed. Several such tools were developed and improved in close collaboration of several members of the Zürich group. Figure 4.3 shows the visualisation of the result from a two stage alignment. First the full TT and all the individual layers were aligned. This was then followed by an alignment of the half-modules while keeping the other components fixed at the position from the first stage. The positive slope of the individual layers corresponds to a scaling of the detector in x. The absolute shifts in x is proportional to the position of the half-module in x. At the end, several

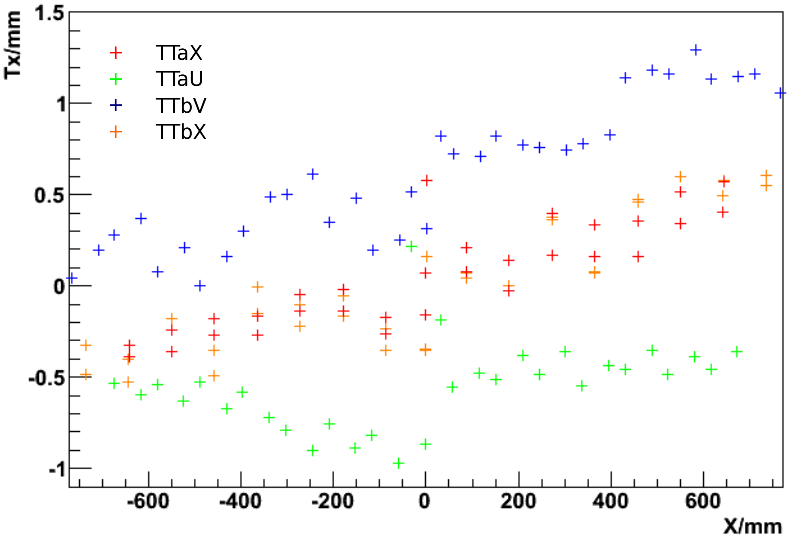

Figure 4.3: Visualisation of a two stage alignment. Shown are the positions of individual half-modules. The x-axis corresponds to the nominal x-position of the half-modules while the y-axis gives the shift resulting from the alignment. Different colours correspond to different layers: TTaX (red), TTaU (green), TTbV (blue), TTbX (orange).

problems outside the software alignment where identified as culprits for the observed unphysical behaviour. The tracks used in the alignment are deflected by the magnetic field. Therefore the strength of this field over the full trajectory up to TT needs to be taken into account when reconstructing tracks. During the technical stop in winter 2010/2011 the magnetic field was remeasured and the improved field map introduced. In addition two mistakes in the detector description of TT were found and corrected. First, a wrong value for the distance between two neighbouring readout electrodes was stored. Second, the wrong value had been entered for the overlap between two modules on each side of the detector in TTb. The change from small to large overlap in the detector description happened between modules four and five while in reality, this change is between modules five and six. This last bug was found in a systematic check of the detector description. For this one of the visualisation tools was refactored such that it provided a reusable library to access the detector description. This library can be used to query the position of detector elements for visualisation but also interactively from the command line. With the command line mode it was then possible to navigate through the whole tree of detector elements and compare the stored values with the constructional drawings.

Using all these corrections and further improvement from the working group, a significantly improved global alignment was achieved. For example, the 2011 global alignment achieved a mass resolution for the $J/\psi \rightarrow \mu^+\mu^-$ decay of (13.6 ± 0.2) MeV/c^2 (Salzmann 2011).

Chapter 5

Drell-Yan Cross Section Measurements

5.1 Theoretical Context

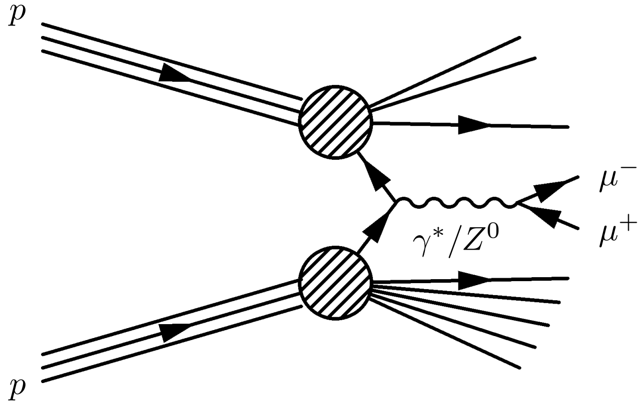

Figure 5.1: Feynman diagram of the Drell-Yan process studied in this thesis.

The Drell-Yan process is the creation of a neutral electroweak gauge boson (γ or Z) in a quark/anti-quark annihilation with a subsequent decay into two leptons. In this thesis only the di-muon final state will be considered. Figure 5.1 shows the corresponding Feynman diagram. As explained in Section 3.3 theoretical calculations of such processes use the factorisation theorem. They depend on the parton distribution functions (PDFs) for the involved quarks as well as the cross section of the hard scattering process, which can be calculated in perturbative Quantum Chromo Dynamics (pQCD).

Predictions for the hard scattering process are available at next-to-next-to-leading order (NNLO) and have an uncertainty between 3 and 10% depending on the rapidity. The dominant theoretical uncertainty for the total cross section is due to the limited knowledge of the PDFs involved.

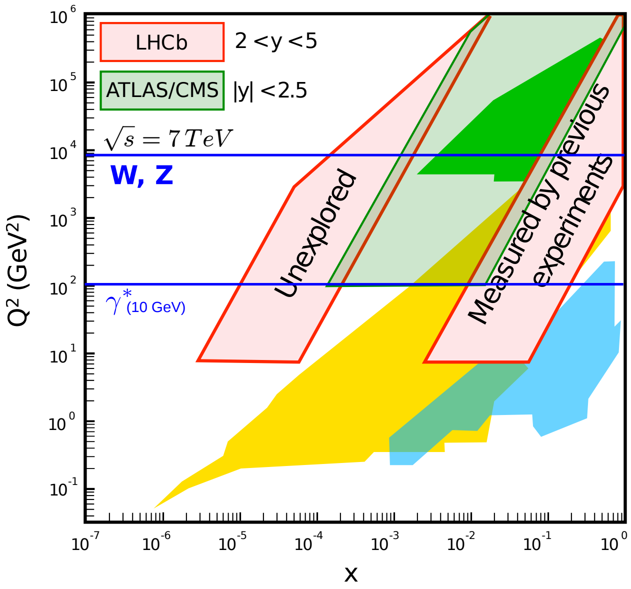

Figure 5.2: The kinematic region x-Q^2 probed by the LHCb measurements of electroweak boson production. Underlaid are the regions probed by measurements of previous experiments as well as ATLAS and CMS (GPDs) (based on a figure from J. S. Anderson 2008).

Figure 5.2 shows the regions in the x-Q^2 plane probed by electroweak boson production in LHCb. Again, x is the longitudinal momentum fraction carried by the interacting parton. Q^2 is the square of the four momentum exchanged in the scattering process. LHCb covers only the forward angle and will not detect particles leaving the collision point at a large zenith angle (θ). For production processes detectable at LHCb, the momenta of the two interacting partons must therefore be highly asymmetric. Such events include one parton at low x and the other at high x. This results in the characteristic shape of the kinematic region of LHCb, with two distinct regions. The cutoff for low x and high Q^2 is due to the fact that for both partons $x \leq 1$ must hold. Measurements of the low mass Drell-Yan process with photons at 10 GeV/c^2 are thus sensitive to x values as low as $8 \cdot 10^{-6}$. As Fig. 5.2 shows, the high-x region has been constrained by previous measurements at fixed target experiments, Tevatron or HERA. The low-x region however has only been probed at very low Q^2 by the HERA experiments. These measurements have quite large uncertainties that affect PDFs determined from them. The figure also shows that measurements at both ATLAS and CMS probe intermediate x-values only. In pseudorapidity (η), there is an overlap region with ATLAS and CMS for $2.0 < \eta < 2.5$ but the region $\eta > 2.5$ is only fully instrumented at LHCb.

As only the LHCb experiment can probe the low x region of the x-Q^2 plane, its measurements provide valuable input for constraining the PDFs. As introduced in Section 3.4, PDFs have to be determined from measurements and are then evolved using the DGLAP equations for use at different Q^2. This induces uncertainties for the predicted cross sections at LHC energies, limiting the power of new physics (NP) searches and Higgs studies. Figure 5.3 shows the MSTW08 PDF uncertainties on the total cross section for the production of $W^{\pm}$ and Z bosons as well as the Drell-Yan cross section for virtual photons with two different masses. The uncertainties in the forward region are large and increase rapidly with increasing rapidity (y) or decreasing mass. For the y range covered by LHCb the uncertainties for $W^{\pm}$ and Z bosons reach a few percent, while for virtual photons they can be an order of magnitude larger.

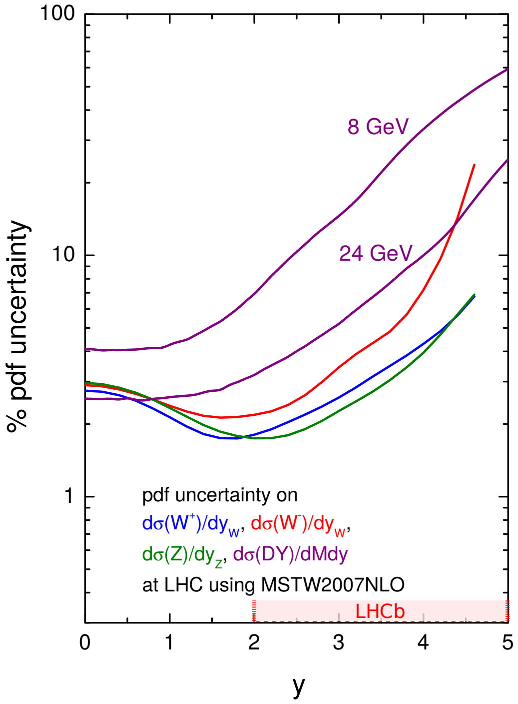

Figure 5.3: PDF uncertainties from MSTW08 on the total cross section for different processes at LHC as a function of y. The two purple lines correspond to virtual photons with masses of 8 GeV/c^2 and 24 GeV/c^2 (from Thorne et al. 2008).

In summary, a measurement of the Drell-Yan production cross sections at LHCb provides valuable input for the determination of PDFs. In addition a precision measurement can test the Standard Model where predictions are most precise.

5.2 Experimental Strategy

The studies presented here determine the cross section for Drell-Yan production and the subsequent decay into two muons as a function of the di-muon invariant mass ($M_{\mu\mu}$) and the di-muon rapidity ($y_{\mu\mu}$).

Experimentally, the cross section (σ) for a given region of phase space, a bin, is determined as

$$\sigma = \frac{\rho f^{\text{bin}}}{\mathcal{L}} \sum_{i=1}^{N} \frac{1}{f_i^{\text{evt}}} \tag{5.1}$$

where ρ is the signal fraction in the bin, $\mathcal{L}$ the integrated luminosity and the sum runs over all events in the bin. The correction factors f^{bin} and f^{evt} account for corrections affecting the full bin and individual events respectively. The former usually covers migration effects, while the latter typically accounts for different efficiencies. These quantities have to be determined preferably from data. In the following the approaches used to determine the signal fraction and the integrated luminosity are presented. The methods used to determine the different efficiencies are explained in the individual analysis descriptions (Chapter 6 and Appendix C).

5.2.1 Backgrounds

The signature of the studied Drell-Yan process are the two muons in the final state. These muons should come directly from the primary vertex (PV) and have no other decay products around them. However this signature can be mimicked by other processes as well. Several sources of backgrounds have been considered:

1. Pions or kaons can be misidentified as muons. Either because they decay in flight into a final state with a muon (*e.g.*: $\pi^+ \to \mu^+\nu_\mu$ or $K^- \to \mu^-\nu_\mu\gamma$) inside the detector or because they punch through the calorimeters and reach the muon chambers.
2. Heavy flavor hadrons, like b-mesons, contribute if they decay semileptonically.
3. Events with one misidentified muon and one muon from semileptonic decays, result in a first mixed background.
4. A second mixed background is due to events with one background muon and one true muon. Such a true muon can be caused by W decays and by Z decays, if only one muon is inside the LHCb acceptance.
5. Drell-Yan events with $\tau^+\tau^-$ final state constitute a background, if both taus decay into muons.
6. For masses below 10 GeV/c^2, decays from Υ mesons into two muons are relevant. The regions of the Υ masses are excluded, however such decays still result in background if part of the energy of the muons is radiated off.

Of these the main background categories are Items 1 and 2. Items 3 to 5 can be included into the main categories by a suitable procedure. Item 6 is relevant for the 2010 analysis only, as the region below these resonances is not used for the 2011 result. The details on the background treatment are described in Section 8.2. For now it is sufficient to know that these backgrounds are taken into account through the signal fraction.

Figures 5.4 to 5.6 shows the distribution of $M_{\mu\mu}$, $y_{\mu\mu}$ and the transverse momentum (p_{T}) of the μ^- for the two main backgrounds. They are determined form data by the procedures described in Section 8.2. In the mass distribution for the background from heavy flavour decays, a contamination of signal events is visible around the Z mass.

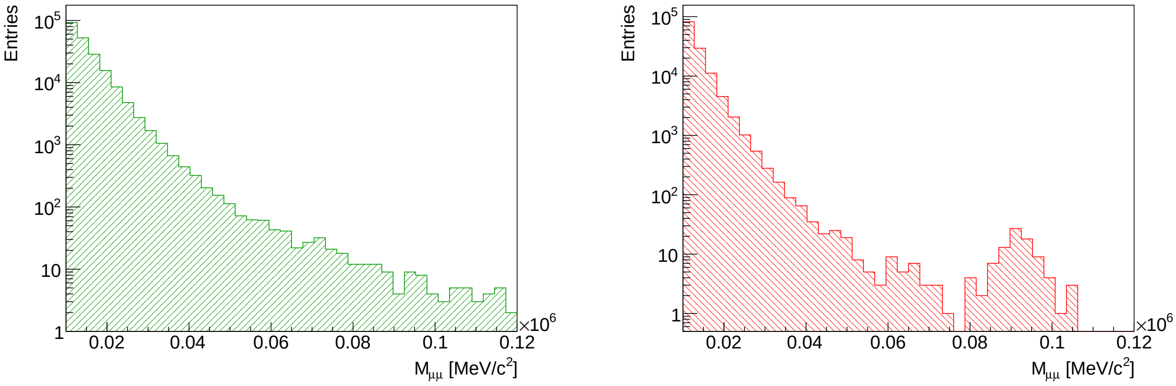

(a) misidentification background (b) background from heavy flavor decays

Figure 5.4: Mass distributions of the two main backgrounds.

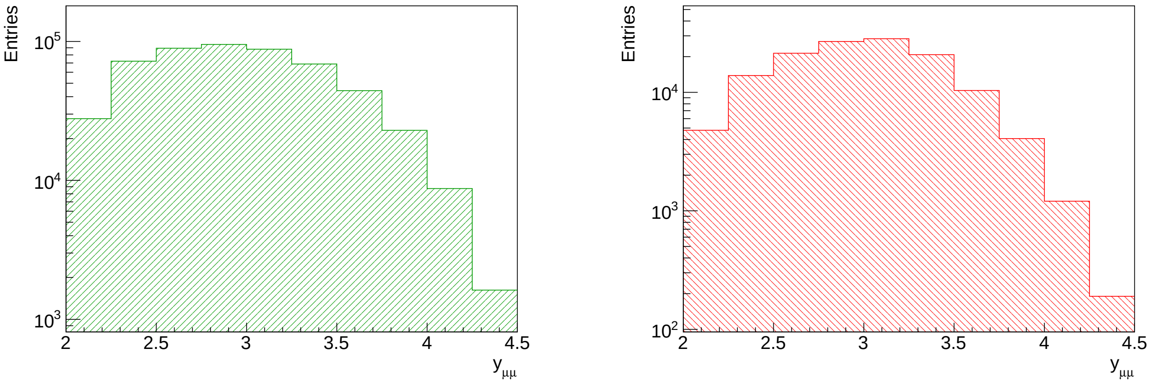

(a) misidentification background (b) background from heavy flavor decays

Figure 5.5: Rapidity distributions of the two main backgrounds.

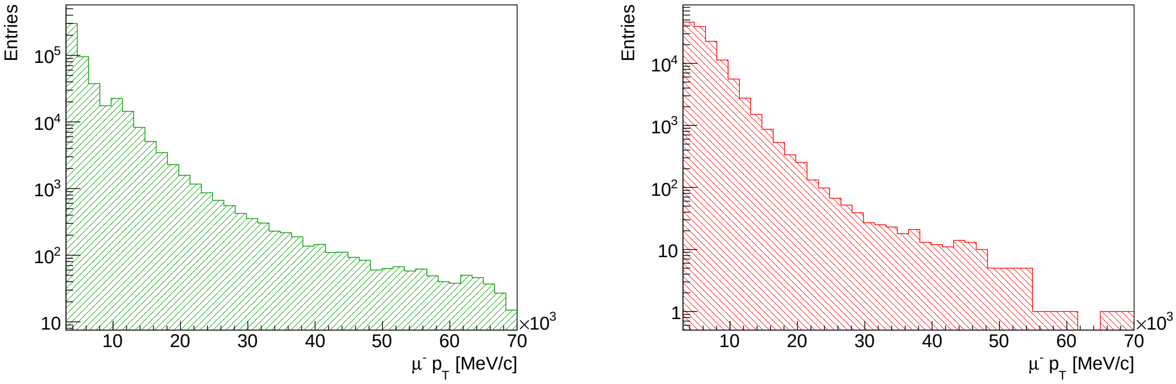

(a) misidentification background (b) background from heavy flavor decays

Figure 5.6: μ^- p_T distributions of the two main backgrounds.

5.2.2 Signal Fraction

The signal fraction corresponds to the probability of an event matching the signature to be a true Drell-Yan event and can be determined by a template fit. A template fit combines template shapes from several inputs, trying to match a given data distribution. This allows the determination of the fraction of each input component in the data without assigning individual events to signal or background. For a template fit to succeed, a variable needs to be found, for which signal and background events have different shapes. In addition, an independent method to determine the input shapes must be available. The two analyses presented both use the TFractionFitter (Filthaut and Wijngaarden 2002) from ROOT (Brun and Rademakers 1996) and use three different template shapes: one shape describing the signal and two shapes for the backgrounds. However the two analyses rely on different variables and determine the template shapes differently. The template shapes are determined from data where possible and simulation is used otherwise. Fig. 5.7 shows an example of a template fit.

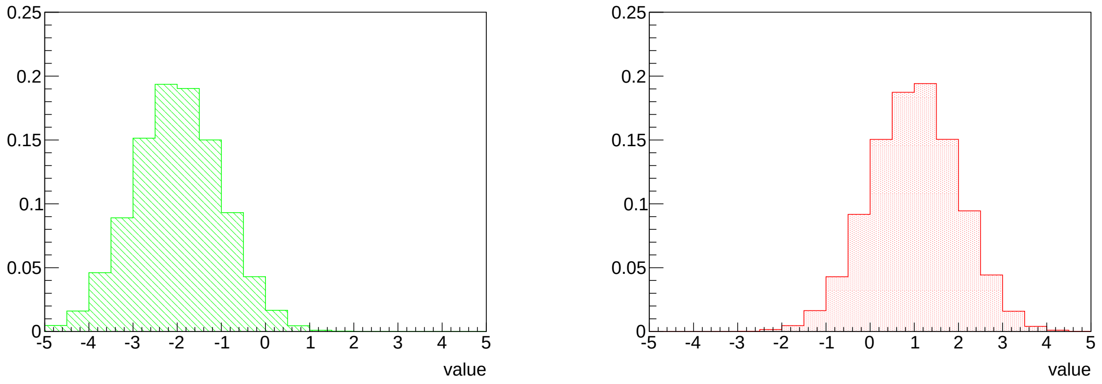

(a) first input shape for template fit

(b) second input shape for template fit

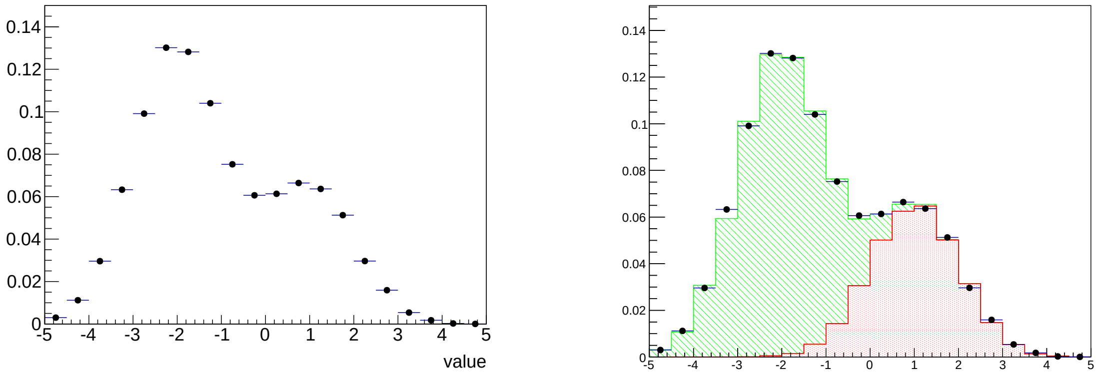

(c) target shape for template fit

(d) fit result

Figure 5.7: Example of a template fit. Figs. 5.7a and 5.7a show the input shapes for the template fit while Fig. 5.7c shows the target shape. Figure 5.7d shows the fit result with the input shapes stacked according to the weights determined by the fit.

5.2.3 Luminosity

The integrated luminosity ($\mathcal{L}$) in the LHCb detector is determined with two standard methods described in (LHCb Collaboration 2012a). The first method uses a van der Meer scan to determine the effective cross section of the colliding beams. During a van der Meer scan, the counting rate is measured as a function of the relative beam positions. From the counting rate the edges of the beams as well as the maximal overlap can then be determined. The second method determines the transverse beam profile from beam-gas interactions. In beam-gas interactions, a beam-particle collides with a particle from the residual gas in the machine. The tracking system of the LHCb detector allows the reconstruction of vertices for beam-beam as well as beam-gas interactions. From the distribution of the vertices of beam-gas interactions the beam profile can then be extracted.

Part II

The Analysis

Chapter 6

Analysis of Data Collected in 2011

This study measures the Drell-Yan production cross section as a function of the di-muon invariant mass ($M_{\mu\mu}$) as well as the di-muon rapidity ($y_{\mu\mu}$). It is based on the data collected by LHCb in 2011 at $\sqrt{s} = 7$ TeV. Overall the analysis covers the phase space $10.5 < M_{\mu\mu} < 120\,\mathrm{GeV}/c^2$ and $2.0 < y_{\mu\mu} < 4.5$. This phase space is divided into several regions where the cross section is measured separately. The analysis as a function of $M_{\mu\mu}$ is performed in 18 $M_{\mu\mu}$ sub-ranges, chosen such that they all contain a reasonable number of events. Each of the measurements for this analysis covers the full $y_{\mu\mu}$ range. For the analysis as a function of $y_{\mu\mu}$, four larger mass ranges are used, each divided into 9 $y_{\mu\mu}$ ranges. The division of the phase space is listed in Tables 6.1 and 6.2.

Table 6.1: Binning used for the measurement as a function of mass.

$M_{\mu\mu}$ [GeV/c^2]	10.5 – 11.0	11.0 – 11.5	11.5 – 12.0
	12.0 – 13.0	13.0 – 14.0	14.0 – 15.0
	15.0 – 17.5	17.5 – 20.0	20.0 – 25.0
	25.0 – 30.0	30.0 – 40.0	40.0 – 60.0
	60.0 – 70.0	70.0 – 80.0	80.0 – 90.0
	90.0 – 100.0	100.0 – 110.0	110.0 – 120.0
y	2.0 – 4.5		

Table 6.2: Binning used for the measurement as a function of rapidity.

$M_{\mu\mu}$ [GeV/c^2]	10.5 – 12.0	12.0 – 15.0	
	15.0 – 20.0	20.0 – 60.0	
y	2.0 – 2.25	2.25 – 2.5	2.5 – 2.75
	2.75 – 3.0	3.0 – 3.25	3.25 – 3.5
	3.5 – 3.75	3.75 – 4.0	4.0 – 4.5

Chapter 7

Data Samples

The data used for this analysis has been collected in 2011 and processed with the reconstruction version 14 and the stripping version 20r1. The dataset corresponds to a integrated luminosity ($\mathcal{L}$) of 584.3 pb^{-1} collected with the magnet polarity Down and 434.5 pb^{-1} collected with polarity Up.

7.1 Trigger & Stripping

Events are required to have fired the di-muon trigger lines in all three stages of the trigger (`L0`, `HLT1`, `HLT2`). The triggers require well reconstructed muon tracks, with momentum (p), transverse momentum (p_T) and di-muon invariant mass ($M_{\mu\mu}$) above different thresholds. The different lines used and their exact thresholds are listed in Table 7.1.

Table 7.1: Trigger lines used and their requirements.

Description	Internal Name	$\sqrt{{p_\mathrm{T}}^{\text{largest}} \cdot {p_\mathrm{T}}^{\text{2nd largest}}}$
Stage 0	`L0DiMuon`	> 1.296 GeV/c

		$p(\mu)$ [GeV/c]	$p_\mathrm{T}(\mu)$ [GeV/c]	$M_{\mu\mu}$ [GeV/c^2]
Stage 1, low mass	`Hlt1DiMuonLowMass`	> 6.0	> 0.5	> 1.0
Stage 1, high mass	`Hlt1DiMuonHighMass`	> 6.0	> 0.5	> 2.7
Stage 2, low mass	`Hlt2DiMuonDY3`			> 10.0
Stage 2, high mass	`Hlt2DiMuonDY4`			> 20.0

In the stripping, the events must have passed one of the high $M_{\mu\mu}$ lines for Drell-Yan events or the line for Z decays. Each of the stripping lines requires two muons and covers a different $M_{\mu\mu}$ interval above 10 GeV/c^2. In addition they put moderate constraints on p and p_T as well as the track reconstruction quality. The track reconstruction quality is expressed as χ^2-probability ($Prob\,(\chi^2)$). The exact values for the different lines are listed in Table 7.2.

Table 7.2: Stripping lines used and their requirements.

Description	Internal Name	$p(\mu)$ [GeV/c]	$p_\mathrm{T}(\mu)$ [GeV/c]	$M_{\mu\mu}$ [GeV/c^2]	$Prob\,(\chi^2)$
low mass γ	`DY2MuMuLine3`	> 10	> 3	10.0 − 20.0	> 0.001
high mass γ	`DY2MuMuLine4`	> 10	> 3	20.0 − 40.0	> 0.001
Z boson	`Z02MuMuLine`	-	> 3	> 40.0	-

Additional trigger and stripping lines are used to obtain the events for the Υ control sample and the misidentification background.

7.2 Selection Requirements

Events selected for the analysis are required to contain two well reconstructed tracks passing the detector well within its acceptance. The two tracks must be identified as muons of opposite charge and originate from a well reconstructed vertex. In addition p and p_T requirements consistent with the highest trigger threshold are enforced. Table 7.3 lists the individual selection criteria.

Table 7.3: Drell-Yan selection requirements.

tacks in acceptance	$2.0 < \eta(\mu) < 4.5$		
track reconstruction quality	$Prob\,(\chi^2)_\mathrm{track}$	$>$	0.001
vertex reconstruction quality	$\chi^2{}_\mathrm{vertex}/\mathrm{d.o.f}$	$<$	5
momentum ([GeV/c]) above thresholds	$p(\mu)$	$>$	10.0
	$p_\mathrm{T}(\mu)$	$>$	3.0

7.3 Control Samples

Two regions of the di-muon data used for this analysis are also used for several cross checks.

- Z sample: Events in the $M_{\mu\mu}$ region above 60 GeV/c^2 that pass the main selection. The mass distribution is shown in Fig. 7.1a. The background contamination was studied in (LHCb Collaboration 2012b) and (LHCb Collaboration 2012c) using simulation as well as data-driven methods similar to the ones explained in Section 8.2. Both studies found the contamination to be less then 0.5 %. For most cross checks only events from the tighter range $80 < M_{\mu\mu} < 100$ GeV/c^2 are used.

- Υ sample: Events in the mass range $9.365 < M_{\mu\mu} < 9.515$ GeV/c^2 which pass the main selection. The background in this mass region is extrapolated linearly from the side bands (8.990 GeV/c^2 – 9.290 GeV/c^2 and 9.590 GeV/c^2 – 9.890 GeV/c^2). About 15 % of the events in the signal window are background. Figure 7.1b shows the Υ resonance indicating the two side band regions as well as the signal region and the extrapolated background. When studying other distributions, the shape for background events is determined in the side band regions. This shape is then scaled according to the background in the signal region by 0.25 and subtracted from the signal distribution. This procedure is illustrated in Fig. 7.2 for the isolation variable introduced in Section 8.1

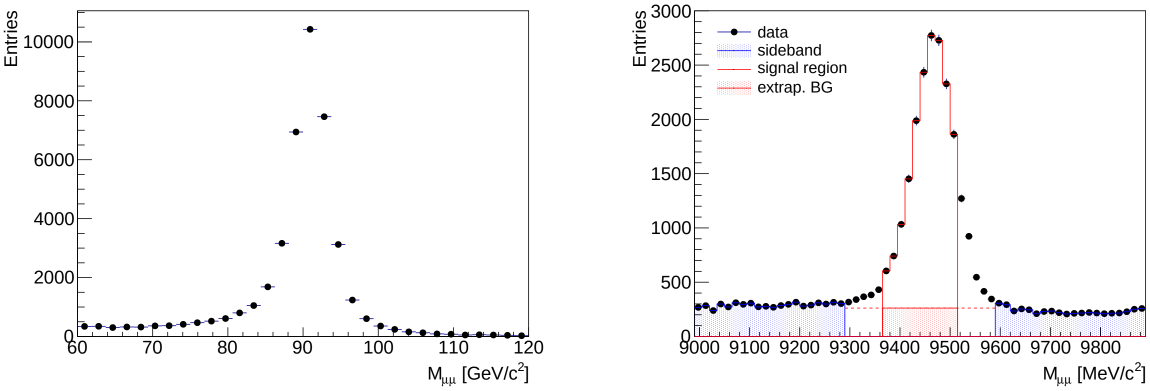

(a) Z (b) Υ

Figure 7.1: Mass distribution in the region of the control samples. No background subtraction has been performed.

7.4 Simulation Samples

While the analysis uses data-driven methods whenever possible, simulation is still used in one of four signal templates. In addition simulated events are used to determine several efficiencies, to study systematic uncertainties and to cross check the analysis.

The simulation was performed using Pythia 6.4 (Sjöstrand, Mrenna, and Skands 2006) with an LHCb configuration (Belyaev et al. 2010) and the Cteq6m parton distribution function (PDF) set. Simulated events were then passed through a Geant4 (GEANT4 Collaboration 2003; GEANT4 Collaboration 2006) based simulation of the LHCb detector. For trigger emulation and event reconstruction the standard LHCb reconstruction software was used.

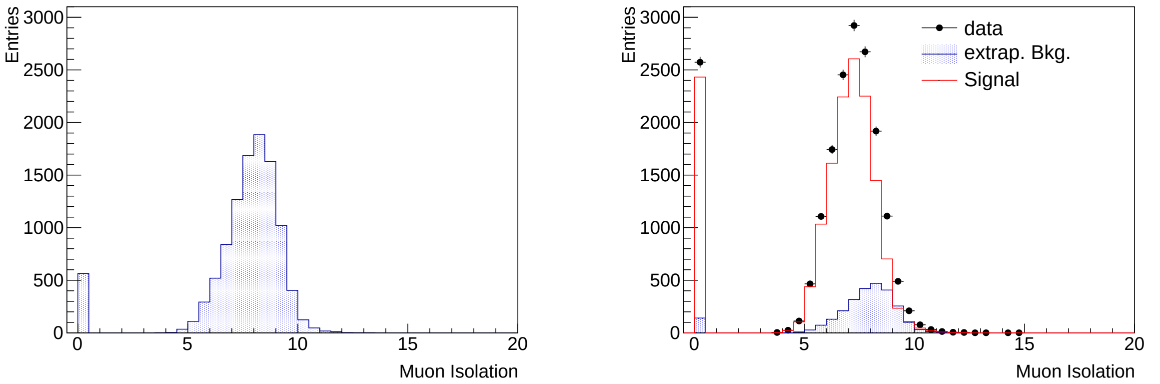

(a) distribution in side bands

(b) distribution in signal region and extrapolated background contribution

Figure 7.2: Illustration of the background subtraction procedure used to obtain shapes from the Υ control sample.

For the signal simulation three different samples are combined. The low mass region is covered by two samples of Drell-Yan events which require a minimal $Z/\gamma^\star$ invariant mass of 5 GeV/c^2 and 10 GeV/c^2 respectively. A sample of Z decays is used for the high mass region. Figure 7.3 shows the distribution of events as a function of $M_{\mu\mu}$ in these samples. For the combination, the events from all sources are treated as one large sample covering the full region of interest.

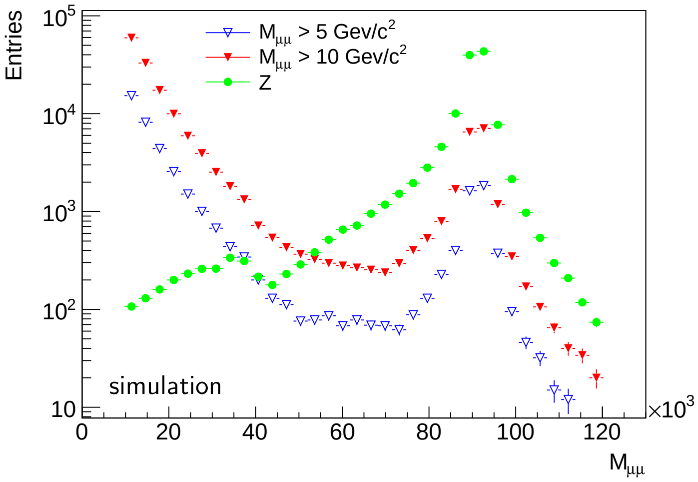

Figure 7.3: Distribution of events in the three samples used for signal simulation.

The occupancy of the detector in the signal simulation does not agree with the occupancy observed in data (see Fig. 7.4). Due to pile up events, the occupancy is generally higher in data. Where relevant, the distributions obtained from simulation are therefore weighted to match the occupancy measured in the IT. The most prominent example of such a distribution is the signal template obtained from simulation.

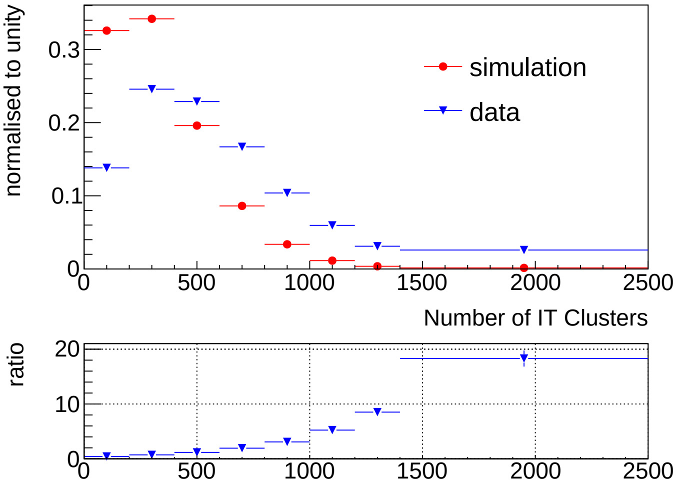

Figure 7.4: Detector Occupancy (Numbers of IT clusters) in simulation and data in the $M_{\mu\mu}$ range 80 GeV/c^2 – 100 GeV/c^2.

In addition, the following samples of non-signal events were used to cross-check the template fit and the tracking efficiency:

- **J/ψ** Simulated events with J/ψ decaying to two muons.
- **Υ** Simulated $\Upsilon(1S)$ decays with two muons in the final state.

Chapter 8

Signal Extraction

As introduced in Section 5.2 the signal fraction is extracted with a template fit. For this a distinguishing feature must be found. Such a feature is the activity in the region around the muons. Muons from true Drell-Yan decays are usually isolated. As background muons are usually produced in a jet, additional particles are expected close to the muon for background events.

8.1 Muon Isolation

Several muon isolation variables were studied. All these variables rely on the activity in a cone around the muon under study. The approach used for the analysis of the 2010 data (Appendix C), uses the fraction of the transverse momentum (p_{T}) carried by the muon relative to the total p_{T} in the cone surrounding the muon. This gives a well defined variable between 0 to 1 with the signal peaking towards 1 and broad background distributions. However the shape of the signal for this variable depends strongly on the di-muon invariant mass ($M_{\mu\mu}$) and cannot be determined from data except in the mass region of the Z.

A variable mostly independent of $M_{\mu\mu}$ can be constructed by considering only the activity in the vicinity of the muon, excluding the muon itself. For this, a cone centred around the muon track is considered. For signal the total p_{T} in such a cone should be low and largely independent of the invariant mass of the scattering process. The signal shape of a variable based on this, can therefore be determined from the di-muon mass range $80 < M_{\mu\mu} < 100$ GeV/c^2. The cone p_{T} variable is defined as

$$p_{\mathrm{T}}{}^{\mathrm{cone}}\left(\mu, R\right) = \sum_{t \in C(\mu, R)} p_{\mathrm{T}}\left(t\right) \tag{8.1}$$

where $C\left(\mu, R\right)$ is the cone with radius parameter R centred at the muon μ and t is a track inside this cone. A track is inside the cone, if the quadratic sum of the differences between the track angles is less than R

$$\sqrt{\Delta\eta\left(t,\mu\right)^2+\Delta\phi\left(t,\mu\right)^2}<R$$

Figure 8.1a shows the distribution of the total p_T in a cone with radius parameter $R = 0.5$, for two $M_{\mu\mu}$ ranges in simulation. A distribution from each end of the studied mass spectrum is shown. As expected the total p_T is small for most of the events with good agreement between the two $M_{\mu\mu}$ ranges. However, the cone variable has a tail to high total p_T. For events with $M_{\mu\mu}$ around the Z mass, this tail has a plateau at 40 GeV/c, due to ghost tracks. Ghost tracks are an artefact of the reconstruction that arise when two tracks share a large fraction of hits. To eliminate such ghost tracks, the total p_T of an inner cone with $R = 0.1$ is subtracted, leading to a variable representing a ring around the muon. Additionally, this variable should be more robust against the effects of photons from bremsstrahlung or final state radiation. Such photons could otherwise transfer p_T from the muon to the p_T measured in the cone. The distribution of the subtracted cone is shown in Fig. 8.1b. The impact of ghost tracks is removed and in the tail better agreement between the two mass regions is observed.

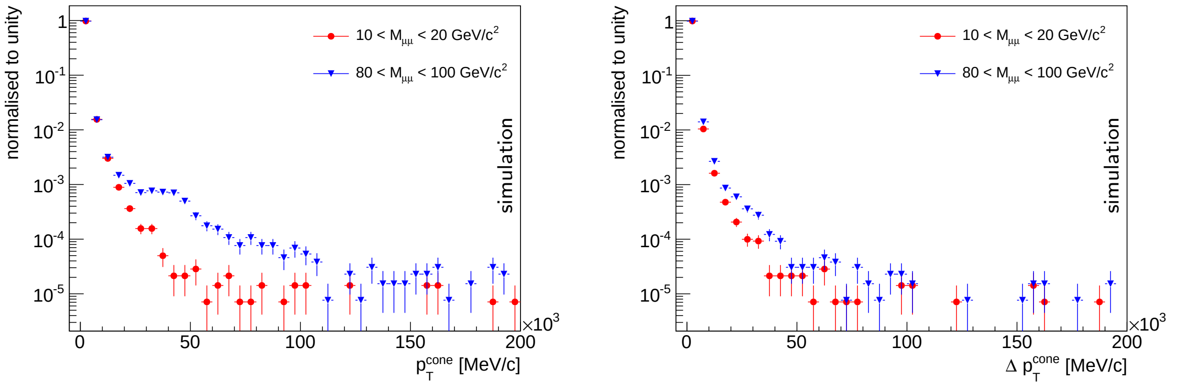

(a) total p_T in cone with radius parameter $R = 0.5$

(b) total p_T in cone with radius parameter $R = 0.5$, excluding inner cone of $R = 0.1$ (ring cone)

Figure 8.1: Studying different cone variables for the template fit.

The tail with low statistics at high total p_T is an additional problem for the planned use as a template when fitting. This problem can be addressed by using the logarithm of the total p_T instead of the p_T directly. The resulting muon isolation (μ_iso) is then defined as

$$\mu_\mathrm{iso} = \log\left(\left({p_\mathrm{T}}^\mathrm{cone}\left(\mu,0.5\right)-{p_\mathrm{T}}^\mathrm{cone}\left(\mu,0.1\right)\right)\cdot\frac{1}{\mathrm{MeV}/c}\right) \tag{8.2}$$

and remains in the range 0 to 20. The distribution is shown in Fig. 8.2 and has a distinct shape. The bin at 0 contains events with truly isolated muons. The gap above this bin is due to reconstruction thresholds. Following the gap is a broad but well defined distribution.

As expected, the central region of the broad distribution as well as the zero bin show only a week dependence on $M_{\mu\mu}$. The sides of the broad distribution however hint at a small shift towards lower values with decreasing $M_{\mu\mu}$. A study performed to correct for this mass dependence will be described in Section 8.1.3.

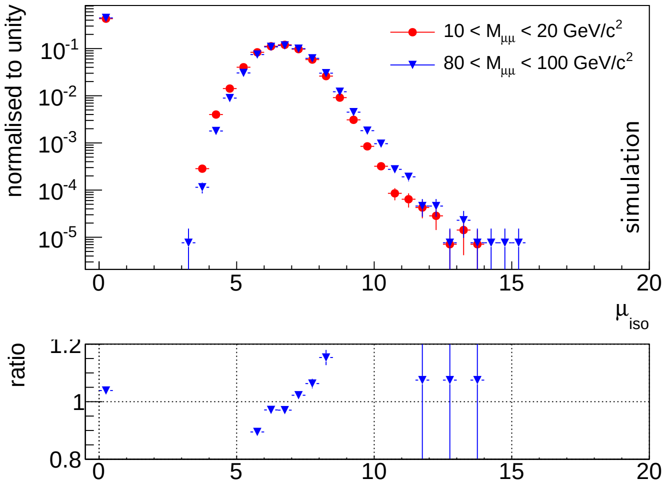

Figure 8.2: Logarithm of total p_{T} in the cone ring.

8.1.1 Isolation for both Muons Combined

The Drell-Yan final state contains two muons. As both muons are expected to be isolated, the information can be combined by using the worst of the two μ_{iso} values. This analysis therefore uses the di-muon isolation ($\mu\mu_{\mathrm{iso}}$):

$$\begin{aligned}\mu\mu_{\mathrm{iso}} &= \max\left({\mu^-}_{\mathrm{iso}}, {\mu^+}_{\mathrm{iso}}\right) && (8.3)\\ &= \log\left(\max\left({p_{\mathrm{T}}}^{\mathrm{cone}}\left(\mu^i, 0.5\right) - {p_{\mathrm{T}}}^{\mathrm{cone}}\left(\mu^i, 0.1\right)\right) \cdot \frac{1}{\mathrm{MeV}/c}\right) \quad \mu^i \in \{\mu^-, \mu^+\} && (8.4)\end{aligned}$$

In the analysis code Eq. (8.4) is used. This computation can be performed faster, as only one logarithm has to be calculated. Figure 8.3 shows the $\mu\mu_{\mathrm{iso}}$ distribution together with the μ_{iso} for the μ^-. As one would expect, the high end of the distribution is increased. The main features of the distribution however remain.

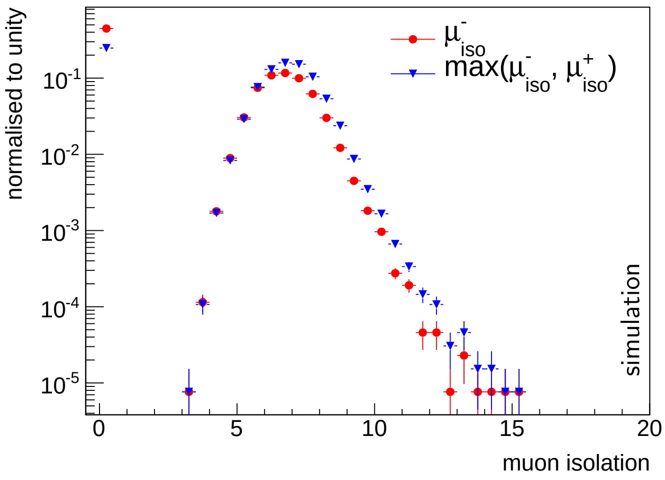

Figure 8.3: $\mu\mu_{\text{iso}}$ compared to the μ_{iso} of the μ^- only

8.1.2 Checking for Mass Dependence in Data

To check for a possible mass dependence, the shapes of the $\mu\mu_{\text{iso}}$ variable in the Z and the Υ control samples were compared. Figure 8.4 shows the comparison for both data and simulation. While very good agreement is observed for the broad distribution in data, the first bin is 20 % lower in the Υ sample. In simulation on the other hand, the first bin is in almost perfect agreement, while the broad distribution is shifted towards lower $\mu\mu_{\text{iso}}$ values. These effects are accounted for by the fit procedure used to extract the signal fraction (ρ). Details are discussed in Section 8.4.

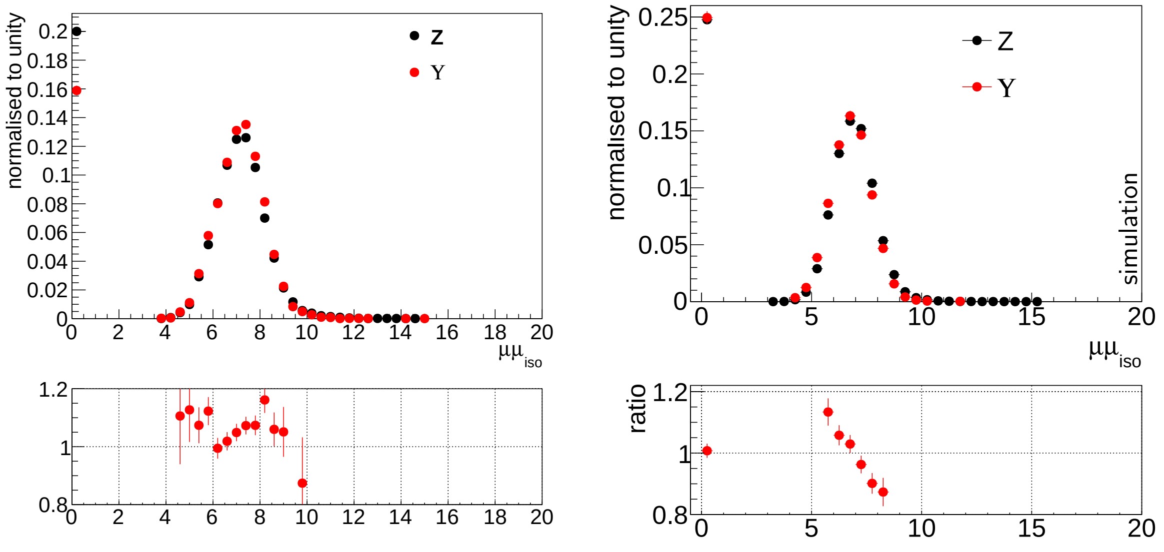

(a) data

(b) simulation

Figure 8.4: Comparing the $\mu\mu_{\text{iso}}$ from Z and Υ in data and simulation.

8.1.3 Determining the Scale Factors

Since a weak mass dependence of μ_{iso} is observed in simulation. A mass dependence for $\mu\mu_{\text{iso}}$ is expected too. As illustrated in Fig. 8.5a, such a dependence is observed. The mass dependence can largely be corrected for by scaling the isolation variable with a mass dependent factor. These scale factors are determined from simulation by minimising the sum of the square of the deviations (χ^2) between the two distributions.

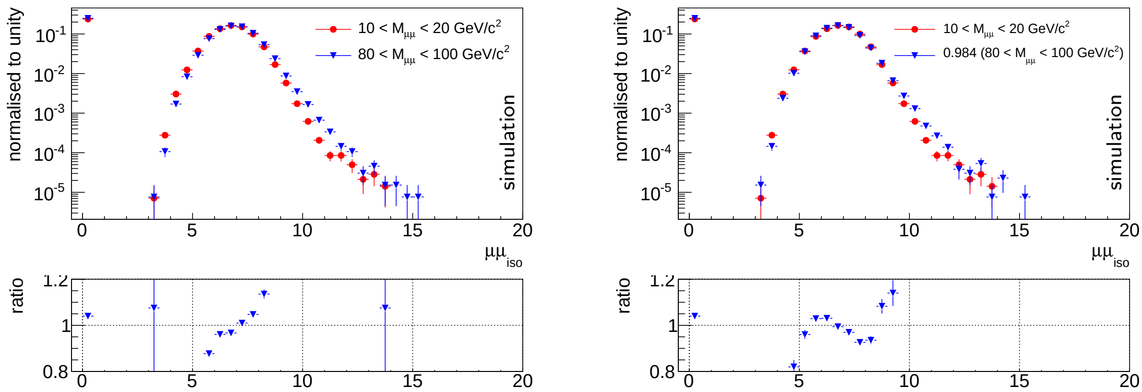

(a) direct comparison, no scale factor is applied

(b) scaled comparison, the reference range ($80 < M_{\mu\mu} < 100\,\text{GeV}/c^2$) is scaled by 0.984

Figure 8.5: Comparing the $\mu\mu_{\text{iso}}$ distribution in the ranges $10 < M_{\mu\mu} < 20\,\text{GeV}/c^2$ and $80 < M_{\mu\mu} < 100\,\text{GeV}/c^2$.

The scale factor for a given $M_{\mu\mu}$ range is obtained by comparing the $\mu\mu_{\text{iso}}$ distribution in this range to the distribution from the Z range ($80 < M_{\mu\mu} < 100\,\text{GeV}/c^2$). For the comparison the Z distribution is scaled by all factors $f \in \{0.970, 0.971, 0.972, \ldots, 1.002\}$ and the factor resulting in a minimal χ^2 value is selected. The boundaries of the scanned interval were chosen based on the observed χ^2 distribution. Figure 8.6a shows an example of χ^2 value corresponding to different scale factors, while Fig. 8.5b shows the effect of the optimal scale factor on the $\mu\mu_{\text{iso}}$ distribution.

Scale factors are determined for several di-muon mass ranges and the result is shown in Fig. 8.6b. No scaling is needed for masses above 40 GeV/c^2 while the scale factors below this value deviate from 1 increasingly. In trying to parametrise this behaviour, a linear and a sigmoid function were fitted to the data. The following parametrisations resulted from the fit:

$$f_{\text{linear}} = 5.26 \cdot 10^{-4} \cdot M_{\mu\mu} + 0.977 \tag{8.5}$$

$$f_{\text{sigmoid}} = \frac{1}{1 + 0.058 \cdot e^{-\frac{M_{\mu\mu}}{10.93}}} \tag{8.6}$$

Both functions are shown in Fig. 8.6b. The linear function is only valid below 45 GeV/c^2 but does not describe the scale factors well. The sigmoid function on the other hand achieves a reasonable description of the observed factors.

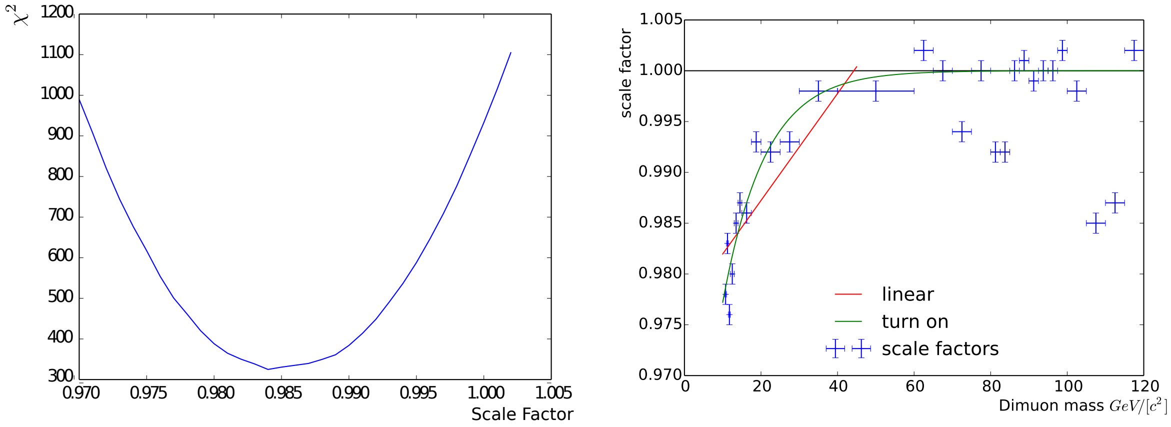

(a) χ^2 optimisation for the di-muon mass range $10 < M_{\mu\mu} < 20\,\mathrm{GeV}/c^2$

(b) Optimal scale factors for the different di-muon mass ranges used in this analysis. The red and green line shows the different parametrisations considered.

Figure 8.6: Illustration of the χ^2 procedure used to determine the scale factors for the signal distribution.

However, the mass range seems to have different effects on the $\mu\mu_{\text{iso}}$ shape taken from data and from simulation (see Section 8.1.2). It is therefore unclear how well the scale factors determined from simulation can be used to correct the signal shape in data. Figure 8.7 compares the $\mu\mu_{\text{iso}}$ distribution in the Υ control sample to the scaled distribution from Z decays. The differences show the expected pattern. Applying a scale factor moves the broad distribution towards lower values but does not mimic the threshold effect responsible for the gap in the distribution. A scale factor will therefore not affect the first bin. In general the agreement seems worse than between the unscaled distributions (Fig. 8.4a). Due to these considerations, the signal fraction (ρ) is determined with both, the scaled and the unscaled template. The results are then combined. The procedure used to obtain the final value for ρ and its uncertainty is described in detail in Section 8.4.

8.1.4 Shape for Bins of Rapidity

For the cross section as a function of rapidity, the same procedure as for the cross section as a function of mass is used. Figure 8.8 shows the $\mu\mu_{\text{iso}}$ distribution from five different di-muon rapidity ($y_{\mu\mu}$) bins. The distribution is slightly different in the different $y_{\mu\mu}$ bins, the first bin and the low flank are most affected. Tracks in the forward direction seem to be less well isolated. This might be expected because the particles from the proton

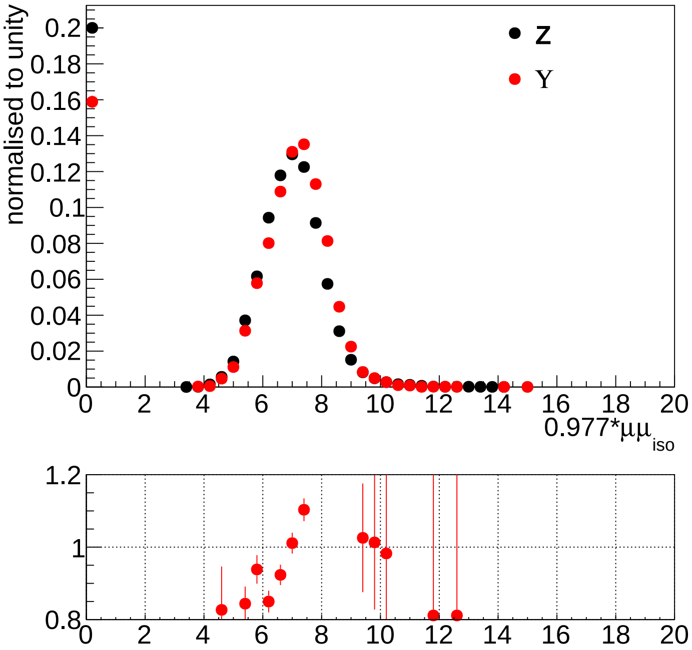

Figure 8.7: Comparison between the signal shape in the Υ control sample and the shape in the Z region scaled by 0.977.

remnant are at high rapidities. To account for such effects, the signal template for a $y_{\mu\mu}$ range is taken from the corresponding range in the Z sample. To increase statistics all events in the range $60 < M_{\mu\mu} < 120$ GeV/c^2 are used.

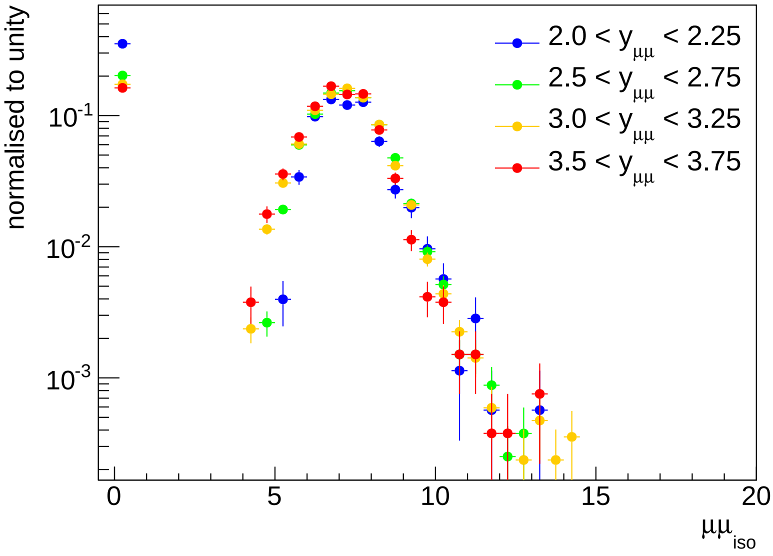

Figure 8.8: Comparison of the $\mu\mu_{\text{iso}}$ distribution for different ranges of $y_{\mu\mu}$.

8.2 Background

The two main backgrounds for this analysis are misidentified pions or kaons (MisId) and semileptonic decays of heavy flavor hadrons (HF). Figure 8.9 shows the $\mu\mu_{\text{iso}}$ distribution of these background categories compared to the signal distribution. As expected, the centre of the signal distribution is at lower values. In addition, the bin at zero contains only a small fraction of the events for both background distributions. Comparing the two backgrounds to each other, the heavy flavour background is slightly more signal like. The template for each of these two backgrounds is determined from two sources separately. These will be discussed in detail below.

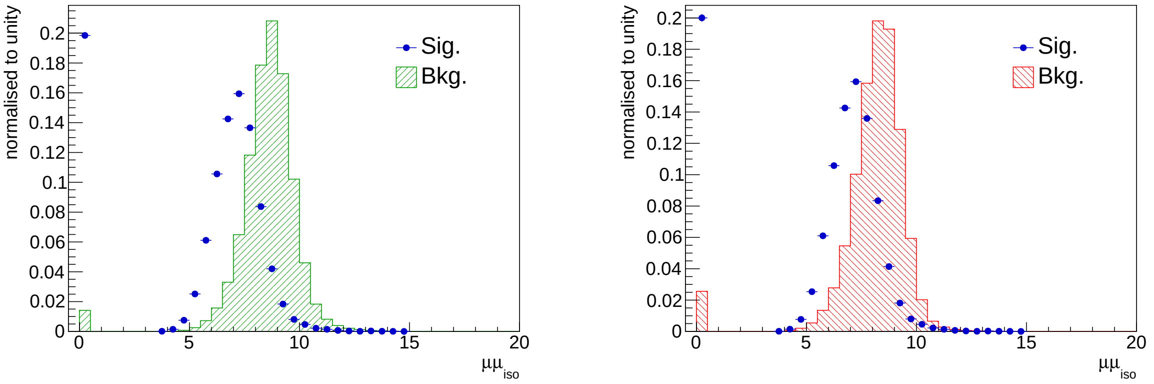

(a) $\mu\mu_{\text{iso}}$ shape of the background from misidentification

(b) $\mu\mu_{\text{iso}}$ shape of the background from heavy flavor decays

Figure 8.9: $\mu\mu_{\text{iso}}$ shape of the main backgrounds. Overlaid in (blue) is the shape for signal.

8.2.1 Misidentification Background

The main template for the MisId background is based on events with two muons of the same charge (SameSign). At least one of the muons in such an event is misidentified offering a straightforward source for a background template. For the template, only events passing the additional selection requirements (Table 8.1) are used. These requirements reduce the overlap between the two background sources.

Table 8.1: Additional requirements for the SameSign background template.

well reconstructed vertex	Z (vertex χ^2)	$<$ 5.0
tracks originating from the primary vertex (PV)	μ^- (MinIP)	< 0.05 mm
	μ^+ (MinIP)	< 0.05 mm

An alternative template for the MisId background is based on events selected with a random trigger (MinBias). From the dataset obtained by such a trigger, events are selected if they contain two tracks with a common vertex. A template describing events with misidentified muons can then be obtained by weighting each event with the probability for its two tracks to be misidentified. Assuming that the minimum bias data contains no true muons, the misidentification probability can be determined from data. The ratio of particles identified as muons to all particles in the dataset describes the misidentification probability and is parametrised as function of the longitudinal momentum of the muon

$$P\left(p_Z\right) = 1 + \alpha - e^{-\beta/p_Z} + \gamma p_Z \tag{8.7}$$

The parameters α, β, and γ are free parameters determined by a fit. The exponential term describes the probability of a hadron to decay in flight, while the linear term accounts for hadrons punching through the calorimeters and leaving hits in the muon station. Figure 8.10 shows, the fit result for both the positive and negative muons while Table 8.2 lists the obtained parameters.

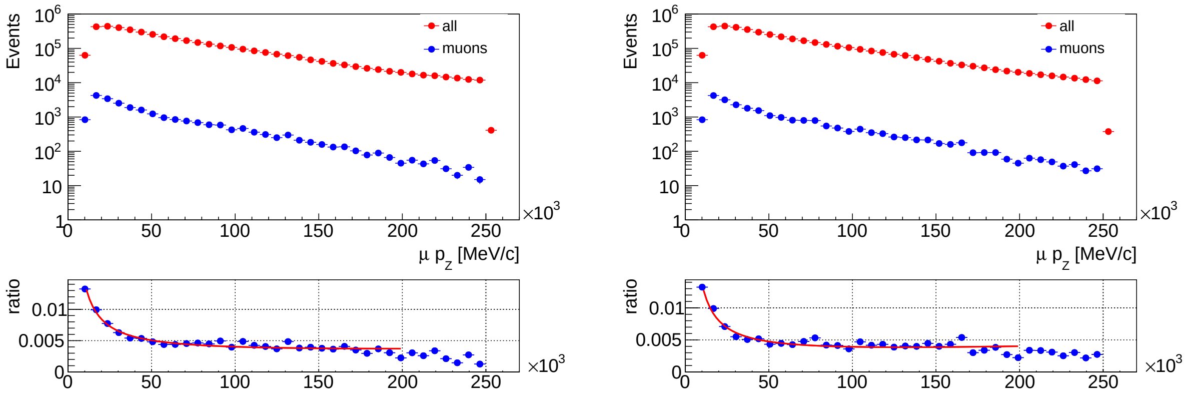

(a) μ^-

(b) μ^+

Figure 8.10: Relevant distributions and fits for the misidentification probability in the minimum bias data.

Table 8.2: Parameters obtained by the fit of the misidentification probability.

	μ^-	μ^+
α	$2.60 \pm 0.16 \times 10^{-3}$	$2.00 \pm 0.16 \times 10^{-3}$
β	116.0 ± 3.7	116.5 ± 3.7
γ	$2.7 \pm 1.2 \times 10^{-9}$	$6.8 \pm 1.2 \times 10^{-9}$

With $\gamma < 1 \times 10^{-8}$ the linear part describing punch through is negligible. In Fig. 8.11 the MinBias template is shown with and without weighting according to the misidentification probability. The effect of this reweighting is small. This is expected, as the activity around a muon candidate measured by $\mu\mu_{\text{iso}}$, should not depend on the candidate's misidentification probability. The two MisId background templates (Fig. 8.12) differ significantly however. Differences are especially pronounced in in the 0-bin and the high $\mu\mu_{\text{iso}}$ side. The MinBias template is therefore used without weighting. This has the advantage of smaller uncertainties in the inputs for the fit. The differences between the two MisId templates are accounted for in the systematic uncertainty of the signal fraction.

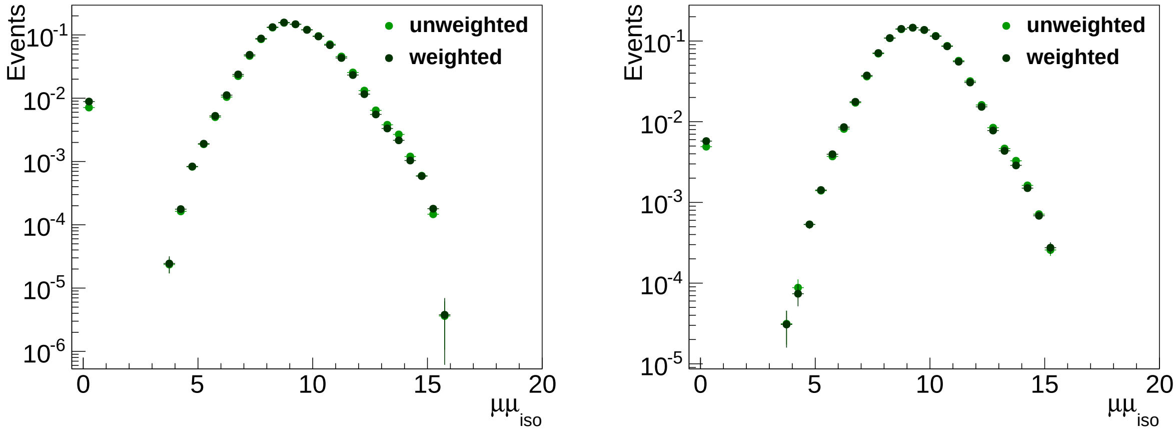

(a) $10 < M_{\mu\mu} < 12$ GeV/c^2 (b) $60 < M_{\mu\mu} < 120$ GeV/c^2

Figure 8.11: Comparing the MinBias template with and without weighting according to the misidentification probability.

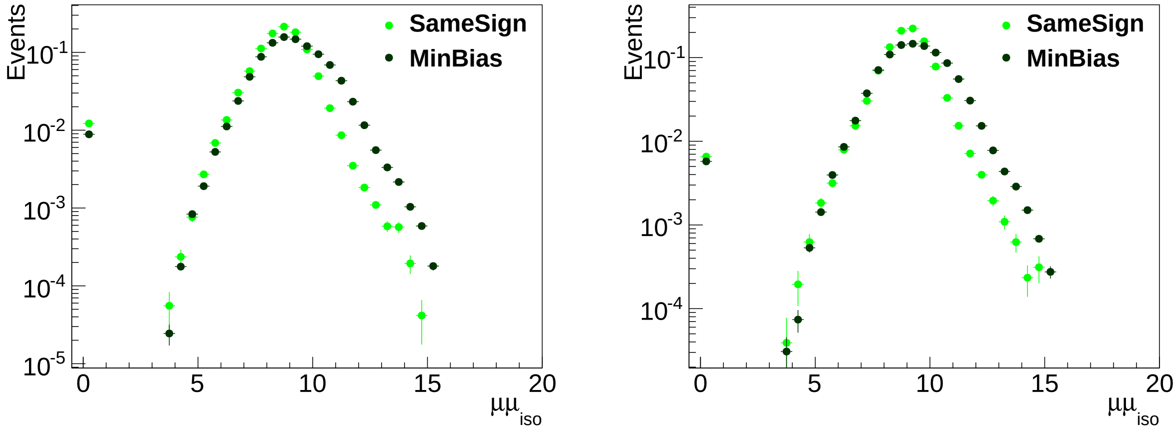

(a) $10 < M_{\mu\mu} < 12$ GeV/c^2 (b) $60 < M_{\mu\mu} < 120$ GeV/c^2

Figure 8.12: $\mu\mu_{\text{iso}}$ distribution for the two MisId templates.

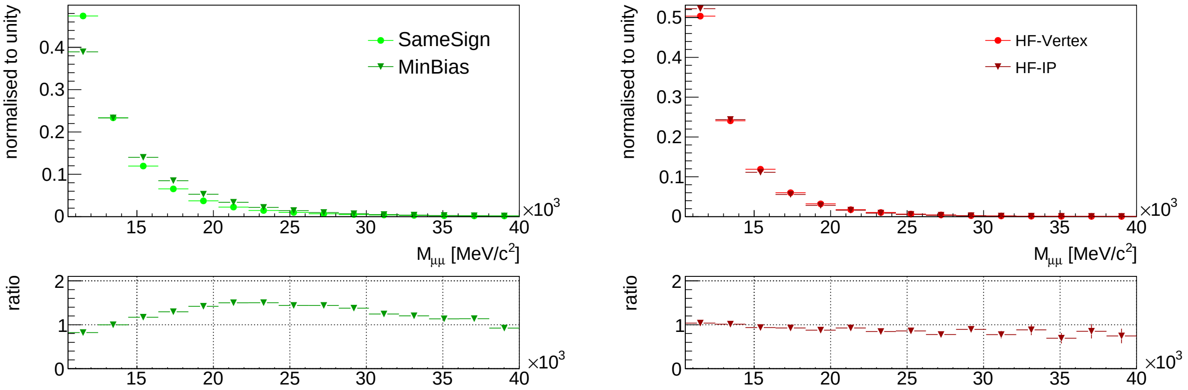

(a) MisId templates (b) HF templates

Figure 8.13: $M_{\mu\mu}$ distribution for the different background templates.

8.2.2 Heavy Flavor Background

Both templates for the background from semileptonic decays of heavy flavor hadrons (HF), are based on the main dataset directly. Events for these templates are selected, if at least one muon is not originating from the PV. The main template requires events with a badly reconstructed di-muon vertex (HF-Vertex), while the alternative template contains events where both muons have a high minimum impact parameter (HF-IP). The precise values used for the selection requirements are listed in Table 8.3 and the resulting distributions are shown in Fig. 8.14.

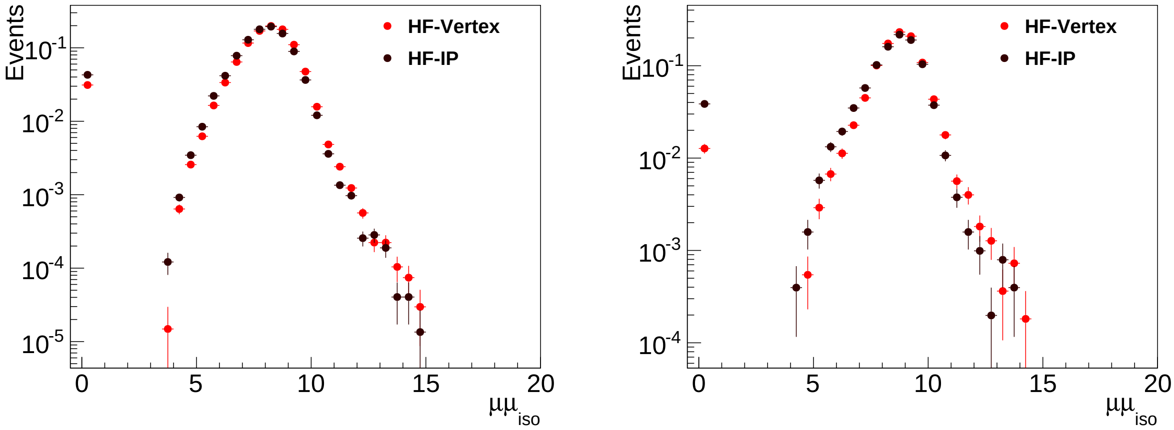

(a) $10 < M_{\mu\mu} < 12$ GeV/c^2 (b) $60 < M_{\mu\mu} < 120$ GeV/c^2

Figure 8.14: $\mu\mu_{\text{iso}}$ distribution for the two HF templates.

Exchanging the two HF background templates is a proper test for the fit only if the templates are largely independent. As a measure of this, the fraction of events contained in both templates is used. Figure 8.15 shows the ratio of events passing both requirements

Table 8.3: Additional requirements for the HF background templates.

HF-Vertex	badly reconstructed vertex	$\mu\mu$ (vertex χ^2) $>$	15.0
HF-IP	tracks not from any PV	μ^- (MinIP)	$> 0.09\,\mathrm{mm}$
		μ^+ (MinIP)	$> 0.09\,\mathrm{mm}$

to events passing the HF-Vertex requirement only. The overlap is below 25 % in the low mass region and falls off towards higher masses.

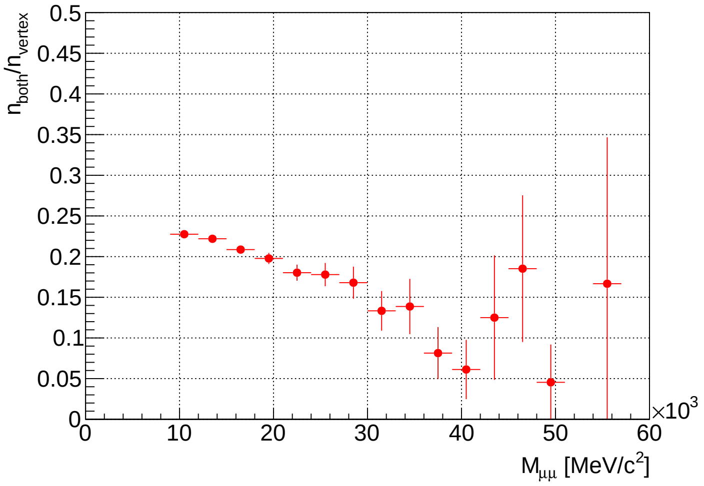

Figure 8.15: Fraction of events from the HF-Vertex template found in the HF-IP templates as function of $M_{\mu\mu}$.

It is also important, to ensure that the HF background templates are not contaminated with signal events. For this, the fraction of signal events passing the background selection requirements was studied in data and simulation. In data, the selection requirements listed in Table 8.3 were applied to the Z control sample, while in simulation the selection requirements were applied to all mass regions. The results for both datasets are listed in Table 8.4. For simulation, the result for the different mass regions is shown in Fig. 8.16 Almost no signal events pass the HF-Vertex requirement, but the HF-IP requirement selects up to 3 % of the signal events in simulation. Therefore, the almost signal free HF-Vertex template is used as the main HF background shape.

Table 8.4: Contamination of the HF background templates with signal events.

template	data [%]	simulation [%]
HF-Vertex	0.2	0.1 - 0.3
HF-IP	0.8	2.0 - 3.2

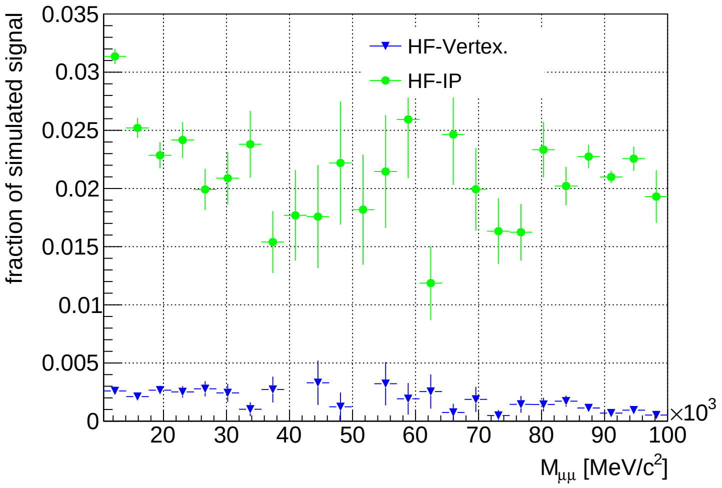

Figure 8.16: Fraction of events in the signal simulation, passing the requirements of the background templates.

8.2.3 Further Considerations

As mentioned in Section 5.2.1 the other relevant background sources can be included into these backgrounds. Mixed background, for example an event with a first muon from a W decay and a second muon from a heavy flavor decay, is covered by the isolation variable chosen. Since the muon with the worst isolation is relevant, every mixed background event will be included in the template for the least isolated muon. The example above, is therefore included in the heavy flavor template. The background from $Z/\gamma^{\star}$ decays to taus is included in the template for the heavy flavour decays.

As illustrated by Fig. 8.13, statistics in the high $M_{\mu\mu}$ region are low for all backgrounds. To ensure reasonable statistics in all templates, events are selected from the mass range $20.0 < M_{\mu\mu} < 60.0$ GeV/c^2 for all measurements above 20.0 GeV/c^2. This at the same time ensures that the signal contamination seen in Fig. 5.4b does not affect the signal fraction.

8.3 Reweighting Templates

The shape of the $\mu\mu_{\text{iso}}$ variable depends on the number of PVs in an event. Events with more than one PV have increased background activity and the isolation of the muons is worse. The templates are therefore corrected to correspond to the same PV distribution as the data. For both background types, the PV distribution of the low mass regions is compared to the distribution of the signal template. The weights are then given by the ratio of the two distributions. Figure 8.17 shows an example of the resulting weights. The distribution for the HF background is close to the reference shape. This is expected as both shapes are based on the main dataset and no mass dependence of the multiplicity is observed in that dataset.

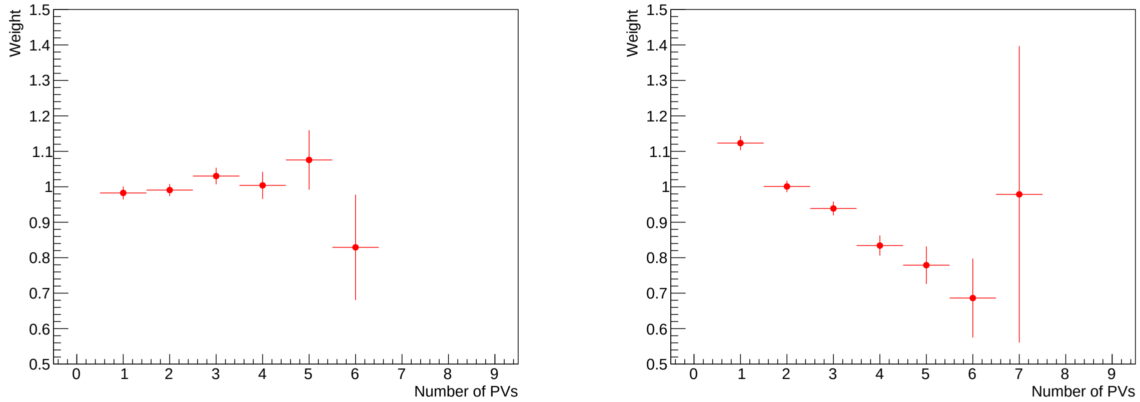

(a) HF-Vertex (b) SameSign

Figure 8.17: Weights used to correct for the number of PVs for the 12 to 13 GeV/c^2 mass range.

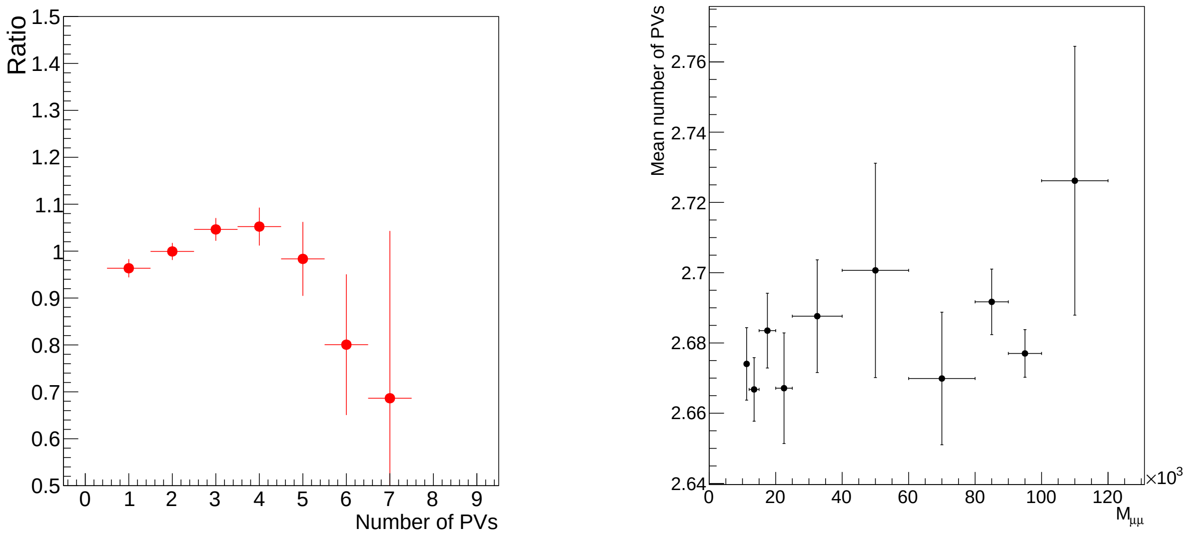

(a) Comparing the PV distribution for Z and $\Upsilon(1S)$ signal events (b) Average number of PV for different mass ranges in simulation

Figure 8.18: Distribution of the number of PV for signal events.

No correction is needed for the signal template, as the PV distribution of signal events is independent of the mass within ±5 %. This has been checked in simulation and by comparing the PV distribution in the Z and $\Upsilon(1S)$ mass range. The results of both checks are shown in Fig. 8.18.

8.4 Signal Yield

To determine the signal fraction (ρ), a separate fit is performed in each of the 54 ($M_{\mu\mu}$, $y_{\mu\mu}$) regions used for this analysis. The fit determines the relative fraction of the three templates describing the signal and the two backgrounds. The resulting signal fractions vary from 14 % for the lowest di-muon mass range to 100 % in the Z region. The signal yield is calculated by multiplying ρ with the total number of entries in the fitted distribution.

The signal yield obtained by the main fit for the different $y_{\mu\mu}$ integrated regions are listed in Table 8.5, while Fig. 8.19 shows six examples of these fits. The χ^2 obtained are in a reasonable range, but it seems that the fraction fitter overestimates the uncertainties. The figures and numbers for the main fits in all 54 regions are included in Appendix B.1.

Table 8.5: Result of fits with the templates: Z, scaled; SameSign; HF-Vertex.

$M_{\mu\mu}$ [GeV/c^2]	$y_{\mu\mu}$	signal yield	ρ	χ^2/ndof
10.5 – 11.0	2.00 – 4.50	17 500 ± 600	0.140 ± 0.005	0.61
11.0 – 11.5	2.00 – 4.50	15 500 ± 600	0.152 ± 0.006	0.79
11.5 – 12.0	2.00 – 4.50	14 200 ± 500	0.167 ± 0.006	1.04
12.0 – 13.0	2.00 – 4.50	25 000 ± 600	0.195 ± 0.005	0.99
13.0 – 14.0	2.00 – 4.50	19 800 ± 500	0.218 ± 0.006	0.77
14.0 – 15.0	2.00 – 4.50	16 300 ± 400	0.255 ± 0.006	0.69
15.0 – 17.5	2.00 – 4.50	30 000 ± 500	0.317 ± 0.005	0.65
17.5 – 20.0	2.00 – 4.50	18 900 ± 300	0.404 ± 0.007	1.15
20.0 – 25.0	2.00 – 4.50	21 200 ± 300	0.515 ± 0.007	1.50
25.0 – 30.0	2.00 – 4.50	10 410 ± 160	0.648 ± 0.010	0.95
30.0 – 40.0	2.00 – 4.50	9360 ± 140	0.767 ± 0.012	1.74
40.0 – 60.0	2.00 – 4.50	6000 ± 100	0.912 ± 0.015	0.75
60.0 – 70.0	2.00 – 4.50	1540 ± 40	0.960 ± 0.030	0.64
70.0 – 80.0	2.00 – 4.50	2240 ± 50	0.990 ± 0.020	0.53
80.0 – 90.0	2.00 – 4.50	6500 ± 400	1.000 ± 0.070	0.50
90.0 – 100.0	2.00 – 4.50	10 890 ± 130	0.994 ± 0.012	0.32
100.0 – 110.0	2.00 – 4.50	840 ± 60	1.000 ± 0.070	0.45
110.0 – 120.0	2.00 – 4.50	240 ± 30	1.000 ± 0.150	0.24

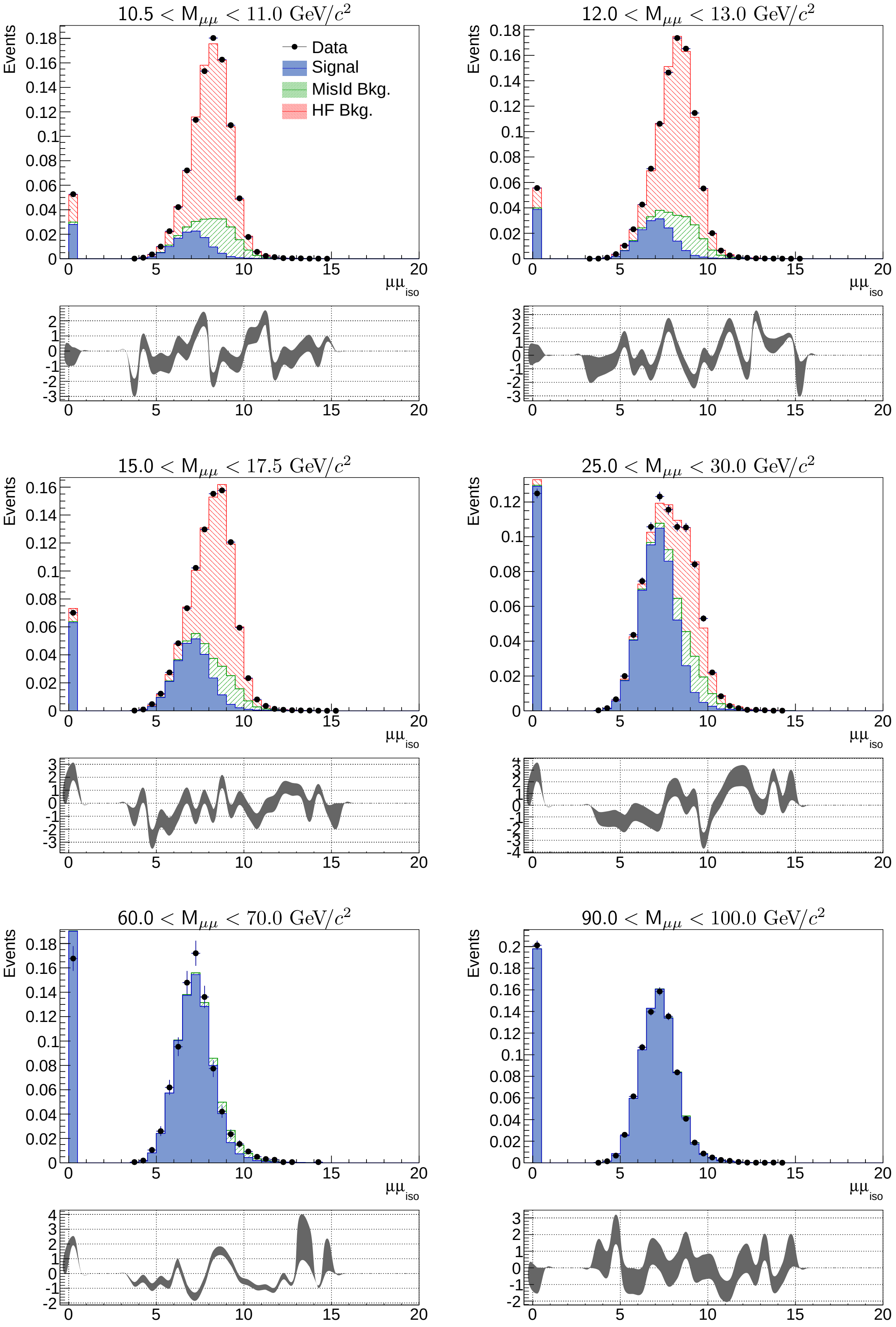

Figure 8.19: Example fits in different mass ranges with the templates: Z, scaled; SameSign; HF-Vertex.

Several templates are available for the signal shape and for each of the two backgrounds. All fits are therefore repeated with the 12 different template combinations listed in Table 8.6. The Z signal shape is taken from data in the mass range 80 to 100 GeV/c^2 and scaled according to the sigmoid function given in Eq. (8.6) The Υ signal is the background subtracted distribution determined from data (see Section 7.3 and Fig. 7.2). The first combination with the signal template from the scaled Z shape plus the HF-Vertex and SameSign background templates is considered the main configuration. The main fit is used for illustration throughout this section but is treated as the other HF-Vertex/SameSign fits in the combination described below. The combination of the HF-IP and the MinBias background templates was not used. Both these templates have known weaknesses, for example signal contributions, and tests with this combination showed that the fit significantly underestimates ρ.

Table 8.6: Template combinations used for the fits. The main fit is set in bold, the result from the first combination of each group is used to determine the central value.

signal	HF	MisId
Z, scaled	**HF-Vertex**	**SameSign**
	HF-Vertex	MinBias
	HF-IP	SameSign
Z, unscaled	HF-Vertex	SameSign
	HF-Vertex	MinBias
	HF-IP	SameSign
Υ	HF-Vertex	SameSign
	HF-Vertex	MinBias
	HF-IP	SameSign
simulation	HF-Vertex	SameSign
	HF-Vertex	MinBias
	HF-IP	SameSign

The 12 values for ρ in a given region are combined to obtain the final ρ and the systematic uncertainty on it. For the central ρ the mean of the four values obtained with the HF-Vertex/SameSign fits is used, while the standard deviation of all 12 values is used as systematic uncertainty. Figure 8.20 compares the signal yields as a function of $M_{\mu\mu}$ obtained with the different template configurations. As expected the low mass region has a relatively large systematic uncertainty while the statistical uncertainty dominates for the high mass region. The full results of all fits are given in the tables in Appendix B.2.

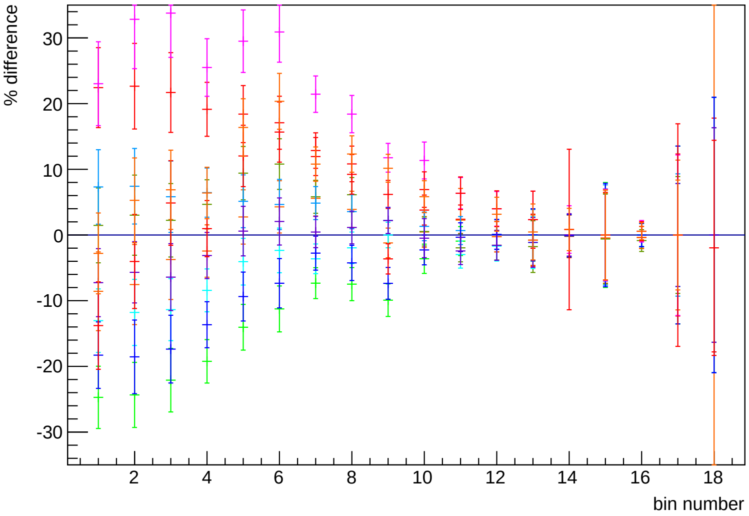

Figure 8.20: Differences in signal yields obtained by fitting with the various template combinations. The main configuration is used as reference. The bins are numbered in order of increasing mass, *i.e.* the 10.5 to 11 GeV/c^2 bin is bin 1, the 110 to 120 GeV/c^2 bin is bin 18.

8.4.1 Applying Fractions

The fractions determined by the fit were cross checked in other variables such as the two angles (η and ϕ) or the p_T of the muons. For this the distributions for the signal and the two backgrounds are weigthed according to the fit result and their sum is then compared to the measured distribution. Figures 8.21 to 8.23 show the resulting comparisons for the 17.5 to 20 GeV/c^2 mass range and the fractions obtained by the main fit. In Fig. 8.21 the signal shape is taken from data using the 80 to 100 GeV/c^2 mass range. While the distributions for the difference in pseudorapidity ($\Delta\eta$) in Fig. 8.21a are in good agreement, Fig. 8.21b shows significant deviations for the difference in azimuthal angle ($\Delta\phi$). This can be explained if the distribution of $\Delta\phi$ for signal events does depend on the mass. The comparison was therefore repeated with the signal shape taken from simulation (Fig. 8.22). The resulting figure shows excellent agreement.

Figure 8.23 shows two more comparison where the signal shape is taken from simulation. For the summed p_T, good agreement is observed. The p_T shapes in all three sources are, however, similar and a strong sensitivity is not expected. Finally, the agreement for the muon isolation variable as used in the 2010 analysis was checked. Figure 8.23b shows reasonable agreement. A significant deviation is only observed for a jet-isolation close to one.

The cross check was repeated with the fractions obtained by the fits with the unscaled

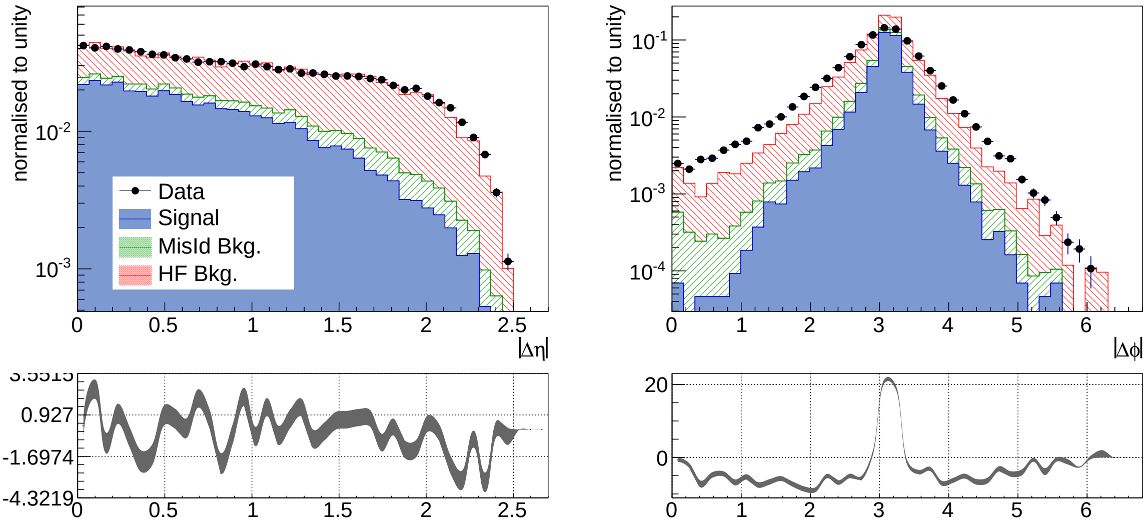

(a) $|\Delta\eta|$

(b) $|\Delta\phi|$

Figure 8.21: Checking the fitted fractions on the distributions of $\Delta\eta$ and $\Delta\phi$. The templates from the main fit are used and the 17.5 to 20 GeV/c^2 mass bin is shown.

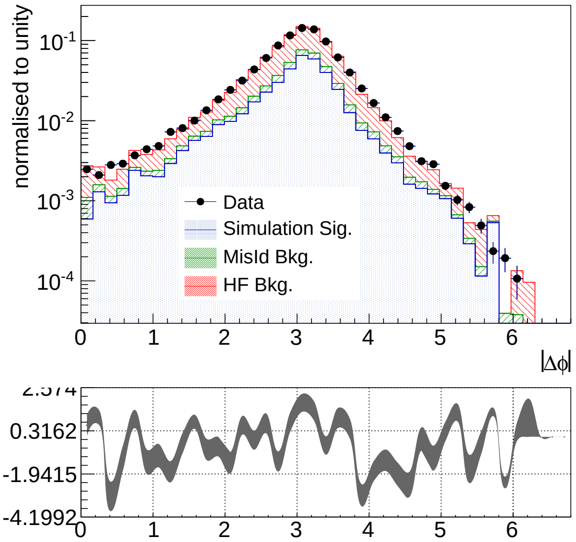

Figure 8.22: Checking the fitted fractions on the distributions of $\Delta\phi$. The signal shapes are taken from simulation and the SameSign and HF-Vertex background templates are used. The 17.5 to 20 GeV/c^2 mass bin is shown.

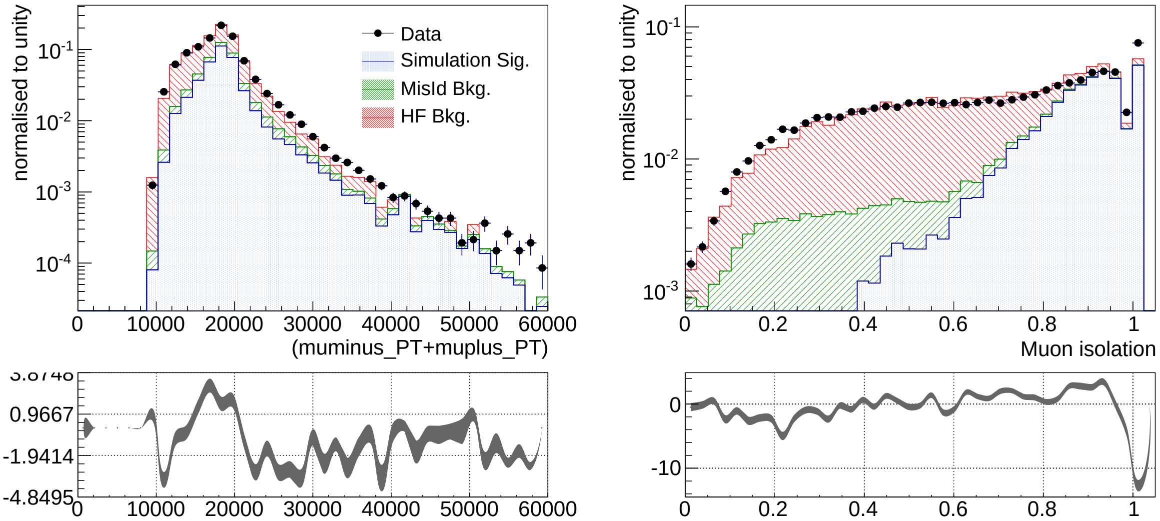

(a) $p_T^- + p_T^+$

(b) muon isolation

Figure 8.23: Checking the fitted fractions on the distributions for summed p_{T} and muon isolation. The signal shapes are taken from simulation and the SameSign and HF-Vertex background templates are used. The 17.5 to 20 GeV/c^2 mass bin is shown.

shape from the Z sample as well as the shape from the Υ sample. In Fig. 8.24 the resulting $\Delta\eta$ comparison is shown. The agreement is as good as in Fig. 8.21a.

Finally the sensitivity of this cross check was assessed by repeating the low mass fits with a background only hypothesis by excluding the signal template from the fit. The resulting fractions were then again applied to the control variables. Figure 8.25 shows the resulting comparisons for $\Delta\eta$ and muon isolation. Clear deviations are visible for both variables indicating that the signal component is missing. In addition the fit returns no MisId component. As both background processes are known to contribute, this shows that the background only hypothesis does not describe the data.

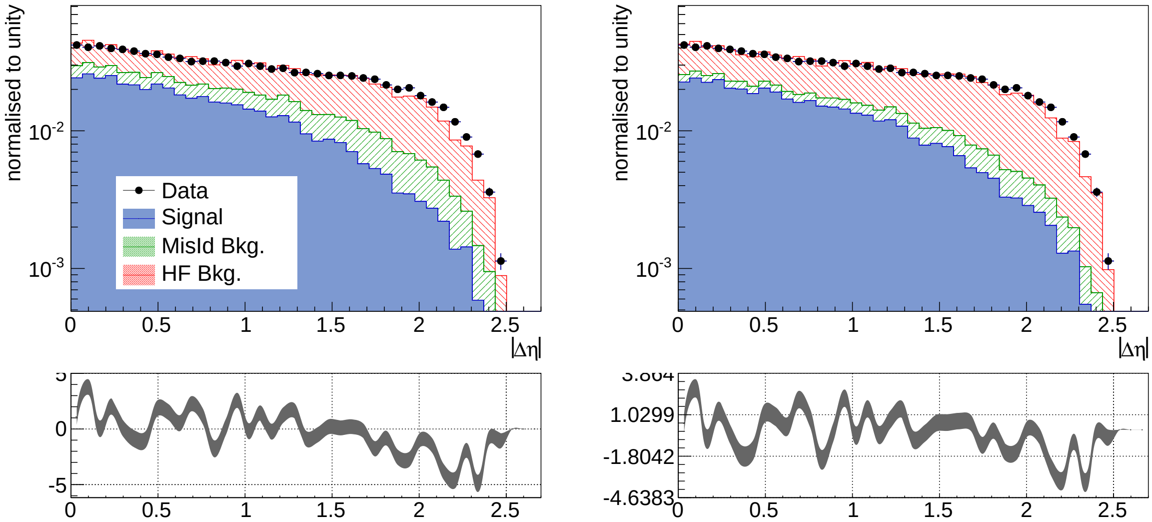

(a) fit with signal from Υ (b) fit with signal from Z, unscaled

Figure 8.24: Applying the fractions from the fit with alternative signal templates to the $\Delta\eta$ distribution. The templates from the main fit are used and the 17.5 to 20 GeV/c^2 mass bin is shown.

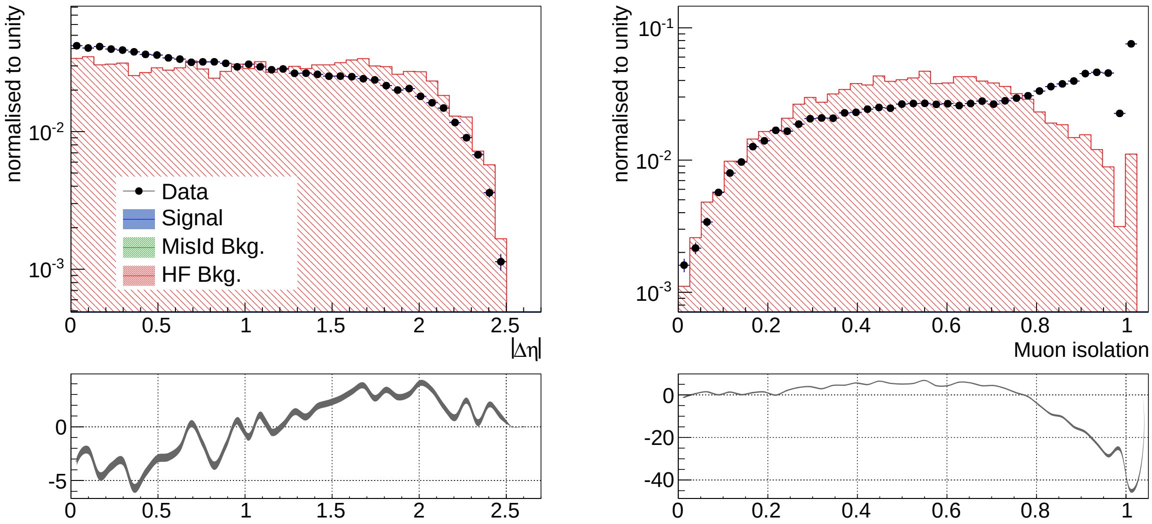

(a) (b)

Figure 8.25: Applying the fractions from the fit with a background only hypothesis. The templates from the main fit are used and the 17.5 to 20 GeV/c^2 mass bin is shown.

8.4.2 Toy Experiments

The reliability of the fit was studied with a large number of toy experiments. For this, toy distributions with known ρ were generated by combining events from all three templates. The toy distributions were then fitted and the resulting ρ compared to the true fraction used while generating. Attention was payed to possible biases of the method. The available events were therefore split into one sample used to generate the toy distribution and an other independent sample used as template in the fit. Figure 8.26a shows an example of a single toy fit while Fig. 8.26b shows a comparison between generated and fitted ρ in the full study. Good agreement between the true fraction and the fraction obtained by the fit is observed for all values of the true fraction. Towards large signal fractions, there is a slight hint that the values returned by the fit are systematically low. The effect is however much smaller than the uncertainty from the different template shapes and therefore neglected in the further study.

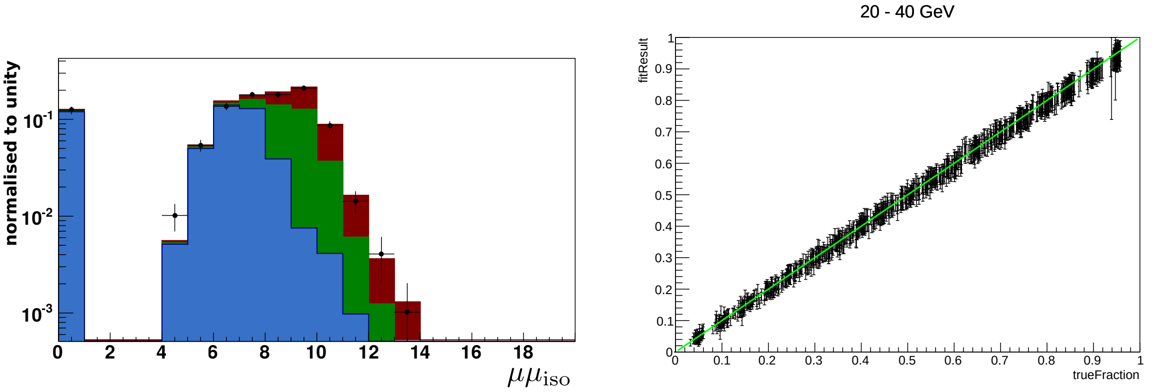

(a) Example of a toy fit with $\rho = 0.5$

(b) Toy study for the 20 GeV/c^2 – 40 GeV/c^2 dimuon mass range

Figure 8.26: Example of the results obtained by the toy fits.

An important result of the toy studies was to limit the mass range to values above the Υ masses. Toy experiments in the 5 to 7 GeV/c^2 mass region had shown, that the fit would overestimate the signal fraction consistently. Despite investing a lot of effort, this problem could not be solved and this mass region had to be excluded from the analysis.

Chapter 9

Corrections

9.1 Trigger Efficiency

The original plan to determine the trigger efficiency for this analysis was to use a tag-and-probe method on data to determine the efficiency of the single muon lines. For this, events fulfilling the following requirements were selected:

- one muon (*e.g.* the μ^+) has fired the single muon trigger;
- the event passes the general momentum (p), transverse momentum (p_T) and pseudorapidity (η) selection;
- the reconstructed di-muon mass agrees with a known state (*e.g.* Z).

The second muon (the μ^- in the example) of an event tagged by these conditions is then probed to see if it has fired the trigger as well. The ratio of muons that fired the trigger to all muons that passed the tag selection, corresponds to the trigger efficiency. Assuming that the efficiency of the di-muon lines factorises, their efficiency could be calculated from the single muon efficiencies. As Fig. 9.1a shows, the product of the single muon trigger efficiencies agrees well with the di-muon efficiency as determined from simulation. The procedure therefore works for muons with a p_T larger than 5 GeV/c. However, the single muon trigger line with a threshold below 5 GeV/c was heavily prescaled. Therefore this approach is not possible for low p_T. As the trigger efficiency for the full range of this analysis, can not be obtained from data, simulation needs to be used. Figure 9.1b shows that the single muon efficiency determined from data and simulation agree. The description of the trigger efficiency in simulation is thus considered reliable. The final di-muon trigger efficiency was therefore estimated from simulation for all three trigger levels combined. The used events are required to pass the main selection (Table 7.3) with the vertex reconstruction quality requirement removed. In addition the events were weighted to match the detector occupancy observed in data. The number of events that have been triggered on all three trigger levels is then divided by the total number of events

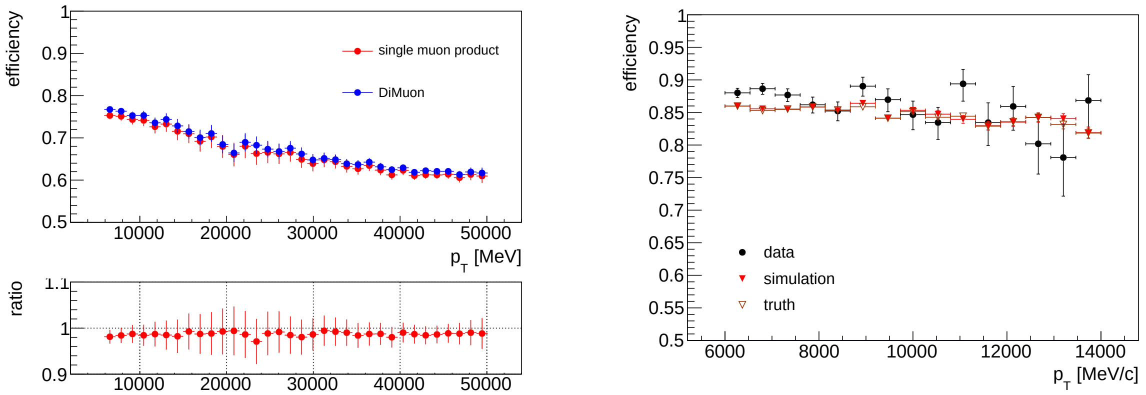

(a) Product of the single muon trigger efficiencies compared to the di-muon trigger efficiency in simulation.

(b) Efficiency of the single muon trigger lines from data compared to simulation. The efficiency for data and simulation is determined with a tag-and-probe method, while the truth efficiency is determined from the truth information directly.

Figure 9.1: Studies for the trigger efficiency.

to obtain the di-muon trigger efficiency. A systematic uncertainty of ±0.01 is assigned to account for the differences between simulation and data and between the single muon product and the di-muon efficiency observed in Fig. 9.1.

The di-muon trigger efficiency is determined as a function of η^+ and η^- separately in nine regions of $({p_{\mathrm{T}}}^+, {p_{\mathrm{T}}}^-)$. Here the superscript signs denote the charge of the muon. The p_{T} regions used and their η integrated efficiencies are listed in Table 9.1. Figure 9.2 shows the efficiency as a function of the muon η for each of these p_{T} regions. The di-muon trigger efficiency reaches 75 % for muons with a low p_{T} and falls off to 50 % towards high p_{T}. As the symmetric distribution shows, the efficiency for the muons of both charges is very similar. For high p_{T} tracks the statistics start to run low, leading to empty bins for very forward tracks. For muons falling into bins with less than 2 events, the average efficiency of the full p_{T} region is used. However this affects only 462 out of more than 850 000 events.

Table 9.1: The η integrated di-muon trigger efficiency in the nine p_{T} regions. p_{T} ranges are given in GeV/c.

	25 – 100	0.636 ± 0.032	0.634 ± 0.015	0.595 ± 0.003
${p_{\mathrm{T}}}^+$	10 – 25	0.717 ± 0.010	0.693 ± 0.009	0.633 ± 0.015
	3 – 10	0.742 ± 0.004	0.724 ± 0.009	0.636 ± 0.031
${p_{\mathrm{T}}}^-$		3 – 10	10 – 25	25 – 100

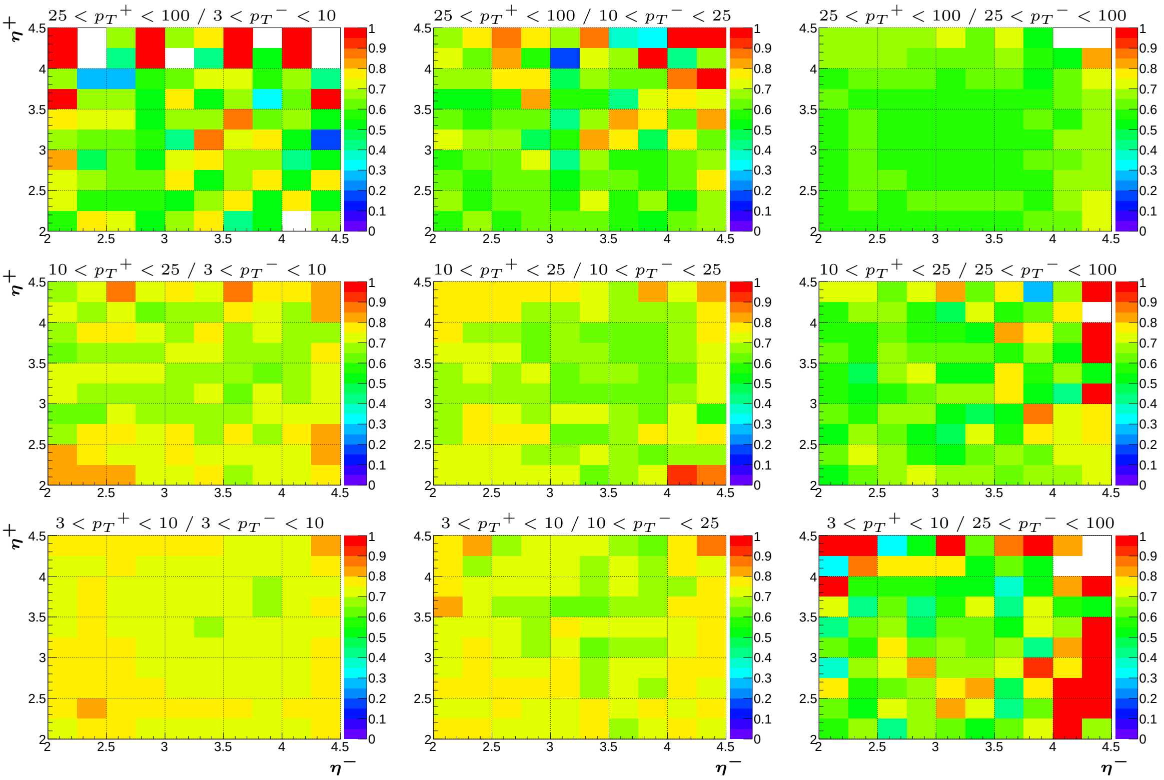

Figure 9.2: The di-muon trigger efficiency. p_{T} values are given in GeV/c.

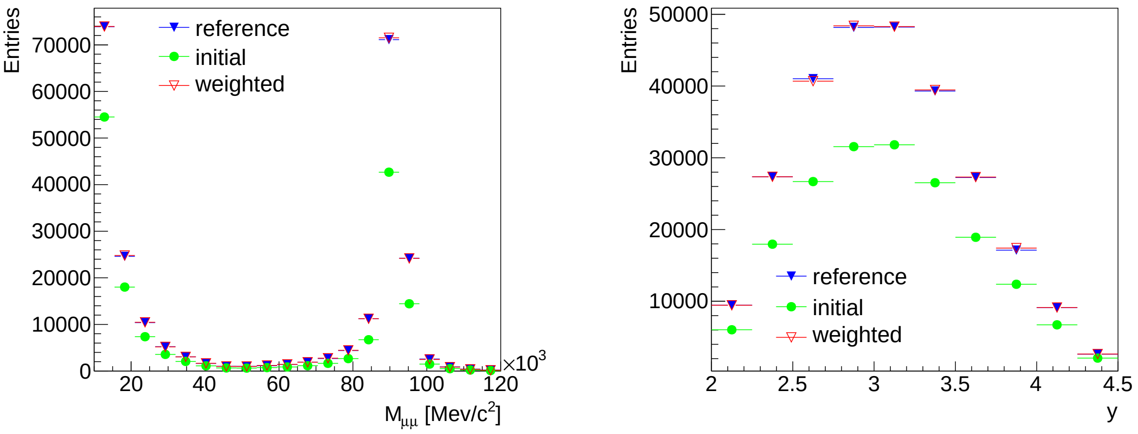

(a) di-muon invariant mass ($M_{\mu\mu}$)

(b) di-muon rapidity ($y_{\mu\mu}$)

Figure 9.3: Testing the trigger efficiencies on the $M_{\mu\mu}$ and $y_{\mu\mu}$ distributions in simulation. The efficiency corrected distributions (weighted) are compared to the distributions without requiring the trigger (reference).

The trigger efficiency was cross checked in simulation by weighting the triggered events with the determined efficiencies. The resulting distribution is then compared in several variables to the distribution obtained without requiring the trigger information. Figure 9.3 shows the comparison for $M_{\mu\mu}$ and $y_{\mu\mu}$. For the bins with good statistics, the corrected distribution shows very good agreement with the reference distribution.

9.2 Muon Identification Efficiency

The trigger efficiency is determined from events selected by the di-muon stripping lines. As mentioned in Section 7.1 these lines require two identified muons. The trigger efficiency determined after the stripping must therefore be combined with the efficiency for the muons to be correctly identified in the first place. As the trigger efficiency is taken from simulation, the muon identification efficiency is determined from simulation as well. The tag-and-probe procedure described in (Farry and Chiapolini 2014) is used. Again events are selected, if they pass the general Drell-Yan selection requirements. However, the track quality requirements used in the note above are added in this study as well. The muon identification efficiency is then given by the fraction of selected events where the probe track is identified as a muon. The resulting efficiencies are shown in Fig. 9.4.

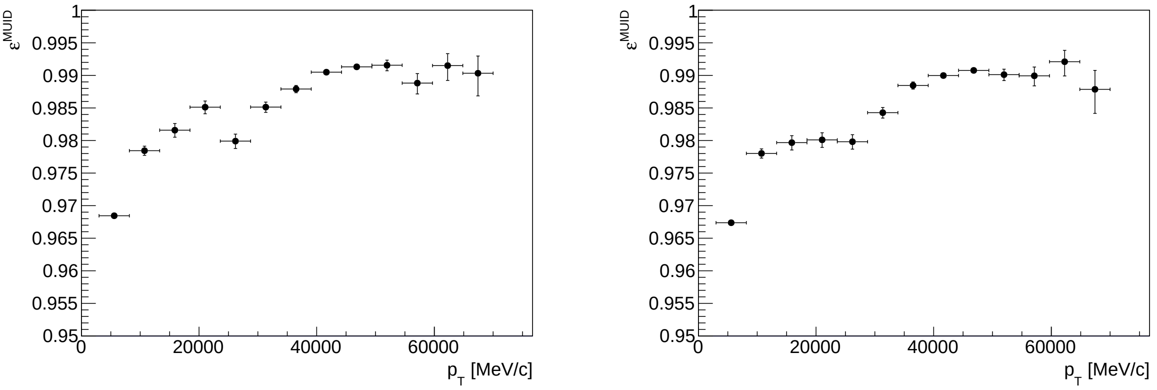

(a) μ^-

(b) μ^+

Figure 9.4: Muon identification efficiency as a function of muon p_T determined from simulation.

The steps in the distribution are expected from the geometry of the muon system and the muon identification algorithm. Muons with lower p_T and therefore p will penetrate the muon system less and have a lower probability to leave hits in all the required muon stations. For the region with $p_\mathrm{T} > 20$ GeV/c, the efficiencies in Fig. 9.4 agree with the efficiencies from the note (Fig. 9.5a) within the uncertainties. In the note the results are also compared to data and found to be in agreement. As shown in Fig. 9.5b, no η dependence is observed below 4.25. Above this value very few events are available, such that any η dependence can be neglected. No dependence on the charge of the muon is expected. The maximum difference between the efficiency for the μ^+ and the μ^- in any bin is used as systematic uncertainty. This yields an uncertainty of ±0.005.

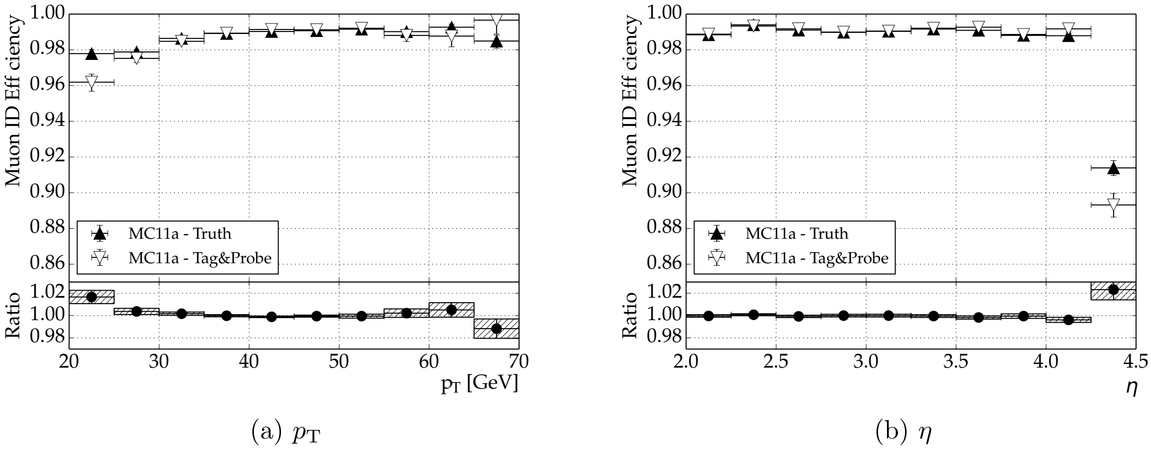

(a) p_{T}

(b) η

Figure 9.5: Muon identification efficiency as a function of muon p_{T} and η determined from simulation (from Farry and Chiapolini 2014).

9.3 Global Event Cuts Efficiency

Global event cuts (GEC) are used to veto events with a very high occupancy. The only GEC applied for the di-muon trigger lines has a threshold at 900 hits in the scintillating-pad detector (SPD-hits). This is a very loose cut and a high efficiency for the GEC is therefore expected.

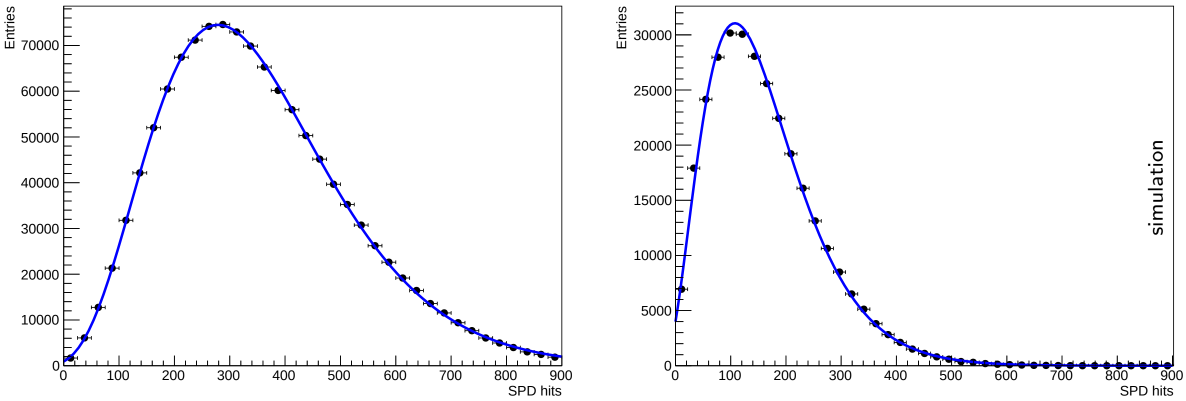

Figure 9.6: Distribution of SPD-hits for the full data sample in data (left) and simulation (right). The solid line shows the fitted Γ-distribution.

The GEC efficiency ($\varepsilon^{\mathrm{GEC}}$) is determined from data by fitting the distribution of SPD-hits and integrating the normalised area below the GEC threshold. Figure 9.6 shows the distribution for the full dataset as well as the fitted function. A Γ-distribution (NIST/SEMATECH 2014) is used to describe the distribution of SPD-hits and good agreement is observed.

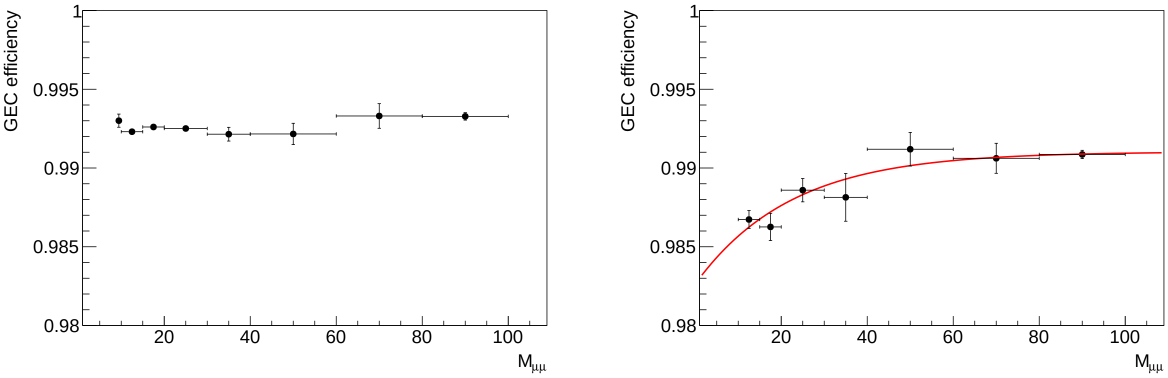

(a) $\varepsilon^{\mathrm{GEC}}$ as a function of $M_{\mu\mu}$ in data

(b) $\varepsilon^{\mathrm{GEC}}$ as a function of $M_{\mu\mu}$ in simulation. The sigmoid function shows the shape of the parametrisation used.

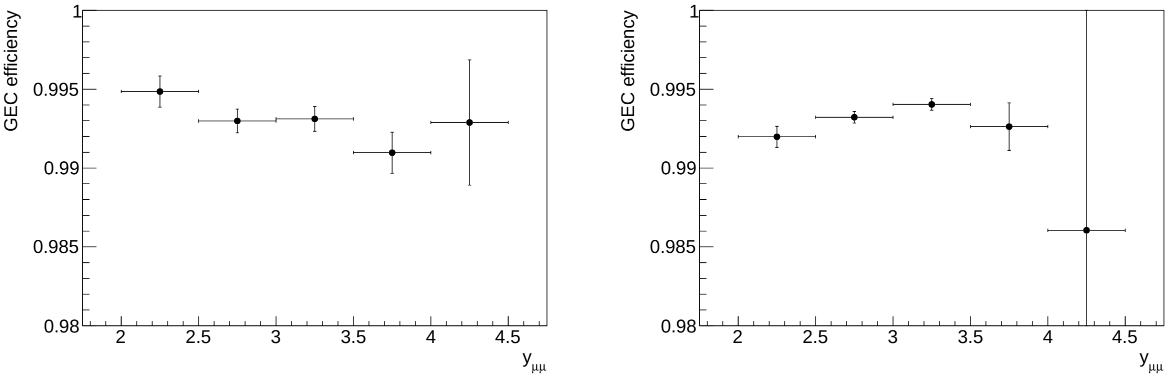

(c) $\varepsilon^{\mathrm{GEC}}$ as a function of y for Υ candidates (background subtracted)

(d) $\varepsilon^{\mathrm{GEC}}$ as a function of y for Z candidates

Figure 9.7: Studying $\varepsilon^{\mathrm{GEC}}$.

The efficiency $\varepsilon^{\mathrm{GEC}}$ was determined in data as a function of $M_{\mu\mu}$ as well as $y_{\mu\mu}$. In addition $\varepsilon^{\mathrm{GEC}}$ was determined from simulation using the same procedure, but adjusting the cut-off value to 500 SPD-hits to achieve a similar overall efficiency as observed in data. Figure 9.7 shows the resulting $\varepsilon^{\mathrm{GEC}}$. The mass dependence in data is shown in Fig. 9.7a. Here the lowest entry is determined from the Υ control sample after subtracting the background. For all the other bins the main data sample is used and no background is subtracted. Despite this, the figure shows no significant dependence on $M_{\mu\mu}$. However, due to possibly different kinematics, this is no conclusive test. The mass dependence was therefore checked in simulation (Fig. 9.7b). Here a mass dependence is observed. This mass dependence has been parametrised with a sigmoid function as shown in the figure. A possible $y_{\mu\mu}$ dependence was studied for events from the background subtracted Υ control sample (Fig. 9.7c) and for the Z ressonance (Fig. 9.7d). Both distributions are flat within the uncertainties.

Based on these studies, the shape of $\varepsilon^{\mathrm{GEC}}$ is determined from the sigmoid function in simulation while the overall normalisation value is taken from data. The normalisation value is determined by including the full mass range in a single fit.

The difference between the determined $\varepsilon^{\mathrm{GEC}}$ and the constant value calculated from data is assigned as a systematic uncertainty. The resulting systematic uncertainties vary within 0 to 0.006

9.4 Track Reconstruction Efficiency

The measurement is corrected for the tracking efficiency in different bins of muon η. The tracking efficiency for muons with high p_{T} has been published in an LHCb-note (Farry and Chiapolini 2014). As the track reconstruction efficiency is expected to be independent of the muon p_{T} for $p_{\mathrm{T}} > 3$ GeV/c, the efficiencies determined in the note can be used for muons from events with lower di-muon mass too. A study showing the p_{T} independence was performed and is presented below.[1]

The procedure used to determine the tracking efficiency is described in the note above as well as (LHCb Collaboration 2014c). It uses a tag-and-probe approach, and is based on tracks reconstructed from hits in the TT and the muon stations only (Muon-TT track). These tracks are independent of the default track reconstruction and can therefore be used as tag-tracks. More precisely, a combination of a Muon-TT track and a long track that match a chosen di-muon decay are used as tag. A tagged event is then probed for the second long track and the ratio of found to expected long tracks is used as the track reconstruction efficiency.

The p_{T} dependence of the efficiency has been studied with events from Z, low-mass Drell-Yan and J/ψ decays in simulation and cross-checked in data. Within a systematic uncertainty of ±1%, the distributions were indeed found to be p_{T} independent. The study below does not apply any of the corrections mentioned in (Farry and Chiapolini 2014) as these do not affect the comparison. Otherwise it uses the same requirements and methodology. In contrast to the Z dataset, a significant background is admitted to the J/ψ sample and the number of signal events cannot be determined with a simple mass selection. As described in (LHCb Collaboration 2014c), the number of tag-and-probe events are therefore determined by fitting the J/ψ mass distribution. A Crystal Ball

---

[1] A mostly identical copy of this text is attached to (Farry and Chiapolini 2014) as an Appendix.

function (Skwarnicki 1986) is used to describe the signal component and an exponential function to describe the combinatorial background.

Figure 9.8a compares the track reconstruction efficiency calculated from truth information for all three decay types as a function of p_T. The resulting efficiencies agree within 0.5 % and show no significant dependence on the muon p_T. The efficiency is presented as a function of η in Fig. 9.8b and the resulting efficiencies show a good level of agreement between the samples despite their different underlying p_T distributions.

Figure 9.9 repeats the comparison with efficiencies calculated by applying the tag-and-probe method to the simulation. Again the efficiencies from both ends of the p_T spectrum show no significant difference. The figure includes the efficiencies from Z and J/ψ decays only. The Drell-Yan sample is affected by impurities resulting from the tag-and-probe method as explained in Section 9.4.1.

The efficiencies were also determined from data with the resulting comparison shown in Fig. 9.10 as a function of p_T and η. The Z events have been reweighted to match the detector occupancy distribution seen in J/ψ events. In addition, only J/ψ events that match the tighter global event cut requirements from the Z selection ($SPD - hits < 600$) have been included. As the data samples have different underlying η distributions, a more accurate comparison as a function of p_T is made by restricting the selection to the range $2.5 < \eta < 4.25$ where the efficiencies are expected to be flat as a function of η (see Fig. 9.9b). Due to low statistics the uncertainties are large but the results agree with the assumption that the efficiencies are p_T independent within ±0.01. A systematic uncertainty of ±0.01 is assigned to the tracking efficiencies to account for a possible remaining dependence on the muon p_T.

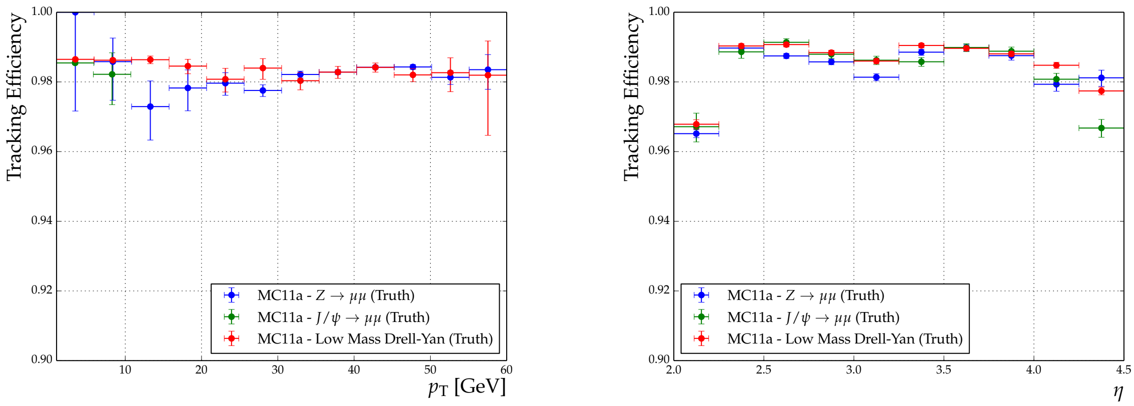

(a) p_T

(b) η

Figure 9.8: Track reconstruction efficiencies from truth information calculated using muons from Z, Drell-Yan and J/ψ decays.

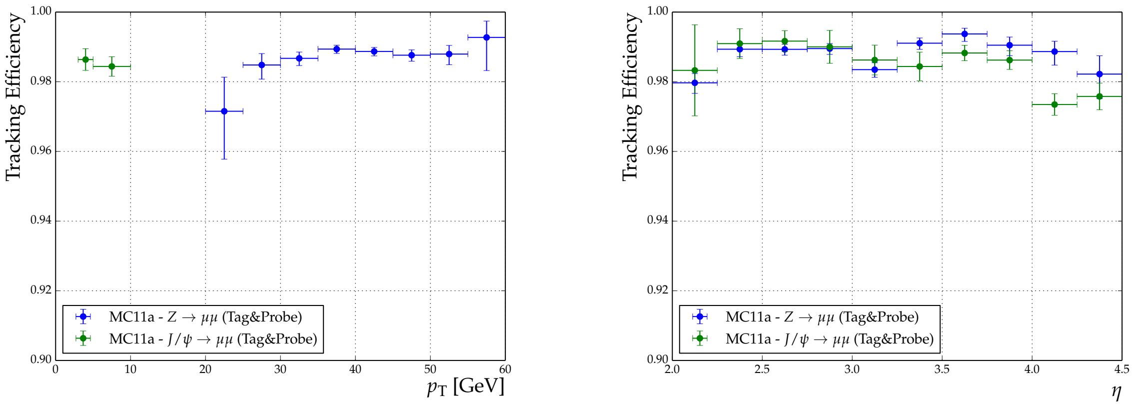

(a) p_T (b) η

Figure 9.9: Track reconstruction efficiencies in simulation calculated using muons from Z and J/ψ decays.

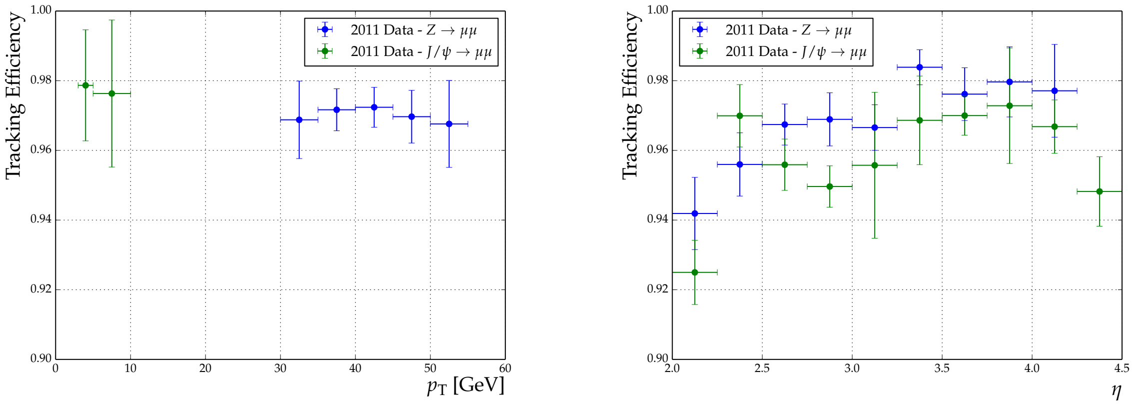

(a) p_T (b) η

Figure 9.10: Track reconstruction efficiencies in data calculated using muons from Z and J/ψ decays.

9.4.1 Pollution by Badly Reconstructed Muon-TT Tracks

The tag-and-probe method relies on the proper reconstruction of Muon-TT tracks and the matching of these with long tracks. Badly reconstructed Muon-TT tracks will have a low matching probability and artificially reduce the reconstruction efficiency. Therefore several quality cuts are applied to the Muon-TT tracks and the remaining effect should be corrected for by the matching efficiency. In Z and J/ψ decays the quality of the Muon-TT tracks can be controlled with a tight mass window cut. This is not possible for the sample of simulated Drell-Yan events.

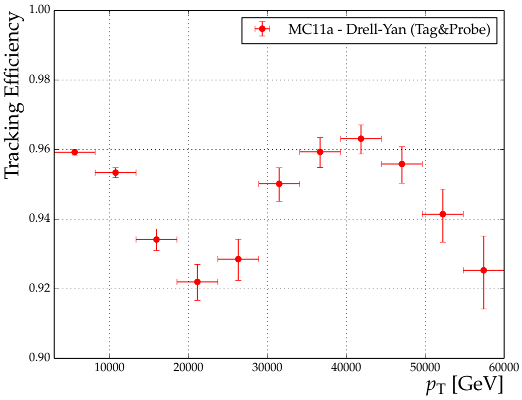

Figure 9.11: Track reconstruction efficiencies from Drell-Yan simulation.

Figure 9.11 illustrates that using the standard quality requirements for Drell-Yan decays results in an erratic efficiency distribution. Comparing the track segments in the TT and the muon stations with the truth information shows that this can be explained by badly reconstructed tracks ("Bad Tracks"). A track is considered to be a Bad Track if one or both segments are not matched to a truth-level particle. Figure 9.12a shows the distribution of Bad Tracks as a function of the muon p_T. On average, 15 % of Bad Tracks consist of two unmatched segments, while in the remaining cases one of the two segments corresponds to a true track.[2] Bad tracks are dominated by tracks with an unmatched muon segment. However, tracks with an unmatched TT segment have a significant contribution in the region of p_T around 20 GeV/c or above 50 GeV/c (Fig. 9.12b).

---

[2] There is a negligible contribution of 72 events where the bad track is made up of two segments matched to two different true tracks.

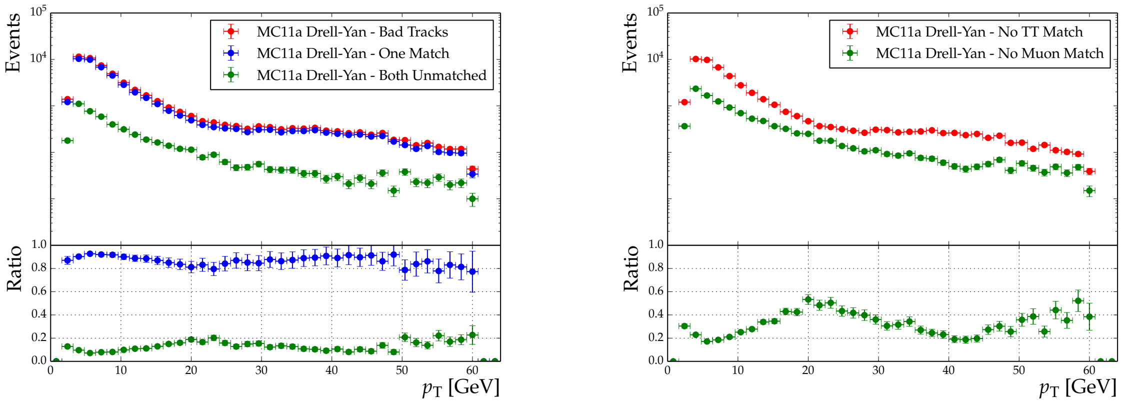

(a) p_T distribution for bad tracks, showing tracks with just one unmatched segment and with both segments unmatched

(b) comparing the p_T distribution for tracks with an unmatched muon or TT segment

Figure 9.12: Studying badly reconstructed Muon-TT tracks.

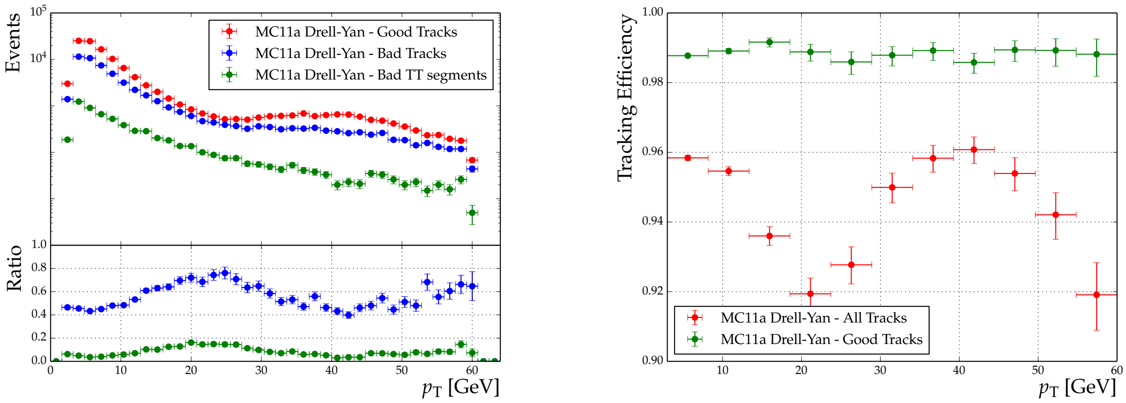

(a) comparing the p_T distribution for good and bad tracks

(b) comparing track reconstruction efficiencies from Drell-Yan simulation with and without excluding bad tracks

Figure 9.13: Studying the effects of badly reconstructed Muon-TT tracks.

Figure 9.13a compares the p_T distribution of Bad Tracks to tracks with a matching true track ("Good Tracks") and to the subset of Bad Tracks where only the TT segment is unmatched ("Bad TT segments"). For p_T values corresponding to the dip in the uncorrected efficiency, the fraction of bad tracks significantly increases. However there is a contribution of more than 30 % over the full p_T range. Figure 9.13b shows that removing all bad tracks results in a perfectly flat efficiency distribution in agreement with the values from J/ψ and Z simulation.

While investigating the badly reconstructed Muon-TT tracks, a data based method to handle such tracks was developed as well. To select against badly reconstructed Muon-TT tracks, without relying on truth information, a similar p_{T} for both muons can be required. Photons tend to decay symmetrically, therefore such a requirement predominantly selects events with a well-reconstructed Muon-TT track. Figure 9.14 requires the p_{T} of the probe muon to be within 30 % of the tag muon. As Fig. 9.14a shows, applying this requirement results in a flat contribution of Bad Tracks over the full p_{T} range. There is however still a significant amount of Bad Tracks left. The contribution of tracks with a Bad TT segment is below 5 % and falls off towards higher p_{T}. Tracks with only a bad muon segment are usually assigned the momentum of the TT segment and associated with a corresponding long track. Such tracks therefore do not affect the efficiency. This is reflected in the efficiency distribution determined after applying the relative p_{T} requirement (Fig. 9.14b). The efficiency agrees with the efficiency from Good Tracks for high p_{T} and falls of by 2 percentage points towards low p_{T} where a larger contamination of Bad Tracks with Bad TT segments remains.

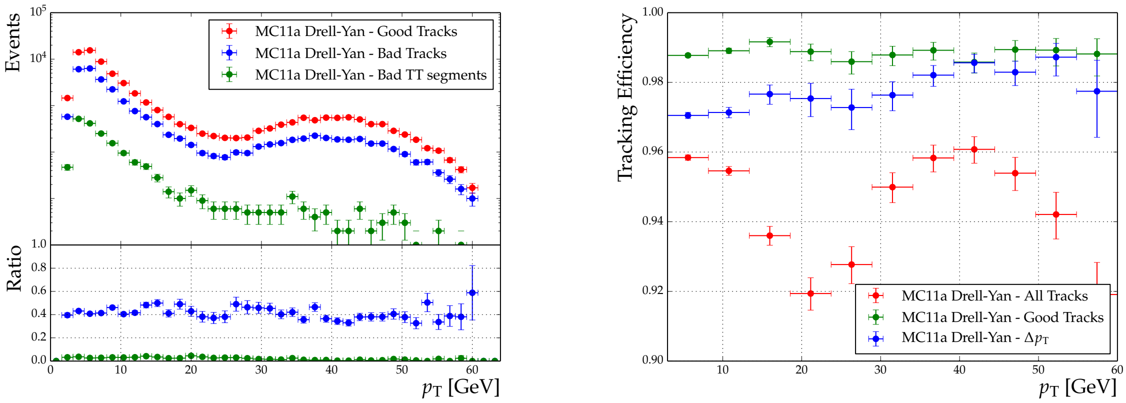

(a) comparing the p_{T} distribution for good and bad tracks

(b) comparing track reconstruction efficiencies from Drell-Yan simulation with and without excluding Bad tracks

Figure 9.14: Studying the effects of badly reconstructed Muon-TT tracks after applying a cut on the relative p_{T}.

9.5 Selection Efficiency

The only selection requirement that has to be corrected for is the one on the reconstruction quality of the vertex. The fits for the signal fraction are possible but less stable without this requirement. The effect of the vertex quality requirement is therefore assessed by comparing the fits for the main configuration. Figure 9.15 shows the signal loss determined by this comparison. The effect of the additional requirement is independent of $M_{\mu\mu}$. The mean and standard deviation of the values in Fig. 9.15 are used as common correction factor and systematic uncertainty. This results in a global correction of 0.951 ± 0.01.

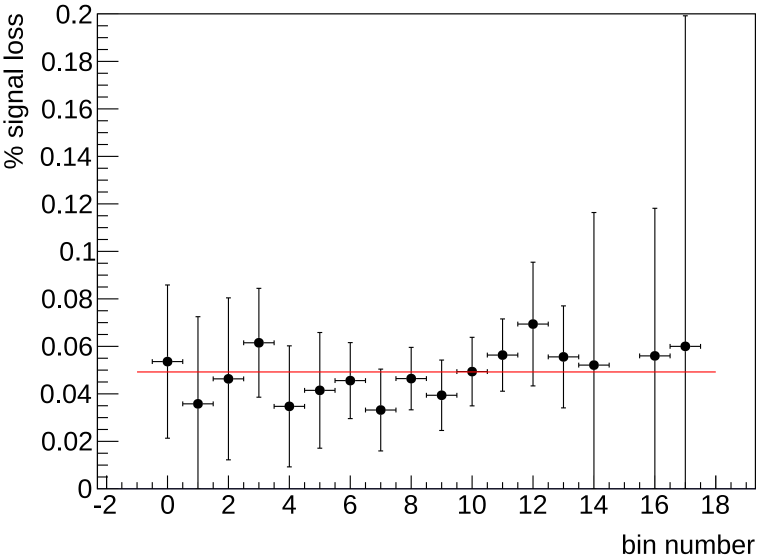

Figure 9.15: Loss of signal events due to the selection requirement on the vertex reconstruction quality. The uncertainties correspond to the statistical uncertainty of the fit with the vertex quality requirement applied. The bins are numbered in order of increasing mass, *i.e.* the 10.5 to 11 GeV/c^2 bin is bin 0, the 110 to 120 GeV/c^2 bin is bin 17.

9.6 Further Corrections

As the other selection requirements correspond to thresholds applied by the trigger and the limits of the acceptance, no additional efficiency is needed. The cross section is given in the kinematic range of the measurement and therefore not corrected for the acceptance.

Corrections are additionally applied for bin-to-bin migrations. These corrections include migrations into and out of the phase space as well as the effects of final state radiation and bremsstrahlung. The correction factors are estimated from simulation. For all events passing the selection requirement of the analysis, the distribution of the true and the reconstructed mass is plotted. The correction factors are then given by the ratio of the true distribution to the reconstructed one:

$$f^{\mathrm{MIG}} = \frac{N_i^{\mathrm{true}}}{N_i^{\mathrm{rec}}} \tag{9.1}$$

Here i denominates the mass bin while N^{true} and N^{rec} are the number of events in the true and reconstructed distribution respectively. Figure 9.16 shows the two mass distributions as well as the obtained correction factors. Table 9.2 lists the corresponding numbers. The bin-to-bin migration is negligible for low masses but has a large effect for the bins below the Z mass. Here the effects of statistics, final state radiation and bremsstrahlung reinforce each other. The bin-to-bin migration in $y_{\mu\mu}$ was studied with an analogous approach and found to be negligible. The systematic uncertainty for these correction factors is estimated by moving the bin edges up and down by Δw. Δw for a given edge is chosen as $0.1 * w$, where w is the width of the bin above the edge. These variations are comparable to the mass resolution. The resulting uncertainties vary between 0.5 ‰ and 3.5 %, except for the 80 to 90 GeV/c^2 mass bin where the uncertainty is 18 %. This is attributed to the effect of bremsstrahlung, since the migration due to bremsstrahlung should decrease rapidly with increasing distance to the Z mass.

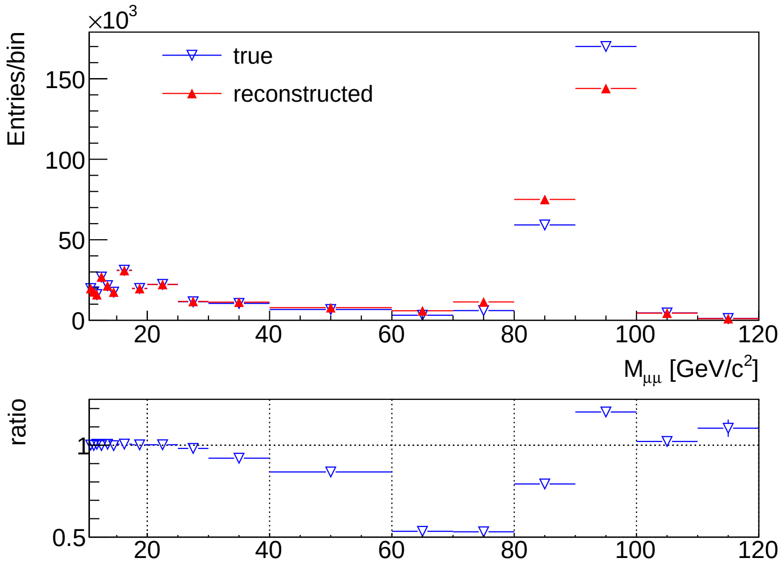

Figure 9.16: Distribution of true and reconstructed mass (top) and the correction factors for bin-to-bin migration (bottom).

Table 9.2: Bin-to-bin migration as a function of $M_{\mu\mu}$.

$M_{\mu\mu}$ [GeV/c^2]	y	f^{MIG}	stat.	syst.
10.5 – 11.0	2.00 - 4.50	1.00	0.01	0.00
11.0 – 11.5	2.00 - 4.50	1.00	0.01	0.00
11.5 – 12.0	2.00 - 4.50	1.01	0.01	0.00
12.0 – 13.0	2.00 - 4.50	1.00	0.01	0.00
13.0 – 14.0	2.00 - 4.50	1.01	0.01	0.00
14.0 – 15.0	2.00 - 4.50	1.00	0.01	0.00
15.0 – 17.5	2.00 - 4.50	1.01	0.01	0.00
17.5 – 20.0	2.00 - 4.50	1.00	0.01	0.00
20.0 – 25.0	2.00 - 4.50	1.00	0.01	0.00
25.0 – 30.0	2.00 - 4.50	0.98	0.01	0.00
30.0 – 40.0	2.00 - 4.50	0.93	0.01	0.00
40.0 – 60.0	2.00 - 4.50	0.85	0.01	0.03
60.0 – 70.0	2.00 - 4.50	0.53	0.01	0.01
70.0 – 80.0	2.00 - 4.50	0.53	0.01	0.01
80.0 – 90.0	2.00 - 4.50	0.79	0.00	0.13
90.0 – 100.0	2.00 - 4.50	1.18	0.00	0.01
100.0 – 110.0	2.00 - 4.50	1.02	0.02	0.00
110.0 – 120.0	2.00 - 4.50	1.09	0.05	0.01

Chapter 10

Cross Section Determination

Including all correction factors, the cross section presented here is calculated according to

$$\sigma = \frac{\rho \cdot f^{\mathrm{MIG}}}{\mathcal{L} \cdot \varepsilon^{\mathrm{SEL}}} \sum_{i=1}^{N} \frac{1}{\varepsilon_i^{\mathrm{TRIG}} \cdot \varepsilon_i^{\mathrm{MUID}} \cdot \varepsilon_i^{\mathrm{GEC}} \cdot \varepsilon_i^{\mathrm{TRACK}}} \tag{10.1}$$

where the sum runs over all events in a given bin. The different factors correspond to the following quantities and are treated in the sections listed.

$\boldsymbol{\rho}$	signal fraction	(Section 8.4)
$\boldsymbol{f}^{\mathbf{MIG}}$	correction for bin-to-bin migrations	(Section 9.6)
$\boldsymbol{\mathcal{L}}$	integrated luminosity	(Section 5.2.3)
$\boldsymbol{\varepsilon}^{\mathbf{SEL}}$	efficiency of the vertex quality requirement	(Section 9.5)
$\boldsymbol{\varepsilon}^{\mathbf{TRIG}}$	trigger efficiency	(Section 9.1)
$\boldsymbol{\varepsilon}^{\mathbf{MUID}}$	muon identification efficiency	(Section 9.2)
$\boldsymbol{\varepsilon}^{\mathbf{GEC}}$	global event cut efficiency	(Section 9.3)
$\boldsymbol{\varepsilon}^{\mathbf{TRACK}}$	tracking efficiency	(Section 9.4)

10.1 Cross Section Numbers

Table 10.1 lists the cross section measured differentially as a function of di-muon invariant mass ($M_{\mu\mu}$). The corresponding numbers for the measurements as a function of di-muon rapidity ($y_{\mu\mu}$) are included in in Appendix A.

Table 10.1: Cross section measured as a function of $M_{\mu\mu}$.

$M_{\mu\mu}$ [GeV/c^2]	y	σ [pb]	stat.	syst.
10.5 – 11.0	2.00 - 4.50	32.29	0.69	6.55
11.0 – 11.5	2.00 - 4.50	29.18	0.65	5.96
11.5 – 12.0	2.00 - 4.50	26.85	0.57	5.14
12.0 – 13.0	2.00 - 4.50	45.99	0.70	7.36
13.0 – 14.0	2.00 - 4.50	36.78	0.60	5.05
14.0 – 15.0	2.00 - 4.50	30.20	0.49	3.92
15.0 – 17.5	2.00 - 4.50	54.39	0.63	5.34
17.5 – 20.0	2.00 - 4.50	33.78	0.45	3.04
20.0 – 25.0	2.00 - 4.50	37.33	0.44	3.27
25.0 – 30.0	2.00 - 4.50	18.22	0.29	1.17
30.0 – 40.0	2.00 - 4.50	15.45	0.24	0.87
40.0 – 60.0	2.00 - 4.50	9.45	0.18	0.57
60.0 – 70.0	2.00 - 4.50	1.57	0.04	0.08
70.0 – 80.0	2.00 - 4.50	2.29	0.05	0.11
80.0 – 90.0	2.00 - 4.50	20.00	0.42	3.64
90.0 – 100.0	2.00 - 4.50	49.63	0.34	2.26
100.0 – 110.0	2.00 - 4.50	1.67	0.08	0.07
110.0 – 120.0	2.00 - 4.50	0.50	0.04	0.02

10.2 Theoretical Predictions

The experimental results are compared to theoretical predictions calculated at next-to-next-to-leading order (NNLO). The calculations are performed for the fiducial volume of the measurement with Fewz (Gavin et al. 2011) using the Mstw08 parton distribution function (PDF) set. In contrast to the analysis of data collected in 2010 (Appendix C), no other program or PDF set is used. Due to the fine binning used in this analysis, calculations with several tools or PDF sets were too time consuming.

The theoretical predictions are affected by two types of uncertainties. First, the uncertainty on the PDFs propagates to the predicted cross section. The uncertainty on the PDF set is given as a set of orthogonal eigenvector directions in the parameter space of the PDFs. An eigenvalue is associated with each eigenvector, such that a variation of the parameters by the eigenvalue corresponds to a defined change in probability (A. Martin, Roberts, et al. 2003). To propagate this uncertainty to the observable physical quantities, the parameters are varied along each eigenvector by one standard deviation and the cross section recalculated. The difference between the resulting cross section and the central value then gives the uncertainty at 68 % confidence level. As the eigenvectors form an orthogonal set, the uncertainties obtained for each eigenvector are uncorrelated and are summed in quadrature to obtain the total uncertainty.

The second uncertainty on the cross section prediction is due to higher order corrections. For the central values, the factorisation and renormalisation scales are fixed to the average mass of each measurement. To estimate the uncertainties, both scales are varied by factors of two around this nominal value together and independently.

For the final uncertainty on the predictions, the PDF uncertainties and the scale uncertainties are added in quadrature. The resulting predictions as well as the final uncertainties are listed in Table 10.2

Table 10.2: NNLO predictions calculated with FEWZ using the MSTW08 PDF set.

$M_{\mu\mu}$ [GeV/c^2]	σ [pb]	Δ_{up}	Δ_{down}
10.5 – 11.0	35.80	2.31	1.36
11.0 – 11.5	32.03	2.00	1.19
11.5 – 12.0	28.54	1.72	1.02
12.0 – 13.0	47.97	2.75	1.63
13.0 – 14.0	37.91	2.05	1.23
14.0 – 15.0	30.80	1.56	0.94
15.0 – 17.5	55.03	2.56	1.56
17.5 – 20.0	34.33	1.42	0.88
20.0 – 25.0	38.22	1.38	0.89
25.0 – 30.0	18.98	0.59	0.41
30.0 – 40.0	16.61	0.40	0.31
40.0 – 60.0	9.70	0.22	0.18
60.0 – 70.0	2.08	0.04	0.04
70.0 – 80.0	2.35	0.05	0.04
80.0 – 90.0	17.91	0.37	0.33
90.0 – 100.0	51.09	1.09	0.96
100.0 – 110.0	1.53	0.03	0.03
110.0 – 120.0	0.44	0.01	0.01

10.3 Systematic Uncertainties

The main sources of experimental uncertainties are due to the determination of the signal fraction and the efficiencies. They have been introduced in the relevant sections and are summarised below.

The following sources of systematic uncertainties have been considered:

- Signal fraction (ρ): The uncertainty on ρ is dominated by the limited knowledge of the shape of distributions used for the fit. The systematic uncertainty is determined for each ($M_{\mu\mu}$, $y_{\mu\mu}$)-region separately, by calculating the standard deviation of the signal fraction obtained with the 12 different combinations used.
- Bin-to-bin migration: The systematic uncertainty for these correction factors is estimated by moving the bin edges up and down by Δw. Δw for a given edge is chosen as $0.1 * w$, where w is the width of the bin above the edge. These variations are comparable to the mass resolution. The resulting uncertainties vary between 0.5 ‰ and 3.5 %, except for the 80 to 90 GeV/c^2 mass bin where the uncertainty is 18 %.
- Luminosity: The uncertainty on the integrated luminosity ($\mathcal{L}$) determined with the standard methods is 3.5 % (LHCb Collaboration 2012a).
- Vertex quality requirement: The correction for the vertex quality requirement is assigned a systematic uncertainty of 1 % based on the standard deviation observed in Fig. 9.15.
- Trigger efficiency: A systematic uncertainty of ±0.01 is assigned to account for the differences between simulation and data and between the single muon product and the di-muon efficiency observed in Fig. 9.1.
- Muon identification efficiency: The maximum difference between the efficiency for the μ^+ and the μ^- in any bin is used as systematic uncertainty. This yields an uncertainty of ±0.005.
- Global event cuts: The difference between the determined GEC efficiency ($\varepsilon^{\mathrm{GEC}}$) and the constant value calculated from data is assigned as a systematic uncertainty. The resulting systematic uncertainties vary within 0 to 0.006
- Track reconstruction efficiency: A systematic uncertainty of ±0.01 is assigned to the tracking efficiencies to account for a possible remaining dependence on the muon transverse momentum (p_{T}).

Table 10.3 lists the total corrections resulting for each of the $M_{\mu\mu}$ region of the $y_{\mu\mu}$ integrated study. The corresponding uncertainties are listed in Table 10.4, for all corrections they are dominated by the systematic uncertainties. The corresponding numbers for the study of the cross section as a function of $y_{\mu\mu}$, can be found in Appendix A.

Table 10.3: Average di-muon mass and event dependent efficiencies for each mass range.

$M_{\mu\mu}$ [GeV/c^2]	$y_{\mu\mu}$	$\overline{M_{\mu\mu}}$	$\varepsilon^{\mathrm{TRIG}}$	$\varepsilon^{\mathrm{MUID}}$	$\varepsilon^{\mathrm{GEC}}$	$\varepsilon^{\mathrm{TRACK}}$	Total
10.5 – 11.0	2.00 – 4.50	10.7	0.745	0.938	0.987	0.920	0.635
11.0 – 11.5	2.00 – 4.50	11.2	0.745	0.939	0.987	0.919	0.634
11.5 – 12.0	2.00 – 4.50	11.7	0.744	0.939	0.987	0.919	0.634
12.0 – 13.0	2.00 – 4.50	12.5	0.743	0.940	0.987	0.918	0.633
13.0 – 14.0	2.00 – 4.50	13.5	0.742	0.941	0.987	0.918	0.633
14.0 – 15.0	2.00 – 4.50	14.5	0.740	0.942	0.988	0.918	0.632
15.0 – 17.5	2.00 – 4.50	16.1	0.737	0.945	0.988	0.918	0.631
17.5 – 20.0	2.00 – 4.50	18.6	0.731	0.948	0.988	0.918	0.629
20.0 – 25.0	2.00 – 4.50	22.1	0.718	0.952	0.989	0.919	0.622
25.0 – 30.0	2.00 – 4.50	27.2	0.700	0.957	0.990	0.921	0.611
30.0 – 40.0	2.00 – 4.50	34.0	0.688	0.960	0.990	0.922	0.603
40.0 – 60.0	2.00 – 4.50	47.8	0.657	0.964	0.991	0.923	0.580
60.0 – 70.0	2.00 – 4.50	65.0	0.618	0.969	0.992	0.923	0.548
70.0 – 80.0	2.00 – 4.50	75.5	0.604	0.973	0.992	0.924	0.538
80.0 – 90.0	2.00 – 4.50	87.3	0.599	0.977	0.992	0.923	0.537
90.0 – 100.0	2.00 – 4.50	92.5	0.597	0.979	0.992	0.923	0.535
100.0 – 110.0	2.00 – 4.50	103.6	0.598	0.980	0.992	0.921	0.535
110.0 – 120.0	2.00 – 4.50	114.2	0.595	0.981	0.992	0.923	0.534

Table 10.4: Average systematic uncertainties. The upper part shows the uncertainties on the factors applied bin wise, The lower part the uncertainties on the event dependent efficiency corrections listed in Table 10.3. Values are given in %.

S^{ρ}	0.0 – 19.9
S^{MIG}	0.0 – 17.7
S^{SEL}	1.1 – 1.1
S^{TRIG}	1.3 – 1.7
S^{MUID}	0.7 – 0.7
S^{GEC}	0.8 – 1.3
S^{TRACK}	1.5 – 1.5
Total	2.4 – 2.5

Chapter 11

Results

Figure 11.1 shows the differential cross section as a function of di-muon invariant mass ($M_{\mu\mu}$) together with the theoretical prediction at next-to-leading order (NLO) and next-to-next-to-leading order (NNLO). Generally the NLO prediction is slightly lower then the NNLO prediction. Predictions are calculated using Fewz (Gavin et al. 2011) and the Mstw08 (A. Martin, W. Stirling, et al. 2009) parton distribution function (PDF) set. The measurement is in agreement with the predictions for the full mass range.

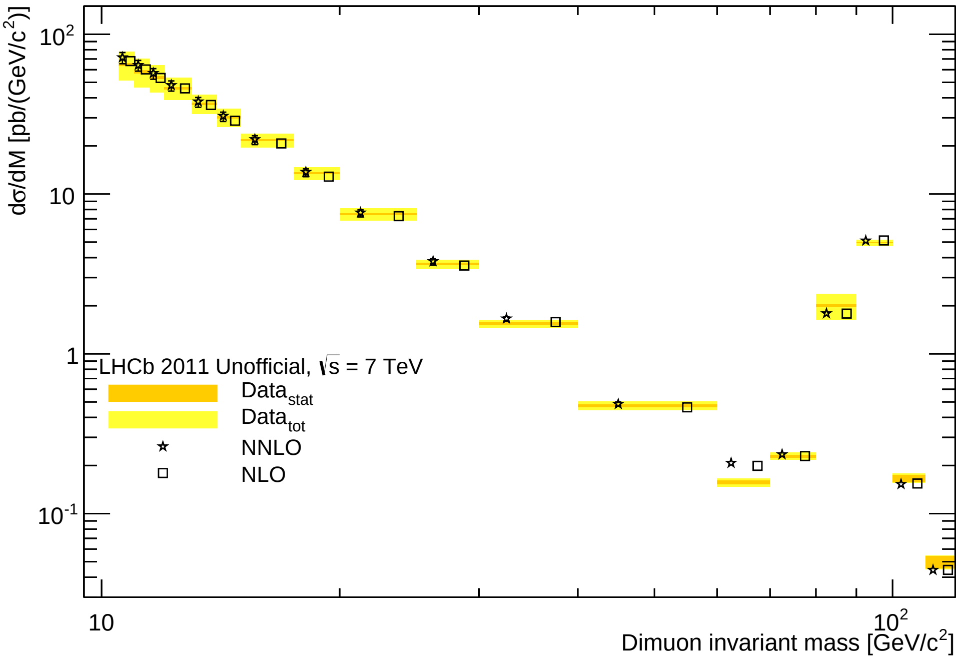

Figure 11.1: Cross section as a function of $M_{\mu\mu}$ for $2.0 < y_{\mu\mu} < 4.5$. The orange and yellow bands show the data with statistical and total uncertainties respectively. The superimposed Fewz predictions are displaced horizontally for presentation.

The total cross section for the Z mass range (60 to 120 GeV/c^2) is

$$\sigma_Z = 75.6 \pm 0.5(\text{stat}) \pm 3.4(\text{syst}) \pm 2.6(\text{lumi})\,\text{pb} \tag{11.1}$$

The first uncertainty is statistical, the second systematic and the third due to the luminosity determination. The measurement is in good agreement with the result obtained by the $Z \to \mu\mu$ measurement (LHCb Collaboration 2014a)

$$\sigma_Z^{\text{LHCb}} = 76.5 \pm 0.3(\text{stat}) \pm 0.8(\text{syst}) \pm 2.7(\text{lumi})\,\text{pb} \tag{11.2}$$

and the prediction

$$\sigma_Z = 74.7^{+1.6}_{-1.4}(\text{PDF})^{+0.4}_{-0.4}(\text{Theory})\,\text{pb} \tag{11.3}$$

Here, the first uncertainty is from the PDF uncertainty and the second from higher order corrections.

The cross section as a function of di-muon rapidity ($y_{\mu\mu}$) is shown for the four different mass ranges in Figs. 11.2 to 11.5. For masses above 12 GeV/c^2, the measurement is in excellent agreement with the predictions but affected by large systematic uncertainties. For the lowest mass range, measurement and predictions agree in shape but the prediction overestimates the cross section consistently.

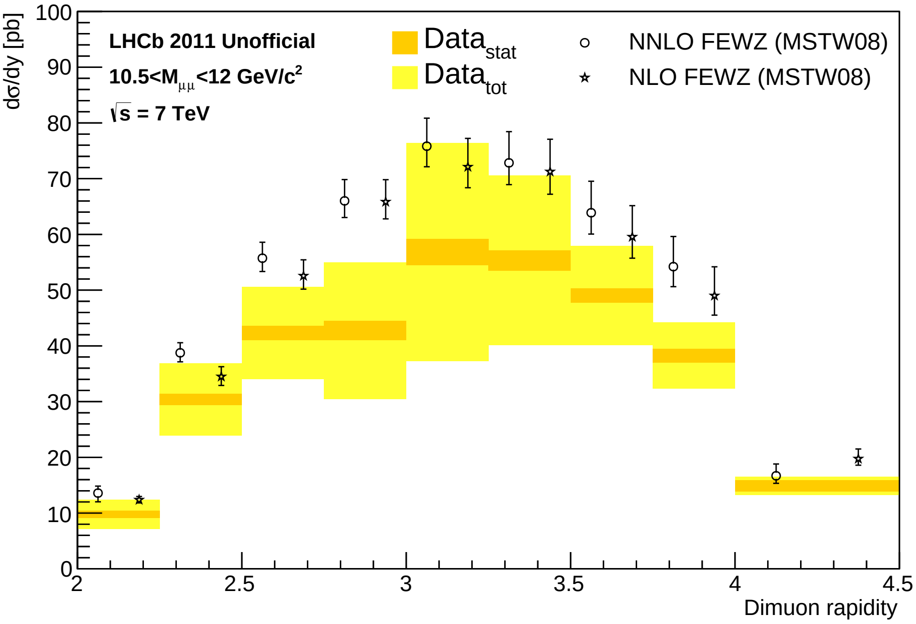

Figure 11.2: Cross section as a function of $y_{\mu\mu}$ for $10.5 < M_{\mu\mu} < 12$ GeV/c^2. The orange and yellow bands show the data with statistical and total uncertainties respectively. The superimposed Fewz predictions are displaced horizontally for presentation.

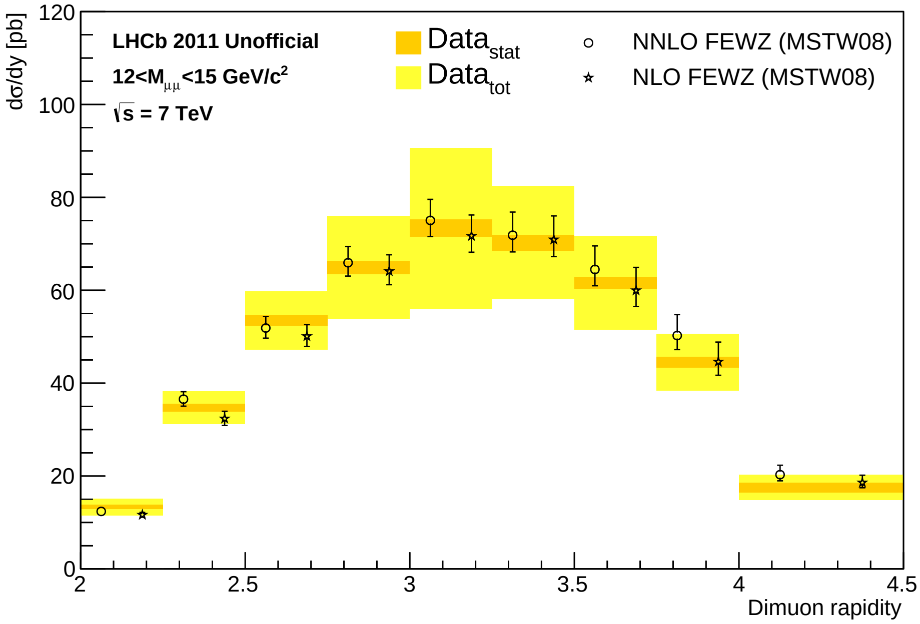

Figure 11.3: Cross section as a function of $y_{\mu\mu}$ for $12 < M_{\mu\mu} < 15$ GeV/c^2. The orange and yellow bands show the data with statistical and total uncertainties respectively. The superimposed Fewz predictions are displaced horizontally for presentation.

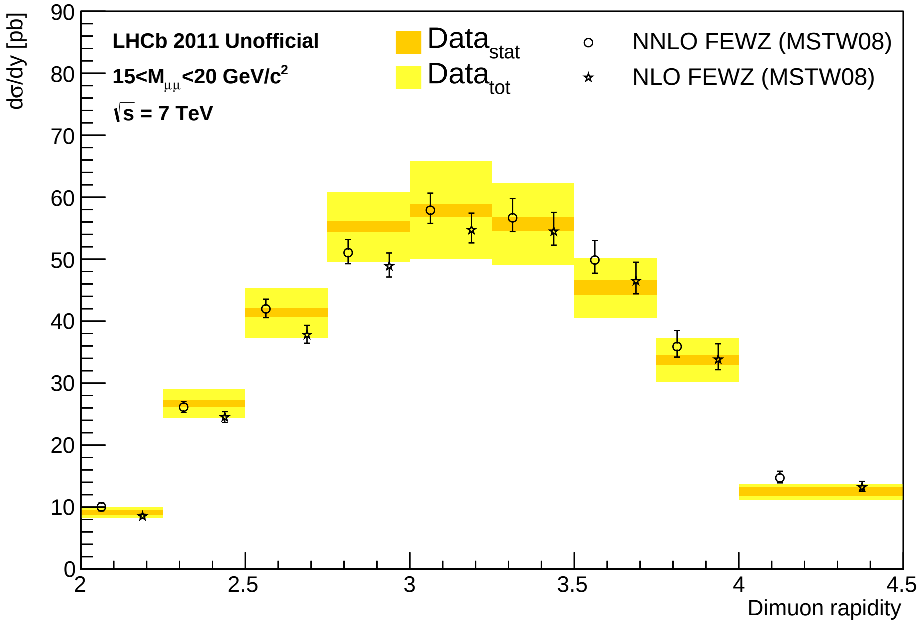

Figure 11.4: Cross section as a function of $y_{\mu\mu}$ for $15 < M_{\mu\mu} < 20$ GeV/c^2. The orange and yellow bands show the data with statistical and total uncertainties respectively. The superimposed Fewz predictions are displaced horizontally for presentation.

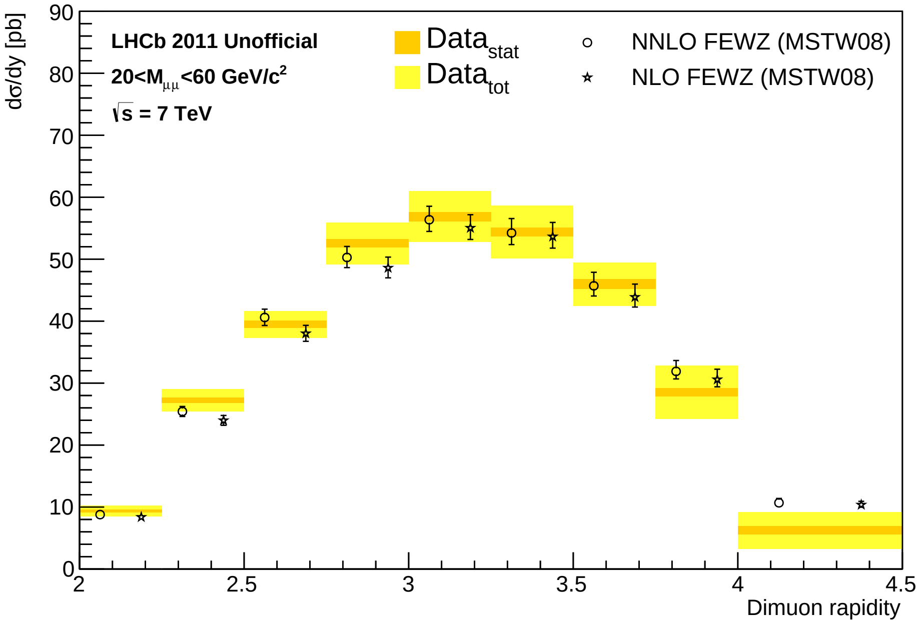

Figure 11.5: Cross section as a function of $y_{\mu\mu}$ for $20 < M_{\mu\mu} < 60$ GeV/c^2. The orange and yellow bands show the data with statistical and total uncertainties respectively. The superimposed FEWZ predictions are displaced horizontally for presentation.

11.1 Outlook on Possible Improvements

To improve on these results, several areas can be studied further. The most relevant for the low mass measurements is the systematic uncertainty determined from the 12 fits. Looking at these fit results shows two effects.

1. The signal fraction (ρ) determined with the Υ signal template is higher than the one determined from the scaled and unscaled Z template. In addition ρ determined using the Υ template agrees best with the values obtained using simulation. This could be an effect of a remaining mass dependence of the di-muon isolation ($\mu\mu_{\text{iso}}$). A better understanding of such a mass dependence might help to reduce the spread between the four fits used for the central value.

2. The alternative background templates both tend to result in lower ρ. At least for the HF-IP template this could be due to the remaining signal contamination. Here, a detailed study of the signal contamination could allow to correct for its effect. Improving the alternative templates should generally result in a smaller standard deviation for the results and reduce the systematic uncertainty on the cross section.

For the corrections the muon identification efficiencies, the trigger efficiency and the bin-to-bin migration would profit most from improvements. The muon identification efficiency has a relatively small systematic uncertainty, however it has been taken from simulation. It has been studied thoroughly for muons with a transverse momentum (p_{T}) above 20 GeV/c and for this range the efficiency could be taken from data. Below that value however, not the same level of detail was achieved and the numbers are not yet available from data. The trigger efficiency is determined from simulation as well and contributes the largest uncertainty. If the low-p_{T} trigger efficiency could be estimated from data, improvements might be possible. For the bin-to-bin migration especially the 80 to 90 GeV/c^2 mass bin could profit from a reduction in the systematic uncertainty. An unfolding approach as used in (LHCb Collaboration 2014a) might allow to improve here.

Finally it would be of large interest to extend the measurement to masses below the Υ resonances and to include a detailed study of the correlations between the different bins.

Chapter 12

Software

The cross section measurements presented here involve a large number of fits with many different configurations. Even more configurations had to be studied during the planning and preparations of the analysis. A big part of the effort was therefore spent on developing tools to simplify and automate these studies and manage the different settings. The resulting code base comprises roughly 20 000 lines of code. Although the software was developed specifically for this study, many of the covered tasks are common to most high energy physics analyses.

During the development of the software attention was paid to reusability. However due to constantly changing requirements and the usual time pressure the code is in parts not as general as it should be. In addition, the code is still based on Root 5.34. Nevertheless several classes and many of the approaches might be of interest to other physicists as well. These classes will be presented in the following together with hints at their shortcomings and general pitfalls.

12.1 Classes of common interest

12.1.1 `MSS` – Measurements with Uncertainties

Every physics analysis has to propagate uncertainties. Doing this correctly can require very elaborate procedures, but often the procedure is straight forward. Still no common tool existed, that would allow to perform simple calculations while automatically propagating statistical and systematic uncertainties.

The `MSS` class provides such a tool. It represents a measurement with statistical and systematic uncertainties and implements the basic arithmetic operations, including correct propagation of the uncertainties. This is achieved by implementing the standard propagation formula for a function f of two variables x and y with uncertainties σ_x and σ_y:

$$\sigma_f = \sqrt{\left(\frac{\partial f}{\partial x}\right)^2 \sigma_x^2 + \left(\frac{\partial f}{\partial y}\right)^2 \sigma_y^2 + 2 \cdot \frac{\partial f}{\partial x}\frac{\partial f}{\partial y} \cdot \sigma_x \sigma_y \rho} \tag{12.1}$$

To correctly propagate the uncertainties, the correlation coefficient ρ has to be specified for each operation. As these are 0 in many cases, this value is assumed if no value is specified. This allows to overload the standard operators `+`, `-`, `*` and `/` such that they work correctly for operations with uncorrelated values.

For this class a minimal test harness was written, to ensure the implemented operations yield the expected results for basic cases. The following two examples are based on simple exercises from the second year data analysis course taught in Zürich. They are included in the test harness.

Listing 12.1.1: Using `MSS` to calculate $U = R \cdot I$

```
MSS R = MSS(1400, 30, 0);
MSS I = MSS(1.120, 0.010, 0);
MSS U = R*I;
```

Listing 12.1.2: Using `MSS` to calculate $R = \frac{U_2 - U_1}{I_2 - I_1}$

```
MSS U_1(  10, 20e-3, 50e-3);
MSS I_1( 11e-3, 0.2e-3, 0.5e-3);
MSS I_2( 32e-3, 0.2e-3, 0.5e-3);
MSS U_2(  30, 20e-3, 50e-3);

MSS R   = MSS::div(
            MSS::sub(U_2, U_1, 0, 1), MSS::sub(I_2, I_1, 0, 1)
          );
```

12.1.2 Data Sources

Two classes are used to manage different datasets and their properties, from input files to weights. `DataSrc` stores the information on a single source. This includes a name, the input chain or tree, the selection, information for weighting and the details on how to display this particular source in plots. `DataProvider` loads and configures the different datasets. For this purpose it defines different source types, each completely defining a dataset. It allows access to the sources through a public member variable. Additionally the class provides several helper functions to load the most used combinations of datasets. This setup allows to add or adjust a data source centrally and immediately use it in all parts of the software. The probability for inconsistent datasets is thereby reduced significantly.

The downside of this is that all plots based on these datasets are dynamically generate each time they are used. This is a time consuming task, but could potentially be mitigated by implementing some type of caching. A second weakness of the implementation is the treatment of the weighting. It is fully tailored to the needs of this analysis and rather limited in scope. Concerning the `DataProvider` a possible improvement would be a global configuration mechanism. The current implementation requires either a separate source type for each test with a slightly different dataset or temporary changes to the default datasets.

12.1.3 Histograms and Fitting

The class `DYhisto` wraps the standard histogram from ROOT (`TH1F`). It represents a histogram from a chosen data source and manages additional selection requirements and the binning. The class also manages the way the histogram is displayed. The implementation is based on `TTree::Draw()`. This allows for low overhead when configuring simple histograms, but requires some fragile workarounds for more complex requirements. Here improvements would be necessary, if this class should be of broader use. A thing to keep in mind will be, that the syntax should still allow to transparently parallelise the creation of the histogram.

A second class, `DYfitter`, wraps the `TFractionFitter` and provides several very useful extensions and helper functions. The most low-level one is, that it performs the fit in a separate thread. This allows the main thread to notice if a fit gets stuck and kill such a fit. Fits getting stuck happened regularly during the early studies and is especially annoying when several different configurations should be run over night.

Once the fit has been performed, several drawing functions are available. The internal plot of the fit result from `TFractionFitter` does not always correspond to the sum of the templates. The reason for this was not fully identified, but it seems that templates are varied within their uncertainties when calculating the sum. The `DYfitter` therefore provides functions to calculate and draw the weighted sum of the histograms. In addition a function is implemented to draw the result as stacked histogram. Finally the pull of the comparison between the target shape and the fit result can be calculated and drawn.

12.1.4 Efficiencies

One of the most common tasks in high energy physics is to correct measured quantities for efficiencies. The results of efficiency studies are usually histograms giving the efficiency as a function of one or more variables. Several classes provided by ROOT help to manage efficiencies, but all lack features needed by this analysis.

The `EffGraph` and `EffHisto` classes therefore wrap the existing tools `TGraph` and `TH1F` or `TH2F` respectively. `EffGraph` loads a `TGraph` and provides functions to extract the efficiency for a given value of the x-variable. In addition it offers the possibility to set a fixed value that will be used above a given threshold. This allows to handle turn-on behaviour, without the need to extend the efficiency graph values far from the turn-on.

`EffHisto` is a template class to mange efficiencies stored in several `TH1F` or `TH2F` histograms, with each histogram valid for a given condition. In the analysis presented here this class is used for the trigger efficiency and the condition defining the validity is the transverse momentum (p_T) range of the two muons. Each of the individual histograms is added to `EffHisto` together with a pointer to a Boolean function. The function must return `true` if the histogram is valid for the passed arguments.

Listing 12.1.3: Usage of `EffHisto` to provide the trigger efficiency of this analysis.

```
bool fine(std::vector< double > &ptVals, d_pair binM, d_pair binP) {
  if (binM.first < ptVals[0] and ptVals[0] < binM.second and
      binP.first < ptVals[1] and ptVals[1] < binP.second) {
    return true;
  } else {
    return false;
  }
}

void NumberService initTriggerEff(TString eff_path) {
  m_trigger = new EffHisto< TH2F >(eff_path);
  vector< pair<double, double> > bins = { make_pair(3e3, 10e3),
    make_pair(10e3, 25e3), make_pair(25e3, 100e4) };
  for( uint m = 0; m < bins.size(); m++) {
    for( uint p = 0; p < bins.size(); p++) {
        // binding the $p_T$ arguments of the boolean function
        auto func = bind(fine, _1, bins[m], bins[p]);
        m_trigger->addEffHisto( func,
          // form the file name based on the $\mu^-$ and $\mu^+$ bin
          Form(strings::triggerFilePattern, m, p)  );
    }
  }
}

MSS NumberService::getTriggerEff(double minus_Eta, double minus_PT,
                                 double plus_Eta, double plus_PT) {
  vector< Double_t > ptVals(2);
  ptVals[charge::minus] = minus_PT;
  ptVals[charge::plus] = plus_PT;
  d_pair eff = m_trigger->getEff(minus_Eta, plus_Eta, ptVals);
  return MSS(eff.first, eff.second, 0.01);
}
```

12.1.5 Canvases and Pads

If an analysis script creates a large number of figures, managing the canvases and especially adjusting their layout gets tedious quickly. To simplify this task, a canvas manager was implemented. The canvas manager handles several independent figures with one or two subplots each. The subplots can be arranged in different predefined layouts (*e.g.* a large plot on top and a small one below). The margins are updated automatically when a different layout is activated.

The abstract base class `CanvasManagerBase`, provides the common interface for different implementations. Two derived classes were implemented for this analysis: `CanvasSplitter` and `CanvasCloner`. The first class splits the main canvas into sub-figures, resulting in a single-page pdf-document. This can be used to create a canvas showing an overview of several fits. For a large number of fits and for the use in publications or presentations the second class is more useful however. It creates a new canvas for each sub-figure and stores each canvas in its own pdf-document. This ensures a reasonable size for each sub-figure and allows to use them independently. To combine the individual pages an external tool like `pdftk` (PDFLabs 2014) can be used on the resulting documents.

12.2 lookat

`lookat` is a `pyRoot` tool, developed to help inspect ROOT files and to simplify data exploration. `lookat` provides a command-line interface based on `IPython`. During its development, possible reuse by other physicists as well as reliability and maintainability were important goals. The source code is therefore extensively documented and test cases are provided for the basic usage. Thanks to `python`'s inherited treatment of comments, the full documentation is available inline during interactive sessions.

Listing 12.2.1 shows an example session producing Fig. 12.1. `lookat` tries to make sensible default choices but still provides full access to the underlying ROOT-objects. This helps to reduce the amount of typing needed to create useful plots. One of its most helpful features is the management of text elements. `lookat` tracks which ROOT-object is responsible for the visible axis titles on a given canvas and updates this object accordingly. In addition, the font size is defined globally and legends, labels and axis title will be scaled automatically, even if the canvas is subdivided.

The latest version of `lookat` is availabel online from GitHub at `https://github.com/nchiapol/lookat`.

Listing 12.2.1: Usage Example of lookat.

```
"""
lookat is started from the command line with
   lookat toy_inputs.root
upon start it prints

toy_inputs.root added to gFiles.
use:
  load( '<tree>' )
to load a tree.

TFile**         toy_inputs.root
 TFile*         toy_inputs.root
  KEY: TTree    gauss_tree;1
  KEY: TTree    uniform_tree;1
"""
load("gauss_tree")
# print the list of branches in gauss_tree
h = draw("value")
h.SetMarkerStyle(23)
draw("value+2")
draw_ratio()
gCanvs[-1].set_yrange(0, 4, "ratio")
put_texts(ylabel="Entries")
l = legend(["reference", "shifted"], pos=(0.2, 0.7, 0.4, 0.9))
l.SetBorderSize(0)
# save to illustration.pdf and illustration.cxx
gCanvs[-1].SaveAs("illustration")

"""
The commands can then be saved into a file using
ipython's magic functions:
   %save illustration.py 0-10
the following lines will be added to the beginning
of the resulting script
"""
from lookat import *
path = '<path to file>'
add_file( path+'toy_inputs.root' )
```

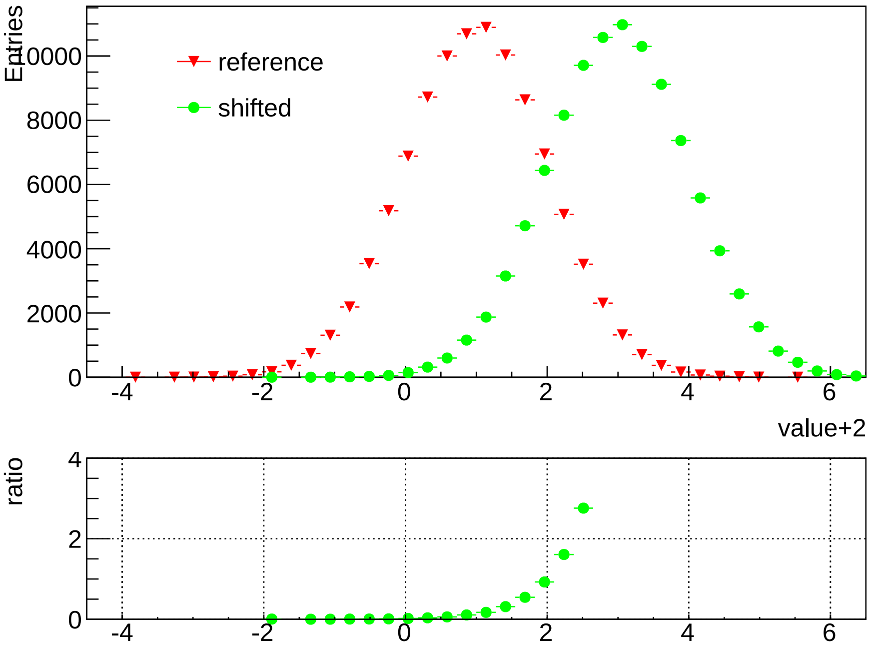

Figure 12.1: Figure resulting from Listing 12.2.1.

Chapter 13

Conclusions

In Chapter 4 a small contribution to the alignment of TT was presented. Many different test-alignments and a thorough review of the detector description stored in the internal database were performed. This allowed to identify and correct a wrong value in the stored module positions affecting the alignment.

In its main part, this thesis presented a measurement of the Drell-Yan production cross section with subsequent decay into two muons. The full integrated luminosity of 1 fb^{-1} collected by LHCb in 2011 at $\sqrt{s} = 7$ TeV was analysed. The cross section was measured differentially as a function of the di-muon mass and the di-muon rapidity. The measurement as a function of mass covers the range 10.5 to 120 GeV/c^2, while the one as a function of rapidity was performed in four mass bins: 10.5 to 12 GeV/c^2, 12 to 15 GeV/c^2, 15 to 20 GeV/c^2 and 20 to 60 GeV/c^2. The signal was extracted using a template fit to an optimised variable based on the isolation of the two muons. The uncertainty on the templates, is the dominant systematic uncertainty at low masses and for the differential measurement. The results obtained are in agreement with the predictions calculated at next-to-next-to-leading order in perturbative Quantum Chromo Dynamics using FEWZ and the MSTW08 set of parton distribution functions (PDFs).

The measurement covers the very forward rapidities and will help to constrain the PDFs in these regions. The analysis required the development of a large code base, parts of which will hopefully be useful to later analyses as well.

References

Altarelli, G. and G. Parisi (1977). “Asymptotic Freedom in Parton Language”. In: *Nucl.Phys.* B126, p. 298. DOI: 10.1016/0550-3213(77)90384-4.

Alves Jr., A. A. et al. (2013). “Performance of the LHCb muon system”. In: *JINST* 8, P02022. DOI: 10.1088/1748-0221/8/02/P02022.

Anderson, C. D. (1933). “The Positive Electron”. In: *Physical Review* 43, pp. 491–494. DOI: 10.1103/PhysRev.43.491.

Anderson, J. S. (2008). “Testing the electroweak sector and determining the absolute luminosity at LHCb using dimuon final states”. CERN-THESIS-2009-020. PhD thesis. University College Dublin.

Andersson, B. et al. (1983). “Parton fragmentation and string dynamics”. In: *Phys.Rept.* 97, pp. 31–145. DOI: 10.1016/0370-1573(83)90080-7.

Arink, R. et al. (2014). “Performance of the LHCb Outer Tracker”. In: *JINST* 9, P01002. DOI: 10.1088/1748-0221/9/01/P01002.

ATLAS Collaboration (2012). “Observation of a new particle in the search for the Standard Model Higgs boson with the ATLAS detector at the LHC”. In: *Physics Letters B* 716.1, pp. 1–29. ISSN: 0370-2693. DOI: 10.1016/j.physletb.2012.08.020.

Ball, R. D. et al. (2010). “A first unbiased global NLO determination of parton distributions and their uncertainties”. In: *Nucl.Phys.* B838, pp. 136–206. DOI: 10.1016/j.nuclphysb.2010.05.008.

Belyaev, I. et al. (2010). “Handling of the generation of primary events in Gauss, the LHCb simulation framework”. In: *Nuclear Science Symposium Conference Record (NSS/MIC), 2010 IEEE*, pp. 1155–1161. DOI: 10.1109/NSSMIC.2010.5873949.

Bernstein, R. H. and P. S. Cooper (2013). “Charged Lepton Flavor Violation: An Experimenter’s Guide”. In: *Phys.Rept.* 532, pp. 27–64. DOI: 10.1016/j.physrep.2013.07.002.

Brun, R. and F. Rademakers (1996). “ROOT - An Object Oriented Data Analysis Framework”. In: *Nucl. Inst. & Meth. in Phys. Res.* Proceedings AIHENP’96 Workshop A.389 (1997), pp. 81–86. DOI: 10.1016/S0168-9002(97)00048-X.

Cabibbo, N. (1963). “Unitary Symmetry and Leptonic Decays”. In: *Phys. Rev. Lett.* 10 (12), pp. 531–533. DOI: `10.1103/PhysRevLett.10.531`.

Callot, O. and S. Hansmann-Menzemer (2007). *The Forward Tracking: Algorithm and Performance Studies*. Tech. rep. CERN-LHCb-2007-015. Geneva: CERN.

Campbell, J. M., J. W. Huston, and W. J. Stirling (2007). “Hard interactions of quarks and gluons: a primer for LHC physics”. In: *Reports on Progress in Physics* 70.1, p. 89. DOI: `10.1088/0034-4885/70/1/R02`.

Caron, J.-L. (2001). *Accelerators chain of CERN : operating and approved projects*. URL: `http://cds.cern.ch/record/43487` (visited on 2014-09-22).

CDF Collaboration (1995). “Observation of Top Quark Production in $\overline{p}p$ Collisions with the Collider Detector at Fermilab”. In: *Phys. Rev. Lett.* 74 (14), pp. 2626–2631. DOI: `10.1103/PhysRevLett.74.2626`.

CERN (2014a). *Member states*. URL: `http://home.web.cern.ch/about/member-states` (visited on 2014-05-06).

CERN (2014b). *The history of CERN*. URL: `https://timeline.web.cern.ch/timelines/The-history-of-CERN` (visited on 2014-05-06).

CERN, AC Team (1999). *Diagram of an LHC dipole magnet*. URL: `http://cds.cern.ch/record/40524` (visited on 2014-09-22).

Cleveland, B. T. et al. (1998). “Measurement of the Solar Electron Neutrino Flux with the Homestake Chlorine Detector”. In: *The Astrophysical Journal* 496.1, p. 505. DOI: `10.1086/305343`.

CMS Collaboration (2012). “Observation of a new boson at a mass of 125 GeV with the CMS experiment at the LHC”. In: *Physics Letters B* 716.1, pp. 30–61. ISSN: 0370-2693. DOI: `10.1016/j.physletb.2012.08.021`.

Corcella, G. et al. (2001). “HERWIG 6: An Event generator for hadron emission reactions with interfering gluons (including supersymmetric processes)”. In: *JHEP* 0101, p. 010. DOI: `10.1088/1126-6708/2001/01/010`.

D0 Collaboration (1995). “Search for High Mass Top Quark Production in $p\overline{p}$ Collisions at $\sqrt{s} =$ 1.8 TeV”. In: *Phys. Rev. Lett.* 74 (13), pp. 2422–2426. DOI: `10.1103/PhysRevLett.74.2422`.

De Cian, M. et al. (2013). “Track Reconstruction Efficiency and Analysis of $B^0 \to K^{*0}\mu^+\mu^-$ at the LHCb Experiment”. CERN-THESIS-2013-145. PhD thesis. Universität Zürich.

De Lorenzi, F. and R. Mc Nulty (2011). “Parton Distribution Function Studies and a Measurement of Drell-Yan Produced Muon Pairs at LHCb”. CERN-THESIS-2011-237. PhD thesis. University College Dublin.

Elsasser, C. (2014). "The LHCb Silicon Tracker". In: *JINST* 9.01, p. C01009. DOI: `10.1088/1748-0221/9/01/C01009`.

Evans, L. and P. Bryant (2008). "LHC Machine". In: *JINST* 3.08, S08001. DOI: `10.1088/1748-0221/3/08/S08001`.

Farry, S. and N. Chiapolini (2014). *A measurement of high-pT muon reconstruction efficiencies in 2011 and 2012 data.* Tech. rep. CERN-LHCb-INT-2014-030. Geneva: CERN.

Filthaut, F. and B. Wijngaarden (2002). *TFractionFitter.* ROOT Reference Guide. URL: `http://root.cern.ch/root/html/TFractionFitter.html` (visited on 2014-09-22).

Gavin, R. et al. (2011). "FEWZ 2.0: A code for hadronic Z production at next-to-next-to-leading order". In: *Comput.Phys.Commun.* 182, pp. 2388–2403. DOI: `10.1016/j.cpc.2011.06.008`.

GEANT4 Collaboration (2003). "GEANT4: A simulation toolkit". In: *Nucl. Instrum. Meth.* A506, p. 250. DOI: `10.1016/S0168-9002(03)01368-8`.

GEANT4 Collaboration (2006). "Geant4 developments and applications". In: *IEEE Trans.Nucl.Sci.* 53, p. 270. DOI: `10.1109/TNS.2006.869826`.

Glashow, S. L., J. Iliopoulos, and L. Maiani (1970). "Weak Interactions with Lepton-Hadron Symmetry". In: *Phys. Rev. D* 2 (7), pp. 1285–1292. DOI: `10.1103/PhysRevD.2.1285`.

Gottschalk, T. D. (1984). "An Improved Description of Hadronization in the QCD Cluster Model for e^+e^- Annihilation". In: *Nucl.Phys.* B239, p. 349. DOI: `10.1016/0550-3213(84)90253-0`.

Horejsi, J. (2002). *Fundamentals of Electroweak Theory.* Karolinum Press. ISBN: 978-8-024-60639-2.

Hulsbergen, W. (2009). "The global covariance matrix of tracks fitted with a Kalman filter and an application in detector alignment". In: *Nuclear Instruments and Methods in Physics Research Section A: Accelerators, Spectrometers, Detectors and Associated Equipment* 600.2, pp. 471–477. ISSN: 0168-9002. DOI: `10.1016/j.nima.2008.11.094`.

Kalman R. E. (1960). "A New Approach to Linear Filtering and Prediction Problems". In: *Journal of Fluids Engineering* 82.1. 10.1115/1.3662552, pp. 35–45. ISSN: 0098-2202. DOI: `10.1115/1.3662552`.

Kobayashi, M. and T. Maskawa (1973). "CP-Violation in the Renormalizable Theory of Weak Interaction". In: *Progress of Theoretical Physics* 49.2, pp. 652–657. DOI: `10.1143/PTP.49.652`.

LHCb Collaboration (2001). *LHCb VELO (VErtex LOcator): Technical Design Report.* Technical Design Report LHCb. CERN-LHCC-2001-011. Geneva: CERN.

LHCb Collaboration (2002). *LHCb inner tracker: Technical Design Report*. Technical Design Report LHCb. CERN-LHCC-2002-029. Geneva: CERN.

LHCb Collaboration (2008). "The LHCb detector at the LHC". In: *JINST* 3, S08005. DOI: `10.1088/1748-0221/3/08/S08005`.

LHCb Collaboration (2012a). "Absolute luminosity measurements with the LHCb detector at the LHC". In: *JINST* 7, P01010. DOI: `10.1088/1748-0221/7/01/P01010`.

LHCb Collaboration (2012b). "Inclusive low mass Drell-Yan production in the forward region at $\sqrt{s} = 7$ TeV". In: 20th International Workshop on Deep-Inelastic Scattering and Related Subjects, Bonn, Germany, 26 - 30 Mar 2012. CERN-LHCb-CONF-2012-013.

LHCb Collaboration (2012c). "Inclusive W and Z production in the forward region at $\sqrt{s} = 7$ TeV". In: *JHEP* 1206, p. 058. DOI: `10.1007/JHEP06(2012)058`.

LHCb Collaboration (2013). "The LHCb trigger and its performance in 2011". In: *JINST* 8, P04022. DOI: `10.1088/1748-0221/8/04/P04022`.

LHCb Collaboration (2014a). "A study of the Z production cross-section in pp collisions at $\sqrt{s} = 7$ TeV using muon final states". In: *in preparation*.

LHCb Collaboration (2014b). *LHCb Trigger Schematic*. URL: `http://lhcb.web.cern.ch/lhcb/speakersbureau/html/TriggerScheme.html` (visited on 2014-09-22).

LHCb Collaboration (2014c). *Measurement of the track reconstruction efficiency at LHCb*. Tech. rep. CERN-LHCB-DP-2013-002. Geneva: CERN.

Martin, A., R. Roberts, et al. (2003). "Uncertainties of predictions from parton distributions. 1: Experimental errors". In: *Eur.Phys.J.* C28, pp. 455–473. DOI: `10.1140/epjc/s2003-01196-2`.

Martin, A., W. Stirling, et al. (2009). "Parton distributions for the LHC". In: *Eur.Phys.J.* C63, pp. 189–285. DOI: `10.1140/epjc/s10052-009-1072-5`.

Martin, B. R. and G. Shaw (2005). *Particle Physics*. Second Edition. Wiley. ISBN: 978-0-471-97252-5.

Nadolsky, P. M. et al. (2008). "Implications of CTEQ global analysis for collider observables". In: *Phys.Rev.* D78, p. 013004. DOI: `10.1103/PhysRevD.78.013004`.

Needham, M. and J. Van Tilburg (2007). *Performance of the track matching*. Tech. rep. CERN-LHCb-2007-020. Geneva: CERN.

NIST/SEMATECH (2014). *Gamma Distribution*. e-Handbook of Statistical Methods. URL: `http://www.itl.nist.gov/div898/handbook/eda/section3/eda366b.htm` (visited on 2014-09-22).

Particle Data Group (2012). "Review of particle physics". In: *Phys. Rev.* D86. and 2013 partial update for the 2014 edition, p. 010001. DOI: `10.1103/PhysRevD.86.010001`.

PDFLabs (2014). *pdftk - The PDF Toolkit.* URL: `http://www.pdftk.com` (visited on 2014-09-22).

Salzmann, C. (2011). “LHCb Spectrometer Alignment and Verification of its Performance using the Decay $B_d^0 \to K^{*0} J/\psi$”. CERN-THESIS-2011-201. PhD thesis. Universität Zürich.

Sjöstrand, T., S. Mrenna, and P. Skands (2006). “PYTHIA 6.4 physics and manual”. In: *JHEP* 05, p. 026. DOI: `10.1088/1126-6708/2006/05/026`.

Skwarnicki, T. (1986). “A study of the radiative cascade transitions between the Upsilon-prime and Upsilon resonances”. DESY-F31-86-02. PhD thesis. Institute of Nuclear Physics, Krakow.

Super-Kamiokande Collaboration (1998). “Evidence for Oscillation of Atmospheric Neutrinos”. In: *Phys. Rev. Lett.* 81 (8), pp. 1562–1567. DOI: `10.1103/PhysRevLett.81.1562`.

Thorne, R. et al. (2008). “Parton Distributions and QCD at LHCb”. In: 16th International Workshop on Deep Inelastic Scattering and Related Subjects (DIS 2008), London, England, 7 - 11 Apr 2008. DOI: `10.3360/dis.2008.30`.

Tobin, M. (2013). “Performance of the LHCb Tracking Detectors”. In: Vertex 2012, Jeju, Republic Of Korea, 16 - 21 Sep 2012. CERN-LHCb-PROC-2013-015.

UA1 Collaboration (1987). “Intermediate vector boson cross-sections at the CERN super proton synchrotron collider and the number of neutrino types”. In: *Phys.Lett.* B198, p. 271. DOI: `10.1016/0370-2693(87)91510-3`.

UA2 Collaboration (1992). “A measurement of the W and Z production cross-sections and a determination of Γ (W) at the CERN $\bar{p}p$ collider”. In: *Phys.Lett.* B276, pp. 365–374. DOI: `10.1016/0370-2693(92)90333-Y`.

Van Tilburg, J. and M. Merk (2005). “Track simulation and reconstruction in LHCb”. CERN-THESIS-2005-040. PhD thesis. Vrije Universiteit Amsterdam.

Weisstein, E. W. (2014). *Runge-Kutta Method.* MathWorld – A Wolfram Web Resource. URL: `http://mathworld.wolfram.com/Runge-KuttaMethod.html` (visited on 2014-09-22).

Part III

The Appendix

Appendix A

Cross Section as a Function of Rapidity

Table A.1: Cross section measured as a function of di-muon rapidity ($y_{\mu\mu}$). (1. Part)

$M_{\mu\mu}$ [GeV/c^2]	y	σ [pb]	stat.	syst.
10.5 – 12.0	2.00 – 2.25	2.44	0.16	0.64
10.5 – 12.0	2.25 – 2.50	7.59	0.25	1.60
10.5 – 12.0	2.50 – 2.75	10.58	0.32	2.04
10.5 – 12.0	2.75 – 3.00	10.69	0.43	3.03
10.5 – 12.0	3.00 – 3.25	14.22	0.59	4.85
10.5 – 12.0	3.25 – 3.50	13.83	0.46	3.77
10.5 – 12.0	3.50 – 3.75	12.25	0.31	2.20
10.5 – 12.0	3.75 – 4.00	9.57	0.31	1.45
10.5 – 12.0	4.00 – 4.50	7.46	0.51	0.63
12.0 – 15.0	2.00 – 2.25	3.34	0.12	0.43
12.0 – 15.0	2.25 – 2.50	8.68	0.21	0.85
12.0 – 15.0	2.50 – 2.75	13.39	0.27	1.55
12.0 – 15.0	2.75 – 3.00	16.22	0.36	2.76
12.0 – 15.0	3.00 – 3.25	18.34	0.47	4.30
12.0 – 15.0	3.25 – 3.50	17.56	0.43	3.01
12.0 – 15.0	3.50 – 3.75	15.41	0.31	2.50
12.0 – 15.0	3.75 – 4.00	11.13	0.28	1.50
12.0 – 15.0	4.00 – 4.50	8.76	0.54	1.26

Table A.2: Cross section measured as a function of $y_{\mu\mu}$. (2. Part)

$M_{\mu\mu}$ [GeV/c^2]	y	σ [pb]	stat.	syst.
15.0 – 20.0	2.00 – 2.25	2.27	0.08	0.19
15.0 – 20.0	2.25 – 2.50	6.68	0.13	0.58
15.0 – 20.0	2.50 – 2.75	10.33	0.18	0.98
15.0 – 20.0	2.75 – 3.00	13.80	0.22	1.40
15.0 – 20.0	3.00 – 3.25	14.46	0.27	1.96
15.0 – 20.0	3.25 – 3.50	13.90	0.27	1.63
15.0 – 20.0	3.50 – 3.75	11.35	0.29	1.17
15.0 – 20.0	3.75 – 4.00	8.43	0.19	0.88
15.0 – 20.0	4.00 – 4.50	6.23	0.36	0.52
20.0 – 60.0	2.00 – 2.25	2.34	0.06	0.20
20.0 – 60.0	2.25 – 2.50	6.81	0.11	0.44
20.0 – 60.0	2.50 – 2.75	9.87	0.14	0.52
20.0 – 60.0	2.75 – 3.00	13.13	0.17	0.83
20.0 – 60.0	3.00 – 3.25	14.21	0.19	1.00
20.0 – 60.0	3.25 – 3.50	13.60	0.18	1.05
20.0 – 60.0	3.50 – 3.75	11.50	0.19	0.85
20.0 – 60.0	3.75 – 4.00	7.14	0.16	1.06
20.0 – 60.0	4.00 – 4.50	3.12	0.32	1.45

Table A.3: Average systematic uncertainties for the measurement as a function of $y_{\mu\mu}$. The upper part shows the uncertainties on the factors applied bin wise, The lower part the uncertainties on the event dependent efficiency corrections listed in Table A.4. Values are given in %.

S^{ρ}	3.0	–	46.3
S^{MIG}	0.1	–	3.6
S^{SEL}	1.1	–	1.1
S^{TRIG}	1.3	–	1.5
S^{MUID}	0.7	–	0.7
S^{GEC}	1.1	–	1.3
S^{TRACK}	1.5	–	1.5
Total	2.4	–	2.5

Table A.4: Average di-muon mass and event dependent efficiencies for each bin.

$M_{\mu\mu}$ [GeV/c^2]	y	$\overline{M_{\mu\mu}}$	$\varepsilon^{\mathrm{TRIG}}$	$\varepsilon^{\mathrm{MUID}}$	$\varepsilon^{\mathrm{GEC}}$	$\varepsilon^{\mathrm{TRACK}}$	Total
10.5 – 12.0	2.00 – 2.25	11.2	0.761	0.941	0.987	0.879	0.622
10.5 – 12.0	2.25 – 2.50	11.2	0.773	0.940	0.987	0.906	0.649
10.5 – 12.0	2.50 – 2.75	11.2	0.754	0.939	0.987	0.917	0.641
10.5 – 12.0	2.75 – 3.00	11.2	0.740	0.938	0.987	0.924	0.633
10.5 – 12.0	3.00 – 3.25	11.2	0.735	0.938	0.987	0.924	0.629
10.5 – 12.0	3.25 – 3.50	11.2	0.740	0.938	0.987	0.923	0.632
10.5 – 12.0	3.50 – 3.75	11.2	0.740	0.938	0.987	0.926	0.635
10.5 – 12.0	3.75 – 4.00	11.2	0.733	0.939	0.987	0.926	0.629
10.5 – 12.0	4.00 – 4.50	11.2	0.749	0.940	0.987	0.902	0.627
12.0 – 15.0	2.00 – 2.25	13.2	0.766	0.944	0.987	0.880	0.628
12.0 – 15.0	2.25 – 2.50	13.2	0.767	0.943	0.987	0.906	0.647
12.0 – 15.0	2.50 – 2.75	13.2	0.749	0.942	0.987	0.917	0.639
12.0 – 15.0	2.75 – 3.00	13.2	0.735	0.941	0.987	0.923	0.630
12.0 – 15.0	3.00 – 3.25	13.2	0.735	0.940	0.987	0.921	0.628
12.0 – 15.0	3.25 – 3.50	13.2	0.736	0.940	0.987	0.920	0.629
12.0 – 15.0	3.50 – 3.75	13.3	0.738	0.940	0.987	0.925	0.634
12.0 – 15.0	3.75 – 4.00	13.3	0.732	0.942	0.987	0.924	0.629
12.0 – 15.0	4.00 – 4.50	13.3	0.750	0.943	0.987	0.902	0.630
15.0 – 20.0	2.00 – 2.25	16.9	0.768	0.949	0.988	0.880	0.634
15.0 – 20.0	2.25 – 2.50	16.9	0.757	0.949	0.988	0.906	0.643
15.0 – 20.0	2.50 – 2.75	16.9	0.741	0.947	0.988	0.918	0.637
15.0 – 20.0	2.75 – 3.00	16.9	0.730	0.945	0.988	0.921	0.628
15.0 – 20.0	3.00 – 3.25	16.9	0.728	0.944	0.988	0.921	0.626
15.0 – 20.0	3.25 – 3.50	16.9	0.727	0.944	0.988	0.922	0.625
15.0 – 20.0	3.50 – 3.75	17.0	0.731	0.946	0.988	0.923	0.630
15.0 – 20.0	3.75 – 4.00	17.0	0.727	0.948	0.988	0.924	0.629
15.0 – 20.0	4.00 – 4.50	17.0	0.753	0.949	0.988	0.901	0.635
20.0 – 60.0	2.00 – 2.25	27.3	0.716	0.958	0.989	0.880	0.597
20.0 – 60.0	2.25 – 2.50	27.5	0.711	0.957	0.989	0.906	0.610
20.0 – 60.0	2.50 – 2.75	27.4	0.714	0.957	0.989	0.917	0.620
20.0 – 60.0	2.75 – 3.00	27.1	0.705	0.955	0.989	0.923	0.615
20.0 – 60.0	3.00 – 3.25	27.3	0.703	0.954	0.989	0.926	0.615
20.0 – 60.0	3.25 – 3.50	27.3	0.699	0.954	0.989	0.927	0.612
20.0 – 60.0	3.50 – 3.75	27.3	0.690	0.955	0.989	0.928	0.605
20.0 – 60.0	3.75 – 4.00	27.4	0.696	0.957	0.989	0.924	0.609
20.0 – 60.0	4.00 – 4.50	27.0	0.733	0.958	0.989	0.902	0.627

Table A.5: Next-to-next-to-leading order (NNLO) predictions calculated with Fewz using the Mstw08 parton distribution function (PDF) set.

$M_{\mu\mu}$ [GeV/c^2]	y	σ [pb]	Δ_{up}	Δ_{down}
10.5 – 12.0	2.00 – 2.25	3.40	0.30	0.37
10.5 – 12.0	2.25 – 2.50	9.69	0.30	0.22
10.5 – 12.0	2.50 – 2.75	13.93	0.52	0.34
10.5 – 12.0	2.75 – 3.00	16.50	0.76	0.47
10.5 – 12.0	3.00 – 3.25	18.96	1.07	0.64
10.5 – 12.0	3.25 – 3.50	18.21	1.25	0.74
10.5 – 12.0	3.50 – 3.75	15.97	1.30	0.78
10.5 – 12.0	3.75 – 4.00	13.55	1.27	0.76
10.5 – 12.0	4.00 – 4.50	8.34	1.02	0.61
12.0 – 15.0	2.00 – 2.25	3.10	0.07	0.06
12.0 – 15.0	2.25 – 2.50	9.14	0.25	0.20
12.0 – 15.0	2.50 – 2.75	12.97	0.43	0.30
12.0 – 15.0	2.75 – 3.00	16.48	0.66	0.43
12.0 – 15.0	3.00 – 3.25	18.76	0.93	0.57
12.0 – 15.0	3.25 – 3.50	17.96	1.08	0.64
12.0 – 15.0	3.50 – 3.75	16.12	1.13	0.67
12.0 – 15.0	3.75 – 4.00	12.56	1.04	0.62
12.0 – 15.0	4.00 – 4.50	10.15	0.95	0.56
15.0 – 20.0	2.00 – 2.25	2.51	0.15	0.15
15.0 – 20.0	2.25 – 2.50	6.53	0.15	0.13
15.0 – 20.0	2.50 – 2.75	10.49	0.28	0.22
15.0 – 20.0	2.75 – 3.00	12.76	0.42	0.29
15.0 – 20.0	3.00 – 3.25	14.47	0.58	0.37
15.0 – 20.0	3.25 – 3.50	14.17	0.69	0.42
15.0 – 20.0	3.50 – 3.75	12.47	0.72	0.42
15.0 – 20.0	3.75 – 4.00	8.975	0.61	0.35
15.0 – 20.0	4.00 – 4.50	7.35	0.50	0.35
20.0 – 60.0	2.00 – 2.25	2.20	0.04	0.04
20.0 – 60.0	2.25 – 2.50	6.35	0.12	0.11
20.0 – 60.0	2.50 – 2.75	10.15	0.21	0.19
20.0 – 60.0	2.75 – 3.00	12.57	0.30	0.25
20.0 – 60.0	3.00 – 3.25	14.09	0.40	0.30
20.0 – 60.0	3.25 – 3.50	13.56	0.46	0.31
20.0 – 60.0	3.50 – 3.75	11.42	0.46	0.28
20.0 – 60.0	3.75 – 4.00	7.97	0.39	0.22
20.0 – 60.0	4.00 – 4.50	5.34	0.32	0.18

Appendix B

Fit Results for 2011 Data

This chapter contains the results for the different fits. Appendix B.1 shows the figures resulting from the main fit while the following sections list the results from all fits performed.

B.1 Figures for the Main Fit

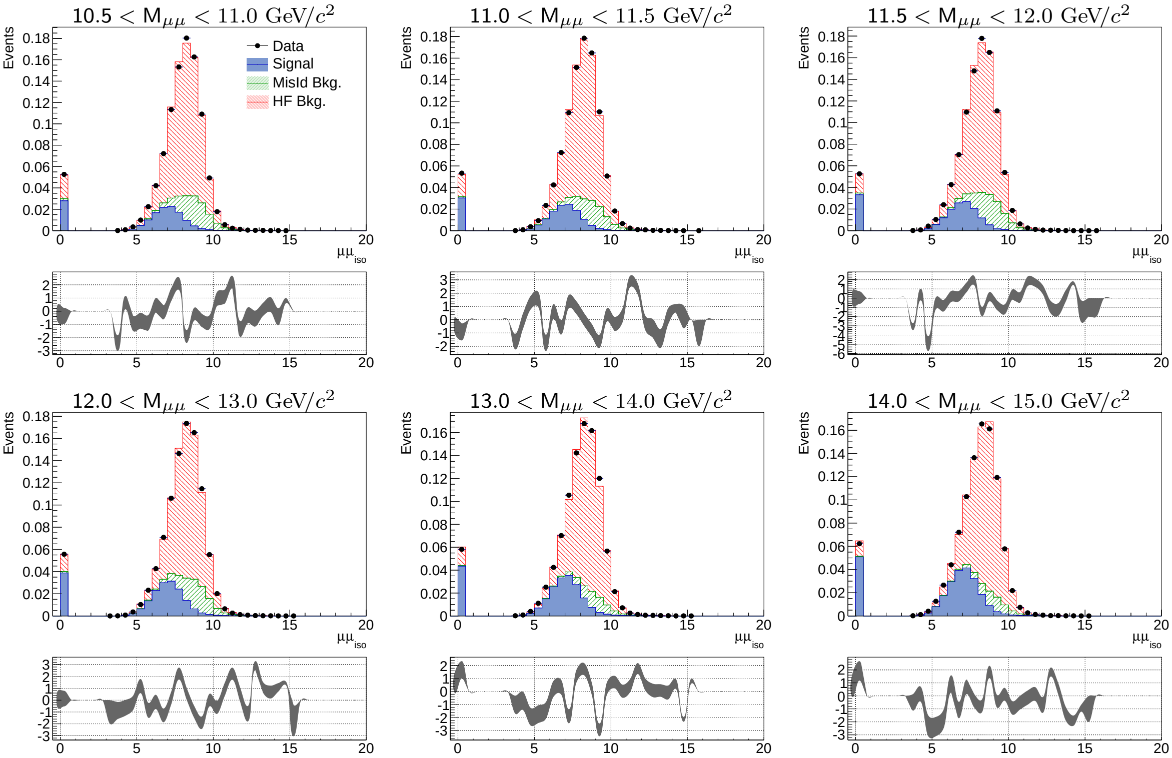

Figure B.1: Fits with the templates: Z, scaled; SameSign; HF-Vertex. (1. Part)

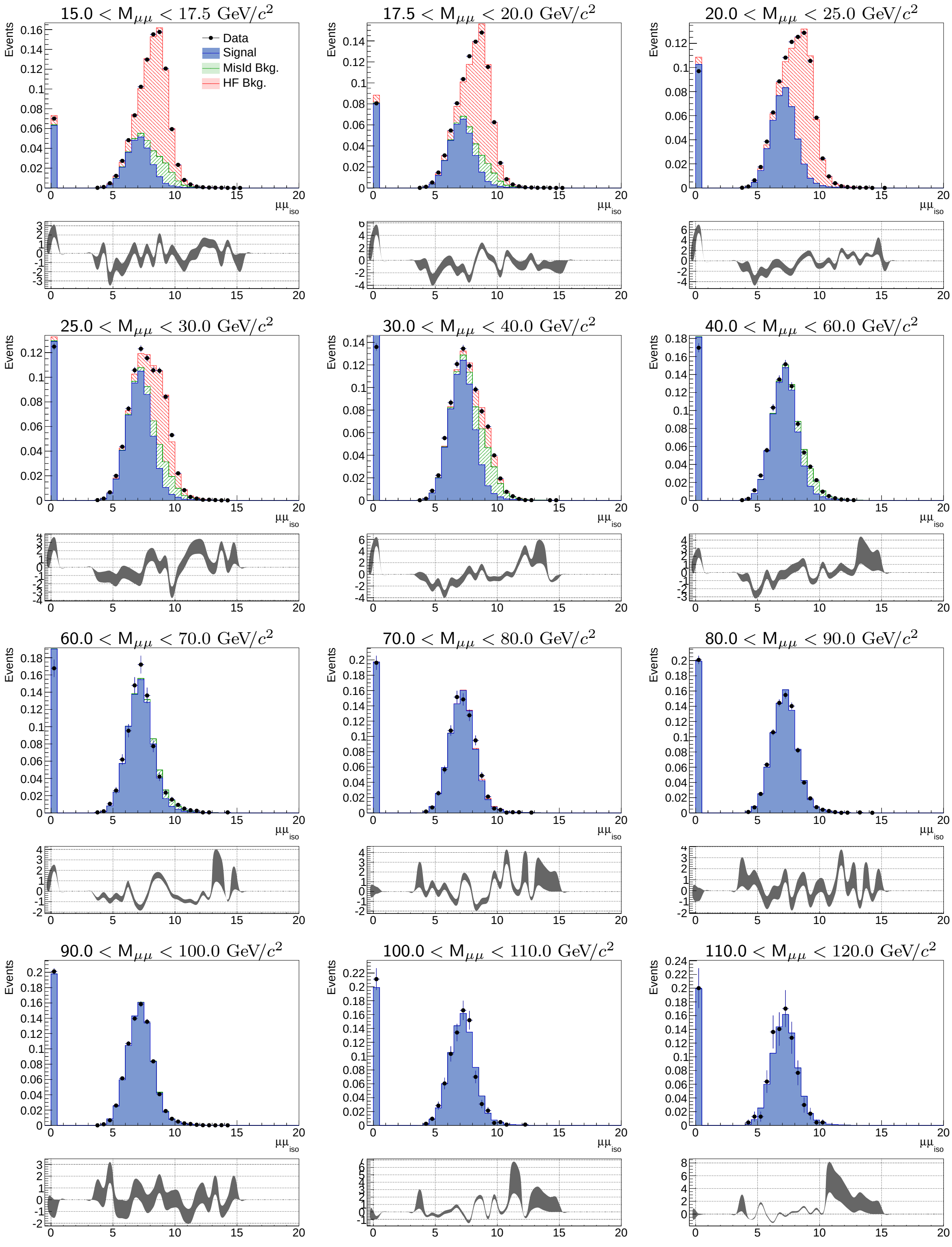

Figure B.2: Fits with the templates: Z, scaled; SameSign; HF-Vertex. (2. Part)

B.2 Signal Yields of all Fits

B.2.1 Signal Yield as a Function of Mass

Table B.1: Fit results for templates: Υ; SameSign; HF-Vertex

$M_{\mu\mu}$ [GeV/c^2]	y	signal yield	ρ	χ^2/ndof
10.5 - 11.0	2.00 - 4.50	$21\,409.2 \pm 774.8$	0.172 ± 0.006	1.01
11.0 - 11.5	2.00 - 4.50	$18\,991.8 \pm 703.7$	0.187 ± 0.007	1.07
11.5 - 12.0	2.00 - 4.50	$17\,270.4 \pm 601.0$	0.203 ± 0.007	1.55
12.0 - 13.0	2.00 - 4.50	$29\,792.5 \pm 724.6$	0.232 ± 0.006	1.56
13.0 - 14.0	2.00 - 4.50	$23\,390.6 \pm 595.8$	0.258 ± 0.007	1.05
14.0 - 15.0	2.00 - 4.50	$19\,120.3 \pm 444.8$	0.299 ± 0.007	0.79
15.0 - 17.5	2.00 - 4.50	$33\,860.9 \pm 578.7$	0.358 ± 0.006	1.12
17.5 - 20.0	2.00 - 4.50	$20\,948.4 \pm 352.0$	0.448 ± 0.008	0.69
20.0 - 25.0	2.00 - 4.50	$22\,510.0 \pm 329.8$	0.547 ± 0.008	1.00
25.0 - 30.0	2.00 - 4.50	$10\,813.9 \pm 169.2$	0.672 ± 0.011	1.66
30.0 - 40.0	2.00 - 4.50	9585.1 ± 141.4	0.785 ± 0.012	1.36
40.0 - 60.0	2.00 - 4.50	5986.6 ± 99.7	0.910 ± 0.015	1.71
60.0 - 70.0	2.00 - 4.50	1531.5 ± 43.4	0.948 ± 0.027	0.88
70.0 - 80.0	2.00 - 4.50	2233.7 ± 52.0	0.990 ± 0.023	1.18
80.0 - 90.0	2.00 - 4.50	$13\,082.4 \pm 225.3$	0.995 ± 0.017	2.73
90.0 - 100.0	2.00 - 4.50	$21\,609.4 \pm 248.2$	0.991 ± 0.011	4.37
100.0 - 110.0	2.00 - 4.50	843.0 ± 87.9	1.000 ± 0.104	0.83
110.0 - 120.0	2.00 - 4.50	235.0 ± 23.2	1.000 ± 0.099	0.34

Table B.2: Fit results for templates: Υ; SameSign; HF-IP

$M_{\mu\mu}$ [GeV/c^2]	y	signal yield	ρ	χ^2/ndof
10.5 - 11.0	2.00 - 4.50	$15\,987.2 \pm 894.9$	0.128 ± 0.007	2.24
11.0 - 11.5	2.00 - 4.50	$14\,316.0 \pm 770.8$	0.141 ± 0.008	1.94
11.5 - 12.0	2.00 - 4.50	$13\,662.0 \pm 711.8$	0.161 ± 0.008	1.25
12.0 - 13.0	2.00 - 4.50	$24\,397.8 \pm 798.8$	0.190 ± 0.006	1.85
13.0 - 14.0	2.00 - 4.50	$20\,297.5 \pm 615.7$	0.224 ± 0.007	0.99
14.0 - 15.0	2.00 - 4.50	$17\,029.1 \pm 484.4$	0.266 ± 0.008	1.00
15.0 - 17.5	2.00 - 4.50	$31\,680.4 \pm 605.6$	0.335 ± 0.006	1.14
17.5 - 20.0	2.00 - 4.50	$19\,639.4 \pm 388.4$	0.420 ± 0.008	0.70
20.0 - 25.0	2.00 - 4.50	$20\,944.5 \pm 382.7$	0.509 ± 0.009	0.72
25.0 - 30.0	2.00 - 4.50	$10\,465.9 \pm 183.9$	0.651 ± 0.011	1.25
30.0 - 40.0	2.00 - 4.50	9572.8 ± 426.7	0.784 ± 0.035	1.36
40.0 - 60.0	2.00 - 4.50	5986.3 ± 99.7	0.910 ± 0.015	1.71
60.0 - 70.0	2.00 - 4.50	1531.5 ± 40.7	0.948 ± 0.025	0.88
70.0 - 80.0	2.00 - 4.50	n/a	n/a	n/a
80.0 - 90.0	2.00 - 4.50	$13\,081.0 \pm 153.1$	0.995 ± 0.012	2.73
90.0 - 100.0	2.00 - 4.50	$21\,609.6 \pm 254.3$	0.991 ± 0.012	4.37
100.0 - 110.0	2.00 - 4.50	843.0 ± 78.5	1.000 ± 0.093	0.83
110.0 - 120.0	2.00 - 4.50	235.0 ± 161.5	1.000 ± 0.687	0.34

Table B.3: Fit results for templates: Υ; MinBias; HF-Vertex

$M_{\mu\mu}$ [GeV/c^2]	y	signal yield	ρ	χ^2/ndof
10.5 - 11.0	2.00 - 4.50	$17\,741.8 \pm 791.9$	0.142 ± 0.006	2.77
11.0 - 11.5	2.00 - 4.50	$15\,952.2 \pm 723.6$	0.157 ± 0.007	2.38
11.5 - 12.0	2.00 - 4.50	$14\,509.7 \pm 599.6$	0.171 ± 0.007	3.00
12.0 - 13.0	2.00 - 4.50	$26\,174.9 \pm 682.7$	0.204 ± 0.005	3.75
13.0 - 14.0	2.00 - 4.50	$21\,614.9 \pm 563.7$	0.239 ± 0.006	1.84
14.0 - 15.0	2.00 - 4.50	$18\,092.6 \pm 430.1$	0.283 ± 0.007	1.16
15.0 - 17.5	2.00 - 4.50	$31\,748.6 \pm 532.1$	0.335 ± 0.006	2.47
17.5 - 20.0	2.00 - 4.50	$20\,062.0 \pm 340.1$	0.429 ± 0.007	1.23
20.0 - 25.0	2.00 - 4.50	n/a	n/a	n/a
25.0 - 30.0	2.00 - 4.50	$10\,474.0 \pm 163.0$	0.651 ± 0.010	2.61
30.0 - 40.0	2.00 - 4.50	9177.3 ± 142.8	0.752 ± 0.012	3.00
40.0 - 60.0	2.00 - 4.50	5908.6 ± 95.8	0.898 ± 0.015	2.20
60.0 - 70.0	2.00 - 4.50	1516.3 ± 43.5	0.938 ± 0.027	0.70
70.0 - 80.0	2.00 - 4.50	n/a	n/a	n/a
80.0 - 90.0	2.00 - 4.50	$13\,064.5 \pm 153.0$	0.994 ± 0.012	2.71
90.0 - 100.0	2.00 - 4.50	$21\,506.3 \pm 245.6$	0.986 ± 0.011	4.26
100.0 - 110.0	2.00 - 4.50	843.0 ± 50.4	1.000 ± 0.060	0.83
110.0 - 120.0	2.00 - 4.50	235.0 ± 16.2	1.000 ± 0.069	0.34

Table B.4: Fit results for templates: Υ; MinBias; HF-IP

$M_{\mu\mu}$ [GeV/c^2]	y	signal yield	ρ	χ^2/ndof
10.5 - 11.0	2.00 - 4.50	6507.1 ± 1003.5	0.052 ± 0.008	8.33
11.0 - 11.5	2.00 - 4.50	6473.9 ± 849.1	0.064 ± 0.008	6.06
11.5 - 12.0	2.00 - 4.50	7907.0 ± 723.5	0.093 ± 0.009	4.55
12.0 - 13.0	2.00 - 4.50	17 042.9 ± 784.8	0.133 ± 0.006	6.77
13.0 - 14.0	2.00 - 4.50	15 533.6 ± 644.7	0.172 ± 0.007	4.63
14.0 - 15.0	2.00 - 4.50	14 588.1 ± 455.2	0.228 ± 0.007	2.70
15.0 - 17.5	2.00 - 4.50	27 992.7 ± 567.5	0.296 ± 0.006	3.84
17.5 - 20.0	2.00 - 4.50	18 099.7 ± 356.0	0.387 ± 0.008	1.58
20.0 - 25.0	2.00 - 4.50	20 073.5 ± 340.0	0.488 ± 0.008	0.80
25.0 - 30.0	2.00 - 4.50	9871.9 ± 167.7	0.614 ± 0.010	2.06
30.0 - 40.0	2.00 - 4.50	8925.9 ± 145.8	0.731 ± 0.012	2.75
40.0 - 60.0	2.00 - 4.50	5872.8 ± 104.2	0.893 ± 0.016	2.16
60.0 - 70.0	2.00 - 4.50	1516.4 ± 43.5	0.938 ± 0.027	0.70
70.0 - 80.0	2.00 - 4.50	2232.4 ± 48.0	0.989 ± 0.021	1.18
80.0 - 90.0	2.00 - 4.50	13 064.3 ± 148.3	0.994 ± 0.011	2.71
90.0 - 100.0	2.00 - 4.50	21 506.2 ± 245.6	0.986 ± 0.011	4.26
100.0 - 110.0	2.00 - 4.50	843.0 ± 40.7	1.000 ± 0.048	0.83
110.0 - 120.0	2.00 - 4.50	235.0 ± 17.9	1.000 ± 0.076	0.34

Table B.5: Fit results for templates: Z, scaled; SameSign; HF-Vertex

$M_{\mu\mu}$ [GeV/c^2]	y	signal yield	ρ	χ^2/ndof
10.5 - 11.0	2.00 - 4.50	17 486.2 ± 596.1	0.140 ± 0.005	0.61
11.0 - 11.5	2.00 - 4.50	15 484.4 ± 589.3	0.152 ± 0.006	0.79
11.5 - 12.0	2.00 - 4.50	14 192.2 ± 507.5	0.167 ± 0.006	1.04
12.0 - 13.0	2.00 - 4.50	25 007.9 ± 610.8	0.195 ± 0.005	0.99
13.0 - 14.0	2.00 - 4.50	19 754.8 ± 521.5	0.218 ± 0.006	0.77
14.0 - 15.0	2.00 - 4.50	16 329.6 ± 415.0	0.255 ± 0.006	0.69
15.0 - 17.5	2.00 - 4.50	30 003.7 ± 503.0	0.317 ± 0.005	0.65
17.5 - 20.0	2.00 - 4.50	18 903.0 ± 336.8	0.404 ± 0.007	1.15
20.0 - 25.0	2.00 - 4.50	21 200.5 ± 292.3	0.515 ± 0.007	1.50
25.0 - 30.0	2.00 - 4.50	10 418.3 ± 160.8	0.648 ± 0.010	0.95
30.0 - 40.0	2.00 - 4.50	9360.4 ± 142.1	0.767 ± 0.012	1.74
40.0 - 60.0	2.00 - 4.50	6002.0 ± 96.8	0.912 ± 0.015	0.75
60.0 - 70.0	2.00 - 4.50	1543.6 ± 43.2	0.955 ± 0.027	0.64
70.0 - 80.0	2.00 - 4.50	2238.3 ± 50.9	0.992 ± 0.023	0.53
80.0 - 90.0	2.00 - 4.50	6512.0 ± 441.4	1.000 ± 0.068	0.50
90.0 - 100.0	2.00 - 4.50	10 887.7 ± 133.2	0.994 ± 0.012	0.32
100.0 - 110.0	2.00 - 4.50	843.0 ± 55.5	1.000 ± 0.066	0.45
110.0 - 120.0	2.00 - 4.50	235.0 ± 34.8	1.000 ± 0.148	0.24

Table B.6: Fit results for templates: Z, scaled; SameSign; HF-IP

$M_{\mu\mu}$ [GeV/c^2]	y	signal yield	ρ	χ^2/ndof
10.5 - 11.0	2.00 - 4.50	$13\,163.8 \pm 696.5$	0.106 ± 0.006	1.51
11.0 - 11.5	2.00 - 4.50	$11\,714.4 \pm 624.0$	0.115 ± 0.006	1.37
11.5 - 12.0	2.00 - 4.50	$11\,055.9 \pm 561.5$	0.130 ± 0.007	0.88
12.0 - 13.0	2.00 - 4.50	$20\,198.3 \pm 663.8$	0.157 ± 0.005	1.14
13.0 - 14.0	2.00 - 4.50	$16\,980.4 \pm 521.4$	0.188 ± 0.006	0.62
14.0 - 15.0	2.00 - 4.50	$14\,491.9 \pm 436.3$	0.227 ± 0.007	0.61
15.0 - 17.5	2.00 - 4.50	$27\,803.3 \pm 529.3$	0.294 ± 0.006	0.74
17.5 - 20.0	2.00 - 4.50	$17\,488.8 \pm 359.7$	0.374 ± 0.008	1.14
20.0 - 25.0	2.00 - 4.50	$19\,096.9 \pm 455.1$	0.464 ± 0.011	1.84
25.0 - 30.0	2.00 - 4.50	$10\,041.2 \pm 173.0$	0.624 ± 0.011	0.74
30.0 - 40.0	2.00 - 4.50	9273.2 ± 150.8	0.760 ± 0.012	1.72
40.0 - 60.0	2.00 - 4.50	n/a	n/a	n/a
60.0 - 70.0	2.00 - 4.50	1543.6 ± 43.3	0.955 ± 0.027	0.64
70.0 - 80.0	2.00 - 4.50	2235.2 ± 51.1	0.990 ± 0.023	0.53
80.0 - 90.0	2.00 - 4.50	6512.0 ± 275.1	1.000 ± 0.042	0.50
90.0 - 100.0	2.00 - 4.50	$10\,887.0 \pm 141.9$	0.994 ± 0.013	0.32
100.0 - 110.0	2.00 - 4.50	843.0 ± 99.7	1.000 ± 0.118	0.45
110.0 - 120.0	2.00 - 4.50	235.0 ± 34.9	1.000 ± 0.148	0.24

Table B.7: Fit results for templates: Z, scaled; MinBias; HF-Vertex

$M_{\mu\mu}$ [GeV/c^2]	y	signal yield	ρ	χ^2/ndof
10.5 - 11.0	2.00 - 4.50	$15\,205.6 \pm 667.6$	0.122 ± 0.005	1.95
11.0 - 11.5	2.00 - 4.50	$13\,659.0 \pm 580.9$	0.134 ± 0.006	1.69
11.5 - 12.0	2.00 - 4.50	$12\,579.0 \pm 496.4$	0.148 ± 0.006	2.04
12.0 - 13.0	2.00 - 4.50	$22\,900.1 \pm 593.9$	0.178 ± 0.005	2.34
13.0 - 14.0	2.00 - 4.50	$18\,952.1 \pm 492.4$	0.209 ± 0.005	1.06
14.0 - 15.0	2.00 - 4.50	$15\,946.5 \pm 380.1$	0.250 ± 0.006	0.71
15.0 - 17.5	2.00 - 4.50	$28\,914.6 \pm 475.8$	0.305 ± 0.005	1.08
17.5 - 20.0	2.00 - 4.50	$18\,533.6 \pm 312.5$	0.396 ± 0.007	1.05
20.0 - 25.0	2.00 - 4.50	$21\,200.7 \pm 292.3$	0.515 ± 0.007	1.50
25.0 - 30.0	2.00 - 4.50	n/a	n/a	n/a
30.0 - 40.0	2.00 - 4.50	9081.7 ± 135.0	0.744 ± 0.011	2.42
40.0 - 60.0	2.00 - 4.50	5900.7 ± 98.0	0.897 ± 0.015	1.03
60.0 - 70.0	2.00 - 4.50	1525.8 ± 43.5	0.944 ± 0.027	0.53
70.0 - 80.0	2.00 - 4.50	n/a	n/a	n/a
80.0 - 90.0	2.00 - 4.50	6512.0 ± 119.9	1.000 ± 0.018	0.50
90.0 - 100.0	2.00 - 4.50	n/a	n/a	n/a
100.0 - 110.0	2.00 - 4.50	843.0 ± 35.8	1.000 ± 0.042	0.45
110.0 - 120.0	2.00 - 4.50	235.0 ± 16.2	1.000 ± 0.069	0.24

Table B.8: Fit results for templates: Z, scaled; MinBias; HF-IP

$M_{\mu\mu}$ [GeV/c^2]	y	signal yield	ρ	χ^2/ndof
10.5 - 11.0	2.00 - 4.50	6834.5 ± 783.9	0.055 ± 0.006	7.63
11.0 - 11.5	2.00 - 4.50	6469.2 ± 653.5	0.064 ± 0.006	5.44
11.5 - 12.0	2.00 - 4.50	7225.3 ± 591.5	0.085 ± 0.007	3.90
12.0 - 13.0	2.00 - 4.50	$15\,268.1 \pm 678.7$	0.119 ± 0.005	5.35
13.0 - 14.0	2.00 - 4.50	$13\,861.9 \pm 543.1$	0.153 ± 0.006	3.44
14.0 - 15.0	2.00 - 4.50	$12\,976.3 \pm 406.5$	0.203 ± 0.006	1.70
15.0 - 17.5	2.00 - 4.50	$25\,447.1 \pm 507.5$	0.269 ± 0.005	2.24
17.5 - 20.0	2.00 - 4.50	$16\,636.3 \pm 347.2$	0.356 ± 0.007	1.29
20.0 - 25.0	2.00 - 4.50	$18\,972.1 \pm 324.0$	0.461 ± 0.008	1.63
25.0 - 30.0	2.00 - 4.50	9632.7 ± 159.6	0.599 ± 0.010	1.07
30.0 - 40.0	2.00 - 4.50	8816.0 ± 137.8	0.722 ± 0.011	2.35
40.0 - 60.0	2.00 - 4.50	5854.1 ± 94.2	0.890 ± 0.014	1.01
60.0 - 70.0	2.00 - 4.50	1525.7 ± 44.9	0.944 ± 0.028	0.53
70.0 - 80.0	2.00 - 4.50	n/a	n/a	n/a
80.0 - 90.0	2.00 - 4.50	6511.6 ± 53.7	1.000 ± 0.008	0.50
90.0 - 100.0	2.00 - 4.50	n/a	n/a	n/a
100.0 - 110.0	2.00 - 4.50	843.0 ± 37.9	1.000 ± 0.045	0.45
110.0 - 120.0	2.00 - 4.50	235.0 ± 16.3	1.000 ± 0.069	0.24

Table B.9: Fit results for templates: Z, unscaled; SameSign; HF-Vertex

$M_{\mu\mu}$ [GeV/c^2]	y	signal yield	ρ	χ^2/ndof
10.5 - 11.0	2.00 - 4.50	$18\,765.7 \pm 756.6$	0.151 ± 0.006	1.02
11.0 - 11.5	2.00 - 4.50	$16\,633.8 \pm 626.1$	0.163 ± 0.006	0.99
11.5 - 12.0	2.00 - 4.50	$15\,018.8 \pm 554.0$	0.177 ± 0.007	1.48
12.0 - 13.0	2.00 - 4.50	$26\,621.4 \pm 672.6$	0.207 ± 0.005	1.53
13.0 - 14.0	2.00 - 4.50	$20\,768.1 \pm 575.3$	0.229 ± 0.006	1.49
14.0 - 15.0	2.00 - 4.50	$17\,087.8 \pm 447.5$	0.267 ± 0.007	1.23
15.0 - 17.5	2.00 - 4.50	$31\,460.4 \pm 539.7$	0.332 ± 0.006	1.39
17.5 - 20.0	2.00 - 4.50	$19\,574.5 \pm 347.9$	0.418 ± 0.007	1.59
20.0 - 25.0	2.00 - 4.50	$21\,667.3 \pm 298.8$	0.526 ± 0.007	2.00
25.0 - 30.0	2.00 - 4.50	$10\,555.1 \pm 159.2$	0.656 ± 0.010	1.19
30.0 - 40.0	2.00 - 4.50	9423.4 ± 139.5	0.772 ± 0.011	1.83
40.0 - 60.0	2.00 - 4.50	6007.1 ± 92.8	0.913 ± 0.014	0.79
60.0 - 70.0	2.00 - 4.50	1544.0 ± 40.9	0.955 ± 0.025	0.64
70.0 - 80.0	2.00 - 4.50	n/a	n/a	n/a
80.0 - 90.0	2.00 - 4.50	6512.0 ± 229.1	1.000 ± 0.035	0.50
90.0 - 100.0	2.00 - 4.50	$10\,887.7 \pm 133.2$	0.994 ± 0.012	0.32
100.0 - 110.0	2.00 - 4.50	843.0 ± 55.5	1.000 ± 0.066	0.45
110.0 - 120.0	2.00 - 4.50	235.0 ± 34.8	1.000 ± 0.148	0.24

Table B.10: Fit results for templates: Z, unscaled; SameSign; HF-IP

$M_{\mu\mu}$ [GeV/c^2]	y	signal yield	ρ	χ^2/ndof
10.5 - 11.0	2.00 - 4.50	$14\,287.4 \pm 738.7$	0.115 ± 0.006	1.63
11.0 - 11.5	2.00 - 4.50	$12\,612.0 \pm 723.0$	0.124 ± 0.007	1.56
11.5 - 12.0	2.00 - 4.50	$11\,726.5 \pm 599.9$	0.138 ± 0.007	1.15
12.0 - 13.0	2.00 - 4.50	$21\,590.9 \pm 699.4$	0.168 ± 0.005	1.41
13.0 - 14.0	2.00 - 4.50	$17\,903.7 \pm 564.1$	0.198 ± 0.006	1.20
14.0 - 15.0	2.00 - 4.50	$15\,130.1 \pm 477.6$	0.237 ± 0.007	1.11
15.0 - 17.5	2.00 - 4.50	$29\,175.9 \pm 603.5$	0.308 ± 0.006	1.32
17.5 - 20.0	2.00 - 4.50	$18\,100.3 \pm 392.5$	0.387 ± 0.008	1.57
20.0 - 25.0	2.00 - 4.50	$19\,640.2 \pm 435.0$	0.477 ± 0.011	2.25
25.0 - 30.0	2.00 - 4.50	$10\,181.3 \pm 176.8$	0.633 ± 0.011	0.94
30.0 - 40.0	2.00 - 4.50	9328.8 ± 148.6	0.764 ± 0.012	1.79
40.0 - 60.0	2.00 - 4.50	6007.2 ± 97.5	0.913 ± 0.015	0.79
60.0 - 70.0	2.00 - 4.50	1544.0 ± 43.3	0.955 ± 0.027	0.64
70.0 - 80.0	2.00 - 4.50	2235.6 ± 51.0	0.990 ± 0.023	0.53
80.0 - 90.0	2.00 - 4.50	6512.0 ± 260.1	1.000 ± 0.040	0.50
90.0 - 100.0	2.00 - 4.50	$10\,887.0 \pm 141.9$	0.994 ± 0.013	0.32
100.0 - 110.0	2.00 - 4.50	843.0 ± 99.7	1.000 ± 0.118	0.45
110.0 - 120.0	2.00 - 4.50	235.0 ± 34.9	1.000 ± 0.148	0.24

Table B.11: Fit results for templates: Z, unscaled; MinBias; HF-Vertex

$M_{\mu\mu}$ [GeV/c^2]	y	signal yield	ρ	χ^2/ndof
10.5 - 11.0	2.00 - 4.50	$16\,217.0 \pm 717.3$	0.130 ± 0.006	2.36
11.0 - 11.5	2.00 - 4.50	$14\,604.8 \pm 460.5$	0.143 ± 0.005	1.89
11.5 - 12.0	2.00 - 4.50	$13\,281.9 \pm 544.7$	0.156 ± 0.006	2.42
12.0 - 13.0	2.00 - 4.50	$24\,225.9 \pm 649.9$	0.189 ± 0.005	2.92
13.0 - 14.0	2.00 - 4.50	$19\,871.7 \pm 529.2$	0.220 ± 0.006	1.76
14.0 - 15.0	2.00 - 4.50	$16\,665.7 \pm 404.0$	0.261 ± 0.006	1.25
15.0 - 17.5	2.00 - 4.50	$30\,138.7 \pm 505.3$	0.318 ± 0.005	1.97
17.5 - 20.0	2.00 - 4.50	$19\,119.2 \pm 326.3$	0.409 ± 0.007	1.57
20.0 - 25.0	2.00 - 4.50	$21\,667.2 \pm 297.3$	0.526 ± 0.007	2.00
25.0 - 30.0	2.00 - 4.50	$10\,367.9 \pm 264.6$	0.645 ± 0.016	1.53
30.0 - 40.0	2.00 - 4.50	9133.0 ± 135.9	0.748 ± 0.011	2.60
40.0 - 60.0	2.00 - 4.50	5908.0 ± 98.1	0.898 ± 0.015	1.08
60.0 - 70.0	2.00 - 4.50	1526.2 ± 40.0	0.944 ± 0.025	0.53
70.0 - 80.0	2.00 - 4.50	2238.7 ± 51.2	0.992 ± 0.023	0.53
80.0 - 90.0	2.00 - 4.50	6512.0 ± 110.3	1.000 ± 0.017	0.50
90.0 - 100.0	2.00 - 4.50	n/a	n/a	n/a
100.0 - 110.0	2.00 - 4.50	843.0 ± 35.8	1.000 ± 0.042	0.45
110.0 - 120.0	2.00 - 4.50	235.0 ± 16.2	1.000 ± 0.069	0.24

Table B.12: Fit results for templates: Z, unscaled; MinBias; HF-IP

$M_{\mu\mu}$ [GeV/c^2]	y	signal yield	ρ	χ^2/ndof
10.5 - 11.0	2.00 - 4.50	7225.3 ± 861.9	0.058 ± 0.007	7.77
11.0 - 11.5	2.00 - 4.50	6813.1 ± 728.5	0.067 ± 0.007	5.59
11.5 - 12.0	2.00 - 4.50	7582.1 ± 637.9	0.089 ± 0.008	4.10
12.0 - 13.0	2.00 - 4.50	$16\,200.5 \pm 716.9$	0.126 ± 0.006	5.67
13.0 - 14.0	2.00 - 4.50	$14\,458.6 \pm 526.5$	0.160 ± 0.006	3.96
14.0 - 15.0	2.00 - 4.50	$13\,531.4 \pm 448.2$	0.212 ± 0.007	2.16
15.0 - 17.5	2.00 - 4.50	$26\,481.4 \pm 535.2$	0.280 ± 0.006	3.00
17.5 - 20.0	2.00 - 4.50	$17\,128.6 \pm 362.7$	0.366 ± 0.008	1.78
20.0 - 25.0	2.00 - 4.50	$19\,399.2 \pm 321.9$	0.471 ± 0.008	2.07
25.0 - 30.0	2.00 - 4.50	9755.5 ± 160.7	0.607 ± 0.010	1.34
30.0 - 40.0	2.00 - 4.50	8866.1 ± 138.7	0.726 ± 0.011	2.50
40.0 - 60.0	2.00 - 4.50	5862.2 ± 100.1	0.891 ± 0.015	1.06
60.0 - 70.0	2.00 - 4.50	1526.2 ± 42.1	0.944 ± 0.026	0.53
70.0 - 80.0	2.00 - 4.50	n/a	n/a	n/a
80.0 - 90.0	2.00 - 4.50	6512.0 ± 102.5	1.000 ± 0.016	0.50
90.0 - 100.0	2.00 - 4.50	n/a	n/a	n/a
100.0 - 110.0	2.00 - 4.50	843.0 ± 37.9	1.000 ± 0.045	0.45
110.0 - 120.0	2.00 - 4.50	235.0 ± 16.3	1.000 ± 0.069	0.24

Table B.13: Fit results for templates: Drell-Yan, simulation; SameSign; HF-Vertex

$M_{\mu\mu}$ [GeV/c^2]	y	signal yield	ρ	χ^2/ndof
10.5 - 11.0	2.00 - 4.50	$21\,513.7 \pm 842.2$	0.173 ± 0.007	2.46
11.0 - 11.5	2.00 - 4.50	$20\,568.6 \pm 860.3$	0.202 ± 0.008	2.59
11.5 - 12.0	2.00 - 4.50	$18\,986.5 \pm 674.9$	0.223 ± 0.008	2.41
12.0 - 13.0	2.00 - 4.50	$31\,384.3 \pm 784.0$	0.244 ± 0.006	4.07
13.0 - 14.0	2.00 - 4.50	$25\,583.1 \pm 654.7$	0.283 ± 0.007	3.42
14.0 - 15.0	2.00 - 4.50	$21\,376.4 \pm 518.6$	0.334 ± 0.008	3.13
15.0 - 17.5	2.00 - 4.50	$36\,436.4 \pm 563.9$	0.385 ± 0.006	8.60
17.5 - 20.0	2.00 - 4.50	$22\,381.9 \pm 360.0$	0.478 ± 0.008	4.10
20.0 - 25.0	2.00 - 4.50	$23\,693.6 \pm 329.7$	0.575 ± 0.008	7.25
25.0 - 30.0	2.00 - 4.50	$11\,600.2 \pm 231.3$	0.721 ± 0.014	5.21
30.0 - 40.0	2.00 - 4.50	9955.5 ± 164.4	0.816 ± 0.013	6.20
40.0 - 60.0	2.00 - 4.50	6241.3 ± 121.7	0.949 ± 0.018	4.94
60.0 - 70.0	2.00 - 4.50	1579.6 ± 50.4	0.977 ± 0.031	1.05
70.0 - 80.0	2.00 - 4.50	2257.0 ± 62.6	1.000 ± 0.028	2.37
80.0 - 90.0	2.00 - 4.50	$13\,144.0 \pm 215.0$	1.000 ± 0.016	13.37
90.0 - 100.0	2.00 - 4.50	$21\,815.0 \pm 234.5$	1.000 ± 0.011	21.32
100.0 - 110.0	2.00 - 4.50	842.7 ± 86.8	1.000 ± 0.103	2.22
110.0 - 120.0	2.00 - 4.50	n/a	n/a	n/a

Table B.14: Fit results for templates: Drell-Yan, simulation; SameSign; HF-IP

$M_{\mu\mu}$ [GeV/c^2]	y	signal yield	ρ	χ^2/ndof
10.5 - 11.0	2.00 - 4.50	15 074.7 ± 1044.3	0.121 ± 0.008	3.75
11.0 - 11.5	2.00 - 4.50	14 860.1 ± 953.4	0.146 ± 0.009	3.34
11.5 - 12.0	2.00 - 4.50	14 884.0 ± 742.2	0.175 ± 0.009	1.93
12.0 - 13.0	2.00 - 4.50	25 249.7 ± 873.5	0.197 ± 0.007	4.30
13.0 - 14.0	2.00 - 4.50	22 131.8 ± 714.0	0.245 ± 0.008	3.13
14.0 - 15.0	2.00 - 4.50	18 888.6 ± 572.7	0.296 ± 0.009	3.19
15.0 - 17.5	2.00 - 4.50	33 586.0 ± 661.9	0.355 ± 0.007	7.33
17.5 - 20.0	2.00 - 4.50	20 648.1 ± 434.5	0.441 ± 0.009	3.30
20.0 - 25.0	2.00 - 4.50	20 429.0 ± 397.4	0.496 ± 0.010	4.79
25.0 - 30.0	2.00 - 4.50	11 138.7 ± 222.8	0.693 ± 0.014	4.81
30.0 - 40.0	2.00 - 4.50	9955.7 ± 176.7	0.816 ± 0.014	6.20
40.0 - 60.0	2.00 - 4.50	6242.0 ± 129.0	0.949 ± 0.020	4.94
60.0 - 70.0	2.00 - 4.50	1579.6 ± 50.4	0.977 ± 0.031	1.05
70.0 - 80.0	2.00 - 4.50	2257.0 ± 268.7	1.000 ± 0.119	2.37
80.0 - 90.0	2.00 - 4.50	13 144.0 ± 119.5	1.000 ± 0.009	13.37
90.0 - 100.0	2.00 - 4.50	21 814.9 ± 171.1	1.000 ± 0.008	21.32
100.0 - 110.0	2.00 - 4.50	842.9 ± 131.6	1.000 ± 0.156	2.22
110.0 - 120.0	2.00 - 4.50	230.4 ± 17.8	0.980 ± 0.076	0.67

Table B.15: Fit results for templates: Drell-Yan, simulation; MinBias; HF-Vertex

$M_{\mu\mu}$ [GeV/c^2]	y	signal yield	ρ	χ^2/ndof
10.5 - 11.0	2.00 - 4.50	16 996.5 ± 906.7	0.136 ± 0.007	4.26
11.0 - 11.5	2.00 - 4.50	16 301.9 ± 783.2	0.160 ± 0.008	3.96
11.5 - 12.0	2.00 - 4.50	15 169.1 ± 662.3	0.178 ± 0.008	4.10
12.0 - 13.0	2.00 - 4.50	26 607.5 ± 732.9	0.207 ± 0.006	6.52
13.0 - 14.0	2.00 - 4.50	22 988.5 ± 615.1	0.254 ± 0.007	4.37
14.0 - 15.0	2.00 - 4.50	19 652.6 ± 482.8	0.307 ± 0.008	3.77
15.0 - 17.5	2.00 - 4.50	33 241.9 ± 551.1	0.351 ± 0.006	10.44
17.5 - 20.0	2.00 - 4.50	21 233.8 ± 362.1	0.454 ± 0.008	4.92
20.0 - 25.0	2.00 - 4.50	23 354.4 ± 315.1	0.567 ± 0.008	7.38
25.0 - 30.0	2.00 - 4.50	11 025.6 ± 187.9	0.686 ± 0.012	6.68
30.0 - 40.0	2.00 - 4.50	n/a	n/a	n/a
40.0 - 60.0	2.00 - 4.50	6191.8 ± 118.8	0.941 ± 0.018	4.74
60.0 - 70.0	2.00 - 4.50	1550.7 ± 49.5	0.960 ± 0.031	0.95
70.0 - 80.0	2.00 - 4.50	2257.0 ± 50.7	1.000 ± 0.022	2.37
80.0 - 90.0	2.00 - 4.50	13 144.0 ± 130.3	1.000 ± 0.010	13.37
90.0 - 100.0	2.00 - 4.50	21 815.0 ± 83.4	1.000 ± 0.004	21.32
100.0 - 110.0	2.00 - 4.50	843.0 ± 43.5	1.000 ± 0.052	2.22
110.0 - 120.0	2.00 - 4.50	n/a	n/a	n/a

Table B.16: Fit results for templates: Drell-Yan, simulation; MinBias; HF-IP

$M_{\mu\mu}$ [GeV/c^2]	y	signal yield	ρ	χ^2/ndof
10.5 - 11.0	2.00 - 4.50	3824.2 ± 1134.2	0.031 ± 0.009	8.96
11.0 - 11.5	2.00 - 4.50	4669.1 ± 952.5	0.046 ± 0.009	6.77
11.5 - 12.0	2.00 - 4.50	7563.5 ± 793.8	0.089 ± 0.009	5.16
12.0 - 13.0	2.00 - 4.50	15 949.0 ± 774.7	0.124 ± 0.006	8.82
13.0 - 14.0	2.00 - 4.50	15 794.7 ± 720.4	0.175 ± 0.008	6.66
14.0 - 15.0	2.00 - 4.50	15 420.1 ± 569.3	0.241 ± 0.009	4.95
15.0 - 17.5	2.00 - 4.50	28 529.7 ± 586.3	0.301 ± 0.006	9.95
17.5 - 20.0	2.00 - 4.50	18 825.6 ± 408.1	0.402 ± 0.009	4.04
20.0 - 25.0	2.00 - 4.50	n/a	n/a	n/a
25.0 - 30.0	2.00 - 4.50	10 391.5 ± 192.8	0.646 ± 0.012	5.67
30.0 - 40.0	2.00 - 4.50	n/a	n/a	n/a
40.0 - 60.0	2.00 - 4.50	6191.6 ± 127.8	0.941 ± 0.019	4.74
60.0 - 70.0	2.00 - 4.50	1550.5 ± 51.8	0.959 ± 0.032	0.95
70.0 - 80.0	2.00 - 4.50	2257.0 ± 45.8	1.000 ± 0.020	2.37
80.0 - 90.0	2.00 - 4.50	13 144.0 ± 147.3	1.000 ± 0.011	13.37
90.0 - 100.0	2.00 - 4.50	21 814.8 ± 59.0	1.000 ± 0.003	21.32
100.0 - 110.0	2.00 - 4.50	843.0 ± 25.6	1.000 ± 0.030	2.22
110.0 - 120.0	2.00 - 4.50	230.3 ± 14.6	0.980 ± 0.062	0.67

B.2.2 Signal Yield as a Function of Rapidity

Table B.17: Fitresults for templates: Υ; SameSign; HF-Vertex

$M_{\mu\mu}$ [GeV/c^2]	y	signal yield	ρ	χ^2/ndof
10.5 - 12.0	2.00 - 2.25	1369.2 ± 184.7	0.119 ± 0.016	0.24
10.5 - 12.0	2.25 - 2.50	4962.3 ± 336.5	0.154 ± 0.010	0.81
10.5 - 12.0	2.50 - 2.75	6617.8 ± 427.4	0.140 ± 0.009	0.80
10.5 - 12.0	2.75 - 3.00	7503.5 ± 600.8	0.127 ± 0.010	0.61
10.5 - 12.0	3.00 - 3.25	9241.7 ± 943.6	0.143 ± 0.015	0.75
10.5 - 12.0	3.25 - 3.50	9349.2 ± 629.4	0.189 ± 0.013	0.62
10.5 - 12.0	3.50 - 3.75	7962.5 ± 476.7	0.302 ± 0.018	0.84
10.5 - 12.0	3.75 - 4.00	5941.2 ± 339.2	0.441 ± 0.025	0.77
10.5 - 12.0	4.00 - 4.50	4435.5 ± 281.1	0.608 ± 0.039	0.46
12.0 - 15.0	2.00 - 2.25	1944.7 ± 161.5	0.197 ± 0.016	0.36
12.0 - 15.0	2.25 - 2.50	5654.5 ± 298.8	0.206 ± 0.011	0.55
12.0 - 15.0	2.50 - 2.75	8071.4 ± 365.3	0.197 ± 0.009	0.41
12.0 - 15.0	2.75 - 3.00	10 231.2 ± 510.9	0.195 ± 0.010	1.00
12.0 - 15.0	3.00 - 3.25	11 828.4 ± 640.0	0.202 ± 0.011	1.42
12.0 - 15.0	3.25 - 3.50	11 698.6 ± 607.3	0.250 ± 0.013	0.90
12.0 - 15.0	3.50 - 3.75	9782.5 ± 447.9	0.373 ± 0.017	0.72
12.0 - 15.0	3.75 - 4.00	7088.8 ± 346.1	0.533 ± 0.026	0.69
12.0 - 15.0	4.00 - 4.50	4988.6 ± 283.9	0.687 ± 0.039	0.53
15.0 - 20.0	2.00 - 2.25	1333.2 ± 109.4	0.284 ± 0.023	0.44
15.0 - 20.0	2.25 - 2.50	4096.4 ± 181.2	0.312 ± 0.014	0.68
15.0 - 20.0	2.50 - 2.75	6131.6 ± 238.7	0.307 ± 0.012	0.45
15.0 - 20.0	2.75 - 3.00	8673.4 ± 312.7	0.334 ± 0.012	0.91
15.0 - 20.0	3.00 - 3.25	9102.3 ± 371.1	0.333 ± 0.014	1.08
15.0 - 20.0	3.25 - 3.50	8855.0 ± 387.0	0.385 ± 0.017	0.78
15.0 - 20.0	3.50 - 3.75	7352.8 ± 309.1	0.491 ± 0.021	0.67
15.0 - 20.0	3.75 - 4.00	5208.6 ± 223.6	0.663 ± 0.028	0.76
15.0 - 20.0	4.00 - 4.50	3797.2 ± 193.5	0.845 ± 0.043	0.34
20.0 - 60.0	2.00 - 2.25	1227.5 ± 74.6	0.514 ± 0.031	0.59
20.0 - 60.0	2.25 - 2.50	3934.5 ± 145.1	0.572 ± 0.021	0.43
20.0 - 60.0	2.50 - 2.75	5767.6 ± 187.4	0.556 ± 0.018	0.32
20.0 - 60.0	2.75 - 3.00	7636.1 ± 226.9	0.577 ± 0.017	0.97
20.0 - 60.0	3.00 - 3.25	8490.8 ± 263.0	0.619 ± 0.019	0.67
20.0 - 60.0	3.25 - 3.50	8129.8 ± 258.6	0.673 ± 0.021	1.00
20.0 - 60.0	3.50 - 3.75	6748.8 ± 218.2	0.745 ± 0.024	0.81
20.0 - 60.0	3.75 - 4.00	4488.7 ± 163.7	0.846 ± 0.031	0.62
20.0 - 60.0	4.00 - 4.50	2769.0 ± 134.4	0.917 ± 0.045	0.56

Table B.18: Fitresults for templates: Υ; SameSign; HF-IP

$M_{\mu\mu}$ [GeV/c^2]	y	signal yield	ρ	χ^2/ndof
10.5 - 12.0	2.00 - 2.25	1093.2 ± 198.1	0.095 ± 0.017	0.22
10.5 - 12.0	2.25 - 2.50	3960.3 ± 358.7	0.123 ± 0.011	0.78
10.5 - 12.0	2.50 - 2.75	5601.0 ± 429.4	0.118 ± 0.009	0.81
10.5 - 12.0	2.75 - 3.00	4689.8 ± 658.9	0.079 ± 0.011	1.54
10.5 - 12.0	3.00 - 3.25	4482.9 ± 862.1	0.069 ± 0.013	1.01
10.5 - 12.0	3.25 - 3.50	5755.5 ± 707.7	0.116 ± 0.014	1.21
10.5 - 12.0	3.50 - 3.75	6487.5 ± 466.8	0.246 ± 0.018	1.04
10.5 - 12.0	3.75 - 4.00	5427.0 ± 336.5	0.403 ± 0.025	0.79
10.5 - 12.0	4.00 - 4.50	4248.5 ± 281.9	0.583 ± 0.039	0.39
12.0 - 15.0	2.00 - 2.25	1636.3 ± 165.8	0.165 ± 0.017	0.39
12.0 - 15.0	2.25 - 2.50	5432.8 ± 301.9	0.198 ± 0.011	0.33
12.0 - 15.0	2.50 - 2.75	7381.0 ± 368.9	0.180 ± 0.009	0.80
12.0 - 15.0	2.75 - 3.00	8360.6 ± 568.1	0.160 ± 0.011	0.97
12.0 - 15.0	3.00 - 3.25	7822.5 ± 702.4	0.134 ± 0.012	1.17
12.0 - 15.0	3.25 - 3.50	9297.3 ± 612.4	0.198 ± 0.013	0.78
12.0 - 15.0	3.50 - 3.75	8130.5 ± 494.6	0.310 ± 0.019	1.13
12.0 - 15.0	3.75 - 4.00	6817.1 ± 359.2	0.512 ± 0.027	0.83
12.0 - 15.0	4.00 - 4.50	4481.6 ± 270.0	0.617 ± 0.037	0.56
15.0 - 20.0	2.00 - 2.25	1237.6 ± 140.3	0.264 ± 0.030	0.60
15.0 - 20.0	2.25 - 2.50	4087.3 ± 181.9	0.311 ± 0.014	0.65
15.0 - 20.0	2.50 - 2.75	5978.5 ± 239.9	0.299 ± 0.012	0.26
15.0 - 20.0	2.75 - 3.00	7876.7 ± 324.8	0.303 ± 0.013	0.78
15.0 - 20.0	3.00 - 3.25	7808.1 ± 403.9	0.286 ± 0.015	1.01
15.0 - 20.0	3.25 - 3.50	8299.8 ± 396.1	0.361 ± 0.017	0.68
15.0 - 20.0	3.50 - 3.75	6976.3 ± 334.2	0.465 ± 0.022	0.80
15.0 - 20.0	3.75 - 4.00	4982.6 ± 241.5	0.634 ± 0.031	0.61
15.0 - 20.0	4.00 - 4.50	3798.8 ± 215.2	0.845 ± 0.048	0.37
20.0 - 60.0	2.00 - 2.25	1172.8 ± 80.4	0.491 ± 0.034	0.35
20.0 - 60.0	2.25 - 2.50	3765.5 ± 155.2	0.547 ± 0.023	0.36
20.0 - 60.0	2.50 - 2.75	5697.3 ± 198.2	0.549 ± 0.019	0.42
20.0 - 60.0	2.75 - 3.00	7418.7 ± 233.6	0.561 ± 0.018	0.75
20.0 - 60.0	3.00 - 3.25	7804.9 ± 310.6	0.569 ± 0.023	0.70
20.0 - 60.0	3.25 - 3.50	7640.5 ± 408.1	0.633 ± 0.034	0.82
20.0 - 60.0	3.50 - 3.75	6437.3 ± 243.8	0.711 ± 0.027	0.68
20.0 - 60.0	3.75 - 4.00	3548.7 ± 273.8	0.669 ± 0.052	0.66
20.0 - 60.0	4.00 - 4.50	2472.8 ± 185.7	0.819 ± 0.062	0.45

Table B.19: Fitresults for templates: Υ; MinBias; HF-Vertex

$M_{\mu\mu}$ [GeV/c^2]	y	signal yield	ρ	χ^2/ndof
10.5 - 12.0	2.00 - 2.25	915.6 ± 196.9	0.080 ± 0.017	0.73
10.5 - 12.0	2.25 - 2.50	3746.8 ± 336.1	0.117 ± 0.010	1.85
10.5 - 12.0	2.50 - 2.75	5012.2 ± 415.2	0.106 ± 0.009	2.02
10.5 - 12.0	2.75 - 3.00	5505.9 ± 566.2	0.093 ± 0.010	1.39
10.5 - 12.0	3.00 - 3.25	7589.8 ± 707.1	0.118 ± 0.011	1.27
10.5 - 12.0	3.25 - 3.50	8188.1 ± 601.2	0.166 ± 0.012	1.01
10.5 - 12.0	3.50 - 3.75	7566.1 ± 410.8	0.287 ± 0.016	1.01
10.5 - 12.0	3.75 - 4.00	5852.8 ± 335.2	0.434 ± 0.025	0.80
10.5 - 12.0	4.00 - 4.50	4406.2 ± 274.4	0.604 ± 0.038	0.53
12.0 - 15.0	2.00 - 2.25	1754.8 ± 158.2	0.177 ± 0.016	0.61
12.0 - 15.0	2.25 - 2.50	4918.1 ± 288.7	0.180 ± 0.011	1.00
12.0 - 15.0	2.50 - 2.75	7393.2 ± 340.6	0.180 ± 0.008	0.77
12.0 - 15.0	2.75 - 3.00	8686.6 ± 453.7	0.166 ± 0.009	1.92
12.0 - 15.0	3.00 - 3.25	10 453.5 ± 565.9	0.179 ± 0.010	1.84
12.0 - 15.0	3.25 - 3.50	10 764.8 ± 568.2	0.230 ± 0.012	1.22
12.0 - 15.0	3.50 - 3.75	9402.4 ± 418.6	0.359 ± 0.016	0.88
12.0 - 15.0	3.75 - 4.00	6933.7 ± 334.3	0.521 ± 0.025	0.77
12.0 - 15.0	4.00 - 4.50	4968.3 ± 265.7	0.684 ± 0.037	0.53
15.0 - 20.0	2.00 - 2.25	1235.9 ± 105.4	0.263 ± 0.022	0.52
15.0 - 20.0	2.25 - 2.50	3884.4 ± 176.7	0.296 ± 0.013	0.89
15.0 - 20.0	2.50 - 2.75	5857.4 ± 228.6	0.293 ± 0.011	0.68
15.0 - 20.0	2.75 - 3.00	7915.8 ± 292.8	0.305 ± 0.011	1.43
15.0 - 20.0	3.00 - 3.25	8370.7 ± 338.9	0.306 ± 0.012	1.47
15.0 - 20.0	3.25 - 3.50	8294.0 ± 351.7	0.360 ± 0.015	0.98
15.0 - 20.0	3.50 - 3.75	7089.7 ± 296.5	0.473 ± 0.020	0.70
15.0 - 20.0	3.75 - 4.00	5096.8 ± 219.7	0.649 ± 0.028	0.88
15.0 - 20.0	4.00 - 4.50	3628.2 ± 181.6	0.807 ± 0.040	0.49
20.0 - 60.0	2.00 - 2.25	1212.4 ± 76.7	0.508 ± 0.032	0.69
20.0 - 60.0	2.25 - 2.50	3856.1 ± 144.8	0.560 ± 0.021	0.52
20.0 - 60.0	2.50 - 2.75	5618.4 ± 182.5	0.542 ± 0.018	0.43
20.0 - 60.0	2.75 - 3.00	7510.2 ± 225.2	0.568 ± 0.017	1.07
20.0 - 60.0	3.00 - 3.25	8212.0 ± 264.4	0.599 ± 0.019	0.81
20.0 - 60.0	3.25 - 3.50	8130.6 ± 258.1	0.673 ± 0.021	1.00
20.0 - 60.0	3.50 - 3.75	6445.8 ± 223.3	0.711 ± 0.025	1.11
20.0 - 60.0	3.75 - 4.00	n/a	n/a	n/a
20.0 - 60.0	4.00 - 4.50	2667.4 ± 141.6	0.884 ± 0.047	0.65

Table B.20: Fitresults for templates: Υ; MinBias; HF-IP

$M_{\mu\mu}$ [GeV/c^2]	y	signal yield	ρ	χ^2/ndof
10.5 - 12.0	2.00 - 2.25	200.7 ± 214.1	0.017 ± 0.019	1.21
10.5 - 12.0	2.25 - 2.50	1137.5 ± 468.5	0.035 ± 0.015	3.37
10.5 - 12.0	2.50 - 2.75	2186.5 ± 531.2	0.046 ± 0.011	4.22
10.5 - 12.0	2.75 - 3.00	0.0 ± 1116.2	0.000 ± 0.019	3.11
10.5 - 12.0	3.00 - 3.25	0.1 ± 1774.7	0.000 ± 0.027	2.51
10.5 - 12.0	3.25 - 3.50	3318.0 ± 776.5	0.067 ± 0.016	2.16
10.5 - 12.0	3.50 - 3.75	5853.6 ± 411.5	0.222 ± 0.016	1.52
10.5 - 12.0	3.75 - 4.00	5301.0 ± 326.8	0.393 ± 0.024	0.87
10.5 - 12.0	4.00 - 4.50	4261.1 ± 278.5	0.584 ± 0.038	0.42
12.0 - 15.0	2.00 - 2.25	1172.3 ± 181.2	0.119 ± 0.018	1.02
12.0 - 15.0	2.25 - 2.50	4157.7 ± 293.8	0.152 ± 0.011	2.08
12.0 - 15.0	2.50 - 2.75	5831.1 ± 349.8	0.142 ± 0.009	2.60
12.0 - 15.0	2.75 - 3.00	5396.7 ± 525.1	0.103 ± 0.010	2.81
12.0 - 15.0	3.00 - 3.25	4588.5 ± 640.8	0.078 ± 0.011	2.61
12.0 - 15.0	3.25 - 3.50	7306.3 ± 565.7	0.156 ± 0.012	1.71
12.0 - 15.0	3.50 - 3.75	7395.2 ± 429.1	0.282 ± 0.016	1.55
12.0 - 15.0	3.75 - 4.00	6600.2 ± 336.0	0.496 ± 0.025	0.96
12.0 - 15.0	4.00 - 4.50	4481.8 ± 268.7	0.617 ± 0.037	0.56
15.0 - 20.0	2.00 - 2.25	1137.6 ± 114.5	0.242 ± 0.024	0.64
15.0 - 20.0	2.25 - 2.50	3803.2 ± 179.9	0.290 ± 0.014	0.92
15.0 - 20.0	2.50 - 2.75	5503.6 ± 229.2	0.276 ± 0.011	0.68
15.0 - 20.0	2.75 - 3.00	6758.8 ± 311.0	0.260 ± 0.012	1.71
15.0 - 20.0	3.00 - 3.25	6504.1 ± 345.0	0.238 ± 0.013	1.60
15.0 - 20.0	3.25 - 3.50	7169.8 ± 363.0	0.311 ± 0.016	1.33
15.0 - 20.0	3.50 - 3.75	6488.3 ± 296.6	0.433 ± 0.020	0.89
15.0 - 20.0	3.75 - 4.00	4727.1 ± 363.1	0.602 ± 0.046	0.68
15.0 - 20.0	4.00 - 4.50	3492.0 ± 187.7	0.777 ± 0.042	0.58
20.0 - 60.0	2.00 - 2.25	1121.0 ± 85.6	0.469 ± 0.036	0.40
20.0 - 60.0	2.25 - 2.50	3540.9 ± 151.2	0.515 ± 0.022	0.53
20.0 - 60.0	2.50 - 2.75	5349.2 ± 194.2	0.516 ± 0.019	0.58
20.0 - 60.0	2.75 - 3.00	7101.6 ± 228.2	0.537 ± 0.017	1.00
20.0 - 60.0	3.00 - 3.25	7527.4 ± 268.8	0.549 ± 0.020	0.73
20.0 - 60.0	3.25 - 3.50	n/a	n/a	n/a
20.0 - 60.0	3.50 - 3.75	6038.7 ± 232.9	0.667 ± 0.026	0.78
20.0 - 60.0	3.75 - 4.00	3549.3 ± 270.0	0.669 ± 0.051	0.66
20.0 - 60.0	4.00 - 4.50	2472.7 ± 184.8	0.819 ± 0.061	0.45

Table B.21: Fitresults for templates: Z, scaled; SameSign; HF-Vertex

$M_{\mu\mu}$ [GeV/c^2]	y	signal yield	ρ	χ^2/ndof
10.5 - 12.0	2.00 - 2.25	1350.8 ± 167.3	0.118 ± 0.015	0.19
10.5 - 12.0	2.25 - 2.50	4221.2 ± 263.7	0.131 ± 0.008	0.91
10.5 - 12.0	2.50 - 2.75	5863.2 ± 346.1	0.124 ± 0.007	0.93
10.5 - 12.0	2.75 - 3.00	5941.4 ± 463.7	0.100 ± 0.008	0.68
10.5 - 12.0	3.00 - 3.25	7112.3 ± 496.6	0.110 ± 0.008	0.57
10.5 - 12.0	3.25 - 3.50	6956.7 ± 458.1	0.141 ± 0.009	0.42
10.5 - 12.0	3.50 - 3.75	6235.5 ± 308.5	0.236 ± 0.012	0.52
10.5 - 12.0	3.75 - 4.00	n/a	n/a	n/a
10.5 - 12.0	4.00 - 4.50	4374.0 ± 756.5	0.600 ± 0.104	0.83
12.0 - 15.0	2.00 - 2.25	1902.5 ± 130.9	0.192 ± 0.013	0.37
12.0 - 15.0	2.25 - 2.50	4944.4 ± 222.7	0.181 ± 0.008	0.51
12.0 - 15.0	2.50 - 2.75	7359.6 ± 288.0	0.179 ± 0.007	0.81
12.0 - 15.0	2.75 - 3.00	8613.9 ± 375.7	0.164 ± 0.007	0.82
12.0 - 15.0	3.00 - 3.25	9524.5 ± 460.4	0.163 ± 0.008	0.91
12.0 - 15.0	3.25 - 3.50	9062.3 ± 419.7	0.193 ± 0.009	0.74
12.0 - 15.0	3.50 - 3.75	8057.4 ± 326.4	0.307 ± 0.012	0.52
12.0 - 15.0	3.75 - 4.00	5860.7 ± 337.9	0.440 ± 0.025	0.76
12.0 - 15.0	4.00 - 4.50	4827.1 ± 764.8	0.665 ± 0.105	0.76
15.0 - 20.0	2.00 - 2.25	1326.2 ± 89.6	0.282 ± 0.019	0.46
15.0 - 20.0	2.25 - 2.50	3816.7 ± 137.6	0.291 ± 0.010	0.50
15.0 - 20.0	2.50 - 2.75	5788.1 ± 185.4	0.290 ± 0.009	0.66
15.0 - 20.0	2.75 - 3.00	7617.5 ± 217.9	0.293 ± 0.008	0.65
15.0 - 20.0	3.00 - 3.25	7755.3 ± 264.1	0.284 ± 0.010	0.96
15.0 - 20.0	3.25 - 3.50	7318.3 ± 274.5	0.318 ± 0.012	0.36
15.0 - 20.0	3.50 - 3.75	6167.8 ± 226.0	0.412 ± 0.015	0.67
15.0 - 20.0	3.75 - 4.00	4576.6 ± 245.3	0.582 ± 0.031	0.79
15.0 - 20.0	4.00 - 4.50	3861.4 ± 563.1	0.859 ± 0.125	0.74
20.0 - 60.0	2.00 - 2.25	1279.7 ± 57.1	0.536 ± 0.024	0.74
20.0 - 60.0	2.25 - 2.50	3832.8 ± 109.0	0.557 ± 0.016	0.48
20.0 - 60.0	2.50 - 2.75	5737.0 ± 145.9	0.553 ± 0.014	0.42
20.0 - 60.0	2.75 - 3.00	7423.0 ± 164.2	0.561 ± 0.012	0.28
20.0 - 60.0	3.00 - 3.25	7928.5 ± 193.3	0.578 ± 0.014	0.44
20.0 - 60.0	3.25 - 3.50	7564.9 ± 178.0	0.627 ± 0.015	0.76
20.0 - 60.0	3.50 - 3.75	6227.1 ± 237.1	0.687 ± 0.026	0.82
20.0 - 60.0	3.75 - 4.00	3957.6 ± 202.2	0.746 ± 0.038	0.72
20.0 - 60.0	4.00 - 4.50	1958.8 ± 326.3	0.649 ± 0.108	1.04

Table B.22: Fitresults for templates: Z, scaled; SameSign; HF-IP

$M_{\mu\mu}$ [GeV/c^2]	y	signal yield	ρ	χ^2/ndof
10.5 - 12.0	2.00 - 2.25	1025.8 ± 185.9	0.089 ± 0.016	0.26
10.5 - 12.0	2.25 - 2.50	3300.1 ± 301.3	0.103 ± 0.009	0.85
10.5 - 12.0	2.50 - 2.75	4908.2 ± 354.6	0.104 ± 0.007	0.90
10.5 - 12.0	2.75 - 3.00	3914.0 ± 525.3	0.066 ± 0.009	1.29
10.5 - 12.0	3.00 - 3.25	3628.9 ± 605.6	0.056 ± 0.009	0.80
10.5 - 12.0	3.25 - 3.50	4240.4 ± 471.4	0.086 ± 0.010	1.02
10.5 - 12.0	3.50 - 3.75	5016.2 ± 315.9	0.190 ± 0.012	0.73
10.5 - 12.0	3.75 - 4.00	4120.9 ± 290.1	0.306 ± 0.022	0.79
10.5 - 12.0	4.00 - 4.50	3690.5 ± 694.5	0.506 ± 0.095	0.83
12.0 - 15.0	2.00 - 2.25	1595.8 ± 147.9	0.161 ± 0.015	0.45
12.0 - 15.0	2.25 - 2.50	4757.5 ± 228.5	0.174 ± 0.008	0.48
12.0 - 15.0	2.50 - 2.75	6759.5 ± 290.6	0.165 ± 0.007	0.95
12.0 - 15.0	2.75 - 3.00	6837.2 ± 401.8	0.130 ± 0.008	0.88
12.0 - 15.0	3.00 - 3.25	6403.3 ± 486.1	0.109 ± 0.008	0.72
12.0 - 15.0	3.25 - 3.50	7170.5 ± 446.1	0.153 ± 0.010	0.48
12.0 - 15.0	3.50 - 3.75	6571.6 ± 332.9	0.251 ± 0.013	0.74
12.0 - 15.0	3.75 - 4.00	5454.1 ± 326.5	0.410 ± 0.025	0.79
12.0 - 15.0	4.00 - 4.50	5240.8 ± 1131.3	0.722 ± 0.156	0.94
15.0 - 20.0	2.00 - 2.25	1265.9 ± 93.3	0.270 ± 0.020	0.46
15.0 - 20.0	2.25 - 2.50	3802.9 ± 138.5	0.290 ± 0.011	0.51
15.0 - 20.0	2.50 - 2.75	5612.3 ± 190.5	0.281 ± 0.010	0.54
15.0 - 20.0	2.75 - 3.00	6881.9 ± 239.9	0.265 ± 0.009	0.45
15.0 - 20.0	3.00 - 3.25	6429.1 ± 320.6	0.235 ± 0.012	0.95
15.0 - 20.0	3.25 - 3.50	6805.7 ± 289.2	0.296 ± 0.013	0.64
15.0 - 20.0	3.50 - 3.75	5732.7 ± 265.8	0.382 ± 0.018	0.92
15.0 - 20.0	3.75 - 4.00	4177.8 ± 243.9	0.532 ± 0.031	0.80
15.0 - 20.0	4.00 - 4.50	3665.9 ± 600.3	0.815 ± 0.134	0.74
20.0 - 60.0	2.00 - 2.25	1212.6 ± 65.7	0.508 ± 0.028	0.34
20.0 - 60.0	2.25 - 2.50	3600.8 ± 126.2	0.523 ± 0.018	0.46
20.0 - 60.0	2.50 - 2.75	5607.5 ± 163.5	0.541 ± 0.016	0.60
20.0 - 60.0	2.75 - 3.00	7198.0 ± 175.2	0.544 ± 0.013	0.30
20.0 - 60.0	3.00 - 3.25	n/a	n/a	n/a
20.0 - 60.0	3.25 - 3.50	6989.3 ± 202.6	0.579 ± 0.017	0.56
20.0 - 60.0	3.50 - 3.75	5913.8 ± 207.0	0.653 ± 0.023	0.58
20.0 - 60.0	3.75 - 4.00	3205.2 ± 277.2	0.604 ± 0.052	0.59
20.0 - 60.0	4.00 - 4.50	1977.9 ± 332.8	0.655 ± 0.110	0.82

Table B.23: Fitresults for templates: Z, scaled; MinBias; HF-Vertex

$M_{\mu\mu}$ [GeV/c^2]	y	signal yield	ρ	χ^2/ndof
10.5 - 12.0	2.00 - 2.25	949.9 ± 186.1	0.083 ± 0.016	0.67
10.5 - 12.0	2.25 - 2.50	3366.0 ± 291.7	0.105 ± 0.009	1.74
10.5 - 12.0	2.50 - 2.75	4536.5 ± 357.1	0.096 ± 0.008	2.01
10.5 - 12.0	2.75 - 3.00	4616.8 ± 491.0	0.078 ± 0.008	1.30
10.5 - 12.0	3.00 - 3.25	6194.0 ± 484.7	0.096 ± 0.008	0.97
10.5 - 12.0	3.25 - 3.50	6374.5 ± 445.6	0.129 ± 0.009	0.70
10.5 - 12.0	3.50 - 3.75	6083.0 ± 293.5	0.230 ± 0.011	0.59
10.5 - 12.0	3.75 - 4.00	n/a	n/a	n/a
10.5 - 12.0	4.00 - 4.50	4374.5 ± 754.4	0.600 ± 0.103	0.83
12.0 - 15.0	2.00 - 2.25	1745.2 ± 137.6	0.176 ± 0.014	0.58
12.0 - 15.0	2.25 - 2.50	4510.0 ± 228.3	0.165 ± 0.008	0.85
12.0 - 15.0	2.50 - 2.75	6867.4 ± 281.4	0.167 ± 0.007	1.06
12.0 - 15.0	2.75 - 3.00	7690.2 ± 353.1	0.147 ± 0.007	1.48
12.0 - 15.0	3.00 - 3.25	8890.7 ± 429.6	0.152 ± 0.007	1.13
12.0 - 15.0	3.25 - 3.50	8618.7 ± 407.5	0.184 ± 0.009	0.89
12.0 - 15.0	3.50 - 3.75	7940.2 ± 315.6	0.303 ± 0.012	0.56
12.0 - 15.0	3.75 - 4.00	n/a	n/a	n/a
12.0 - 15.0	4.00 - 4.50	4826.1 ± 731.2	0.665 ± 0.101	0.76
15.0 - 20.0	2.00 - 2.25	1241.9 ± 89.0	0.264 ± 0.019	0.51
15.0 - 20.0	2.25 - 2.50	3678.0 ± 132.2	0.280 ± 0.010	0.64
15.0 - 20.0	2.50 - 2.75	5611.9 ± 182.3	0.281 ± 0.009	0.81
15.0 - 20.0	2.75 - 3.00	7241.3 ± 211.4	0.279 ± 0.008	0.90
15.0 - 20.0	3.00 - 3.25	7499.0 ± 247.6	0.274 ± 0.009	1.08
15.0 - 20.0	3.25 - 3.50	7139.4 ± 251.3	0.310 ± 0.011	0.40
15.0 - 20.0	3.50 - 3.75	6193.8 ± 223.2	0.413 ± 0.015	0.65
15.0 - 20.0	3.75 - 4.00	4561.4 ± 228.8	0.581 ± 0.029	0.79
15.0 - 20.0	4.00 - 4.50	3861.4 ± 551.7	0.859 ± 0.123	0.74
20.0 - 60.0	2.00 - 2.25	1264.5 ± 61.6	0.529 ± 0.026	0.87
20.0 - 60.0	2.25 - 2.50	3796.2 ± 110.4	0.552 ± 0.016	0.51
20.0 - 60.0	2.50 - 2.75	5632.7 ± 139.5	0.543 ± 0.013	0.48
20.0 - 60.0	2.75 - 3.00	n/a	n/a	n/a
20.0 - 60.0	3.00 - 3.25	7885.5 ± 174.7	0.575 ± 0.013	0.44
20.0 - 60.0	3.25 - 3.50	7564.9 ± 177.8	0.627 ± 0.015	0.76
20.0 - 60.0	3.50 - 3.75	6167.6 ± 185.4	0.681 ± 0.020	0.82
20.0 - 60.0	3.75 - 4.00	3957.9 ± 199.1	0.746 ± 0.038	0.72
20.0 - 60.0	4.00 - 4.50	3014.6 ± 2545.6	0.999 ± 0.843	0.74

Table B.24: Fitresults for templates: Z, scaled; MinBias; HF-IP

$M_{\mu\mu}$ [GeV/c^2]	y	signal yield	ρ	χ^2/ndof
10.5 - 12.0	2.00 - 2.25	235.4 ± 235.8	0.020 ± 0.021	1.21
10.5 - 12.0	2.25 - 2.50	1181.9 ± 358.2	0.037 ± 0.011	3.28
10.5 - 12.0	2.50 - 2.75	2019.2 ± 354.9	0.043 ± 0.007	4.18
10.5 - 12.0	2.75 - 3.00	642.1 ± 497.4	0.011 ± 0.008	3.11
10.5 - 12.0	3.00 - 3.25	819.3 ± 672.5	0.013 ± 0.010	2.48
10.5 - 12.0	3.25 - 3.50	2785.3 ± 475.6	0.056 ± 0.010	1.93
10.5 - 12.0	3.50 - 3.75	4680.9 ± 293.6	0.177 ± 0.011	1.10
10.5 - 12.0	3.75 - 4.00	4059.0 ± 282.7	0.301 ± 0.021	0.81
10.5 - 12.0	4.00 - 4.50	3693.9 ± 693.0	0.507 ± 0.095	0.83
12.0 - 15.0	2.00 - 2.25	1148.0 ± 178.2	0.116 ± 0.018	1.02
12.0 - 15.0	2.25 - 2.50	3776.5 ± 255.9	0.138 ± 0.009	2.03
12.0 - 15.0	2.50 - 2.75	5423.9 ± 300.8	0.132 ± 0.007	2.61
12.0 - 15.0	2.75 - 3.00	4779.9 ± 426.2	0.091 ± 0.008	2.45
12.0 - 15.0	3.00 - 3.25	4313.7 ± 506.6	0.074 ± 0.009	2.13
12.0 - 15.0	3.25 - 3.50	5926.8 ± 427.8	0.126 ± 0.009	1.27
12.0 - 15.0	3.50 - 3.75	6201.3 ± 322.1	0.237 ± 0.012	0.98
12.0 - 15.0	3.75 - 4.00	5376.5 ± 316.6	0.404 ± 0.024	0.85
12.0 - 15.0	4.00 - 4.50	5241.3 ± 1090.6	0.722 ± 0.150	0.94
15.0 - 20.0	2.00 - 2.25	1159.7 ± 100.8	0.247 ± 0.021	0.51
15.0 - 20.0	2.25 - 2.50	3597.9 ± 144.1	0.274 ± 0.011	0.73
15.0 - 20.0	2.50 - 2.75	5252.1 ± 190.8	0.263 ± 0.010	0.84
15.0 - 20.0	2.75 - 3.00	6176.5 ± 240.0	0.238 ± 0.009	1.15
15.0 - 20.0	3.00 - 3.25	5746.3 ± 291.8	0.210 ± 0.011	1.25
15.0 - 20.0	3.25 - 3.50	6147.0 ± 277.5	0.267 ± 0.012	1.05
15.0 - 20.0	3.50 - 3.75	5640.9 ± 232.7	0.376 ± 0.016	0.86
15.0 - 20.0	3.75 - 4.00	4177.7 ± 241.1	0.532 ± 0.031	0.80
15.0 - 20.0	4.00 - 4.50	3664.8 ± 600.6	0.815 ± 0.134	0.74
20.0 - 60.0	2.00 - 2.25	1152.8 ± 66.9	0.483 ± 0.028	0.40
20.0 - 60.0	2.25 - 2.50	3451.7 ± 124.1	0.502 ± 0.018	0.51
20.0 - 60.0	2.50 - 2.75	5314.0 ± 154.6	0.512 ± 0.015	0.68
20.0 - 60.0	2.75 - 3.00	6960.6 ± 172.8	0.526 ± 0.013	0.46
20.0 - 60.0	3.00 - 3.25	7136.5 ± 216.1	0.520 ± 0.016	0.46
20.0 - 60.0	3.25 - 3.50	6989.2 ± 201.6	0.579 ± 0.017	0.56
20.0 - 60.0	3.50 - 3.75	5704.6 ± 195.6	0.630 ± 0.022	0.55
20.0 - 60.0	3.75 - 4.00	3205.3 ± 274.0	0.604 ± 0.052	0.59
20.0 - 60.0	4.00 - 4.50	1978.1 ± 332.1	0.655 ± 0.110	0.82

Table B.25: Fitresults for templates: Z, unscaled; SameSign; HF-Vertex

$M_{\mu\mu}$ [GeV/c^2]	y	signal yield	ρ	χ^2/ndof
10.5 - 12.0	2.00 - 2.25	1446.1 ± 176.2	0.126 ± 0.015	0.18
10.5 - 12.0	2.25 - 2.50	4559.6 ± 280.7	0.142 ± 0.009	0.92
10.5 - 12.0	2.50 - 2.75	6586.7 ± 371.7	0.139 ± 0.008	0.73
10.5 - 12.0	2.75 - 3.00	6499.8 ± 513.5	0.110 ± 0.009	0.71
10.5 - 12.0	3.00 - 3.25	7955.5 ± 561.2	0.123 ± 0.009	0.42
10.5 - 12.0	3.25 - 3.50	7685.7 ± 486.5	0.155 ± 0.010	0.48
10.5 - 12.0	3.50 - 3.75	6757.8 ± 343.0	0.256 ± 0.013	0.81
10.5 - 12.0	3.75 - 4.00	4978.6 ± 335.8	0.369 ± 0.025	0.64
10.5 - 12.0	4.00 - 4.50	4871.5 ± 905.0	0.668 ± 0.124	0.74
12.0 - 15.0	2.00 - 2.25	2050.1 ± 137.5	0.207 ± 0.014	0.34
12.0 - 15.0	2.25 - 2.50	5243.5 ± 237.8	0.191 ± 0.009	0.43
12.0 - 15.0	2.50 - 2.75	8035.2 ± 309.2	0.196 ± 0.008	0.42
12.0 - 15.0	2.75 - 3.00	9342.9 ± 385.0	0.178 ± 0.007	0.60
12.0 - 15.0	3.00 - 3.25	$10\,256.6 \pm 496.5$	0.175 ± 0.008	0.95
12.0 - 15.0	3.25 - 3.50	9793.2 ± 454.5	0.209 ± 0.010	0.76
12.0 - 15.0	3.50 - 3.75	8628.7 ± 351.2	0.329 ± 0.013	0.58
12.0 - 15.0	3.75 - 4.00	6151.3 ± 357.7	0.462 ± 0.027	0.65
12.0 - 15.0	4.00 - 4.50	5600.3 ± 992.4	0.771 ± 0.137	0.78
15.0 - 20.0	2.00 - 2.25	1375.3 ± 91.5	0.293 ± 0.019	0.40
15.0 - 20.0	2.25 - 2.50	3921.5 ± 143.8	0.299 ± 0.011	0.61
15.0 - 20.0	2.50 - 2.75	6105.9 ± 190.4	0.306 ± 0.010	0.44
15.0 - 20.0	2.75 - 3.00	7986.1 ± 228.3	0.308 ± 0.009	0.62
15.0 - 20.0	3.00 - 3.25	8197.6 ± 268.0	0.300 ± 0.010	0.85
15.0 - 20.0	3.25 - 3.50	7674.0 ± 287.8	0.333 ± 0.013	0.44
15.0 - 20.0	3.50 - 3.75	6441.0 ± 505.1	0.430 ± 0.034	0.77
15.0 - 20.0	3.75 - 4.00	4719.3 ± 239.0	0.601 ± 0.030	0.71
15.0 - 20.0	4.00 - 4.50	4003.2 ± 600.6	0.890 ± 0.134	0.67
20.0 - 60.0	2.00 - 2.25	1281.8 ± 57.3	0.537 ± 0.024	0.76
20.0 - 60.0	2.25 - 2.50	3846.8 ± 109.5	0.559 ± 0.016	0.50
20.0 - 60.0	2.50 - 2.75	5769.6 ± 150.4	0.556 ± 0.015	0.41
20.0 - 60.0	2.75 - 3.00	7460.6 ± 165.4	0.564 ± 0.013	0.29
20.0 - 60.0	3.00 - 3.25	7988.0 ± 191.6	0.582 ± 0.014	0.45
20.0 - 60.0	3.25 - 3.50	7595.8 ± 178.7	0.629 ± 0.015	0.77
20.0 - 60.0	3.50 - 3.75	6262.6 ± 203.1	0.691 ± 0.022	0.81
20.0 - 60.0	3.75 - 4.00	4033.6 ± 213.7	0.760 ± 0.040	0.62
20.0 - 60.0	4.00 - 4.50	1958.8 ± 326.3	0.649 ± 0.108	1.04

Table B.26: Fitresults for templates: Z, unscaled; SameSign; HF-IP

$M_{\mu\mu}$ [GeV/c^2]	y	signal yield	ρ	χ^2/ndof
10.5 - 12.0	2.00 - 2.25	1089.8 ± 199.2	0.095 ± 0.017	0.27
10.5 - 12.0	2.25 - 2.50	3618.0 ± 316.7	0.113 ± 0.010	0.79
10.5 - 12.0	2.50 - 2.75	5551.0 ± 389.8	0.117 ± 0.008	0.79
10.5 - 12.0	2.75 - 3.00	4487.1 ± 588.6	0.076 ± 0.010	1.20
10.5 - 12.0	3.00 - 3.25	4274.2 ± 553.3	0.066 ± 0.009	0.70
10.5 - 12.0	3.25 - 3.50	4792.1 ± 539.4	0.097 ± 0.011	0.99
10.5 - 12.0	3.50 - 3.75	5417.8 ± 357.9	0.205 ± 0.014	1.10
10.5 - 12.0	3.75 - 4.00	4505.7 ± 319.7	0.334 ± 0.024	0.68
10.5 - 12.0	4.00 - 4.50	4364.3 ± 838.6	0.599 ± 0.115	0.72
12.0 - 15.0	2.00 - 2.25	1737.4 ± 148.6	0.176 ± 0.015	0.26
12.0 - 15.0	2.25 - 2.50	5044.0 ± 241.5	0.184 ± 0.009	0.40
12.0 - 15.0	2.50 - 2.75	7390.1 ± 307.4	0.180 ± 0.007	0.76
12.0 - 15.0	2.75 - 3.00	7539.1 ± 422.2	0.144 ± 0.008	0.64
12.0 - 15.0	3.00 - 3.25	6940.2 ± 521.7	0.119 ± 0.009	0.74
12.0 - 15.0	3.25 - 3.50	7761.9 ± 469.0	0.166 ± 0.010	0.58
12.0 - 15.0	3.50 - 3.75	7047.9 ± 360.6	0.269 ± 0.014	0.80
12.0 - 15.0	3.75 - 4.00	5756.5 ± 341.4	0.432 ± 0.026	0.68
12.0 - 15.0	4.00 - 4.50	7180.9 ± 5929.4	0.989 ± 0.816	0.85
15.0 - 20.0	2.00 - 2.25	1307.3 ± 95.5	0.278 ± 0.020	0.39
15.0 - 20.0	2.25 - 2.50	3914.6 ± 143.9	0.298 ± 0.011	0.59
15.0 - 20.0	2.50 - 2.75	5934.9 ± 194.7	0.297 ± 0.010	0.29
15.0 - 20.0	2.75 - 3.00	7221.9 ± 251.0	0.278 ± 0.010	0.51
15.0 - 20.0	3.00 - 3.25	6868.4 ± 317.8	0.251 ± 0.012	0.82
15.0 - 20.0	3.25 - 3.50	7155.5 ± 301.1	0.311 ± 0.013	0.73
15.0 - 20.0	3.50 - 3.75	6010.6 ± 281.2	0.401 ± 0.019	1.14
15.0 - 20.0	3.75 - 4.00	n/a	n/a	n/a
15.0 - 20.0	4.00 - 4.50	4155.8 ± 646.7	0.924 ± 0.144	0.69
20.0 - 60.0	2.00 - 2.25	1215.2 ± 66.0	0.509 ± 0.028	0.36
20.0 - 60.0	2.25 - 2.50	3615.7 ± 126.4	0.525 ± 0.018	0.47
20.0 - 60.0	2.50 - 2.75	5648.7 ± 160.2	0.545 ± 0.015	0.58
20.0 - 60.0	2.75 - 3.00	7242.6 ± 177.3	0.548 ± 0.013	0.33
20.0 - 60.0	3.00 - 3.25	n/a	n/a	n/a
20.0 - 60.0	3.25 - 3.50	7020.4 ± 203.3	0.581 ± 0.017	0.57
20.0 - 60.0	3.50 - 3.75	5944.0 ± 206.5	0.656 ± 0.023	0.58
20.0 - 60.0	3.75 - 4.00	3268.6 ± 279.9	0.616 ± 0.053	0.58
20.0 - 60.0	4.00 - 4.50	1977.9 ± 332.8	0.655 ± 0.110	0.82

Table B.27: Fitresults for templates: Z, unscaled; MinBias; HF-Vertex

$M_{\mu\mu}$ [GeV/c^2]	y	signal yield	ρ	χ^2/ndof
10.5 - 12.0	2.00 - 2.25	1007.7 ± 202.9	0.088 ± 0.018	0.69
10.5 - 12.0	2.25 - 2.50	3570.7 ± 312.1	0.111 ± 0.010	1.80
10.5 - 12.0	2.50 - 2.75	5034.7 ± 397.6	0.106 ± 0.008	1.97
10.5 - 12.0	2.75 - 3.00	5014.2 ± 505.1	0.085 ± 0.009	1.35
10.5 - 12.0	3.00 - 3.25	6889.3 ± 545.0	0.107 ± 0.008	0.87
10.5 - 12.0	3.25 - 3.50	6943.3 ± 491.0	0.140 ± 0.010	0.80
10.5 - 12.0	3.50 - 3.75	6561.3 ± 328.2	0.249 ± 0.012	0.90
10.5 - 12.0	3.75 - 4.00	4945.3 ± 359.5	0.367 ± 0.027	0.64
10.5 - 12.0	4.00 - 4.50	4870.2 ± 900.8	0.668 ± 0.124	0.74
12.0 - 15.0	2.00 - 2.25	1843.9 ± 141.8	0.186 ± 0.014	0.63
12.0 - 15.0	2.25 - 2.50	4761.2 ± 239.5	0.174 ± 0.009	0.82
12.0 - 15.0	2.50 - 2.75	7433.6 ± 296.4	0.181 ± 0.007	0.78
12.0 - 15.0	2.75 - 3.00	8289.9 ± 379.8	0.158 ± 0.007	1.35
12.0 - 15.0	3.00 - 3.25	9506.0 ± 459.5	0.162 ± 0.008	1.21
12.0 - 15.0	3.25 - 3.50	9242.4 ± 436.0	0.197 ± 0.009	0.94
12.0 - 15.0	3.50 - 3.75	8462.4 ± 337.3	0.323 ± 0.013	0.63
12.0 - 15.0	3.75 - 4.00	6078.3 ± 343.7	0.457 ± 0.026	0.67
12.0 - 15.0	4.00 - 4.50	5595.9 ± 941.8	0.771 ± 0.130	0.78
15.0 - 20.0	2.00 - 2.25	1288.3 ± 91.7	0.274 ± 0.020	0.47
15.0 - 20.0	2.25 - 2.50	3780.8 ± 142.6	0.288 ± 0.011	0.75
15.0 - 20.0	2.50 - 2.75	5886.7 ± 187.4	0.295 ± 0.009	0.66
15.0 - 20.0	2.75 - 3.00	7565.2 ± 223.3	0.291 ± 0.009	0.92
15.0 - 20.0	3.00 - 3.25	7871.9 ± 250.5	0.288 ± 0.009	1.01
15.0 - 20.0	3.25 - 3.50	7445.2 ± 262.6	0.323 ± 0.011	0.51
15.0 - 20.0	3.50 - 3.75	n/a	n/a	n/a
15.0 - 20.0	3.75 - 4.00	4684.1 ± 233.3	0.596 ± 0.030	0.72
15.0 - 20.0	4.00 - 4.50	4003.0 ± 600.7	0.890 ± 0.134	0.67
20.0 - 60.0	2.00 - 2.25	1266.6 ± 61.8	0.530 ± 0.026	0.89
20.0 - 60.0	2.25 - 2.50	3810.3 ± 112.4	0.554 ± 0.016	0.53
20.0 - 60.0	2.50 - 2.75	5659.6 ± 139.9	0.546 ± 0.013	0.48
20.0 - 60.0	2.75 - 3.00	7398.4 ± 162.7	0.559 ± 0.012	0.33
20.0 - 60.0	3.00 - 3.25	7935.4 ± 175.4	0.579 ± 0.013	0.44
20.0 - 60.0	3.25 - 3.50	7596.0 ± 178.5	0.629 ± 0.015	0.77
20.0 - 60.0	3.50 - 3.75	6193.7 ± 185.6	0.684 ± 0.020	0.81
20.0 - 60.0	3.75 - 4.00	3997.6 ± 200.2	0.753 ± 0.038	0.62
20.0 - 60.0	4.00 - 4.50	3014.6 ± 2545.6	0.999 ± 0.843	0.74

Table B.28: Fitresults for templates: Z, unscaled; MinBias; HF-IP

$M_{\mu\mu}$ [GeV/c^2]	y	signal yield	ρ	χ^2/ndof
10.5 - 12.0	2.00 - 2.25	224.0 ± 260.0	0.019 ± 0.023	1.22
10.5 - 12.0	2.25 - 2.50	1193.0 ± 391.8	0.037 ± 0.012	3.31
10.5 - 12.0	2.50 - 2.75	2164.8 ± 495.2	0.046 ± 0.010	4.23
10.5 - 12.0	2.75 - 3.00	788.3 ± 599.6	0.013 ± 0.010	3.10
10.5 - 12.0	3.00 - 3.25	978.2 ± 693.3	0.015 ± 0.011	2.47
10.5 - 12.0	3.25 - 3.50	3072.3 ± 556.5	0.062 ± 0.011	1.96
10.5 - 12.0	3.50 - 3.75	5000.6 ± 343.2	0.189 ± 0.013	1.48
10.5 - 12.0	3.75 - 4.00	4420.9 ± 303.5	0.328 ± 0.023	0.72
10.5 - 12.0	4.00 - 4.50	4363.5 ± 834.8	0.598 ± 0.114	0.72
12.0 - 15.0	2.00 - 2.25	1266.9 ± 163.3	0.128 ± 0.017	0.92
12.0 - 15.0	2.25 - 2.50	3986.4 ± 233.7	0.146 ± 0.009	2.02
12.0 - 15.0	2.50 - 2.75	5863.2 ± 327.7	0.143 ± 0.008	2.61
12.0 - 15.0	2.75 - 3.00	5247.9 ± 424.9	0.100 ± 0.008	2.38
12.0 - 15.0	3.00 - 3.25	4598.3 ± 528.5	0.079 ± 0.009	2.19
12.0 - 15.0	3.25 - 3.50	6318.1 ± 440.0	0.135 ± 0.009	1.42
12.0 - 15.0	3.50 - 3.75	6608.8 ± 347.5	0.252 ± 0.013	1.07
12.0 - 15.0	3.75 - 4.00	5660.5 ± 329.1	0.425 ± 0.025	0.75
12.0 - 15.0	4.00 - 4.50	n/a	n/a	n/a
15.0 - 20.0	2.00 - 2.25	1212.0 ± 102.4	0.258 ± 0.022	0.45
15.0 - 20.0	2.25 - 2.50	3703.7 ± 144.6	0.282 ± 0.011	0.80
15.0 - 20.0	2.50 - 2.75	5528.2 ± 205.5	0.277 ± 0.010	0.69
15.0 - 20.0	2.75 - 3.00	6453.2 ± 250.5	0.249 ± 0.010	1.26
15.0 - 20.0	3.00 - 3.25	6073.6 ± 302.4	0.222 ± 0.011	1.19
15.0 - 20.0	3.25 - 3.50	6402.9 ± 290.6	0.278 ± 0.013	1.18
15.0 - 20.0	3.50 - 3.75	5872.2 ± 243.7	0.392 ± 0.016	1.09
15.0 - 20.0	3.75 - 4.00	4307.3 ± 244.3	0.548 ± 0.031	0.68
15.0 - 20.0	4.00 - 4.50	4155.3 ± 735.0	0.924 ± 0.163	0.69
20.0 - 60.0	2.00 - 2.25	1156.5 ± 70.8	0.484 ± 0.030	0.42
20.0 - 60.0	2.25 - 2.50	3465.6 ± 124.7	0.504 ± 0.018	0.53
20.0 - 60.0	2.50 - 2.75	5344.6 ± 154.3	0.515 ± 0.015	0.68
20.0 - 60.0	2.75 - 3.00	6997.8 ± 173.7	0.529 ± 0.013	0.49
20.0 - 60.0	3.00 - 3.25	7187.0 ± 215.9	0.524 ± 0.016	0.46
20.0 - 60.0	3.25 - 3.50	7020.6 ± 202.3	0.582 ± 0.017	0.57
20.0 - 60.0	3.50 - 3.75	5731.8 ± 196.0	0.633 ± 0.022	0.56
20.0 - 60.0	3.75 - 4.00	3268.7 ± 274.9	0.616 ± 0.052	0.58
20.0 - 60.0	4.00 - 4.50	1978.1 ± 332.1	0.655 ± 0.110	0.82

Table B.29: Fitresults for templates: Drell-Yan, simulation; SameSign; HF-Vertex

$M_{\mu\mu}$ [GeV/c^2]	y	signal yield	ρ	χ^2/ndof
10.5 - 12.0	2.00 - 2.25	1689.6 ± 220.7	0.147 ± 0.019	0.36
10.5 - 12.0	2.25 - 2.50	5324.2 ± 343.6	0.166 ± 0.011	1.27
10.5 - 12.0	2.50 - 2.75	7061.2 ± 408.7	0.149 ± 0.009	1.18
10.5 - 12.0	2.75 - 3.00	7321.8 ± 586.4	0.124 ± 0.010	0.93
10.5 - 12.0	3.00 - 3.25	9948.4 ± 760.6	0.154 ± 0.012	1.12
10.5 - 12.0	3.25 - 3.50	9498.4 ± 610.0	0.192 ± 0.012	1.03
10.5 - 12.0	3.50 - 3.75	8827.5 ± 370.2	0.334 ± 0.014	1.13
10.5 - 12.0	3.75 - 4.00	6369.0 ± 271.6	0.473 ± 0.020	1.76
10.5 - 12.0	4.00 - 4.50	4249.8 ± 221.2	0.583 ± 0.030	2.12
12.0 - 15.0	2.00 - 2.25	2125.6 ± 144.7	0.215 ± 0.015	0.52
12.0 - 15.0	2.25 - 2.50	5686.2 ± 278.8	0.208 ± 0.010	1.21
12.0 - 15.0	2.50 - 2.75	9288.8 ± 353.9	0.226 ± 0.009	0.86
12.0 - 15.0	2.75 - 3.00	$10\,983.8 \pm 454.3$	0.210 ± 0.009	1.66
12.0 - 15.0	3.00 - 3.25	$12\,516.0 \pm 616.5$	0.214 ± 0.011	2.26
12.0 - 15.0	3.25 - 3.50	$11\,698.8 \pm 549.0$	0.250 ± 0.012	2.02
12.0 - 15.0	3.50 - 3.75	$10\,943.0 \pm 356.6$	0.418 ± 0.014	2.40
12.0 - 15.0	3.75 - 4.00	7722.9 ± 316.7	0.580 ± 0.024	3.00
12.0 - 15.0	4.00 - 4.50	5730.7 ± 155.9	0.789 ± 0.021	2.55
15.0 - 20.0	2.00 - 2.25	1471.8 ± 116.2	0.313 ± 0.025	0.70
15.0 - 20.0	2.25 - 2.50	4585.7 ± 172.2	0.349 ± 0.013	1.66
15.0 - 20.0	2.50 - 2.75	7140.2 ± 222.2	0.358 ± 0.011	1.09
15.0 - 20.0	2.75 - 3.00	8890.0 ± 266.6	0.342 ± 0.010	2.72
15.0 - 20.0	3.00 - 3.25	9579.5 ± 340.2	0.351 ± 0.012	2.62
15.0 - 20.0	3.25 - 3.50	9388.6 ± 337.6	0.408 ± 0.015	1.78
15.0 - 20.0	3.50 - 3.75	7377.5 ± 309.1	0.492 ± 0.021	3.06
15.0 - 20.0	3.75 - 4.00	5749.1 ± 165.9	0.732 ± 0.021	3.26
15.0 - 20.0	4.00 - 4.50	3471.8 ± 171.4	0.772 ± 0.038	2.68
20.0 - 60.0	2.00 - 2.25	1483.7 ± 68.5	0.621 ± 0.029	1.03
20.0 - 60.0	2.25 - 2.50	4126.7 ± 126.9	0.600 ± 0.018	2.05
20.0 - 60.0	2.50 - 2.75	6003.1 ± 174.8	0.579 ± 0.017	3.56
20.0 - 60.0	2.75 - 3.00	8245.9 ± 183.6	0.624 ± 0.014	2.60
20.0 - 60.0	3.00 - 3.25	8831.7 ± 186.5	0.644 ± 0.014	2.52
20.0 - 60.0	3.25 - 3.50	8360.0 ± 187.0	0.692 ± 0.015	3.34
20.0 - 60.0	3.50 - 3.75	6919.7 ± 176.6	0.764 ± 0.019	2.48
20.0 - 60.0	3.75 - 4.00	3986.8 ± 150.0	0.751 ± 0.028	2.42
20.0 - 60.0	4.00 - 4.50	713.4 ± 593.1	0.236 ± 0.197	1.13

Table B.30: Fitresults for templates: Drell-Yan, simulation; SameSign; HF-IP

$M_{\mu\mu}$ [GeV/c^2]	y	signal yield	ρ	χ^2/ndof
10.5 - 12.0	2.00 - 2.25	1303.1 ± 250.7	0.113 ± 0.022	0.35
10.5 - 12.0	2.25 - 2.50	4081.4 ± 402.5	0.127 ± 0.013	1.23
10.5 - 12.0	2.50 - 2.75	5955.9 ± 453.1	0.126 ± 0.010	1.15
10.5 - 12.0	2.75 - 3.00	4124.3 ± 673.6	0.070 ± 0.011	1.74
10.5 - 12.0	3.00 - 3.25	4328.1 ± 934.7	0.067 ± 0.014	1.14
10.5 - 12.0	3.25 - 3.50	5497.4 ± 726.8	0.111 ± 0.015	1.48
10.5 - 12.0	3.50 - 3.75	7308.2 ± 429.3	0.277 ± 0.016	1.41
10.5 - 12.0	3.75 - 4.00	5903.9 ± 281.7	0.438 ± 0.021	1.64
10.5 - 12.0	4.00 - 4.50	4379.9 ± 216.1	0.601 ± 0.030	1.92
12.0 - 15.0	2.00 - 2.25	1748.6 ± 171.7	0.177 ± 0.017	0.68
12.0 - 15.0	2.25 - 2.50	5542.5 ± 272.7	0.202 ± 0.010	0.74
12.0 - 15.0	2.50 - 2.75	8557.0 ± 365.9	0.208 ± 0.009	1.28
12.0 - 15.0	2.75 - 3.00	8864.6 ± 525.3	0.169 ± 0.010	1.46
12.0 - 15.0	3.00 - 3.25	7946.1 ± 715.0	0.136 ± 0.012	1.73
12.0 - 15.0	3.25 - 3.50	9266.5 ± 585.2	0.198 ± 0.012	1.47
12.0 - 15.0	3.50 - 3.75	8849.8 ± 465.0	0.338 ± 0.018	2.72
12.0 - 15.0	3.75 - 4.00	7890.5 ± 281.8	0.593 ± 0.021	3.30
12.0 - 15.0	4.00 - 4.50	4641.8 ± 217.7	0.639 ± 0.030	2.13
15.0 - 20.0	2.00 - 2.25	1317.8 ± 160.6	0.281 ± 0.034	0.71
15.0 - 20.0	2.25 - 2.50	4539.8 ± 178.2	0.346 ± 0.014	1.50
15.0 - 20.0	2.50 - 2.75	6987.3 ± 229.6	0.350 ± 0.012	0.93
15.0 - 20.0	2.75 - 3.00	7938.1 ± 302.1	0.306 ± 0.012	2.16
15.0 - 20.0	3.00 - 3.25	7994.9 ± 403.8	0.293 ± 0.015	1.90
15.0 - 20.0	3.25 - 3.50	8703.9 ± 382.0	0.378 ± 0.017	1.56
15.0 - 20.0	3.50 - 3.75	6565.4 ± 297.3	0.438 ± 0.020	2.03
15.0 - 20.0	3.75 - 4.00	4776.5 ± 206.5	0.608 ± 0.026	2.12
15.0 - 20.0	4.00 - 4.50	3233.8 ± 161.6	0.719 ± 0.036	1.92
20.0 - 60.0	2.00 - 2.25	1254.9 ± 84.4	0.525 ± 0.035	0.56
20.0 - 60.0	2.25 - 2.50	3773.7 ± 179.4	0.548 ± 0.026	1.71
20.0 - 60.0	2.50 - 2.75	5570.8 ± 193.5	0.537 ± 0.019	2.57
20.0 - 60.0	2.75 - 3.00	7808.9 ± 226.9	0.590 ± 0.017	1.99
20.0 - 60.0	3.00 - 3.25	7464.0 ± 244.4	0.544 ± 0.018	1.94
20.0 - 60.0	3.25 - 3.50	7566.3 ± 228.8	0.627 ± 0.019	2.44
20.0 - 60.0	3.50 - 3.75	6194.9 ± 232.4	0.684 ± 0.026	2.26
20.0 - 60.0	3.75 - 4.00	2975.7 ± 373.9	0.561 ± 0.070	1.44
20.0 - 60.0	4.00 - 4.50	946.5 ± 361.5	0.314 ± 0.120	0.90

Table B.31: Fitresults for templates: Drell-Yan, simulation; MinBias; HF-Vertex

$M_{\mu\mu}$ [GeV/c^2]	y	signal yield	ρ	χ^2/ndof
10.5 - 12.0	2.00 - 2.25	993.6 ± 246.2	0.087 ± 0.021	0.85
10.5 - 12.0	2.25 - 2.50	3781.5 ± 366.1	0.118 ± 0.011	2.26
10.5 - 12.0	2.50 - 2.75	4970.0 ± 416.5	0.105 ± 0.009	2.51
10.5 - 12.0	2.75 - 3.00	5254.7 ± 579.2	0.089 ± 0.010	1.63
10.5 - 12.0	3.00 - 3.25	7677.3 ± 765.4	0.119 ± 0.012	1.67
10.5 - 12.0	3.25 - 3.50	8039.0 ± 600.0	0.163 ± 0.012	1.50
10.5 - 12.0	3.50 - 3.75	8277.3 ± 351.1	0.314 ± 0.013	1.45
10.5 - 12.0	3.75 - 4.00	6179.1 ± 261.5	0.458 ± 0.019	1.85
10.5 - 12.0	4.00 - 4.50	4249.8 ± 219.9	0.583 ± 0.030	2.12
12.0 - 15.0	2.00 - 2.25	1890.4 ± 157.8	0.191 ± 0.016	0.83
12.0 - 15.0	2.25 - 2.50	4970.8 ± 269.8	0.181 ± 0.010	1.63
12.0 - 15.0	2.50 - 2.75	8364.5 ± 339.2	0.204 ± 0.008	1.33
12.0 - 15.0	2.75 - 3.00	9064.5 ± 460.0	0.173 ± 0.009	2.71
12.0 - 15.0	3.00 - 3.25	$11\,034.6 \pm 582.3$	0.189 ± 0.010	2.61
12.0 - 15.0	3.25 - 3.50	$10\,488.9 \pm 506.1$	0.224 ± 0.011	2.35
12.0 - 15.0	3.50 - 3.75	$10\,334.7 \pm 290.3$	0.394 ± 0.011	2.70
12.0 - 15.0	3.75 - 4.00	n/a	n/a	n/a
12.0 - 15.0	4.00 - 4.50	5562.6 ± 144.2	0.766 ± 0.020	2.81
15.0 - 20.0	2.00 - 2.25	1345.4 ± 108.8	0.287 ± 0.023	0.75
15.0 - 20.0	2.25 - 2.50	4286.4 ± 176.5	0.326 ± 0.013	1.93
15.0 - 20.0	2.50 - 2.75	6549.5 ± 220.5	0.328 ± 0.011	1.81
15.0 - 20.0	2.75 - 3.00	8174.2 ± 263.5	0.315 ± 0.010	3.22
15.0 - 20.0	3.00 - 3.25	8652.4 ± 313.0	0.317 ± 0.011	3.09
15.0 - 20.0	3.25 - 3.50	8737.7 ± 317.6	0.380 ± 0.014	2.00
15.0 - 20.0	3.50 - 3.75	n/a	n/a	n/a
15.0 - 20.0	3.75 - 4.00	5445.6 ± 185.8	0.693 ± 0.024	3.32
15.0 - 20.0	4.00 - 4.50	3471.7 ± 171.1	0.772 ± 0.038	2.68
20.0 - 60.0	2.00 - 2.25	1399.5 ± 73.2	0.586 ± 0.031	1.29
20.0 - 60.0	2.25 - 2.50	4042.3 ± 133.1	0.587 ± 0.019	2.09
20.0 - 60.0	2.50 - 2.75	6003.5 ± 174.3	0.579 ± 0.017	3.56
20.0 - 60.0	2.75 - 3.00	8017.9 ± 189.9	0.606 ± 0.014	2.79
20.0 - 60.0	3.00 - 3.25	8487.9 ± 188.4	0.619 ± 0.014	2.92
20.0 - 60.0	3.25 - 3.50	8359.9 ± 186.7	0.692 ± 0.015	3.34
20.0 - 60.0	3.50 - 3.75	6919.6 ± 175.8	0.764 ± 0.019	2.48
20.0 - 60.0	3.75 - 4.00	3986.7 ± 149.6	0.751 ± 0.028	2.42
20.0 - 60.0	4.00 - 4.50	715.4 ± 577.8	0.237 ± 0.191	1.13

Table B.32: Fitresults for templates: Drell-Yan, simulation; MinBias; HF-IP

$M_{\mu\mu}$ [GeV/c^2]	y	signal yield	ρ	χ^2/ndof
10.5 - 12.0	2.00 - 2.25	9.6 ± 489.4	0.001 ± 0.043	1.23
10.5 - 12.0	2.25 - 2.50	635.1 ± 531.6	0.020 ± 0.017	3.47
10.5 - 12.0	2.50 - 2.75	1635.1 ± 518.9	0.035 ± 0.011	4.43
10.5 - 12.0	2.75 - 3.00	0.0 ± 427.9	0.000 ± 0.007	3.11
10.5 - 12.0	3.00 - 3.25	0.0 ± 437.6	0.000 ± 0.007	2.51
10.5 - 12.0	3.25 - 3.50	2570.6 ± 723.5	0.052 ± 0.015	2.35
10.5 - 12.0	3.50 - 3.75	6366.8 ± 428.4	0.241 ± 0.016	2.04
10.5 - 12.0	3.75 - 4.00	5670.8 ± 284.8	0.421 ± 0.021	1.79
10.5 - 12.0	4.00 - 4.50	4325.3 ± 209.2	0.593 ± 0.029	2.05
12.0 - 15.0	2.00 - 2.25	1119.9 ± 216.4	0.113 ± 0.022	1.22
12.0 - 15.0	2.25 - 2.50	4155.9 ± 291.3	0.152 ± 0.011	2.43
12.0 - 15.0	2.50 - 2.75	6474.9 ± 388.3	0.158 ± 0.009	3.22
12.0 - 15.0	2.75 - 3.00	5201.1 ± 542.2	0.099 ± 0.010	3.26
12.0 - 15.0	3.00 - 3.25	4262.8 ± 720.4	0.073 ± 0.012	2.92
12.0 - 15.0	3.25 - 3.50	6757.0 ± 583.0	0.144 ± 0.012	2.42
12.0 - 15.0	3.50 - 3.75	7718.3 ± 453.5	0.295 ± 0.017	3.14
12.0 - 15.0	3.75 - 4.00	6828.0 ± 269.3	0.513 ± 0.020	3.76
12.0 - 15.0	4.00 - 4.50	4641.8 ± 217.3	0.639 ± 0.030	2.13
15.0 - 20.0	2.00 - 2.25	1227.8 ± 137.8	0.261 ± 0.029	0.73
15.0 - 20.0	2.25 - 2.50	4153.0 ± 184.5	0.316 ± 0.014	1.78
15.0 - 20.0	2.50 - 2.75	6114.9 ± 231.1	0.306 ± 0.012	1.94
15.0 - 20.0	2.75 - 3.00	6782.5 ± 306.0	0.261 ± 0.012	2.92
15.0 - 20.0	3.00 - 3.25	6482.5 ± 352.9	0.237 ± 0.013	2.45
15.0 - 20.0	3.25 - 3.50	7395.1 ± 354.4	0.321 ± 0.015	2.16
15.0 - 20.0	3.50 - 3.75	6311.1 ± 258.9	0.421 ± 0.017	2.05
15.0 - 20.0	3.75 - 4.00	4776.6 ± 206.1	0.608 ± 0.026	2.12
15.0 - 20.0	4.00 - 4.50	3233.8 ± 161.4	0.719 ± 0.036	1.92
20.0 - 60.0	2.00 - 2.25	1254.9 ± 84.1	0.525 ± 0.035	0.56
20.0 - 60.0	2.25 - 2.50	3468.0 ± 168.7	0.504 ± 0.025	1.68
20.0 - 60.0	2.50 - 2.75	5570.7 ± 192.8	0.537 ± 0.019	2.57
20.0 - 60.0	2.75 - 3.00	7380.3 ± 212.4	0.558 ± 0.016	2.10
20.0 - 60.0	3.00 - 3.25	7464.4 ± 237.9	0.544 ± 0.017	1.94
20.0 - 60.0	3.25 - 3.50	7566.1 ± 227.9	0.627 ± 0.019	2.44
20.0 - 60.0	3.50 - 3.75	6195.2 ± 231.7	0.684 ± 0.026	2.26
20.0 - 60.0	3.75 - 4.00	2976.1 ± 367.9	0.561 ± 0.069	1.44
20.0 - 60.0	4.00 - 4.50	946.0 ± 429.6	0.313 ± 0.142	0.90

Appendix C

LHCb-CONF-2012-013: Inclusive low mass Drell-Yan production in the forward region at $\sqrt{s} = 7$ TeV

This chapter contains a verbatim copy of the conference note with the preliminary results for data collected in 2010. The analysis was performed by Jonny Anderson, Katharina Müller and myself.

C.1 Introduction

Measurements of the Z, W and low mass Drell-Yan (DY) cross-sections constitute an important test of the Standard Model at LHC energies. Perturbative QCD predictions of these processes are available at next-to-next-to-leading order (NNLO). Measurements of Z and W cross-sections by LHCb as well as their ratios have already been presented at several conferences and final results are being published (LHCb Collaboration n.d.). At low invariant masses, theoretical uncertainties are dominated by higher order contributions, whereas at masses above 20 GeV/c^2 they are comparable to those from the parton density functions (PDF). The measurements of the DY cross-sections are sensitive to Bjorken-x values as low as 8×10^{-6} for four-momentum transfer $Q^2 = 25$ GeV/c^2, where x is the momentum fraction carried by the struck quark. They will provide important input to the knowledge of the parton density functions and the understanding of the theoretical calculations. DY production has already been measured at LHC in the central pseudorapidity region ($|\eta| < 2.4$) in the dilepton invariant mass range 15-600 GeV/c^2 (CMS Collaboration 2011). The kinematic region ($2.5 < \eta < 4.5$), uniquely accessible to LHCb, has not been probed by other experiments. At low masses theoretical fixed order calculations are not expected to give valid predictions since non-perturbative effects and resummation have to be taken into account.

In this note we describe the differential cross-section measurements of DY production with the LHCb detector at $\sqrt{s} = 7\,\text{TeV}$ using about $37\,\text{pb}^{-1}$ of data collected in 2010. The remainder of the note is organised as follows. Section 2 describes the LHCb detector, Sect. 3 the selection of the DY events and several control samples. Sect. 4 describes the backgrounds, the determination of the signal yield and the efficiencies. The measurement of the cross-sections as well as the systematic uncertainties are discussed in Sect. 5, the results are presented in Sect. 6 and Sect. 7 concludes.

C.2 LHCb detector

The LHCb detector (LHCb Collaboration 2008) is a single-arm forward spectrometer covering the pseudorapdity range $2 < \eta < 5$, designed for the study of particles containing b or c quarks. The detector includes a high precision tracking system consisting of a silicon-strip vertex detector (VELO) surrounding the pp interaction region, a large-area silicon-strip detector (TT) located upstream of a dipole magnet with a bending power of about 4 Tm, and three stations of silicon-strip detectors (IT) and straw drift-tubes (OT) placed downstream. The combined tracking system has a momentum resolution $\Delta p/p$ that varies from 0.4% at $5\,\text{GeV}/c$ to 0.6% at $100\,\text{GeV}/c$, and an impact parameter resolution of $20\,\mu\text{m}$ for tracks with high transverse momentum. Charged hadrons are identified using two ring-imaging Cherenkov detectors. Photon, electron and hadron candidates are identified by a calorimeter system consisting of scintillating-pad and pre-shower detectors, an electromagnetic calorimeter and a hadronic calorimeter. Muons are identified by a muon system composed of alternating layers of iron and multiwire proportional chambers. The trigger consists of a hardware stage, based on information from the calorimeter and muon systems, followed by a software stage which applies a full event reconstruction. To avoid the possibility that a few events with high occupancy dominate the CPU time of the software trigger, a set of global event cuts (GEC) is applied on the hit multiplicities of most subdetectors used in the pattern recognition algorithms.

C.3 Analysis strategy

C.3.1 Data and Monte Carlo samples

The analysis is based on the dataset collected in 2010. During this period LHC collided protons with a centre-of-mass energy of 7 TeV. The data sample of this analysis corresponds to an integrated luminosity of about 37 pb^{-1}. Several Monte Carlo (MC) samples are used to estimate the backgrounds, cross check the efficiencies and to account for the effect of the underlying event. The PYTHIA 6.4 (Sjöstrand, Mrenna, and Skands 2006) generator, configured as described in Ref. (Belyaev et al. 2010), with the CTEQ6ll (Nadolsky et al.

2008) parametrisation for the PDFs is used to simulate the Drell-Yan process $Z/\gamma^\star \to \mu\mu$, $\gamma^\star$ is the virtual photon. The hard partonic interaction is calculated in leading order pQCD and higher order QCD radiation is modelled using initial and final state parton showers in the leading log approximation (Bengtsson and Sjostrand 1988). The fragmentation into hadrons is simulated in PYTHIA by the Lund string model (Andersson et al. 1983). All generated events are passed through a GEANT4 (GEANT4 Collaboration 2003) based detector simulation, trigger emulation and event reconstruction chain of the LHCb experiment.

The results are compared to theoretical predictions calculated at NLO with the program FEWZ (Gavin et al. 2011) (PDF sets of MSTW08 (Martin et al. 2009), NNPDF(Ball et al. 2010) and CTEQ6M (Nadolsky et al. 2008)), and with DYNNLO (PDF sets of MSTW08). DYNNLO is run with the factorisation and renormalisation scales set to the mass of $\gamma^\star$, while FEWZ has the scales fixed to the average mass of the bin of the measurement. The scale uncertainties are estimated with FEWZ by varying the renormalisation and factorisation scales by factors of two around the nominal value which is set to the average $\gamma^\star$ mass in a given mass bin[1]. The uncertainties for each set correspond to the PDF uncertainties at 68%[2] and the scale uncertainties added in quadrature.

C.3.2 Muon reconstruction and identification

Events with two muons are selected using a dimuon trigger which is efficient for muons with transverse momenta larger than 2.5 GeV/c. Tracks are reconstructed starting from the VELO, within which particle trajectories are approximately straight, since the detector is located before the magnet. Candidate tracks are extrapolated to the other side of the magnet and a search is made for compatible hits in the IT and OT sub-detectors. An alternative strategy searches for track segments in both the VELO and IT/OT detectors and extrapolates each to the bending plane of the magnet where they are matched. Once VELO and IT/OT-station hits have been combined, an estimate of the track momentum is available and the full trajectory can be defined. Multiple candidates may be produced by this procedure. A likelihood estimator is used to find unique solutions based on the number of sub-detector hits on the tracks and the quality of the track fits. Finally, hits in the TT sub-detector are added if consistent with the candidate tracks.

Muons are identified by extrapolating the tracks and searching for compatible hits in the four outermost muon stations.

---

[1] For the definition of the mass bins see Sect. C.4.2

[2] The uncertainties for the PDF sets from CTEQ6M and ABKM09 which are given at 90% CL are divided by 1.645.

C.3.3 Selection of Drell-Yan candidates

Candidate events are selected by requiring a pair of well-reconstructed tracks of opposite charge identified as muons which combine to an invariant mass in the range $5 \leq M_{\mu\mu} \leq 120\,\mathrm{GeV}/c^2$. Each muon track must have a momentum $p > 10\,\mathrm{GeV}/c$, a transverse momentum $p_{\mathrm{T}}^{\mu} > 3\,\mathrm{GeV}/c$ and lie in the pseudorapidity range $2 \leq \eta \leq 4.5$. For $M_{\mu\mu} > 40\,\mathrm{GeV}/c^2$ the cut on the transverse momentum is increased to $p_{\mathrm{T}} > 15\,\mathrm{GeV}/c$. The relative uncertainty on the momentum measurement is required to be less than 10% and the probability χ^2 of the track fit $\mathrm{Prob}(\chi^2/\mathrm{ndf}) > 0.1\%$. No cut on the isolation or the impact parameter of the muons is imposed. For masses above $60\,\mathrm{GeV}/c^2$, resonant Z production dominates the sample.

C.3.4 Control samples

Several control samples are used in this analysis to check the agreement between data and simulation:

- Z sample: $Z \rightarrow \mu\mu$ decays with the events fulfilling the DY selection with an invariant mass $60 \leq M_{\mu\mu} \leq 120\,\mathrm{GeV}/c^2$. This sample has a purity exceeding 0.99 (LHCb Collaboration n.d.), no background subtraction is done.
- Υ sample: $\Upsilon \rightarrow \mu\mu$ decays with the events fulfilling the DY selection with an invariant mass $9.01 \leq M_{\mu\mu} \leq 9.91\,\mathrm{GeV}/c^2$. The remaining background in the Υ sample is estimated by fitting an exponential to the side bands ($9.010 - 9.335\,\mathrm{GeV}/c^2$ and $9.585 - 9.910\,\mathrm{GeV}/c^2$) and subtracting the extrapolated background in the mass region of the Υ ($9.335 - 9.585\,\mathrm{GeV}/c^2$) (side band subtraction).
- J/ψ sample: muons from the decay of J/ψ are used to determine the muon identification efficiency for low p_{T}^{μ}. Side band subtraction is used to remove the background. The signal window is $3.07 - 3.12\,\mathrm{GeV}/c^2$ and the side bands $3.895 - 3.945\,\mathrm{GeV}/c^2$ and $3.245 - 3.295\,\mathrm{GeV}/c^2$.
- $J/\psi\,K$ sample: muons from J/ψ decays in the $B^{\pm} \rightarrow J/\psi\,K^{\pm}$ sample. No background subtraction is done. This sample is used to study the tracking efficiency at low p_{T}^{μ}.

Figure C.1 shows the relevant invariant mass distribution for the four control samples.

C.3.5 Backgrounds

While the high mass region $di - muoninvariantmass(M_{\mu\mu})$ is very pure, the background increases significantly towards low masses. Four sources of background have been studied:

- Heavy flavour background: decays of heavy flavour hadrons contribute if they decay semileptonically;

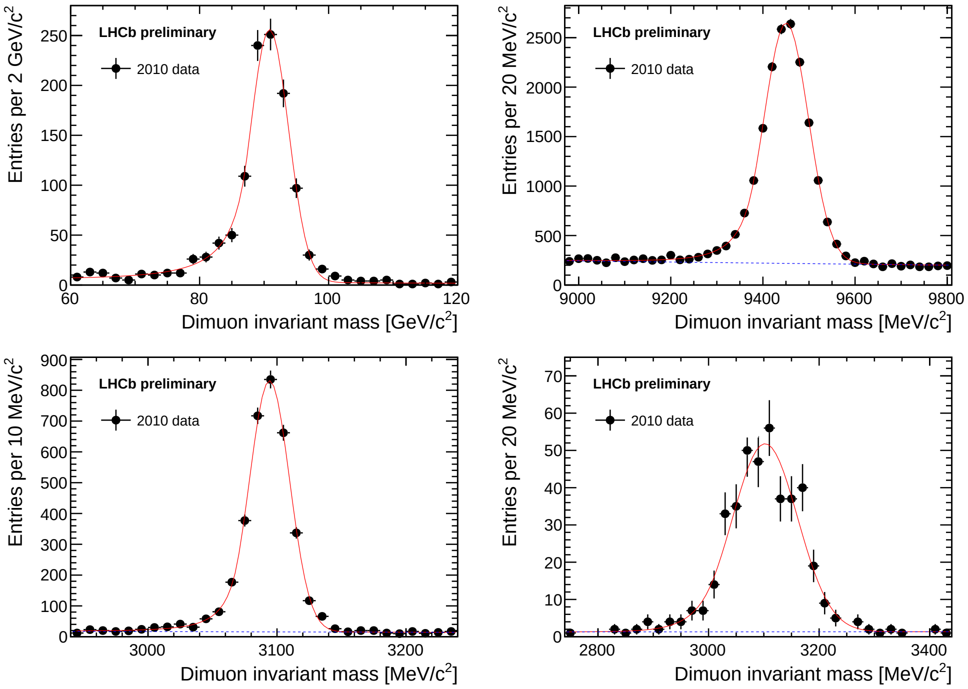

Figure C.1: The top plots show the dimuon invariant mass for the $Z \to \mu\mu$ (left) and the Υ (right) samples. The lower plots show the dimuon invariant mass for J/ψ (left) and the $J/\psi K$ (right) samples used to determine the muon identification and tracking efficiencies. A Crystal Ball function for the signal and an exponential for the background are fitted to all four distributions.

- Misidentification background (MisID): pions or kaons may be misidentified if they decay in flight or if they travel through the calorimeters and are identified as muons in the muon chambers;

- Υ background: for masses below 10 GeV/c^2 there is an additional background contribution from the radiative tail of Υ decays;

- $\gamma^\star/Z \to \tau\tau$ decays contribute if both taus decay leptonically to muons and neutrinos.

There is also a background contribution from events with one muon from a semileptonic decay and a misidentified muon. This is automatically accounted for by the procedure described below. This is also true for muons from a W decay with a misidentified muon in the same event. Control samples have been selected to study the first two background contributions. For the MisID background, events are selected from events which have not fired the muon triggers with two tracks coming from the same vertex (MinBias). Each of the two tracks is then weighted with the probability to be misidentified as a muon. This probability is measured as the fraction of tracks identified as muons in randomly triggered events and is parametrised as a function of the longitudinal momentum p_L by a function of the form

$$1 - e^{-\alpha/p_L} + \beta \cdot p_L + \gamma, \tag{C.1}$$

where α, β and γ are free parameters. The exponential term parametrises the misidentification probability due to decay in flight and the second term due to punch through of hadrons. Figure C.2 shows the misidentification probability due to decay in flight as a function of p_L together with the fit. A second sample is taken from events with two identified muons with the same charge (SameSign). A cut on the impact parameter IP $< 50\,\mu\text{m}$ and a vertex $\chi^2 < 3$ is applied to both muons to remove contributions from heavy quark decays.

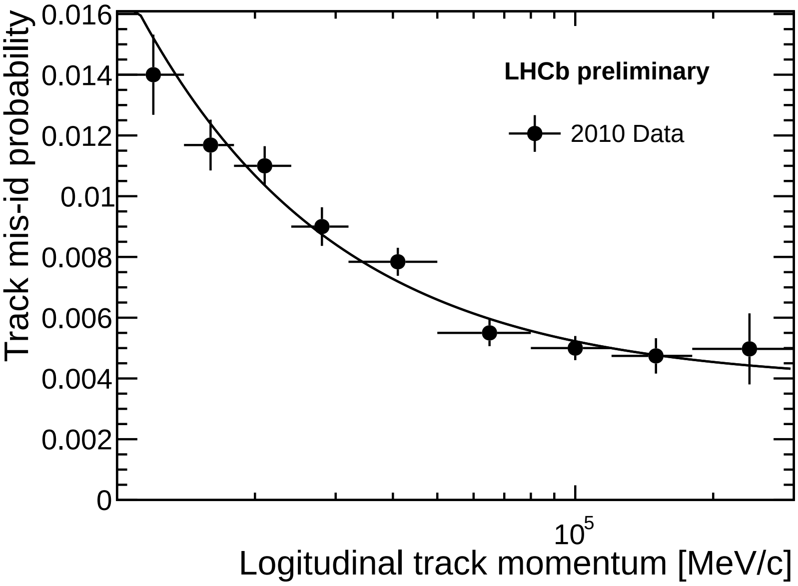

Figure C.2: Misidentification probability for muons due to decay in flight as a function of the longitudinal momentum together with the fit for the misidentification probability.

The heavy quark background is studied with a sample selected from data by requiring that the two muons do not come from the vertex (HQVertex). They must have a vertex $\chi^2 > 5$ and IP $> 30\,\mu\text{m}$. The HQVertex sample also contains any contribution from $\gamma^\star/Z \to \tau\tau$ decays. In addition, a sample was taken from simulated $b\bar{b}$ events decaying into muons (HQMC). For all the background samples, the tracks have to fulfil the standard selection criteria except the muon identification for the MinBias sample.

C.4 Signal extraction

C.4.1 Muon isolation

The extraction of the signal yield makes use of the muon isolation. This is defined as the fraction of the transverse momenta of the muon-jet carried by the muon, $z = p_{\mathrm{T}}^{\mu}/p_{\mathrm{T}}^{Jet}$. The muon-jet is defined as the jet which contains the muon. The jet is reconstructed with the anti-kt algorithm (Cacciari and Salam 2006) with the size $R = \sqrt{\Delta\eta_{ij}^2 + \Delta\varphi_{ij}^2} = 0.5$. Here, $\Delta\eta_{ij}$ and $\Delta\varphi_{ij}$ give the separation of two particles in the jet in η and azimuthal angle φ. The minimum muon isolation (MinIso) of the two muons is used. For the signal the two muons are expected to have an isolation distribution close to unity. Muons in background events tend to have lower values since they are usually produced in the same direction as the other fragmentation products. Taking MinIso ensures that events with a muon from a semileptonic decay and a misidentified muon are correctly taken into account by considering heavy flavour and MisID backgrounds separately.

The Υ and Z samples are used to check that the simulation describes the MinIso distribution. These distributions are shown in Fig. C.3 for background subtracted Υ and Z events together with simulated events. Good agreement between data and simulation is observed. Figure C.4 shows the MinIso distribution for the two background samples used to describe the background of heavy flavour and muon misidentification. Differences in the shapes of the two samples are seen for both of the background types. These differences are accounted for in the systematic uncertainties as described below. As the HQMC sample does not include decays of $c\bar{c}$ events it was checked that the MinIso distribution of $c\bar{c}$ events has a similar distribution as $b\bar{b}$ events. The two distributions are found to be in good agreement which justifies the use of the HQMC sample for a cross check of the heavy quark background.

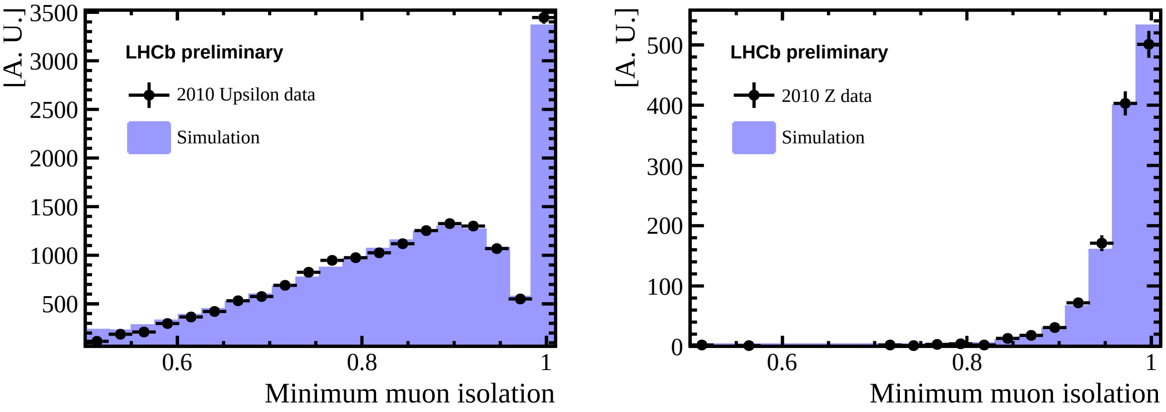

Figure C.3: Comparison of data and simulation of the distribution of the minimum isolation for muons from $\Upsilon \rightarrow \mu\mu$ (left) and $Z \rightarrow \mu\mu$ (right) decays.

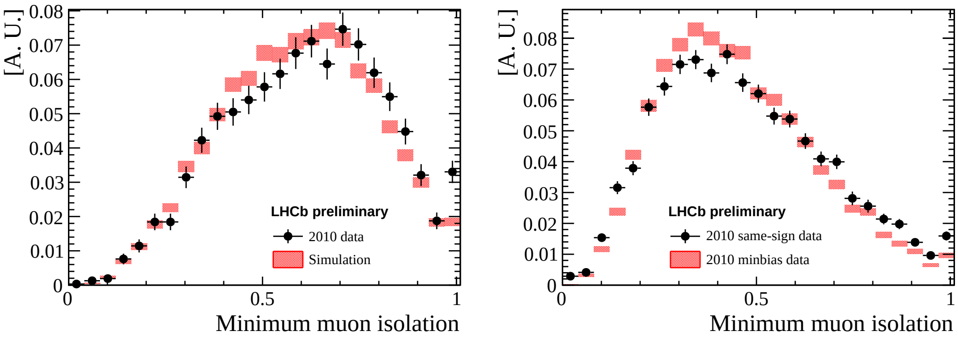

Figure C.4: Comparison of data and simulation of the distribution of the minimum isolation for muons from the two heavy flavour templates (left) and the two templates for MisID (right).

C.4.2 Signal Yield

The signal yield is extracted by a fit to the MinIso distribution of the two muons in data to templates for the signal and the backgrounds. The TFractionFitter ROOT (Filthaut and Wijngaarden 2002) package is used for this fit. Fits are performed in nine different mass bins ([5−7], [7−9.0], [10.5−12.5], [12.5−15], [15−20], [20−30], [30−40], [40−60], [60−120] GeV/c^2) and in five rapidity ($[2-2.5], [2.5-3], [3-3.5], [3.5-4], [4-4.5]$) bins in two mass regions ($[10.5-20], [20-40]$ GeV/c^2). The mass bins are chosen such that the mass range of the Υ is excluded. The following signal and background templates have been used:

- $\gamma^\star \to \mu\mu$: the simulation from PYTHIA is used for the signal template;
- Heavy flavour background: the heavy quark template is taken from data using the HQVertex sample;
- MisID background: the MisID template is taken from data using the MinBias sample;
- Background from Υ decays: the template for Υ decays is taken from MC. The normalisation of the template is fixed to the number of expected Υ events. The normalisation is determined as follows: Υ-MC is used to determine the fraction of Υ events in the bins below 9 GeV/c^2 to the number of Υ events in the range $9.0-10.5$ GeV/c^2. The number of Υ events observed in data in this mass window is then used to calculate normalisation in the two mass bins below 9 GeV/c^2.

In each bin the normalisation of the signal and the heavy quark and MisID background contributions is fitted; the normalisation of different bins in rapidity and mass are allowed to vary independently. The purity, ρ, in each bin is defined as the number of signal events divided by the total number of events in the bin. Figure C.5 shows the fits for the nine mass bins, Figs. C.6-C.7 the fits for the five rapidity bins in two distinct mass regions. The quality of all the fits is good with χ^2 per degree of freedom in the range of one. The small bump visible at MinIso =0.5 comes from cloned muon tracks.

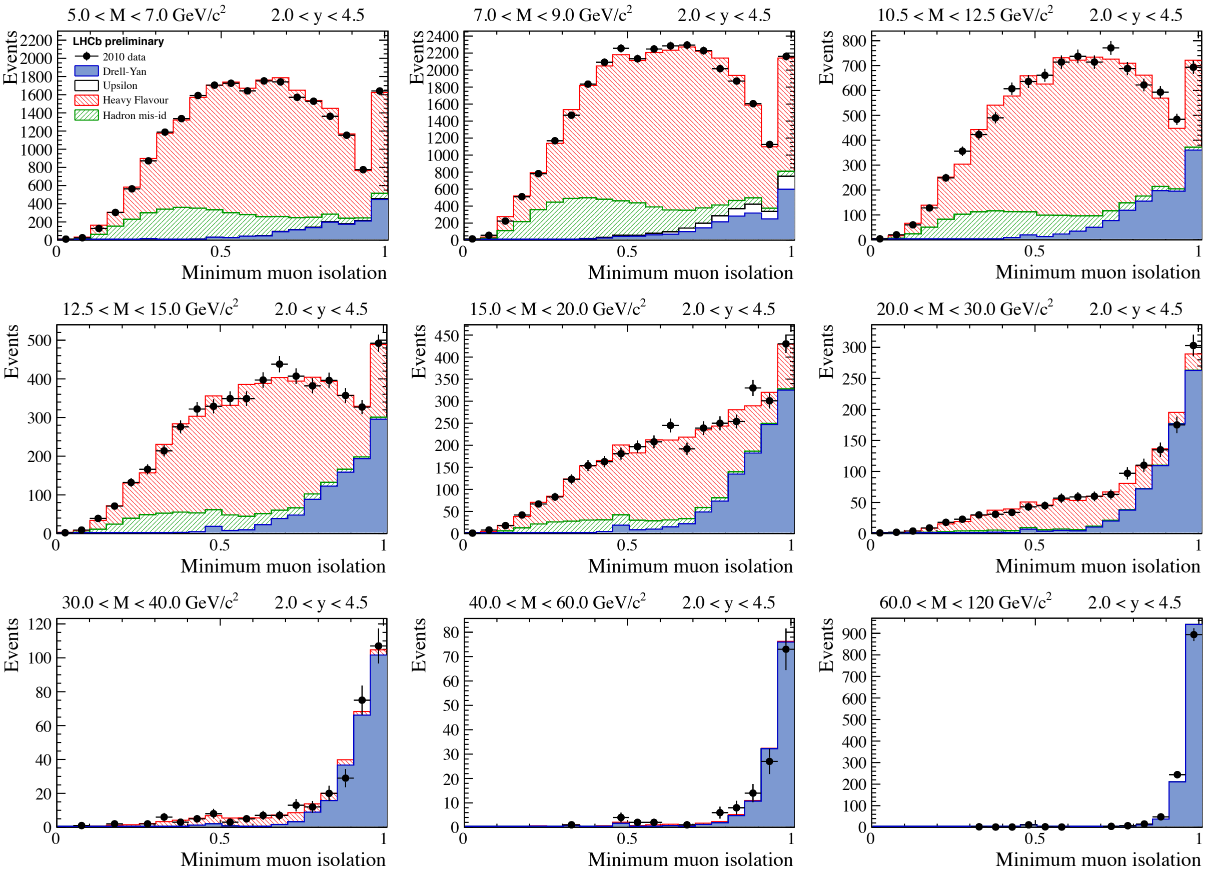

Figure C.5: Template fit to the minimum muon isolation distribution for nine mass bins. The data (points) are compared to the fitted contributions from $\gamma^\star \to \mu\mu$ (blue) and backgrounds from heavy flavour decays (red) and muon misidentification(green).

It was checked that other variables such as pseudorapidity and transverse momentum of the two muons, muon momentum asymmetry, pseudorapidity difference of the two muons, dimuon invariant mass and dimuon rapidity are well described by the sum of signal and background contributions with the normalisation as determined by the fit.

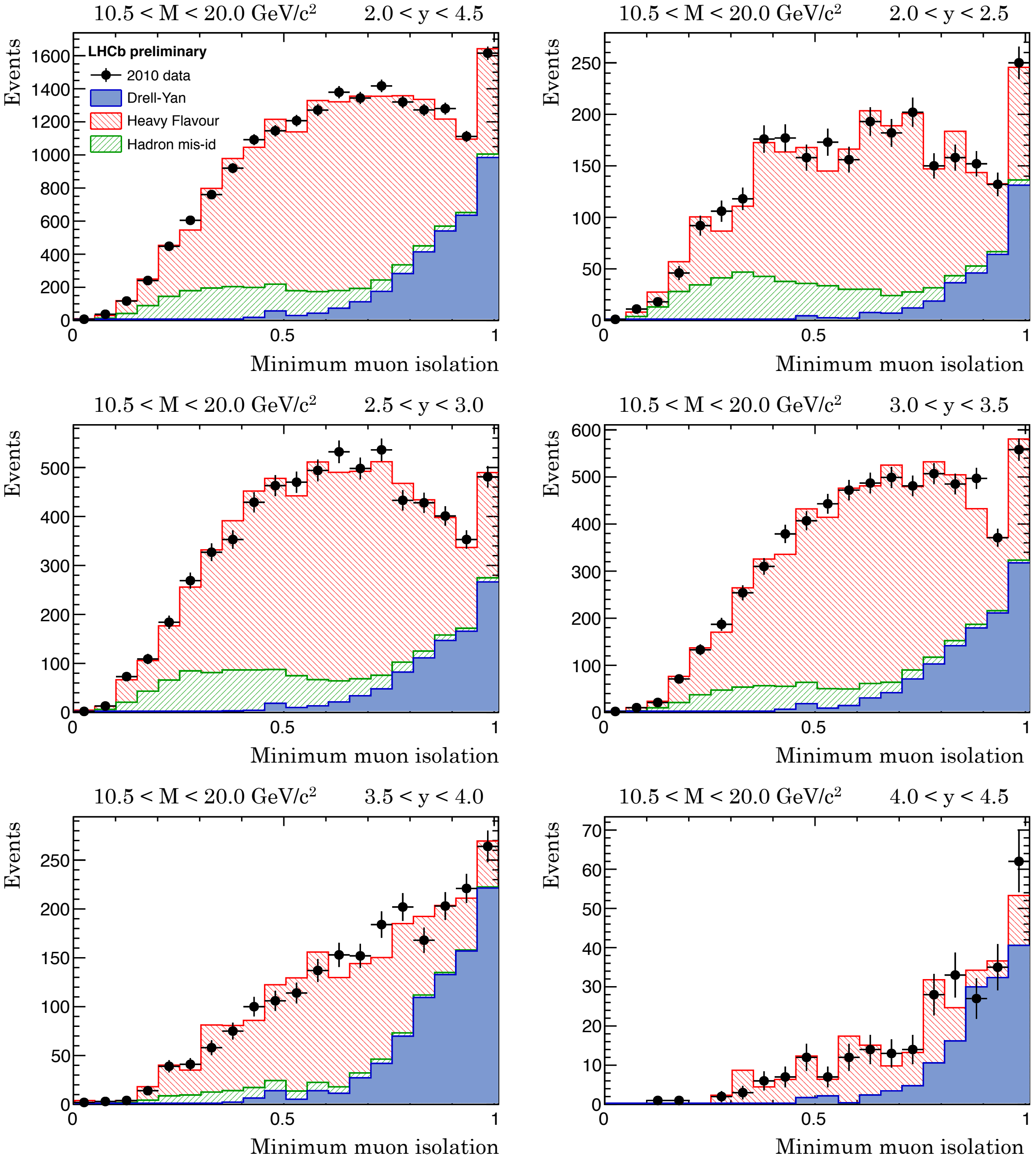

Figure C.6: Template fit to the minimum muon isolation distribution for five rapidity bins and $10.5 < M_{\mu\mu} < 20\,\mathrm{GeV}/c^2$. The first plot shows the fit for the full rapidity range. The data (points) are compared to the fitted contributions from $\gamma^\star \to \mu\mu$ (blue) and backgrounds from heavy flavour (red) decays and muon misidentification (green).

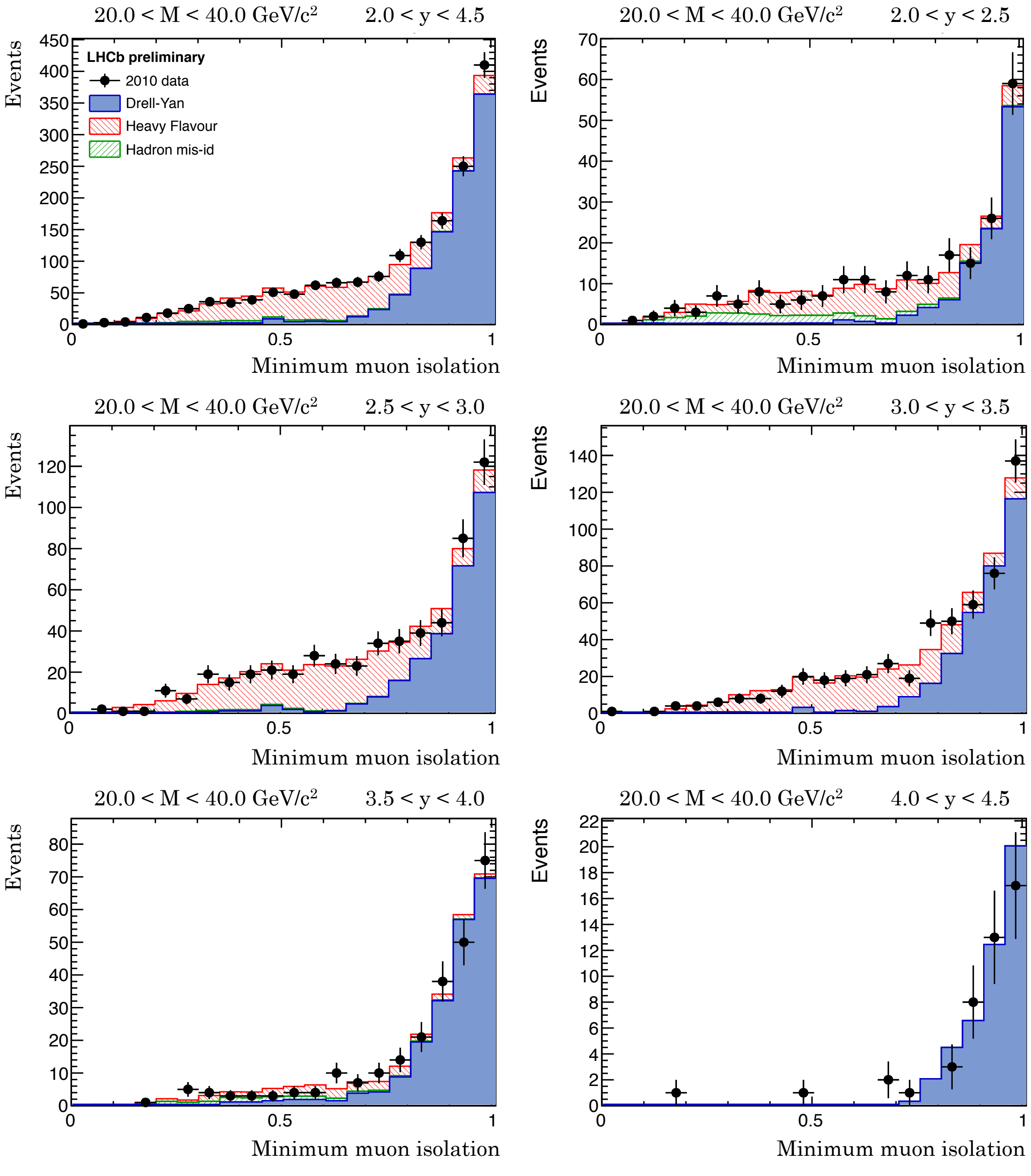

Figure C.7: Template fit to the minimum muon isolation distribution for five rapidity bins and $20 < M_{\mu\mu} < 40\,\mathrm{GeV}/c^2$. The first plot shows the fit for the full rapidity range. The data (points) are compared to the fitted contributions from $\gamma^\star \to \mu\mu$ (blue) and backgrounds from heavy flavour (red) decays and muon misidentification (green).

C.4.3 Stability of the fit

The stability of the fit was checked by repeating the fit with different templates, fitting to different distributions, and varying the cuts for the background and signal samples. The following checks have been done:

1. Heavy quark template: repeat the fit with the template from the HQMC instead of the HQVertex sample, the purity is corrected for the additional contribution from $\gamma^\star/Z \to \tau\tau$ decays;
2. Muon misidentification template: repeat the fit with the template from the SameSign instead of the MinBias sample;
3. Signal template: distort the distribution of the minimum isolation of the two muons by applying a stretching factor, f, of 0.95 and 1.05 to the MinIso distribution:

$$\mathrm{MinIso}' = 1 - (1 - \mathrm{MinIso}) * f;$$

4. Definition of the HQVertex sample: repeat the fit with a cut on $\chi^2 > 4$, $\chi^2 > 6$, IP $> 25\,\mu\mathrm{m}$ and IP $> 50\,\mu\mathrm{m}$ for the HQVertex sample;
5. Change the ratio of signal and background: repeat the fit with a cut on IP $< 150\,\mu\mathrm{m}$ for data.

The last two items are considered as consistency checks of the analysis and are not included in the systematic uncertainty. The observed differences vary within the error of the fit. For the fit with the IP cut for data the fitted number of signal events is corrected for the the loss of events due to the IP cut. This efficiency value is taken from the Z sample.

C.4.4 Efficiencies

C.4.4.1 Trigger

The trigger efficiency of the hardware and first stage software trigger is estimated using a sample triggered by the single muon trigger line which is efficient for muons with transverse momenta larger than $1.5\,\mathrm{GeV}/c$. It is assumed that the dimuon trigger efficiency factorises and it can be determined by multiplying the trigger efficiency of the two muons. A sample with dimuon events is selected with the mass restricted to the Z ($60 < M_{\mu\mu} < 120\,\mathrm{GeV}/c^2$) and Υ ($9 < M_{\mu\mu} < 9.9\,\mathrm{GeV}/c^2$) mass regions. One of the muons is required to trigger the single muon trigger line. The single muon trigger efficiency is then determined as the fraction of events with both muons triggering the muon trigger. The efficiencies determined from the Υ sample are corrected to take into account background by performing a sideband subtraction. The efficiency is determined as a function of p_T for five different bins in η and for both charges individually. It was checked in MC that in fact the assumption of factorisation holds. The dimuon efficiency is then determined as the product of the two single muon efficiencies. The systematic uncertainty of the trigger efficiency is taken as the statistical uncertainty.

The efficiency of the second software trigger stage is determined from simulation and cross checked in data for muons with $p_{\mathrm{T}}^{\mu} > 20\,\mathrm{GeV}/c$ where an independent trigger line was available. It was found that in data the efficiency is 1% lower than in MC with no dependence on the transverse momentum. This correction with an additional systematic uncertainty of 1% is taken into account.

C.4.4.2 Global event cuts

The effect of the global event cuts is evaluated from data. The main effect comes for the requirement that the number of VELO clusters is less than 3000. The efficiency is studied as a function of clusters in the inner tracker by adding randomly triggered events to Drell-Yan events with one primary vertex to simulate higher pile up events. An average efficiency of 91% is found which varies strongly with the amount of activity in the detector. The correction for the GEC efficiency is therefore applied as a function of the number of clusters in the inner tracker.

C.4.4.3 Muon identification efficiency

The muon identification efficiency is measured in data using a tag and probe technique using the J/ψ and Z samples by requiring that there is a good muon and a track which combine to the invariant mass of the J/ψ or Z. The fraction of tracks which are identified as muons gives the overall muon identification efficiency. No dependence on p_{T}^{μ}, momentum and azimuthal angle is observed within the statistical uncertainties. The efficiency is corrected as a function of η^{μ} where a small variation is seen.

C.4.4.4 Tracking efficiency

The track finding efficiency which accounts for both the track reconstruction and the track quality requirements, is also determined using a tag and probe method for muons in the Z and $B \to J/\psi K$ sample. The latter accesses the low transverse momentum range. The two samples cover the range $1 - 70$ GeV/c in transverse momentum. The tag muon is defined as the one which fired the single muon line and passes the standard selection criteria. The probe muon is defined as a track segment (muon-stub) reconstructed in the muon stations. Hits in the TT stations are attached to this segment to improve the resolution. Those track combinations which are consistent with the invariant mass of the Z or the J/ψ are used to determine the efficiency. The efficiency is defined as the fraction of muon-stub tracks associated to a track with all the quality requirements of the analysis. The efficency is corrected in three bins of p_{T}^{μ} ([3-7], [7-30],[30-120] GeV/c]) as a function of η^{μ}.

C.4.5 Acceptance

The cross-section is measured in the kinematic range of the measurement, the only acceptance correction comes from migrations into and out of the phase space. The acceptance is determined from simulation and is consistent with one.

C.4.6 Luminosity

The luminosity is measured by two methods, a Van der Meer scan (van der Meer 1968) where colliding beams are moved transversely across each other to determine the beam profile, and a beam gas method (Ferro-Luzzi 2005; LHCb Collaboration 2012), where reconstructed beam-gas interaction vertices near the beam crossing point determine the beam profile. Both methods give similar results and are estimated to have a precision of order 3.5%. The dataset for this analysis corresponds to an integrated luminosity of 37.1 ± 1.3 pb^{-1}.

C.4.7 Corrections

Corrections are applied for bin-to-bin migrations. They are estimated from MC and found to be small, below 1% for most of the bins. No corrections are yet applied for final state radiation.

C.5 Cross-section measurement

C.5.1 Cross-section definition

Cross-sections are quoted in the kinematical range defined by the kinematic cuts on the muons ($p > 10\,\mathrm{GeV}/c$, $2.5 < \eta^{\mu} < 4.5$, $p_{\mathrm{T}}^{\mu} > 3\,\mathrm{GeV}/c$ and $p_{\mathrm{T}}^{\mu} > 15\,\mathrm{GeV}/c$ for $M_{\mu\mu} > 15\,\mathrm{GeV}/c^2$). The cross-section in a given bin of rapidity y (invariant mass $M_{\mu\mu}$) is defined as

$$\sigma = \frac{\rho}{A\mathcal{L}} \sum_{i=1}^{N} \frac{1}{\varepsilon_i}$$

$\mathcal{L}$ is the integrated luminosity, N the number of candidates in the respective measurement bin, ε the efficiency of the event, ρ the purity and A the acceptance. The sum runs over all events in the bin. Most efficiencies are calculated as a function of the pseudorapidity and transverse momenta of the two muons; for the GEC efficiency is a function of the number of clusters in the inner tracker.

C.5.2 Systematic uncertainties

Systematic uncertainties on the measurement arise from: the knowledge of the luminosity; the efficiency determination; the sample purity. For the latter, the main uncertainty arises from the uncertainty on the shape of the templates.

The following sources have been considered:

- The uncertainty on the luminosity (LHCb Collaboration 2012) contributes 3.5% to the systematic uncertainty.
- The statistical uncertainty of the tracking efficiency is taken as systematic uncertainty. It leads to an uncertainty on the cross-sections between 4 and 10%.
- The statistical uncertainty of the muon identification efficiency is taken as systematic uncertainty. It leads to an uncertainty on the cross-sections of the order of 1.4%.
- The statistical uncertainty of the trigger efficiency is taken as systematic uncertainty. It leads to an uncertainty on the cross-sections between 1.7% at high to 4.3% at low masses.
- The statistical uncertainty of the GEC efficiency is taken as systematic uncertainty. It leads to an uncertainty on the cross-sections of about 1.3%.
- Uncertainty on the shape of the heavy quark template: the fit is repeated with the template from the HQMC instead of the HQVertex sample. Reasonable agreement was found in all the bins between the two fits. Half of the difference is taken as systematic uncertainty, for masses below 9 GeV/c^2 the full difference is taken. The systematic uncertainty due to the shape of the templates was increased for masses below 9 GeV/c^2, since the template shapes are understood less. The systematic uncertainty in the lowest mass bin is 24%, dropping to below 1% for masses larger than 20 GeV/c^2.
- Shape of the template for muon misidentification: the fit is repeated with the template from SameSign instead of the MinBias sample. Half of the difference is taken as systematic uncertainty, for masses below 9 GeV/c^2 the full difference is taken. The systematic uncertainty in the lowest mass bin is 4%, dropping to below 1% for masses larger than 20 GeV/c^2.
- Signal template: the signal template is taken from simulation. To test how well the simulation and data agree the MinIso distribution was distorted by stretching it. Half of the difference of the fit with the stretched distributions is taken to estimate the uncertainty from the signal template. For masses below 9 GeV/c^2 the full difference

is taken. The systematic uncertainty in the lowest mass bin is 8%, dropping to below 1% for masses larger than 20 GeV/c^2.

C.6 Results

Figure C.8 shows the differential cross-section as a function of the invariant mass of the dimuons together with predictions from PYTHIA and NLO calculations. The PYTHIA cross-section is normalised to the cross-section measured in the highest mass bin. NLO predictions are only available for FEWZ for masses larger than 7 GeV/c^2 and for DYNNLO for $M_{\mu\mu} > 12.5\,\text{GeV}/c^2$. The bin between 5 and 7.5 GeV/c^2 has a limited kinematical acceptance due to the cut on the transverse momentum of the muons. Figure C.9 shows the same data in comparison with FEWZ predictions with three different PDF sets. Here, only the uncertainties due to the PDF uncertainty is shown; these are smaller than the theory uncertainties at NLO. Figure C.10 shows the differential cross-section as a function of the rapidity of the dimuons in two different mass bins. PYTHIA underestimates the Drell-Yan cross-section by more than a factor two but describes the shapes in y and mass reasonably well. The FEWZ predictions with three different PDFs describe all the shapes and also the normalisation over the mass region where the calculation is valid. The cross-sections are all listed in Tables C.1 and C.2.

C.7 Conclusions

The Drell-Yan cross-section has been measured for dimuon invariant masses $5 < M_{\mu\mu} < 120\,\text{GeV}/c^2$ using data collected in 2010. The muons are required to have a momentum larger than 10 GeV/c and a transverse momentum larger that 3 GeV/c. For masses above 40 GeV/c^2 the transverse momentum needs to be larger than 15 GeV/c. The signal is extracted by fitting signal and background templates to the isolation distribution of the muons. At low masses the dominant systematic uncertainty comes from the uncertainty of the shapes of the templates. The cross-section is measured as a function of the invariant dimuon mass and as a function of the dimuon rapidity in two different invariant mass regions. While the PYTHIA predictions agree in shape but are too low in normalisation, reasonable agreement is found with NLO predictions in those mass regions where the calculations are available.

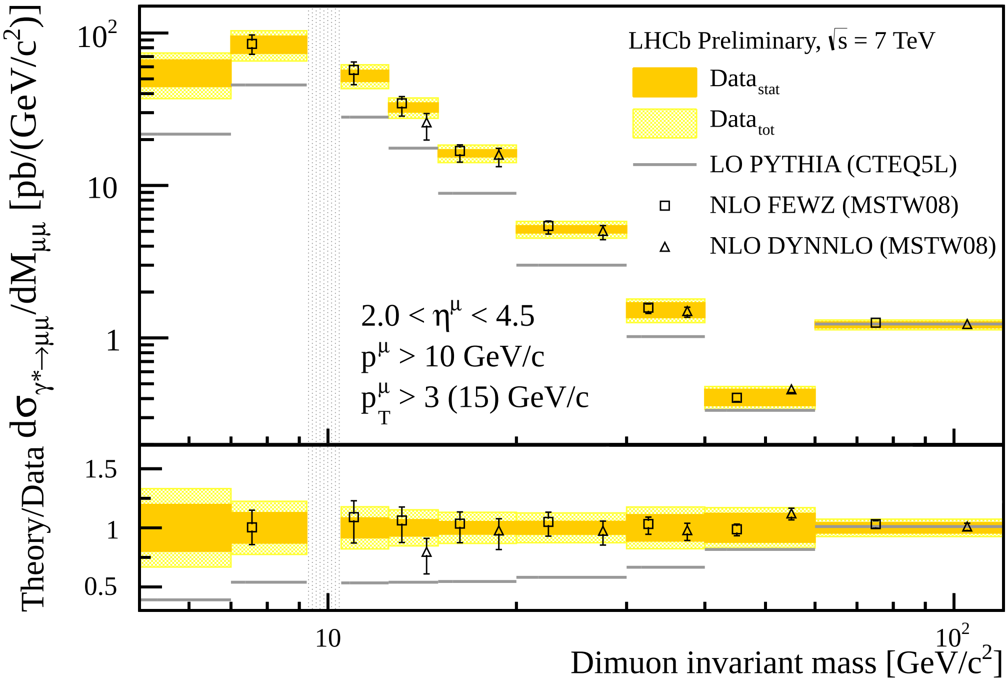

Figure C.8: Differential cross-section for $\gamma^\star \to \mu\mu$ as a function of $M_{\mu\mu}$. The dark shaded (orange) bands correspond to the statistical uncertainties, the light shaded (yellow) band to the statistical and systematic uncertainties added in quadrature. Superimposed are the PYTHIA predictions and the NLO predictions from FEWZ and DYNNLO; they are displaced horizontally for presentation. The shaded vertical band corresponds to the mass region of the Υ which is not included in the measurement. The uncertainties of the NLO predictions contain the PDF uncertainties evaluated at the 68% confidence level and the theoretical errors added in quadrature. The two bins with $M_{\mu\mu} > 40\,\mathrm{GeV}/c$ have a cut of $p_{\mathrm{T}}^{\mu} > 15\,\mathrm{GeV}/c$ for the data and the predictions. The lower plot shows the ratio of the predictions or the uncertainties to the data.

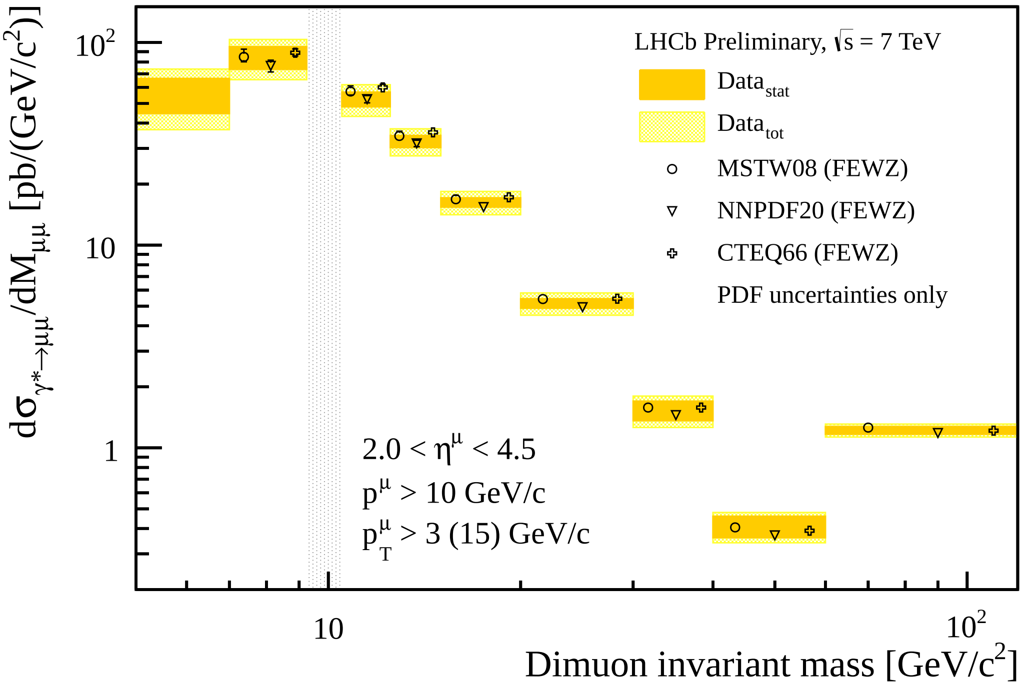

Figure C.9: Differential cross-section for $\gamma^\star \to \mu\mu$ as a function of $M_{\mu\mu}$. The dark shaded (orange) bands correspond to the statistical uncertainties, the light shaded (yellow) band to the statistical and systematic uncertainties added in quadrature. Superimposed are NLO predictions from FEWZ with the PDF sets from MSTW08, NNPDF and CTEQ; they are displaced horizontally for presentation. The NLO uncertainties correspond to the PDF uncertainties evaluated at the 68% confidence level. The two bins with $M_{\mu\mu} > 40\,\mathrm{GeV}/c$ have a cut of $p_\mathrm{T}^\mu > 15\,\mathrm{GeV}/c$ for the data and the predictions.

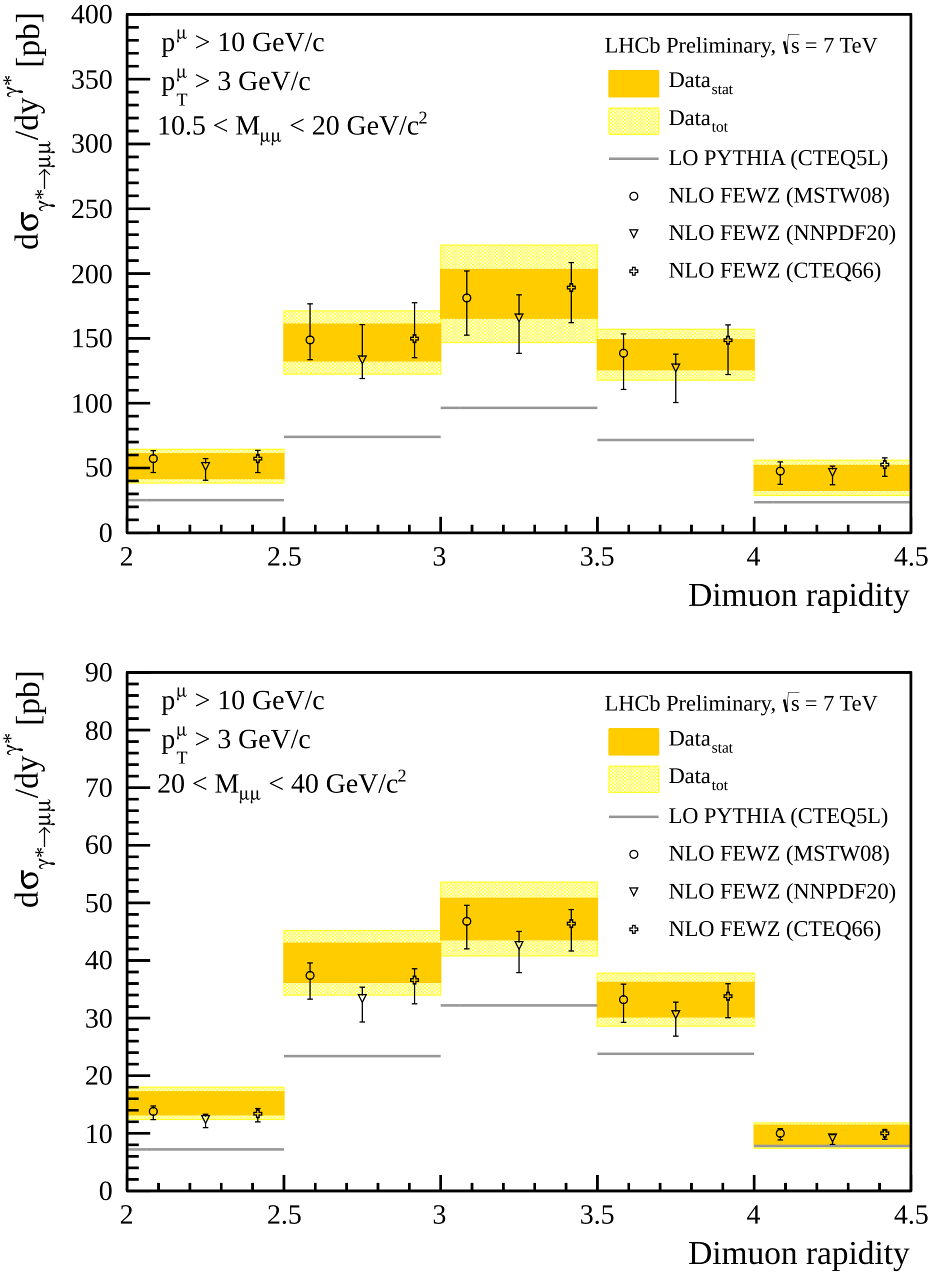

Figure C.10: Differential cross-section for $\gamma^\star \to \mu\mu$ as a function of y for two different mass regions of the dimuon system. The dark shaded (orange) bands correspond to the statistical uncertainties, the light shaded (yellow) band to the statistical and systematic uncertainties added in quadrature. The shaded vertical band corresponds to the mass region of the Υ which is not included in the measurement. Superimposed are NLO predictions from FEWZ with the PDF sets from MSTW08, NNPDF and CTEQ; they are displaced horizontally for presentation. The NLO uncertainties correspond to the PDF uncertainties evaluated at the 68% confidence level.

C.8 Appendix: Tables of results

Table C.1: Cross section in bins of the invariant mass of the muon pair. The two bins with $M_{\mu\mu} > 40\,\mathrm{GeV}/c$ have a cut of $p_{\mathrm{T}}^{\mu} > 15\,\mathrm{GeV}/c$.

$M_{\mu\mu}$ GeV/c^2	Cross-section [pb]	Stat. [pb]	Syst. [pb]	Lumi. [pb]	[pb]
5 - 7	111.0	21.9	29.3	3.9	36.8
7 - 9.25	190.0	24.4	34.4	6.7	42.7
10.5 - 12.5	105.2	8.8	16.1	3.7	18.7
12.5 - 15	81.3	5.6	10.6	2.9	12.4
15 - 20	81.3	4.3	9.4	2.9	10.7
20 - 30	51.6	2.8	5.6	1.8	6.5
30 - 40	15.3	1.7	2.1	0.5	2.7
40 - 60	8.2	1.0	0.9	0.3	1.4
60 - 120	73.2	3.2	3.5	2.6	5.4

Table C.2: Cross section in bins of the rapidity of the dimuons for two different mass regions.

$M_{\mu\mu}$ GeV/c^2	y	Cross-section [pb]	Stat. [pb]	Syst. [pb]	Lumi. [pb]	Total [pb]
10.5 - 20	2.0 - 2.5	25.7	4.8	4.2	0.9	6.5
10.5 - 20	2.5 - 3.0	73.4	7.1	9.6	2.6	12.2
10.5 - 20	3.0 - 3.5	92.2	9.4	16.0	3.2	18.8
10.5 - 20	3.5 - 4.0	68.7	5.8	7.6	2.4	9.8
10.5 - 20	4.0 - 4.5	21.2	4.8	4.8	0.4	6.8
20 - 40	2.0 - 2.5	7.7	1.0	0.9	0.3	1.4
20 - 40	2.5 - 3.0	19.8	1.7	2.2	0.7	2.8
20 - 40	3.0 - 3.5	23.6	1.8	2.5	0.8	3.2
20 - 40	3.5 - 4.0	16.6	1.5	1.6	0.6	2.3
20 - 40	4.0 - 4.5	4.8	0.9	0.6	0.2	1.1

References

Andersson, B. et al. (1983). “Parton fragmentation and string dynamics”. In: *Phys.Rept.* 97, pp. 31–145. DOI: 10.1016/0370-1573(83)90080-7.

Ball, R. D. et al. (2010). “A first unbiased global NLO determination of parton distributions and their uncertainties”. In: *Nucl.Phys.* B838, pp. 136–206. DOI: 10.1016/j.nuclphysb.2010.05.008.

Belyaev, I. et al. (2010). “Handling of the generation of primary events in Gauss, the LHCb simulation framework”. In: *Nuclear Science Symposium Conference Record (NSS/MIC), 2010 IEEE*, pp. 1155–1161. DOI: 10.1109/NSSMIC.2010.5873949.

Bengtsson, M. and T. Sjostrand (1988). “Parton showers in leptoproduction events”. In: *Z.Phys.* C37, p. 465. DOI: `10.1007/BF01578142`.

Cacciari, M. and G. P. Salam (2006). “Dispelling the N^3 myth for the k(t) jet-finder”. In: *Phys. Lett.* B641, pp. 57–61. DOI: `10.1016/j.physletb.2006.08.037`.

CMS Collaboration (2011). “Measurement of the inclusive W and Z production cross sections in pp collisions at $\sqrt{s} = 7$ TeV”. In: *JHEP* 10, p. 132. DOI: `10.1007/JHEP10(2011)132`.

Ferro-Luzzi, M. (2005). “Proposal for an absolute luminosity determination in colliding beam experiments using vertex detection of beam-gas interactions”. In: *Nucl.Instrum.Meth.* A553, pp. 388–399. DOI: `10.1016/j.nima.2005.07.010`.

Filthaut, F. and B. Wijngaarden (2002). *TFractionFitter*. ROOT Reference Guide. URL: `http://root.cern.ch/root/html/TFractionFitter.html` (visited on 2014-09-22).

Gavin, R. et al. (2011). “FEWZ 2.0: A code for hadronic Z production at next-to-next-to-leading order”. In: *Comput.Phys.Commun.* 182, pp. 2388–2403. DOI: `10.1016/j.cpc.2011.06.008`.

GEANT4 Collaboration (2003). “GEANT4: A simulation toolkit”. In: *Nucl. Instrum. Meth.* A506, p. 250. DOI: `10.1016/S0168-9002(03)01368-8`.

LHCb Collaboration. “Updated measurements of W and Z production at $\sqrt{s} = 7$ TeV with the LHCb experiment”. In: LHCb-CONF-2011-039.

LHCb Collaboration (2008). “The LHCb detector at the LHC”. In: *JINST* 3, S08005. DOI: `10.1088/1748-0221/3/08/S08005`.

LHCb Collaboration (2012). “Absolute luminosity measurements with the LHCb detector at the LHC”. In: *JINST* 7, P01010. DOI: `10.1088/1748-0221/7/01/P01010`.

Martin, A. et al. (2009). “Parton distributions for the LHC”. In: *Eur.Phys.J.* C63, pp. 189–285. DOI: `10.1140/epjc/s10052-009-1072-5`.

Nadolsky, P. M. et al. (2008). “Implications of CTEQ global analysis for collider observables”. In: *Phys.Rev.* D78, p. 013004. DOI: `10.1103/PhysRevD.78.013004`.

Sjöstrand, T., S. Mrenna, and P. Skands (2006). “PYTHIA 6.4 physics and manual”. In: *JHEP* 05, p. 026. DOI: `10.1088/1126-6708/2006/05/026`.

van der Meer, S. (1968). *Calibration of the effective beam height in the ISR*. CERN-ISR-PO-68-31.

Acknowledgements

This thesis would not have been possible without the advice and support of many people. It is impossible to name all those who contributed to my happiness and success during these last years. Still I want to explicitly thank the most prominent ones.

I am grateful to Ueli Straumann for the opportunity to do a PhD. His suggestions have been invaluable throughout all my studies and working in his group has been a very agreeable and most instructive experience.

I would like to thank Katharina Müller and Jonny Anderson for their continuous support, collaboration and advice. Katharina I want to thank explicitly for taking care of all the theory calculations needed for this thesis.

The excellent working environment in Ueli Straumann's group would not have been possible without its past and present members. So my sincere thanks go to all of them. I owe many insights, good ideas and happy hour to them.

Finally, I wish to thank my family and friends for their patience, encouragements and support during these last years.

Curriculum Vitae

Personal information:

Last name	Chiapolini
First name	Nicola
Day of Birth	21st June 1982
Hometown	Winterthur, ZH

Education:

2010 - 2014	PhD in particle physics, University of Zurich Thesis: *Low-Mass Drell-Yan Cross-Section Measurements with the LHCb Experiment* Supervisor: U. Straumann
2007 - 2009	Master of Science in physics, University of Zurich Thesis: *Online Monitoring for the Silicon Tracker of the LHCb Experiment* Supervisor: U. Straumann
2003 - 2007	Bachelor of Science in physics, University of Zurich Thesis: *The LHCb TT production database and an overview of quality characteristics of the detector modules* Supervisor: U. Straumann
1997 - 2002	Matura at Kantonsschule Zürcher Oberland, Wetzikon Typus: *C*